Transforming life and reliability of railway overhead power lines

The University Of Sheffield.

Samuel G. Hayes

Supervisor: Prof. D.I. Fletcher
Dr. A.E. Beagles

Department of Mechanical Engineering
University of Sheffield

This dissertation is submitted for the degree of
Doctor of Philosophy

May 2021

To my family . . .

Declaration

I, the author, confirm that the Thesis is my own work. I am aware of the University's Guidance on the Use of Unfair Means (www.sheffield.ac.uk/ssid/unfair-means). This work has not been previously been presented for an award at this, or any other, university.

Samuel G. Hayes
May 2021

Acknowledgements

I would like to thank my supervisors Prof. David Fletcher and Dr. Adam Beagles for their enthusiasm, support and mentorship throughout this PhD. I also want to thank Dr. Rob Howell for his advice and assistance with the wind tunnel experiments and for agreeing to take over from Dr. Beagles as secondary supervisor. I would like to thank Oliver Cooper for his assistance and machining the equipment necessary for the experimental tests in the wind tunnel. Also, to the technicians in the Engineering workshop, my thanks for preparing the wire samples prior to the experimental work. My thanks to Katherine Chan at Furrer+Frey GB for supervising the work and providing data and samples throughout the project along with Noel Dolphin and Rob Daffern for fruitful discussions and supplying the conductor bar.

I would like to acknowledge the support from Patric Mak at Network Rail for providing data for the validation of the work presented in this thesis, and to Chris Bryan for being there from the start and for the fruitful discussions and advice throughout the last four years.

I would like to recognise the financial support provided by the Engineering and Physical Sciences Research Council (EPSRC) [grant number 1802703], the University of Sheffield and Furrer+Frey GB throughout this PhD, without which the project would not have been possible.

Finally, to my friends and the Red Deer. I'd never have made it this far without you.

Abstract

This thesis investigates the dynamic behaviour of an overhead line system interacting with a pantograph under conditions affecting both the mechanical aspects of the system, as well as the geometry of the overhead line. To determine the effects of environmental conditions such as crosswinds, an experiment making use of the Sheffield Large Scale Wind Tunnel was developed to assess the effects of wear and the wind angle of attack on the aerodynamic forces acting on the contact wire. Using the predicted aerodynamic forces, the effect of crosswinds on the catenary pantograph interaction has been investigated. By considering the wear state of the contact wire, the dynamic performance of the system worsens due to larger amplitude oscillations caused by aerodynamic lift forces, and that wear was a bigger driver of contact force variation than lateral deflections due to aerodynamic drag.

This thesis also investigates the effects of contact wire irregularity beyond the wear state of the contact wire. By matching the contact and messenger wire tensions, the contact force variation was found to improve, indicating that better performance of the system can be achieved with only increases in the line tension and avoiding the need for redesigns of existing equipment.

As the overhead line passes under bridges and tunnels it is often necessary to raise or lower the contact wire height and thus impose gradients in the contact wire. In this thesis, the effects of a range of wire gradients on the contact force have been studied using a validated finite element model and the results presented here indicate that maximum permitted gradients are conservative. The minimal effect on the contact wire due to increasing steepness of gradient suggests that there may be opportunities for electrification available without the need for expensive bridge reconstruction, representing significant cost savings.

Table of contents

List of figures

List of tables

Nomenclature

A', B'	Arbitrary points on a circle circumference
A_c	Wire cross–sectional area
A_d	Dataset
$A_{\text{con},0}$	Unworn contact wire cross–sectional area
$A_{c,\text{ice}}$	Cross–sectional area of a contact wire under ice loading
$A_{c,\text{wear}}(\theta)$	Worn contact wire cross–sectional area
C	Arbitrary constant
C_D, C_L	Drag and lift coefficients
$C_D(\theta)$	Drag coefficient as a function of angle of attack
$C_L(\theta)$	Lift coefficient as a function of angle of attack
C_{con}	Damping during contact between the contact wire and pantograph collector mass
C_{fluid}	Aerodynamic damping
C_n	One–dimensional Courant number
C_{DC}	Drag coefficient of circular components of the pantograph frame
C_{DR}	Drag coefficient of rectangular components of the pantograph frame
$D(\mathbf{z})$	Dissipative energy
D_0	Diameter of a contact wire

D_{actual}	Aerodynamic load parallel to the flow
D_{meas}	Measured aerodynamic drag
D_h	Den Hartog coefficient
E	Young's modulus
EI	Bending stiffness, flexural rigidity
F	Force vector
$F(t)$	Aerodynamic load function
$F(x;s)$	Difference between a staggered span length and a planar span length
F_N	Hertzian contact force
F_{Drag}	Aerodynamic drag
$F_{\text{Drag}}(s)$	Fitted drag force curve
F_{Lift}	Aerodynamic lift
$F_{\text{Lift}}(s)$	Fitted lift force curve
$F_{\text{Lift}}(s,\theta)$	Lift force as function of the wind speed and angle of attack
F_{frame}	Drag load on the pantograph frame
F_{head}	Aerodynamic load on pantograph collector head
F_m	Arithmetic mean
F_s	Reaction force
F_t	Tensile force in a dropper
F_x, F_y, F_z	Force in x, y and z-axis directions respectively
F_{DC}	Drag on circular components of pantograph frame
F_{DR}	Drag on rectangular components of pantograph frame
$F_{D_{\max}}$	Discrete force maxima

$F_{D_{\min}}$	Discrete force minima
$F_{S_{\max}}$	Statistical force maxima
$F_{S_{\min}}$	Statistical force minima
$F_{T,i}$	Tensile force in the i^{th} dropper
$F_{\text{lift},0}$	Linear term of $F_{\text{Lift}}(s,\theta)$
$J[\cdot]$	Arbitrary functional
K	Stiffness matrix
K'	Generalised stiffness between two cylinders
K_s	Contact stiffness
L	Arbitrary length
L_0	Unloaded length
L_{actual}	Aerodynamic load orthogonal to the flow
L_{con}	End of model working section
L_{dom}	Length of fluid domain
$L_{\text{fit}}, D_{\text{fit}}$	Fitted curves for lift and drag coefficients
L_{meas}	Measured aerodynamic lift
L_{sep}	Optimal pantograph separation
L_e	Hydrodynamic entry length
L_i	Longitudinal distances of the fluid domain
L_p	Position along an arbitrary length L
L_s	Span length
L_t	Tensioned line segments
L_w	Wire run length

$L_{0,i}$	Unloaded length of the i^{th} span
$M_{\max}$	Maximum Mach number
M_f	Filtered dataset
M_s	Combined mass of dropper and clamps
M_{jj}	Modal masses
N	Number of samples
O	Circle centre
P	Air pressure
P_i'	Pantograph locations
$P(\cdot)$	Power spectral density
P_{sep}	Pantograph separation
Q	Magnitude of force vector
R	Ideal gas constant
R_0	Arbitrary constant
R_1, R_2	Arbitrary circle radii
$R_{con,0}$	Unworn contact wire radius
S	Arbitrary surface
$S_{\tilde{u}}$	Boundary of surface S
T	Wire tension
$T(\dot{\mathrm{z}})$	Kinetic energy
T_{tot}	Time for pantograph to reach end of wire run
T_{con}	Contact wire tension
T_{mes}	Messenger wire tension

U	Free stream velocity
V	Arbitrary volume
$V(\mathbf{z})$	Potential energy
X, Y	Notable locations in wire run
X_i, Y_i	Arbitrary coordinates
$Z(\mathbf{z})$	Interpenetration between the contact wire and pantograph contact strips
$\bar{F}_i$	Body forces
$\bar{N}$	Vector of shape functions
$\bar{N}_i$	Shape functions
$\bar{T}_i$	Stress vector
$\mathbf{C}$	Damping matrix
$\mathbf{F}$	Non–conservative forces
$\mathbf{F}_g$	External force vector
$\mathbf{G}_e$	Flexibility matrix
$\mathbf{K}_G$	Initial length stiffness
$\mathbf{K}_c$	Stiffness of the incremental coordinate
$\mathbf{K}_e^{(1)}$	Linear stiffness matrix
$\mathbf{K}_e^{(2)}$	Stress stiffness matrix
$\mathbf{K}_e^{(3}$	Large deformation stiffness matrix
$\mathbf{K}_g$	Global stiffness matrix
$\mathbf{M}$	Element mass matrix
$\mathscr{L}$	Messenger wire length under tension
$\mathscr{L}(\mathbf{z}, \dot{\mathbf{z}})$	Lagrangian of the interpentration

$\mathscr{T}$	Air temperature
Gauss	Gaussian function
$\mathrm{Re_x}$	Characteristic Reynolds number
$d\mathbf{F}_e$	Stiffness matrix in nodal coordinates
$d\mathbf{L}_0$	Initial length
$d\mathbf{X}$	Incremental length
A	Cross–sectional area
D	Projected area of contact wire in a flow
Re	Free stream Reynolds number at the inlet
$\bar{f}$	Forcing
ℓ	Spring length
ℓ_i	Equilibrium lengths of beam elements
$\tilde{u}$	Exact solution $u(x)$
$\tilde{u}_1, \tilde{u}_2$	Nodal values
$\{\tilde{u}\}$	Vector of nodal values
a, b	Arbitrary constants
a_n, b_n	Fitting constants
c	Arbitrary speed
c_i	Pantograph i^{th} mass damping
c_s	Wave propagation speed
d	Damping coefficient
d_1	Length of carrier wire neutral section
d_2	Pantograph separation

d_i	Spring displacements
e	Restitution coefficient
f	frequency
$f_c(t)$	Coupled contact force between pantograph and contact wire
f_i	The i^{th} nodal force
$f_v(s)$	Fitted curve for the vortex shedding frequency
g	Gravitational acceleration
g_σ	Fitted curve to contact force standard deviation
g_{F_m}	Fitted curve for arithmetic mean of the contact force
h	Vertical amount of contact wire wear
k	Arbitrary stiffness
k_T	Dropper stiffness in tension
k_i	Pantograph i^{th} stiffness
$k_{T,i}$	Dropper stiffness of the i^{th} dropper in tension
kp_i	The i^{th} keypoint
l	Distance between dropper and support
m	Mass
m_{ice}	Mass of ice load
m_{reg}	Concentrated mass of a registration arm
m_i	Pantograph i^{th} mass
m_{con}, m_{mes}	Contact, messenger wire mass per unit length
p	Self–weight
p_i'	Contact wire locations in tunnel case study

q'	Location under a bridge
$q(x,t), q_j(t)$	Force vector
$q_i, \dot{q}_i, \ddot{q}_i$	Displacement, velocity and acceleration of the i^{th} lumped mass
s	Fitted curve wind speed
s_0	Stagger amount
s_c, s_m	Contact, messenger wire sag
s_{c_k}	Contact wire mesh size at the k^{th} iteration
s_{m_k}	Messenger wire mesh size at the k^{th} iteration
t	Time
t_{end}	Time at the end of the second load step
t_p	Pantograph travel time
t_w	Mechanical wave travel time
$u(t), v(t)$	Fluctuating wind components in lift and drag directions
u, v	Wind speed components
$u_j(t)$	Generalised coordinates
v_p	Pantograph speed
$w(t)$	Deflection of a wire
$w_{\text{lat}}(x)$	Lateral deflection of contact wire
x	Horizontal coordinate
x_0	Span midpoint
x_i	Horizontal position of i^{th} dropper
x_j	The j^{th} position
y	Vertical coordinate

$y(t)$	Arbitrary function of time
y^+	Dimensionless wall distance
z	Lateral coordinate
z_1	Height of the topmost mass of the lumped–mass pantograph representation
z_i	Generalised pantograph vertical coordinates
z_{cw}	Contact wire height
z_{ref}	Pantograph reference height
z_{wear}	Radius of a worn contact wire

Greek Symbols

α, θ	Angle of attack
$\bar{\alpha}$	Mathieu equation parameter
β	Viscous damping
δL_t	Line segment extension under load
Δq	Displacement vector
Δt	Time step size
Δx	Mesh spatial element size
$\Delta \ddot{q}$	Acceleration vector
$\Delta \dot{q}$	Velocity vector
δ_l	Laminar boundary layer thickness
δ_t	Turbulent boundary layer thickness
$\dot{\delta}$	Penetration velocity
$\dot{\delta}^{(-)}$	Impact velocity
ε_s	Strain of a line segment

ε_{ij}	Strain due to displacement of i and j^{th} nodes
$\varepsilon_{x,i}$	Strain in the x-direction of the i^{th} span
η, ν	Scalar constants
η_{cw}, ν_{cw}	Contact wire damping scalars
η_{mw}, ν_{mw}	Messenger wire damping scalars
γ	Correction factor
λ	Lagrangian multiplier
μ	Friction coefficient
μ_0	Viscosity
μ_{aero}	Mean aerodynamic load
ω	Frequency
ω_n	Natural frequency
ω_{jj}	Modal frequencies
Φ	Vector of modal shapes
ϕ	Arbitrary angle
Ψ	Residuals
ρ	Air density
ρ_{con}	Contact wire density
σ	Contact force standard deviation
σ_s	Stress in a line segment under load
σ_{ij}	Stress due to displacement of the i and j^{th} nodes
τ	Torque
ξ	Damping factor

ξ_j	The j^{th} damping ratio
ξ_n	The n^{th} damping ratio
ξ_s, ξ_a	Structural and aerodynamic damping
ξ_{cw}, ξ_{mw}	Contact and messenger wire damping ratios

Chapter 1

Introduction

1.1 Background

The railway is a vital and efficient means of transporting passengers and freight. The rail industry faces increasing demand from both passengers and freight to provide a resilient, timely service and due to a desire for increased capacity, reduced journey times and a movement towards a green, carbon neutral society, electrification is now the default means of locomotive traction for high speed rail across the world. Electrification also represents the most energy–efficient means of providing locomotive traction [1]. In the UK, approximately 40% of the rail network is electrified with two–thirds provided by 25 kV AC overhead line equipment and the remaining third provided by third–rail DC. Whilst a minority of the network operates using electric traction, electrified routes account for almost 50% of train miles covered [2].

To continuously transfer power to electric trainsets, in the case of overhead line equipment, a contact wire is suspended from a messenger wire using droppers and a roof–mounted pantograph is raised into contact with the contact wire to permit the transfer of electrical power. The overhead line arrangement, an example of which is shown in Figure 1.1 is widely used around the world and provides satisfactory energy transmission for train speeds up to 400 km/h [3].

During train operation, electric current is collected by the pantograph from the contact wire and then returned along the rails back to the lineside substations. Under normal conditions, the contact between the train wheelsets and the rail is good, so maintaining the contact between the pantograph and the contact wire is the key issue facing the reliable operation of an electric railway. Maintaining good contact has largely been the focus of research into the catenary pantograph interaction during abnormal operation conditions,

Fig. 1.1 Typical UK catenary pantograph interaction between the roof–mounted pantograph and overhead line equipment, Peterborough, UK. Image from [4].

such as severe wear states of the contact wire, interaction between multiple contact wires or multiple pantographs. Less focused has been on the effects of out–of—standard wire geometries such as excessively steep contact wire gradients or aerodynamic effects during train operation. To achieve the required capacity increases required to meet current global emissions targets, more cost–effective methods of electrification must be proposed, either with new or novel techniques or by challenging the existing standards.

In this thesis, numerical modelling has been undertaken to determine the effects of wire gradients, aerodynamics and mechanical system changes on the contact force to better understand the catenary pantograph interaction. To investigate the catenary pantograph interaction, researchers have widely adopted numerical techniques such as finite element analysis, due to the development and emergence of high performance computing availability for commercial and academic purposes. With computer simulations, the effects of various mechanical characteristics can be assessed without the need for prohibitively expensive line tests.

1.2 Aims of this thesis

The overarching aim of the research presented in this thesis *to quantify the dynamic behaviours of the catenary pantograph interaction as a response to mechanical parameter*

variation and aerodynamic effects with a view to identifying potential failure modes and routes to cost effective electrification through the following objectives:

- A comprehensive review of the current state of the art of the catenary pantograph interaction to identify the open problems.
- To determine the aerodynamic forces on an overhead line under steady wind conditions to provide an input for a wind field applied to a numerical model of the catenary pantograph interaction.
- Assess the effects of changes in the mechanical properties of both the overhead line and the pantograph to determine system changes to improve the current collection quality between the train and overhead line.
- Identify the effects of contact wire height changes on the dynamic contact force and wire uplifts with a view to providing more cost effective electrification under low clearance structures.

Steering provided by the industrial collaborators as part of this project highlighted the dynamic response of the overhead line system to a change of contact wire height as an area not widely studied. A variation in the dynamic contact force was known to exist due to the change in contact wire height, however little work had been done to quantify the variation in the contact force. As such this work sought to determine that contact force variation.

1.3 Thesis outline

Beyond the Introduction, the thesis is arranged into six further chapters:

- Chapter 2 presents a literature review of the research and current state of the art with respect to the catenary pantograph interaction. The existing methods of modelling the interaction between a contact wire and train mounted pantograph are discussed, along with existing research into the influence of outside effects such as crosswinds. At the end of this Chapter, the open problems currently existing in the literature are discussed.
- Chapter 3 discusses the methodological approach adopted throughout this work and the experiment designs to answer the research questions posed in Chapter 2.
- Chapter 4 presents the validation process used to assess the validity of the finite element modelling, as well as a discussion of the modelling assumptions made during the

simulation process. The sensitivity of the modelling assumptions are also considered, and justification of the accuracy of the results based on the model sensitivity to the assumptions is provided.

- Chapter 5 demonstrates the methodology used to determine the aerodynamic forces on a railway contact wire using both experimental and numerical approaches, generating an input for the study performed in Chapter 7.

- Chapter 6 presents the results of the numerical modelling of contact wire irregularity not associated with wear of the contact wire such as changes in the wire tensions, or the absence of a dropper. The effect of train speed on the mean contact force is also investigated and compared with the design mean contact force to assess the validity of the modelling.

- Chapter 7 uses the aerodynamic forces calculated in Chapter 5 to establish an aerodynamic load on the overhead line to measure the deflections of the contact wire under load. The forces on a pantograph due to crosswinds are also calculated to investigate the effect of crosswinds on the contact force variation and uplift of the contact wire.

- Chapter 8 presents a validation of a large–scale wire height change model, which is then used to assess the effects of contact wire gradients on the catenary pantograph interaction.

- Chapter 9 concludes the thesis with conclusions based on the work presented throughout with some suggestions for future work.

The modelling methodology provided in Chapter 3 and the results presented in Chapter 8 form the publication:

> Sam Hayes, David I. Fletcher, Adam E. Beagles & Katherine Chan (2020) Effect of contact wire gradient on the dynamic performance of the catenary pantograph system, Vehicle System Dynamics, DOI: 10.1080/00423114.2020.1798473 [5].

Chapter 2

Literature Review

Volk's Electric Railway, the first electrically powered railway in the UK was built in 1883 with power supplied by 110 V DC third rail equipment, whilst the first adoption of a fourth rail system was in 1890 on what is now the Northern Line of the London Underground. The first overhead line systems were installed circa 1910 in South London and Lancashire using 6.6 kV DC equipment, whilst the first 25 kV AC systems were adopted after the publication of the Modernisation of British Railways report in 1955 [6]. The report set 25 kV AC systems as the standard on new electrification projects except for extensions of existing third rail systems. Advantages of overhead line equipment over third rail systems include:

- Higher train speeds. Overhead line system line speeds have been increased in excess of 300 km/h compared with a maximum 160 km/h available to third rail equipment.
- A reduced energy requirement. Third rail DC systems require approximately 20% more electricity during train operation [7].
- There is a reduced risk of electrocution to public and track workers with overhead line equipment compared with third rail systems.

In the UK, a "boom–or–bust" approach has been characteristic of the increase in the number of electrified route kilometres since the Second World War, whereby large electrification projects have been undertaken and the number of electrified route kilometres has increased rapidly, then followed by periods of little to no increase in the amount of electrification. The change in electrified route kilometres, as provided in [8], is shown in Figure 2.1, where key electrification projects such as the West Coast Mainline in the 1960/70s, the East Coast Mainline in the 1980/90s and the Great Western Mainline in the 2010s, can clearly be seen compared with the intervening periods where little electrification occurred.

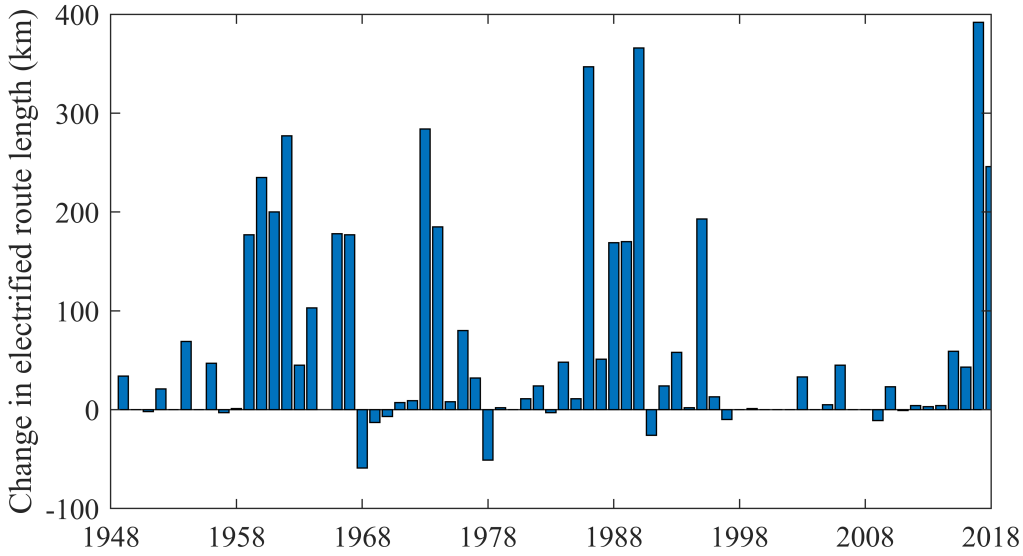

Fig. 2.1 Change in the electrified route kilometres across the GB rail network since 1948.

With a desire to achieve a "net–zero" carbon network by 2050, Network Rail has published the Traction Decarbonisation Network Strategy [9] and identified that electrification of the 11,700 single track kilometres of the remaining network provides the most effective route to decarbonisation of the UK rail network, thus research into cost effective methods of providing the required electrification to achieve a "net–zero", resilient railway is both timely and with the threat of climate change, necessary.

2.1 The overhead catenary system

The overhead contact system (OCS) is a system designed to continuously transmit electrical energy to a train by means of sliding contact between the overhead line equipment (OLE) and the roof-mounted pantograph. Various terms are given for this system, in the UK it known as 'Overhead Line Equipment (OLE or OHLE)', in the US and Europe, Overhead Contact System, and 'Overhead Wiring System' in New Zealand. Throughout, OLE is used to refer to the system of wires supplying electrical energy to a train and OCS to refer to the OLE and pantograph together. Pre–tensioned wires suspended above the track upon which a collector runs along are known as contact wires. Specifications for railway contact wires are provided by [10]. A sample of railway AC–120 contact wire is shown in Figure 2.2. The purpose of contact wires is to provide continuous electrical power to electric trains by way of a roof–mounted pantograph. Wear due to the sliding contact is controlled by the

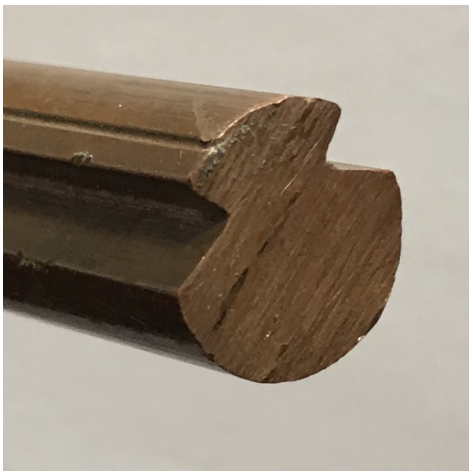

Fig. 2.2 Sample of AC–120 CuAg contact wire.

introduction of stagger, whereby the contact wire lateral position at supports relative to the track is alternated giving a zig–zag profile relative to the track.

Contact wires are grooved to provide clamping positions in order to suspend the contact wire from messenger wires using droppers. Depending on the line speed and therefore the contact force between the contact wire and pantograph, magnitude of electrical current to be transmitted or applied tension, various contact wire cross sections have been adopted globally. Typical contact wires have cross–sections between 80 and 150 mm. The larger profile wire types allow for a larger degree of wear before replacement is required but this is offset by the greater mass to support.

Due to their high conductivity, tensile strength and hardness, hard–drawn copper and copper alloys are well established materials for railway contact wires. For copper alloy contact wires, the addition of other material improves the mechanical or thermal performance permitting increased wire tensions, however the addition also reduces the conductivity of the contact wire. Typical alloy additives include silver (CuAg 0.1%) or magnesium (CuMg 0.5%). Traditionally copper–cadmium contact wires were used, however these have fallen out of favour due to cadmium toxicity. Copper–cadmium is no longer permitted in Austria, Switzerland and Denmark. Copper alloy contact wires are identified by grooved markings along the top surface of the contact wire which are given in Table 2.1.

Whilst the contact wire is formed of one single wire, the messenger wire is typically a stranded conductor such as the one in shown in Figure 2.3. Since the messenger wire does not directly interact with the pantograph, it is only required to transmit electrical energy and withstand mechanical stresses due to tensioning. Typical materials for stranded conductor wires are pure copper or bronze Bz II (CuMg).

Table 2.1 Identification of copper alloy contact wires.

Number (location) of identification grooves	Contact wire type
0	Normal or high strength copper (Cu)
1 (centre)	Copper–Cadmium (CuCd)
1 (off–centre)	Copper–Tin (CuSn)
2	Copper–Silver (CuAg)
3	Copper–Magnesium (CuMg)

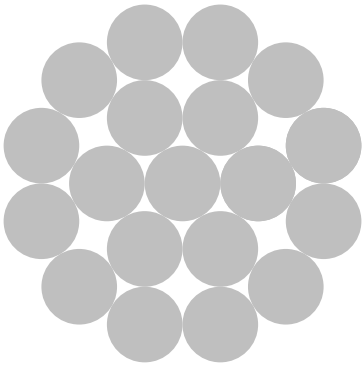

(a) Stranded conductor cross–section.

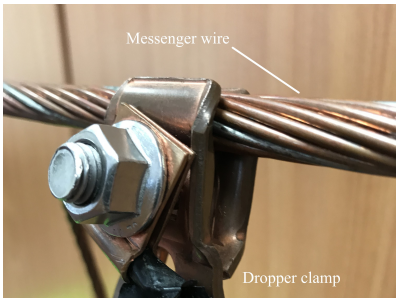

(b) Stranded Bz II messenger wire.

Fig. 2.3 Stranded conductors.

The droppers maintain the contact wire height relative to the messenger wire and are designed to withstand the cyclic loading during pantograph passage. Modern systems have adopted current carrying droppers such as the one shown in Figure 2.4.

2.1.1 Wire configurations

The wire configuration is largely set according to the speed of the line on which it will be installed. Since the contact wire has a large flexibility at midspan compared to at supports, increasing levels of complexity in the wire arrangement are required to give good dynamic performance during train operation.

Trolley wire

The simplest equipment arrangement is known as tramway or trolley wire OLE. This system consists of a contact wire suspended directly from the supports. This type of arrangement is the least complicated version of an overhead line system and has zero flexibility at the supports and high flexibility at the midspan. Since the wire is only supported at structures,

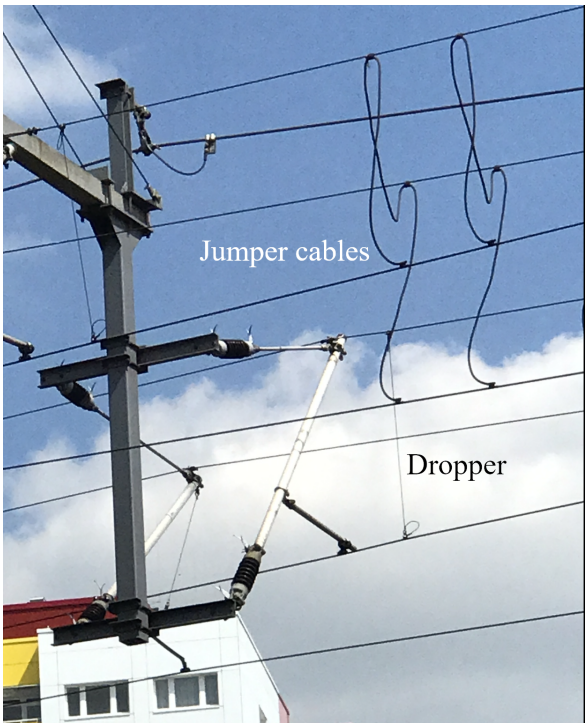

Fig. 2.4 Current carrying dropper, Berlin, Germany.

span lengths are typically between 30 and 40 m to minimise wire sag. As such, this type of arrangement is only suitable for low speed situations (less than 30 km/h) such as tramways or heavy rail sidings. Figure 2.5a shows the typical arrangement of a trolley wire, and Figure 2.5c is an example of such an arrangement. The simple arrangement can be improved by introducing a stitch wire, reducing the contact wire flexibility at the midspan, allowing for a greater train running speed. The length of the stitch can be varied for each system. Longer stitch wires allow for the introduction of droppers to mitigate the sag of the contact wire. A stitched trolley wire schematic can be seen in Figure 2.5b. There appears to be no active research into the dynamics of a trolley wire OLE, likely due to the limited use to tram systems which are relatively low speed compared to their mainline counterparts.

Simple (sagged), stitched and compound equipment

In the previous wire configuration, the horizontal distance of the stitch wire was shorter than the length of the span. Extending the wire to run the whole length of the span introduces a messenger wire into the system. This messenger wire can be used to suspend a contact wire through the use of droppers, as shown in Figure 2.6 when presag is zero, and this system is known as simple catenary OLE as the messenger wire takes the shape of a catenary. A

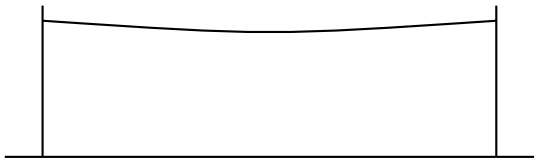

(a) Trolley wire schematic.

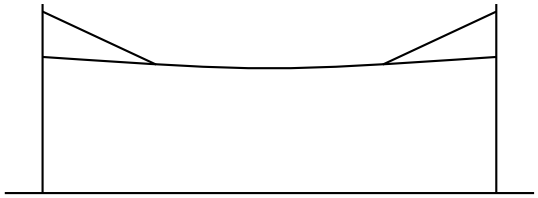

(b) Stitched trolley wire schematic.

(c) Trolley wire overhead line arrangement, Sheffield, UK.

Fig. 2.5 Possible trolley wire arrangements and an installed system.

simple catenary OLE is the simplest system used for mainline electrification. Suspending the contact wire from the messenger wire also allows for a greater contact wire mass to be supported, allowing for the greater traction current required for higher train running speeds up to 120 km/h.

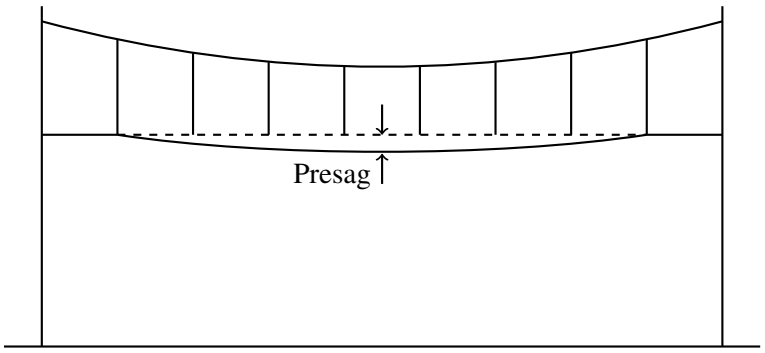

Fig. 2.6 Simply sagged OLE schematic. The simply sagged equipment reduces to simple equipment when presag is zero.

The arrangement where the contact wire is allowed to sag naturally due to self–weight, has largely been superseded by presagged equipment. In this case, the contact wire sags a predetermined amount (typically 1‰ of the span length) between the first and last droppers. The presagged contact wire compensates for the greater flexibility at the midspan, thus the uplifted contact wire is better aligned with the uplift position at the supports. Figure 2.6 shows the presagged system with the presag exaggerated for clarity and an installed example

Fig. 2.7 Simply sagged overhead line equipment supported by headspans, Doncaster, UK.

of simply sagged overhead line equipment supported by headspans is shown in Figure 2.7. The dynamic contact force has been shown to be sensitive to the magnitude of the presag [11, 12], where it was found that the best dynamic performance was attained for a presag between 10 and 60 mm. In [12], the optimal magnitude of the presag is also noted to decrease as the line speed increases. Adoption of presag is also found on stitched overhead line equipment [13]. In a stitched arrangement, such as the one shown in Figure 2.8a, the addition of a stitch wire either side of the support, reduces the stiffness variation across the span, providing good performance up to 400 km/h. The stitch wire also compensates for expansion and contraction as the temperature varies, transmitting the length variation to the contact wire near the supports, giving similar displacement in the contact wire due to temperature across the whole span. In Europe, due to the prevalence of stitched catenary, reference models for stitched catenaries are now included in the validation of numerical models [14] where appropriate.

The most complexity is found in the compound catenary arrangement. With the addition of an auxiliary messenger, as shown in Figure 2.8b, the variation in the vertical stiffness across a span is very low, however the increased maintenance requirements and capital investment means it is not a widely adopted arrangement in the UK.

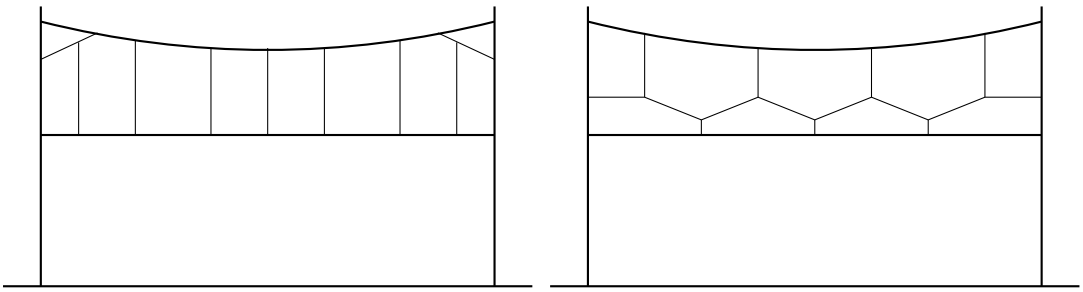

(a) Stitched catenary OLE. (b) Compound catenary OLE.

Fig. 2.8 Overhead line arrangements beyond simply sagged equipment.

Research into the catenary pantograph interaction is largely done using representations of simply sagged and stitched equipment, thus the state of the art with respect to these equipment types is growing quickly.

2.1.2 Tensioning arrangements

To ensure good current collection quality, long spans are subject to tensioning at the end of each wire run to minimise sag due to gravity. For slow speed systems, the tension is typically 8 kN, and increases up to 20 kN on high speed mainlines. Tension is applied to the overhead line using either fixed termination or auto–tensioning. In the case of fixed termination, the overhead equipment is fixed and tensioned at every support, whilst for auto–tensioned systems, the equipment is fixed at a midpoint anchor and tensioned at the end of each wire run. As the ambient temperature varies, so too does the vertical profile of fixed termination equipment. Since the equipment is tensioned at each support, the contact wire sags (rises) as the temperature increases (decreases) and so are not suitable for large temperature variations due to excessive contact wire sag [15, 16]. Whilst the total deflections in the vertical profile are limited by the droppers, the dynamic performance of the equipment changes with respect to temperature and so are not well suited to high speed operation. For auto–tensioned wires, either balance weights or spring tensioners (such as the Tensorex C+ device [17]), provide constant wire tension irrespective of the temperature. Thus auto–tensioned systems provide greater equipment resilience to increasing temperatures due to climate change.

Since each wire run is finite due to limits on the number of stagger changes and also due to the practical limits on the length of wire loaded onto wire drums, it is necessary to split the overhead line up into discrete tensioned sections. Transitioning between discrete sections requires the use of overlaps[1]. Poor messenger wire tensioning causes increased sag

[1] Also useful for electrical separation at neutral sections.

in the contact wire degrading the dynamic performance throughout the overlap section. The effect of wire overlaps on the dynamic contact force is studied in [18], where the simulations predicted an increased force in the intermediate overlap span when the pantograph was in contact with two wires, consistent with the predictions in [19, 20]. The increased contact force is due to the increased vertical stiffness present due to the doubling of the overhead line equipment during the overlap span. In both [21, 22], the introduction of discrete elements into an overhead line system can improve the dynamic performance. In the case of [21], addition of damping elements in the overlap span reduced the amplitude of the returning wave at supports whilst [22] introduced a controller aimed at reducing vertical oscillations. In both cases the addition of discrete control elements were in numerical models, thus no conclusions about the lifetime effects on an installed overhead line were discussed. In [23], the height of the contact wire throughout the overlap was considered, and concluded that maintaining a low contact wire height improved the dynamic performance. The importance of controlling the dynamics throughout the overlap sections is highlighted by the addition of overlaps to the validation process for numerical models in [14], thus is an active research area at present.

2.1.3 Clearances and height restrictions

Largely, conductors in an overhead line system are only insulated at supports, thus safety clearances are imposed between the live components and infrastructure to prevent flashover. Clearances are typically defined with respect to the air gap between conductors and other components of the system. Static electrical clearances are typically larger than dynamic electrical clearances due to the short duration of train passage at given locations reducing the risk of flashover to infrastructure. In the UK, electrical clearances were defined in [24] and specified various clearances for the different circumstances across the network. Each of the four clearance cases are:

1. Enhanced: used wherever possible,
2. Normal: used when enhanced clearances are not possible,
3. Reduced: used when normal clearances are insufficient subject to control measures,
4. Special: used in most limited cases subject to risk assessment, control measures and ongoing assessment.

These clearances given in Table 2.2, were superseded by [25], where electrical clearances were consolidated into 270 mm for static conditions and 200 mm during train passage.

Table 2.2 Electrical clearances for 25 kV AC overhead power lines. All entries in mm.

	Enhanced	Normal	Reduced	Special
Static electrical clearance	≥ 600	270 – 599	200 – 269	150 – 199
Dynamic electrical clearance	≥ 600	≥ 200	150 – 199	125 – 149

Since the working height of the pantograph is limited, the vertical profile of the contact wire is fixed by the limits of the pantograph working height. Beyond the upper limit, the auto–drop feature of the pantograph will cause a loss of contact and power, whilst exceeding the lower limit will breach electrical clearances between the pantograph and the train body. Whilst the working height of the pantograph sets the bounds on the vertical wire profile, lateral clearances are required, particularly at bridges and tunnels. As the train speed increases, clearances must be satisfied with respect to the gauge and kinematic envelope of the vehicle. Clearances between the kinematic envelope of the train body and civil structures must be satisfied to prevent flashover. It is for this reason, bridge reconstruction is often unavoidable if a sufficient air gap cannot be maintained.

Mechanical clearances between the pantograph and contact line equipment is given as 80 mm and clearances between the pantograph and registration arm is a minimum of 15 mm for all wear conditions of the pantograph and contact wire. For this reason, the uplift of the contact wire at supports must be controlled to ensure sufficient space between the pantograph head and the registration arm. For too great a wire uplift, the pantograph and registration arm have the potential to collide. Figure 7.18 shows the overhead line equipment passing under a bridge, where the messenger wire and contact wires have been highlighted to demonstrate the reduction in the messenger wire height to satisfy the clearance to the bridge.

For large sections of an electrified railway, the overhead line can be installed at a constant height relative to the track with no infrastructure clearances besides the registration arms to satisfy. However, at locations such as level crossings, bridges and tunnels, the contact wire height must change to satisfy the required clearances. Without height variations, infrastructure would have to be moved, rebuilt at high cost or be at risk of increased arcing events. Maximum contact wire gradients are fixed according to BS EN 50119 [26], and are dependent on the line speed, e.g., the maximum wire gradient for a line speed of 200 km/h is 1:500. Transitions between level and graded contact wires are set at half the desired gradient, so for a desired wire gradient of 1:500, the transition gradient is 1:1000. In the UK, the required wire gradients are often unachievable due to insufficient spatial separation between for example bridges, where wire heights are typically 4.5 m, and level crossings where wire

Fig. 2.9 Overhead line equipment passing under a bridge in Eccles, UK. The messenger wire height is highlighted indicating the reduction in system height to satisfy clearances.

heights of greater than 5.6 m are required [25] to satisfy the electrical clearances. Figure 2.10 shows a possible situation where the spatial separation L could be insufficient.

To satisfy required clearances under low–clearance structures, novel techniques such as raising the bridge deck [27] and lowering the track bed [28] have been adopted alongside conventional bridge reconstruction [29]. In all of these cases, significant capital investment is required as part of the electrification of existing lines, thus the adoption of new methods to avoid these costs is attractive to infrastructure owners.

Research into the effects of changes in the contact wire height is limited. In [30], the effect of a decreasing wire height is included for train running speeds between 130 and 200 km/h and a contact force increase was predicted leading to an increased wire uplift at supports. The system considered was under relatively low tension (10 kN), thus the dynamic uplift could be mitigated with an increased tension, however thus far this does not appear to have been researched. In [30], only a decreasing wire height was considered, with no increasing wire height included as would be expected at low clearance structures, thus the

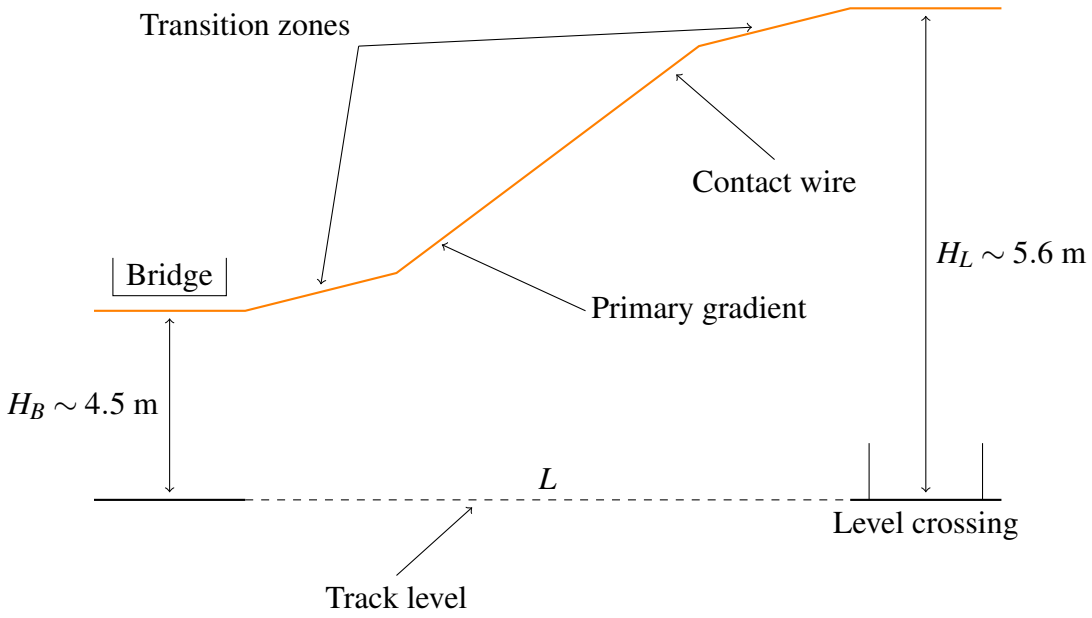

Fig. 2.10 Side view of a wire geometry where the spatial separation L between a bridge and a level crossing may be insufficient for the required contact wire gradients. Supports, droppers and the messenger wire have been omitted for clarity and the vertical scale is exaggerated.

effects of a continuously rising pantograph have not been studied. The vertical transition rate of the pantograph and its effect on the dynamic contact force is also not widely researched [31] and currently no specifications are given with regards to the pantograph performance at high transition speeds [32], only that a pantograph should maintain the static uplift force over the range of the working height. Increases in the line speed have been adopted on the Great Western Mainline for out–of–standard wire gradients in [33], indicating that current standards can be altered allowing for possible infrastructure cost savings in the electrification of railway lines.

Thus far, it appears no assessment of the lifetime cost of out–of–standard wire gradients has been made, and the study of wire gradients is largely an open problem.

2.1.4 Unique features of the overhead line equipment

Overhead conductor bar

Equipping low clearance infrastructure with conventional catenary is limited by the available space subject to clearances. Overhead conductor rail, such as the one shown in Figure 2.11, has become a widely adopted solution (more than 500 km in use globally) to the problem of installing overhead line equipment in tunnels due to the reduced space required to install the

equipment. The typically aluminium bar carries the contact line through the length of the tunnel without the need for a messenger wire or droppers and the contact wire supported by overhead conductor rail is under no axial tension as the bar supports the entire self–weight of the contact wire. Maintenance and renewal of the contact wire is also significantly easier than conventional equipment. Heat expansion in the conductor rail is accounted for using expansion joints which unlike traditional continuous conductor bars can be run at the full line speed, and since temperature fluctuations are smaller in tunnels compared with open track, the overhead equipment is less susceptible to sagging in increased temperatures.

Widespread use across a rail network where otherwise conventional overhead line equipment would be used is unlikely due to the larger supported mass requiring more frequent mast installations compared with conventional catenary. Using a bar to support the contact wire gives much smaller stiffness variations along the length, however is much stiffer than the conventional catenary overhead conductor bars are installed alongside. To manage the stiffness variation, transition zones at each end of the conductor bar gradually alter the stiffness of the equipment [34]. To minimise wear, the conductor bar is staggered following a sinusoid rather than the conventional zig–zag.

Early conductor bar installations limited the line speed, however in [35, 36], the conductor rail profile was optimized indicating that line speed could be increased whilst also improving the current collection quality. Increases in the line speed were also observed in [37] where good performance was measured for line speeds up to 130 km/h and in [38], the overhead conductor system was shown to provide good dynamic performance for line speeds up to 200 km/h. Models of the rigid conductor bar have been validated in [39–44] and [45] provides a further validation of the dynamic performance for a range of system and span lengths. In [46], the overhead conductor bar was adopted to carry the contact wire whilst suspended from the messenger wire by droppers as with conventional catenary. It was found that in this configuration, good performance was measured for span lengths up to 50 m, however the increased investment and maintenance of the addition of the conductor bar rather than only the contact wire, suggests this has not been an active research focus. Considerations are also given to the span length when using overhead conductor bar in [47], where it was found that there exists a range in which the variation of the contact force is reduced when the line speed is 200 km/h, as shown in Figure 2.12, apart from a peak at 3.6 m. No explanation for the peak was given, however it is possible at that span length, the system resonates, increasing the contact force variation. In [48], the effects of various excitation frequencies are investigated to assess the dynamic response of the conductor bar pantograph interface to sinusoidal vibration. It was found that excitation at frequencies close to the second natural

Fig. 2.11 Overhead conductor rail installed in Berlin Hauptbahnhof, Germany.

frequency of the conductor rail acts to reduce the contact loss predicted at other excitation frequencies.

Neutral sections

Neutral sections are adopted to electrically separate different sections of the overhead line supplied by different sub–stations connected to different parts of the National Grid and allow switching between different phases. Electric trains typically coast through neutral sections to reduce occurrences of arcs being drawn from the live section of the overhead line along the neutral section. Neutral sections are also installed where the system voltage differs (most often occurs on the European continental network). Installed neutral sections can be of the inline type where a pantograph moves from a live contact wire to a earthed rod spliced into the contact wire. Arcing horns are placed at each end of the earthed section in the event the pantograph draws current across the neutral section. The alternative neutral sections, most often used on high speed lines, are carrier wire neutral sections (CWNS). A CWNS is formed

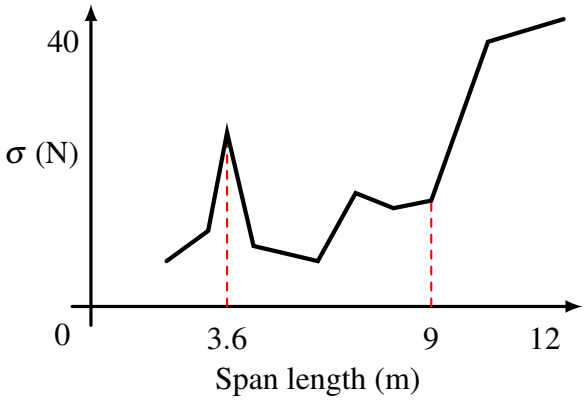

Fig. 2.12 Contact force variation presented in [47] as a function of the span length.

of two overlap sections, whereby the pantograph is transferred from the live contact wire, to a dead wire, and then the reverse happens at a second overlap. In the case of multiple pantograph operation, the length of the CWNS, denoted d_1 is set to either be shorter than the spacing between the two pantographs, denoted d_2, if they are electrically separate (e.g., multiple unit operation), shown in Figure 2.13a, or longer than the pantograph separation (e.g., multiple pantographs on the same unit), as shown in Figure 2.13b.

In the case where there is only single pantograph operation, the neutral section length is less important since there is no secondary pantograph to unite the two separate sections. Research with regards to neutral sections has largely focused on optimization of the spatial location with respect to an electric train's energy consumption whilst traversing neutral sections [49–51]. There appears to be little focus on improving the mechanical characteristics of the neutral section during train operation and as such is an open problem.

2.1.5 Electrical Principles

Voltage

Electrical energy provided by an overhead power line is split into two voltages, the transmission voltage and supply voltage. The transmission voltage determines how energy is transmitted through the overhead line whilst the supply voltage determines how energy is supplied to the train. Typically, these two voltages are the same, however some high speed lines make use of a higher transmission voltage to overcome losses in overhead equipment to provide a greater power at the train.

A range of voltages have been used depending on the type and age of the electrical rail system. In the case of a tram system, 750 V DC is standard to reduce risk in public

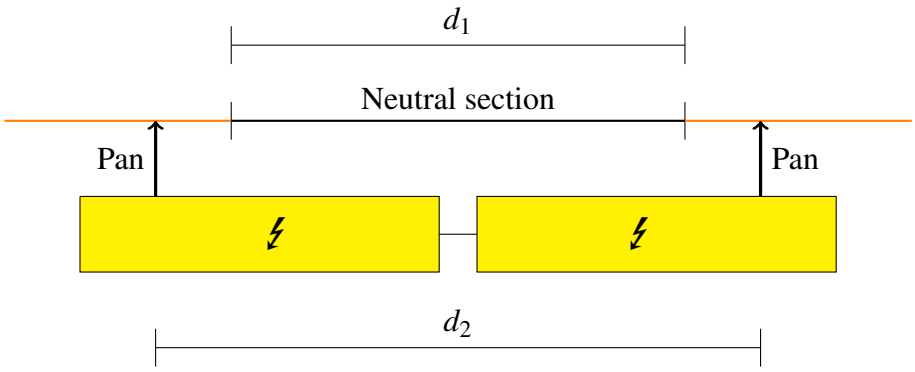

(a) Electrically separate units.

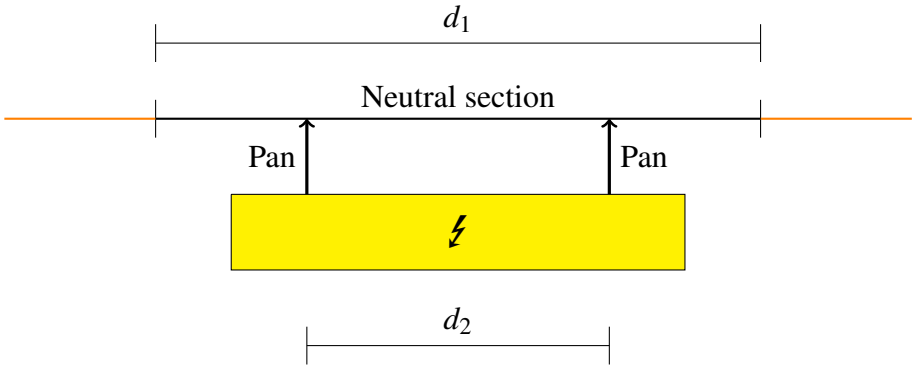

(b) Single electrical unit.

Fig. 2.13 Neutral section design variation. Electrically separate pantographs require $d_1 < d_2$ and electrically united pantographs require $d_1 > d_2$ when passing through a neutral section.

areas whilst 25 kV AC is common for new high speed overhead electrification projects. Other systems include 1500 V DC OLE and in Northern Europe, 15 kV AC. These are now considered legacy systems and 25 kV AC is the preferred method of electrification. In the case of AC electrification, the frequency of the AC supply is matched to the frequency of the industrial supply. In the UK, this is 50 Hz. Supply voltage is usually not constant due to factors such as voltage losses or the magnitude of the load in each electrical section, thus the system must be able to operate at a range of voltages. In the case of UK 25 kV AC systems, a minimum operational voltage of 12.5 kV is allowed for no more than two minutes without a high possibility of equipment damage and a maximum voltage of 29 kV for at most five minutes. In normal operation the minimum and maximum voltages are 16.5 kV and 27.5 kV respectively [52].

Current

The supply current is specified by the desired train power and the number of trains requiring power in a given section. Low voltage DC systems require a higher current to achieve the required power at the train. A 1500 V train for example, draws a current of 1500 A whilst a 25 kV AC passenger train will draw around 200 A due to the significantly higher voltage.

The described current ratings are for nominal operation of the overhead line. The system is also designed to withstand currents during faulty operation without equipment degradation. This maximum fault current is specified for each type of equipment and for a typical UK 25 kV system, is 6 kA.

AC supply

AC systems are advantageous to DC systems as the current direction requires no rectification and arcing of an AC current is easier to distinguish as the current passes zero volts. This allows for the use of higher voltages than DC thus giving a smaller voltage drop in the overhead allowing for greater distances between feeder stations, which can be up to as much as 60 km apart for 25 kV systems.

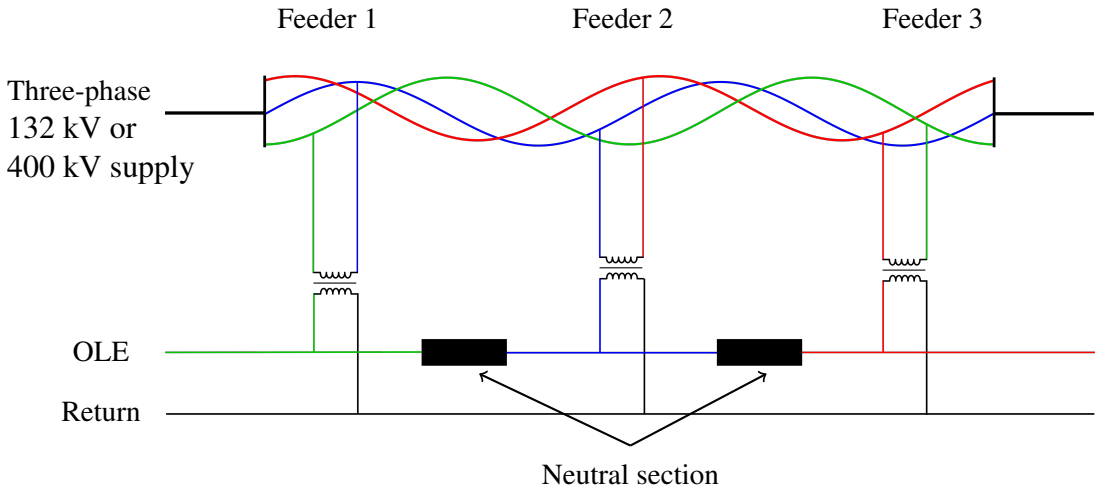

Fig. 2.14 Using a three-phase ESI to feed a single-phase electric railway.

Supplies of the AC equipment in the UK were typically fed from distribution network operators using the 132 kV network and transformed to the required 25 kV. These are being replaced by feeder stations supplied by the 400 kV Electricity Supply Industry (ESI). The overhead line electrical single phase system draws electricity from the three phase network. This phase discrepancy causes a load imbalance. To overcome this, the OLE is split into

distinct electrically separated sections allowing for different phase combinations to be used when drawing electricity. Figure 2.14 shows a simplified schematic for supplying electricity is to the OLE. Different combinations of the three-phase supply are used to supply power to each section. To reduce transmission losses over long distances between feeder stations, autotransformer systems [53, 54] have been adopted on mainline high speed and electric freight trains.

2.2 The pantograph

The pantograph, mounted atop electric trains draws electrical power from the overhead contact wire and is the vital component uniting electric trains to the overhead line equipment. The first pantograph types, used on the Baltimore and Ohio Railroad in 1895 [55], and as patented by J. Brown in 1904 [56], were of a diamond configuration and the single arm configuration widely adopted on high speed lines was invented in 1955 [57]. Modifications to older pantograph types were investigated in [58] with the aim of upgrading operational speeds to those required by the Advanced Passenger Train whilst maintaining good contact with the overhead line. To ensure good continuous electrical transmission, an uplift force generated by a pneumatic actuator raises the pantograph lower arm, whilst either an external arm or internal chain linkage lifts the upper arm, bringing the collector head into contact with the contact wire. Internal means of raising the upper arm are preferred to reduce the aerodynamic effects on the pantograph. The collector head typically supports one or two sprung strips and is designed with a minimal mass to reduce inertia at the contact interface. At the contact interface, sliding contact between the collector strips and the contact wire induces wear, thus carbon has been widely adopted on high speed pantographs for its good electrical conductivity and lower hardness that the contact wire, thus transferring the majority of the wear to the carbon strips.

A large range of pantograph types have been adopted globally (11 types based on four pantograph designs currently operate on GB infrastructure [59, 60]), with early pantograph designs making use of the diamond configuration, later being adapted to the current single arm mechanism such as the Brecknell Willis HSX pantograph. All the pantograph types have their profiles set by [61]. Pantographs operating on UK lines (excluding High Speed 1 where TSI compliant pantographs are used), typically have smaller horizontal profiles than their European counterparts due to more restrictive clearances and smaller loading gauge in the UK.

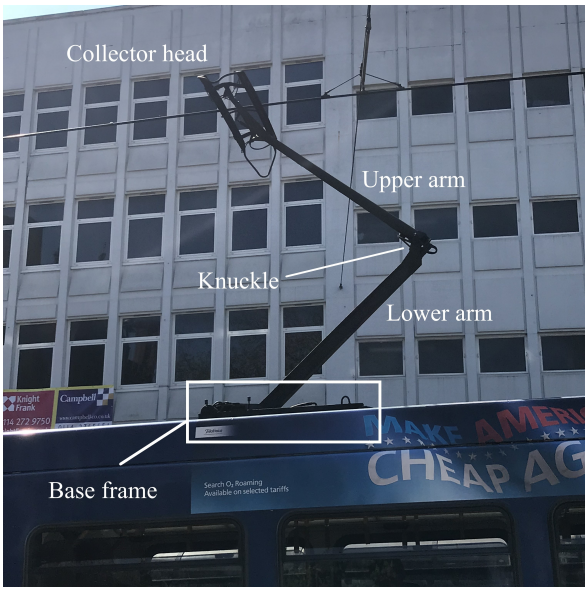

Fig. 2.15 Typical pantograph, Sheffield, UK

Elasticity of the pantograph frame contributes to dynamic phenomena typically in the higher frequencies, thus the dominant dynamic behaviour is set by the composition of the collector strips and the suspension characteristics. In [62, 63], the contact force is found to be highly sensitive to the frame mass and damping, and both [62, 64], show that the stiffness of the pantograph between the collector head and the frame dominates variation in the contact force. In [65], the effect of the suspension characteristics of the pantograph are considered, and predict that the pantograph can be optimized with an increase in the suspension stiffness, giving a reduction in the contact force standard deviation. During train operation, large variations in the Coulomb friction between the contact wire and pantograph is predicted to only cause small variation in the contact force [66], and an improved dynamic force is observed by a reduced pantograph head mass. Improvements in the current collection quality can be obtained using a variable stiffness device in [67]. By replacing a component with static stiffness with air springs, the frequency at which the pantograph adopts to catenary irregularities can be adapted.

It is well known that trailing pantographs suffer from degraded current collection quality [68, 69] compared with their leading counterparts due to the leading pantograph causing a mechanical wave during train operation. In [70], resonance between the trailing pantograph and the contact wire, identified by variation in the displacement of the rear pantograph, can be reduced by installing tuned dampers to the trailing pantograph. On low–tension wires, [71] optimised the separation distance between two pantographs with short separation distances

and in [72], an optimal separation distance for multiple pantograph operation is proposed as

$$L_{\text{sep}} = k\frac{v_p L_s}{\gamma c_s}, \tag{2.1}$$

where $k \geq 3$ is an odd integer, v is the train running speed, c_s the mechanical wave propagation speed and γ a correction parameter for different catenary systems. Proposals to improve multi–pantograph operation include favourable excited conditions by the leading pantograph to give compressive force on the trailing pantograph in locations of low contact force and also the adoption of the leading pantograph as an auxiliary pantograph that draws no electrical power from the overhead line [71, 73], however this presents a problem in the case of multi–train coupling where the two joined units are electrically distinct and thus require current drawing pantographs on both units. In [74], by adopting the pantograph spatial separation given in Equation 2.1, the dynamic performance was predicted to improve beyond using only the optimal pantograph separation, by the installation of damping elements in the contact wire steady arms.

2.2.1 Active pantographs

Active pantograph control is found to improve the dynamic performance of the catenary pantograph interaction in [75, 76], particularly due to the suppression of vibrations in the pantograph head. Due to the variable stiffness in the contact wire, active pantograph control reduces the uplift force at the stiffer locations such as supports, correcting the larger variation in the contact force typical of classic pantograph types. Active pantograph control has been proposed as a promising technique for the interoperability of different pantograph types across a range of networks. Analysis of active pantographs however is largely limited to numerical investigations to determine the benefits of active control, and only a few cases have reached prototyping stage [77, 78], or use in line tests [79].

Proposed methods for active pantographs work in conjunction with the static load applied to passive pantographs, largely to allow for continued pantograph operation in the event of failure of the control systems of the active components. Figure 2.16 shows the locations where actuation of the pantograph can be applied. In Figure 2.16a, the actuation is applied to the pantograph frame and is advantageous as the control for the pantograph can be mounted directly on the train body, avoiding limitations on the size of the kind of actuator used. In the case of the TGV [80], ETR500 and ETR1000 fleets [39], the actuator controls the static preload applied to the pantograph, or to regulate the dynamics of the pantograph frame

[81, 82]. Alternative approaches include torque motors installed between the lower arm and the train body [83], or wire actuation connecting the upper arm to the train body [84].

Actuation in parallel with the pantograph head suspension, as in Figure 2.16b, is more effective in controlling phenomena at higher frequencies than actuation from the base of the train, where dynamic effects of the actuation are damped by the pantograph frame. However, installation of extra components at the pantograph head limit the size due to needing to avoid introducing unwanted dynamic effects on the pantograph catenary interaction. In [77, 79], active control is introduced using pneumatic actuators alongside the suspension mounted in the pantograph head, whilst [85] proposes a torque motor to provide active control. The final location, shown in Figure 2.16c, is directly at the contact interface and significantly limits the installation of active control. Similarly to the first case, [86, 87], propose wire actuation to improve the dynamic performance, whilst [88] proposes a movable wing to control the dynamics of the catenary pantograph interaction through regulation of the aerodynamic lift force during train operation. Thus far, it does not appear these proposals have been adopted widely on pantographs. Additions of aerofoils to the pantograph frame to reduce the effects of aerodynamic loading appears to be the only widely adopted method of pantograph control.

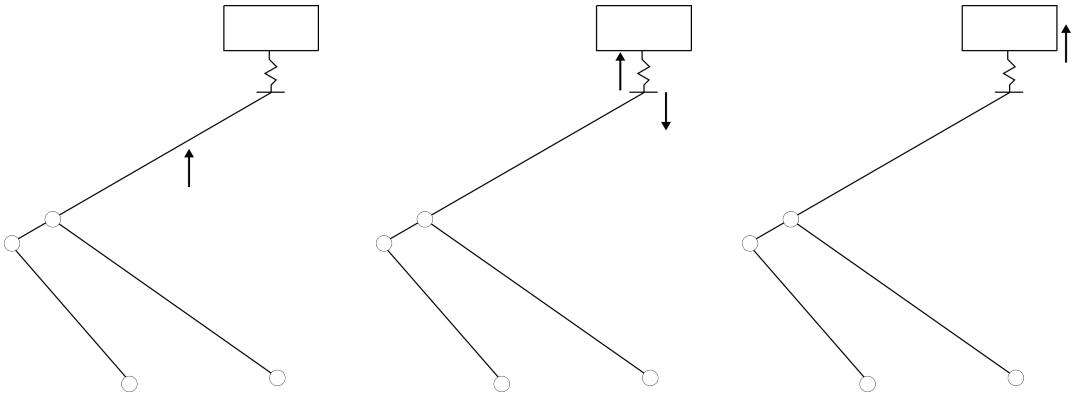

Fig. 2.16 Locations of proposed force actuation in active pantographs: (a) actuation of the pantograph frame, (b) parallel actuation in line with the head suspension, and (c) actuation of the collector strips.

2.3 Contact between the pantograph and overhead line equipment

Examining the dynamic contact between the pantograph collector head and the contact wire has largely been the focus of catenary pantograph interaction studies. Maintaining good contact is vital to the smooth running of rail services, since without contact, electric trains are stranded causing delays and service disruption. Too high a contact force also causes unnecessary wear at the contact interface shortening the service life of the equipment. Loss of contact between the contact surfaces causes arcing, degrading the interface, and in the case of contact loss and the pantograph rises above the wire, catastrophic damage to the pantograph and overhead line can occur. In the lateral direction, deviation of the contact wire lateral position and high winds contribute to large deflections in the contact wire causing dewirements [89]. As such research has focused on minimising the variations in the contact between the pantograph and overhead line and reducing the likelihood of dewirements. Investigations such as in [90], also investigate the effects of the pantograph raising speed on the dynamic force at the contact interface and it was found that increasing the raising speed from 0.1 to 0.7 m/s, increased the contact force approximately 600%, risking damage to either the pantograph or the overhead equipment. Raising the pantograph into contact at clamp locations between the contact wire and droppers was also found to lead to a significant increase in the contact force. In [91], the sliding contact was characterised with respect to the contact resistance, temperature distribution and microstructure.

2.3.1 Wear

To maintain regular traffic operation, maintenance of the contact surfaces on both the pantograph and the overhead line is vital. Wear phenomena caused by the sliding contact during train operation is one aspect of vital maintenance at the pantograph catenary interface. Much research has been undertaken aimed at reducing the wear rate on both the overhead line and the pantograph components to improve the reliability and reduce service life costs of the equipment. Due to the sliding contact between the pantograph carbons and the contact wire, mechanical wear is induced which can be approximated by the Archard wear law [92, 93]. Estimation of the wear due to the sliding contact was performed in [94]. More comprehensively, the sliding contact wear regime is driven by a combination of mechanical and electric wear [95] and factors such as current intensity, mean contact force and arcing are recognized as significant influencing factors on the wear regime. The wear of the contact

wire is dominated by plastic deformation of soft asperities [96] and initially the contact wire wear rate increases rapidly due to a relatively small contact surface, but slows as the contact wire is worn and a larger contact surface is created [97]. To improve the wear regime between the contact surfaces, [98] propose a new circular design of pantograph, found to have reduced temperature profiles during testing. Viscous damping of the pantograph head drives the mechanical wear between the contact surfaces, and degradation of the viscous damping leads to poor wear behaviour [99].

Replication of the contact interface to study the electromechanical interaction between the contact strips and overhead line was performed [100–102] and the effects of various different contact wire and collector strip compositions have been considered. Materials considered include, pure carbon collector strips [103], copper carbon strips [104], iron based strips [105] and composite materials [106]. To extend the laboratory conditions described in [107] to operational environments, numerical modelling of the catenary pantograph interaction coupled with a surface wear model was performed in [101] to predict the wear rates of the contact wire and collector strips. The effects of train body accelerations on the wear between the contact surfaces was investigated in [108]. During train body acceleration, the mechanical wear increased and during deceleration, mechanical wear between the contact surfaces decreased, but an increase in the electrical wear was predicted. Wear models are adopted as part of catenary pantograph interaction models in [101, 109], and electrical wear is noted to be the dominant driver of the wear behaviour. In [109], arcing is predicted to be the least significant contributor to wear, then the mechanical and finally the electrical wear. In [110], the wear due to the sliding contact is found to increase due to electric current and in [97], increasing the electrical current increases the wear rate of the contact wire.

2.3.2 Loss of contact and arcing

Maintaining good contact between the contact wire and the pantograph is vital to the smooth operation of electric trains especially at high speeds. Reattachment after loss of contact induces an impact force between the contact surfaces [111]. Thus it is recommended that the pantograph head collector mass is minimised. When loss of contact between the carbon strips and contact wire occurs, arcing between the contact surfaces occurs. Contact loss events causing arcing leads to melting and vaporisation of the contact wire [93] and pantograph [112] due to thermal effects promotes additional wear, shortening the service life of the equipment.

Contact loss detection typically involves the addition of sensors to the existing system, unavoidably modifying the physical characteristics such as overhead line geometry or mass of the pantograph. In [113, 114], a non-invasive method of detecting contact loss is presented by measuring electromagnetic emissions due to arcing events. The method is suitable for both AC and DC systems. Contact loss in DC systems is also possible through measurement of pantograph voltage loss during such events [115]. The severity of arcing is enhanced for a system under crosswind. In [116], applying a magnetohydrodynamic formulation to a current carrying contact wire and collector strip, increases in the wind speed were found to increase the spatial length of the arc, up to approximately 17 mm when the wind speed was 30 m/s, however the increase in the arc length was found to have little effect on the surface temperature during the arcing which was predominantly set by the arc current.

2.4 Condition monitoring

Evaluating the static state of the overhead line equipment typically involves measurements of the spatial location of the wires and supports and also of the wear state of the contact wire. Measurements of the contact wire position and stagger indicates the deviation from the installation position. Large deviations from the nominal position is undesirable for good current collection quality and degrades the dynamic performance during train operation. Similarly, large contact wire wear requires replacement of the contact wire and also indicates poor dynamic performance if wear levels are higher than expected. As train speeds increase, the tolerances for equipment deviation are reduced. In [117], the concept of contact wire irregularity as an index of the state of the contact wire geometry is proposed. The index includes both surfaces deformations in the contact wire due to wear and deviation of the equipment from a nominal position. The effects of the contact wire irregularity are investigated in [88] based on measurements of installed equipment combined with simulation predictions. From measurements of the pantograph acceleration, the contact wire irregularity can be determined. Using the power spectral density, [118] quantified the contact wire irregularity. Assuming the contact wire irregularity observed a stochastic process, for N samples $x(1), x(2), \ldots$, the power spectral density is described by

$$P(\omega) = \frac{1}{N}|X(\omega)|^2 = \frac{1}{N}\left|\sum_{m=1}^{N} x(m)e^{-im\omega}\right|^2. \tag{2.2}$$

Using a test rig combining hardware–in–the–loop with synthetic wire heights, [119] indicated that discrete frequencies in the contact wire irregularity leads to an increase in the dynamic contact force and contact loss. Using the power spectral density [120] shows that irregularity due to contact wire wear is less significant on the current collection quality than compared to aerodynamic loading or geometry deviations. Localised irregularities such as position defects are considered in [88]. The dynamic effects of the localised irregularities were noted to be highly sensitive to the operating speed and propose that allowable defects are given in terms of the operational train speed.

In [121], a stochastic process is adopted to distribute irregularity in the contact wire and it was found that the contact force variation was greatest due to irregularity in the contact wire height due to deviations in the dropper lengths. Applying the target configuration under dead load formulation, [122] compared representing contact wire irregularities as hard spots rather than exact irregular lengths, it was found that current predictions of the contact force due to irregularity were conservative. The contact force variation due to contact wire height irregularity was also noted to be small (less than 6%). Assuming contact wire irregularity such as incorrect dropper spacing is adopted in [123], where the irregularity is assumed to be a normally distributed random variable, the contact wire height variation was found to be the dominant driver of contact force variation compared with dropper spacing. When irregularities in the contact surface are created, [124] predicts greater contact force if dropper defects are located in the first or last droppers in a span.

Detecting the onset of fatigue of the contact wire during the service life as line speeds are increased is investigated in [125, 126]. Early detection of potential failure modes of the overhead line has developed using a range of sophisticated techniques such as diagnostic tools based on the measurements of pantograph dynamics through the use of accelerometers to assess contact wire irregularity [88], and collector performance [127] alongside conventional techniques of visual and manual inspections by maintenance crews. Installation of measuring devices on commercial rolling stock has allowed for a wealth of daily information to infrastructure owners for the development of condition monitoring techniques currently in use.

Typically accelerations of the pantograph collectors are used as accelerations of the pantograph head are indicative of the corresponding contact force between the pantograph and the overhead line [128]. Identification of faults on the network can be performed through cross–referencing of measured pantograph accelerations across a range of trains operating on the same line. This cross–referencing also identifies out–of–standard pantograph operation particularly in the case of lines operating with the same pantograph type on a majority of

the rolling stock. Further techniques to detect system faults include infrared cameras to detect the temperature across the carbon strips [129] and conventional digital cameras for use by infrastructure owners to identify relevant aspects of the pantograph and overhead line condition. Image processing is also adopted in [130] to detect abnormal operating conditions, and [131] propose a diagnostic technique of the overhead line based on detection of light emissions in the 275–285 nm band due to arcing, not corrupted by natural light

Condition monitoring of the pantograph is performed in [31], identifying faults using a frequency response function, however is limited by requiring multiple excitations at various frequencies to identify faults. Similarly, in [132] using the dynamic frequency response, an index is proposed as a structural health monitoring tool, identifying faults in the equipment based on the degradation of the dynamic response of in–situ equipment. The measurement of in–situ equipment is used to assess the quality of the tensioning quality over time in [133] by measurement of the contact wire accelerations during train passage. Monitoring of the overhead equipment on UK lines is performed by Mentor and New Measurement Train (NMT).

2.5 Wind loading

2.5.1 Aerodynamics of the pantograph

Aerodynamic effects due to pantograph and overhead line dynamics are noted for their effect on the dynamic contact force between the pantograph and overhead line, with regards to both the average contact forces and the dynamic variation [134, 135]. Dynamic effects due to aerodynamic loading acting on the pantograph must be taken into account for train running speeds above 200 km/h, where the dynamic effects are large. The mean drag and lift forces can increase the mean contact force during train operation by acting to increase the uplift force provided by the pantograph [136, 137]. This aerodynamic uplift is driven by the train speed, pantograph working heights [138], and pantograph orientation [139]. Compared with old pantograph configurations such as cross–arm pantographs [140], modern pantographs are asymmetrical and operate with the pantograph knuckle orientation reversed. Operating with the knuckle downstream acts to increase the vertical uplift force [141] due to “opening” of the pantograph and extending the working height. In [142, 141], it was found that the pantograph operation with the knuckle in the upstream orientation is predicted to give the best dynamic performance.

The aerodynamic uplift during train operation also increases during passage through tunnels as the velocity of the air inside the tunnel increases [143]. Attempts at reducing the effect of aerodynamics on the pantograph have included the addition of aerofoils mounted on either side of the pantograph arms. The aerofoils act to increase pantograph stability during operation, however are poorly optimised for both pantograph orientations. To improve stability of the pantograph, in [39], the adoption of varying static preloads related to the train speed and pantograph was found to compensate for the aerodynamic uplift, giving good dynamic performance for a range of speeds and both pantograph orientations.

Poorer current collection quality is observed when steady aerodynamic loads act on independent current collectors mounted on the pantograph head. The aerodynamic forces cause an unbalanced contact load on each of the collector strips leading to non–uniform wear regimes [134].

Aerodynamic effects are not limited to the pantograph however. The overhead line is highly susceptible to wind loading due to the relatively large span lengths and the cable flexibility. Considering aerodynamic loads as a combination of steady and stochastic wind phenomena, behaviours such as vortex–induced vibrations and buffeting are possible [144]. Aerodynamic instability of a railway contact wire due to unsteady aerodynamic forces can be divided into two groups, that of vortex–shedding and turbulence. Due to discontinuities in train bodies such as carriage separation, electrical insulators, cabling, turbulent wakes excite the pantograph, typically at low frequencies where assessment of the current collection quality is made (i.e. in the 0–20 Hz range) [61]. Turbulent wakes are also possible due to upstream pantograph components, thus placing the pantograph itself in the turbulent wake.

High frequency excitation of the pantograph due to vortex shedding in the wake of the pantograph collector head [145] leads to increase likelihood of arcing events during train operation [41], whilst also increasing aerodynamic noise [146]. Aeroacoustic issues relating to flow around the pantograph are also considered in [147], where efforts to reduce aeroacoustic effects during train operation were performed by optimization of the pantograph head shape. In [148], the aeroacoustic are also considered due to aerodynamic interference between the pantograph collector head and the pantograph frame using numerical techniques. Aerodynamic noise also occurs due to the recesses in the train roof. The trailing vertical face of the recesses are the major driver of aerodynamic noise during train operation [149], however this can be overcome by moving the flow reattachment point downstream of the recess by installing spoilers or alteration of the recess geometry. Movement of the reattachment point outside the recesses reduced the aeroacoustic noise.

Typically, research performed to investigate the aerodynamics during electric train operation have been to reduce the aerodynamic effects on the current collection quality [150, 151] using average aerodynamic loads. Non–stationary phenomena is also considered, for example, in [106], however in current technical standards, only average effects are considered when performing evaluation of the contact force variability. Unsteady forces caused by vortex shedding phenomena were investigated in [152] for train speeds up to 350 km/h and found that the vortex shedding acts to increase the contact force variation during train operation.

Experimental efforts to understand aerodynamic effects require validation with track tests, and have become more widely adopted to allow assessment of pantograph aerodynamic behaviour for a range of test conditions. In [153], turbulent flow along the boundary of high speed trains is considered, and it is noted that accurate representation of the boundary layer across the train body is necessary to correctly estimate the dynamic uplift due to aerodynamic loading. The accurate representation of the boundary layer behaviour necessitates validating aerodynamic track testing. Experimental wind tunnel tests also serve as validation of computational fluid dynamics (CFD) techniques, allowing for a much greater range of configurations and test conditions than would be readily available with physical testing. Full–scale testing of pantographs in a wind tunnel is performed in [154, 155] and comparison between the measured and predicted aerodynamic forces is made. CFD techniques also make calculation of drag and lift forces on pantograph components such as the collector strips and pantograph head much more readily available [156] and these models have been extended to full scale pantograph models in [157], where the dynamic effect of the train body close to the pantograph mounting location is considered. Using full scale representations of train bodies, in [158] the aerodynamic loads on a single pantograph are investigated, and in [141] the mounting position for multiple pantograph operation indicates that the aerodynamic loads on the trailing pantograph are greater than the leading pantograph, in expectance with the degraded dynamic performance associated with trailing pantographs.

Optimization of the pantograph using both wind tunnel testing and CFD led to the development of a new pantograph type [150], optimizing the aeroacoustic characteristics [159] as well as the development of active pantograph control techniques to control the aerodynamic characteristics of the pantograph using blown air along the pantograph edge [160].

2.5.2 Aerodynamics of the overhead line

The long spans and high flexibility of overhead railway lines make the system very susceptible to aerodynamic loading, and aerodynamic forces can decrease the contact wire sag [161] and potentially increase wire uplifts in excess of double those in still air [162]. Typically research into the aerodynamic effects on the overhead line have been separated into studies of steady wind where vortex induced vibrations are likely and stochastic wind leading to buffeting. A significant effect of aerodynamic loading of the overhead line is the increased risk of dewirement [163–165], where the contact wire deflects away from the design position and slides off the end of the pantograph. Typically the pantograph then rises above the contact wire and hits the droppers causing damage to the overhead line and pantograph.

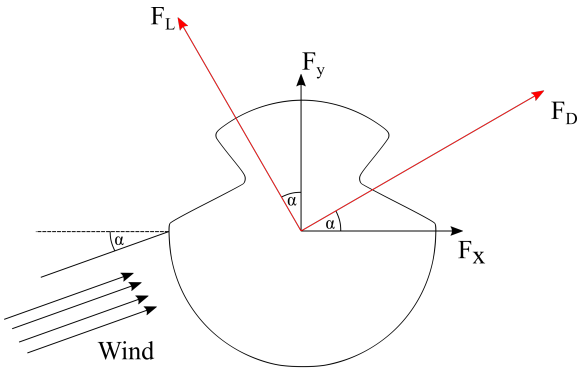

Fig. 2.17 Contact wire cross–section under steady wind with an angle of attack α. Only flow in the F_xF_y plane is considered.

The aerodynamic drag and lift forces, denoted F_D and F_L, on a railway contact wire under steady wind as shown in Figure 2.17, are given by

$$F_{\text{Drag}} = \frac{1}{2}\rho U^2 A L C_D, \tag{2.3}$$

and

$$F_{\text{Lift}} = \frac{1}{2}\rho U^2 D L C_L, \tag{2.4}$$

where ρ is the air density, U is the wind speed, A, the cross–sectional area of the contact wire and L the length under consideration. Considering an angle of attack α, as shown in Figure 2.17, Equations 2.3 and 2.4 can be expressed using a coordinate transformation as

$$\begin{pmatrix} F_x \\ F_y \end{pmatrix} = \begin{pmatrix} \cos\alpha & -\sin\alpha \\ \sin\alpha & \cos\alpha \end{pmatrix} \begin{pmatrix} F_{\text{Drag}} \\ F_{\text{Lift}} \end{pmatrix} \tag{2.5}$$

where F_x and F_y correspond to the original coordinate axes in the untransformed coordinates (i.e. when $\alpha = 0$) and F_{Drag} and F_{Lift} are the drag and lift forces parallel and perpendicular to the flow respectively. The equations for the aerodynamic lift and drag are extended for unsteady fluctuating wind in [166], and the aerodynamic forces can be expressed as

$$F_{\text{Drag}} = \frac{1}{2}\rho UAL\left(2C_D(\alpha)u(t) + \left[\frac{\mathrm{d}C_D(\alpha)}{\mathrm{d}\alpha} - C_L(\alpha)\right]w(t)\right) + \frac{1}{2}\rho U^2 ALC_D(\alpha) \tag{2.6}$$

$$F_{\text{Lift}} = \frac{1}{2}\rho UAL\left(2C_D(\alpha)u(t) + \left[\frac{\mathrm{d}C_L(\alpha)}{\mathrm{d}\alpha} - C_D(\alpha)\right]w(t)\right) + \frac{1}{2}\rho U^2 ALC_L(\alpha), \tag{2.7}$$

where $u(t)$ and $w(t)$ are the fluctuating wind in the lift and drag directions. The fluctuating aerodynamic load leads to large vibrations of the contact wire degrading the current collection quality, however limited to horizontal crosswind flows, aerodynamic loading has little effect on the current collection quality [135].

Symmetric cable aerodynamic instability has been well documented in the literature due to extensive research on power transmission lines and cable stayed bridges [167–169]. Aerodynamic instability such as aeolian and vortex induced vibrations have been observed and mitigation of aerodynamic induced vibration include the use of Stockbridge dampers [170, 171]. Modern tuned mass dampers are effective for a range of frequency modes corresponding to various wind speeds [172]. Compared with studies of symmetric conductors, investigation of the dynamic response of asymmetric cables to wind loading such as railway contact wires is limited. The asymmetric cross–section of a railway contact wire leads to the aerodynamic instability known as conductor gallop [173]. This aerodynamic instability becomes more likely as wear of the contact wire increases and during icing conditions [174–176]. Icing of the contact wire occurs in three ways [177]:

1. Supercooled droplets hit cables at subzero temperatures and freeze. Accretion of ice in this way is slow and depends on the liquid water content of the air.

2. Rain or snow precipitation freezing on contact with surfaces. Accretion in this manner occurs more rapidly and has the potential to cause more damage.

3. Water vapour in the air freezes onto cool surfaces.

In [174], the stability condition for aerodynamic damping for a steady wind load derived from a one–dimensional equation of motion

$$m\left(\frac{\mathrm{d}^2 y}{\mathrm{d}t^2} + 2\xi\omega\frac{\mathrm{d}y}{\mathrm{d}t} + \omega^2 y\right) = -\frac{1}{2}\rho UA\left(\frac{\mathrm{d}C_L}{\mathrm{d}\alpha} + C_D\right)\frac{\mathrm{d}y}{\mathrm{d}t}, \tag{2.8}$$

which gives the damping coefficient for the one–dimensional oscillator as

$$d = 2m\xi\omega + \frac{1}{2}\rho UA\left(\frac{\mathrm{d}C_L}{\mathrm{d}\alpha} + C_D\right). \tag{2.9}$$

Conductor gallop occurs when $d < 0$, which can only occur when

$$\frac{4m\xi\omega}{\rho UA} < -\left(\frac{\mathrm{d}C_L}{\mathrm{d}\alpha} + C_D\right), \tag{2.10}$$

giving the Den Hartog coefficient requirement for conductor gallop

$$\left(\frac{\mathrm{d}C_L}{\mathrm{d}\alpha} + C_D\right) < 0. \tag{2.11}$$

Equation 2.8 strictly considers aerodynamic load for a single degree of freedom. In [178], an angle of attack α is introduced giving,

$$\frac{\mathrm{d}^2y}{\mathrm{d}t^2} + \frac{c}{m}\frac{\mathrm{d}y}{\mathrm{d}t} + \frac{k}{m}y = \frac{\rho A}{2m}U^2\left(C_L(\alpha)\cos\alpha + C_D(\alpha)\sin\alpha\right). \tag{2.12}$$

Introducing the linearization $\alpha \ll 1$, the single degree of freedom oscillator is

$$\frac{\mathrm{d}^2y}{\mathrm{d}t^2} + 2\left(\xi_s + \xi_a\right)\omega_n\frac{\mathrm{d}y}{\mathrm{d}t} + \omega_n^2 y = 2\xi_a\omega_n v, \tag{2.13}$$

where ξ_s and ξ_a are the structural and aerodynamic damping coefficients respectively, ω_n is the natural frequency and u and v are the velocity components of the relative wind speed U, i.e. $U = (u, v)$. The sign of the damping coefficient determines the possibility of conductor gallop. Thus galloping occurs when

$$\xi_s + \xi_a = \xi_s + \frac{\rho Au}{4m\omega_n}H(\alpha) < 0, \tag{2.14}$$

where $H(\alpha) = c_L'(\alpha) + c_D(\alpha)$ [179] with c_L', the derivative of the linearized lift coefficient, and c_D the linearized drag coefficient. This gives the conductor galloping condition $4m\omega_n\xi_a/(\rho Au) < -H(\alpha)$. That is $H(\alpha) < 0$ is required for galloping to occur consistent with the den Hartog condition in Equation 2.10. In [176], the determination of the galloping condition for an overhead line is extended using finite element and computational fluid dynamics techniques. It is predicted that galloping of a 50 m contact wire under static wind with speed 20 m/s occurs at angles of attack in the neighbourhood of 25°. Under icing conditions, the angle of attack for which galloping is possible is highly sensitive to the icing

angle, and that galloping can occur for angles of attack as high as 49°. In [180], the drag coefficient is calculated for contact wires under a range of angles of attack and steady wind conditions. Compared with the accepted drag coefficient of 1.0 [26], the drag coefficient for a contact wire was predicted to be between 1 and 1.8, indicating that compared with a smooth circular cylinder, the grooves of a contact wire have a large effect on the drag coefficient.

To counteract the galloping effects of wind loading, tuned mass dampers were deployed on the East Coast Mainline in the UK in [173] to increase the effective mechanical damping of the system. The wind speed at which galloping occurred was found to increase, however it appears that this method to mitigate aerodynamic instability has not been adopted elsewhere.

Whilst the effect of aerodynamic phenomena on the current collection quality is limited, the interaction between aerodynamic loading and rolling stock is better understood [181–183]. In [184], aerodynamic loads on rolling stock passing bridge towers were determined experimentally. Bridge towers act to protect the rolling stock from crosswind effects thus reducing the aerodynamic loads on the rolling stock. The decrease in the measured aerodynamic drag on the train body is likely to occur on the pantograph as well. In [185], the coupling of aerodynamic loading to moving train bodies predicted the increase in the instability of the train body. Increased instability of the train body would likely cause degradation of the catenary pantograph interaction. Whilst train movement due to vertical displacement on the suspension is small relative to the working height of the pantograph, lateral deflections due to crosswind increase the risk of dewirement. Current collection quality is predicted to decrease due to crosswinds across bridge parapets [34, 186]. The parapets act to direct the crosswind away from the bridge level to the overhead equipment, and lead to an increase in turbulent aerodynamic effects at the contact wire height.

2.6 Modelling the catenary pantograph interaction

Numerical analysis of the catenary pantograph interaction is well documented and a range of methods have been proposed throughout the literature, compared with experimental investigations such as [187, 188], which are limited due to the large physical scales involved in the catenary pantograph interaction. Advantages of numerical modelling of the catenary pantograph interaction include the timely ability to optimise the dynamic contact force for a range of system geometries and pantograph types. In [189, 190], line speed increases on existing lines can be realised by optimizing the dynamic response to pantograph passage and in [191], tuning of the pantograph models is used to determine improvements with regards to the mechanical performance. Early approaches have adopted the use of undamped wave

equations [192], or the damped Klein–Gordon equation in [193], and also those presented in [162] where a 2D catenary model based on Euler–Bernoulli beam theory, such as the beam shown in Figure 2.18 is used.

Fig. 2.18 Simply supported beam model representing a 2D catenary model under tension T and subject to a moving load $q(x,t)$.

The contact line is assumed to be described by the equation

$$\rho A\frac{\partial^2 w}{\partial t^2} = T\frac{\partial^2 w}{\partial x^2} - EI\frac{\partial^4 w}{\partial x^4} - \beta\frac{\partial w}{\partial t} + q(x,t), \tag{2.15}$$

where ρA is the wire self–weight, EI the bending stiffness, T the wire tension and β represents viscous damping of the system. External forces exerted by the pantograph are represented by $q(x,t)$ and the total deflection of the wire is given by $w = w(x,t)$. Equation 2.15 is also adopted as a model of the overhead line in [194], with the damping of the overhead line neglected. Approximating the uplift force due to the pantograph by $q(x,t) = Q\delta\left(x-(L_p+ct)\right)$, where $\delta(\cdot)$ is the Delta distribution, and L_p is a point along the beam of length L, Equation 2.15, when $\beta = 0$, admits the solution

$$w(x,t) = \sum_{m=1}^{\infty} A_m \left(\sin\frac{m\pi\left(L_p+ct\right)}{L} - \frac{1}{\omega_m}\frac{m\pi c}{L}\cos\frac{m\pi c}{L}\sin\omega_m t \right.$$
$$\left. - \sin\frac{m\pi c}{L}\cos\omega_m t \right) \sin\frac{m\pi c x}{L}, \tag{2.16}$$

where

$$A_m = \frac{2Q}{L}\left[EI\left(\frac{m\pi}{L}\right)^4 + T\left(\frac{m\pi}{L}\right)^2 - \rho A\left(\frac{m\pi c}{L}\right)^2\right]^{-1}, \tag{2.17}$$

and

$$\omega_m = (\rho A)^{-1/2}\frac{m\pi}{L}\left[T + \left(\frac{m\pi}{L}\right)^2 EI\right]^{1/2}. \tag{2.18}$$

Neglecting the damping gives the critical wave speed for the contact wire as

$$c_s^2 = \frac{1}{\rho A}\left(\frac{\pi^2 EI}{L^2} + T\right). \tag{2.19}$$

For an overhead line, $\pi^2 EI/L^2$ is small compared to T [194], so the critical wave speed can be approximated by $c_s^2 \approx T/\rho A^2$.

Including viscous damping, i.e. $\beta \neq 0$, the explicit two–step iteration finite difference method

$$y^{(n+1)} = 2y^n - y^{(n-1)} + \Delta t^2 \left(f\left(y^n\right)\right), \tag{2.20}$$

where $n \pm 1$, denotes a time step, and y is the vertical displacement of the wire, was utilized in [162, 195, 196], to solve Equation 2.15. The acceleration f approximated the contact force and satisfied the equation $\ddot{y} - \Omega^2 y = f(y)$, where $\dot{y}$ denotes a time derivative and Ω is the natural frequency of the contact wire.

If the mechanical wave speed given by Equation 2.19 is exceeded by the pantograph speed, large deformations in the contact are similar to the shockwave experienced by aircraft exceeding Mach 1. Approaching the mechanical wave propagation speed, large changes in the contact wire strain are observed, which can be reduced by modification of the contact wire tension or linear density. However, changes in the linear density of the contact wire increase the transmission losses during operation. The speed limit for the train running speed is considered in [197], using vibration measurements and the Gabor wavelet transform to determine the wave velocity, building on preliminary experimental work on the mechanical wave speed presented in [198]. The contact wire uplift contour is adopted in [194, 199] to predict the mechanical wave propagation speed, however assuming the contact wire to be a single string or beam in the adopted method overestimated the group velocity by approximately 13%.

The magnitude of the reflected wave at supports was suppressed in [21] after installing a tuned damper during multiple pantograph operation to improve the current collection quality in overlap sections. In [200] the relationship between travelling waves and the periodic dropper locations is studied using the Laplace transform, however is limited due to numerical instability of the inverse Laplace transform. To minimise contact loss due to reflected waves, [201] adopt the matrix transfer method to evaluate the vibrations in a contact wire and predict that contact loss occurrence can be reduced with an increase in the contact wire tension thus increasing the mechanical wave speed. In [202], a reduction in the dynamic impedance of the messenger wire was found to favour an improved dynamic performance and propose testing new shapes or materials with a reduced linear mass to achieve this.

Use of Euler–Bernoulli beam theory is advantageous to approximating simple instances of the overhead line system as the existence of elementary solutions such as Equation 2.16 or

[2]For the Series 1 overhead line system, $T = 16.5$ kN and $\rho A = 1.07$ kg/m, thus, Equation 2.19 gives a critical speed of 124 m/s $\approx$ 446 km/h.

being amenable to simple time integration algorithms such as Equation 2.20 allow for rapid analysis compared with full finite element or nodal coordinate solutions. However, the linear model given by Equation 2.15 neglects the influence of droppers and the messenger wire on the catenary pantograph interaction. Other early representations of the catenary pantograph interaction include [203], where the forced, damped Mathieu equation

$$\frac{\mathrm{d}^2 y}{\mathrm{d}t^2} + 2\xi \frac{\mathrm{d}y}{\mathrm{d}t} + (1 + \bar{\alpha}\cos t)y = \bar{f}, \tag{2.21}$$

is used and the contact wire is represented by a periodically supported infinite string. The one–dimensional Mathieu equation is limited as an assessment of the catenary pantograph interaction due to averaging the stiffness variations in the contact wire between droppers. Adoption of visco–elastic string models, such as Equation 2.15, is still attractive in more modern representations of the catenary pantograph interaction. In [204], the visco–elastic string model is extended to multiple pantograph operation and a more sophisticated model of damping (the Kelvin–Voigt model). Much like other works, the analytical model is still limited by the lack of nonlinearities and use of uniform stiffness. Since the vertical stiffness along a span varies [205], analytic procedures such as the those described here are insufficient to accurately represent the catenary pantograph interaction particularly at high mean contact force values.

More sophisticated techniques for modelling the catenary pantograph interaction include finite element analysis, or the modal superposition method. In the modal superposition method, such as in [206, 207], the deflections of an overhead line are expressed as

$$y(x,t) = \sum_{j=1}^{n} \phi_j(x) u_j(t), \tag{2.22}$$

where the displacement $y(x,t)$ is the sum of the product of the mode shapes ϕ_j and the generalised coordinates u_j. In an orthogonal basis for the modes ϕ_j (i.e. in the modal coordinates), the equation of motion of can be written as

$$\frac{\mathrm{d}^2 u_j}{\mathrm{d}t^2} + 2\omega_{jj}\xi_j \frac{\mathrm{d}u_j}{\mathrm{d}t} + \omega_{jj}^2 u_j = M_{jj}^{-1} q_j(t), \tag{2.23}$$

where ξ_j is the damping ratio of the j^{th} mode, $q_j(t)$ is the force vector and M_{jj} and ω_{jj} are the modal masses and frequencies in the orthogonal basis respectively. Equation 2.23 can be iterated using a Newmark process to determine the generalised coordinates u_j, giving the displacements by substituting the generalised coordinates into Equation 2.22. Modal

superposition requires a significant number of modes, at least 180 [208], to give good representation of the catenary pantograph interaction. In [209], the dynamic stress response in the catenary under dynamic loading is calculated using the modal superposition method and in [210, 119] a hybrid simulation between the modal representation of the catenary and a pantograph using hardware–in–the loop techniques.

In any chosen method, simulating the catenary pantograph interaction typically involves the realisation of a steady state catenary equilibrium and a transient simulation of the contact between train mounted pantographs and the overhead line. Finding the initial catenary configuration is not trivial [211, 212], however in general, the messenger wire is assumed to be parabolic [13] to determine the length of droppers given a contact wire height, or equivalently the height of the contact wire given the dropper lengths. Whilst in truth the messenger wire under self weight forms a catenary (or hyperbolic cosine), since

$$\frac{T_{mes}}{mg}\cosh\left(\frac{mg}{T_{mes}}(x-x_0)\right)+C=\frac{T_{mes}}{mg}+\frac{1}{2}\left(\frac{mg}{T_{mes}}(x-x_0)^2+\mathscr{O}\left((x-x_0)^4\right)\right)+C \quad (2.24)$$

$$\approx C+\frac{T_{mes}}{mg}+\frac{mg}{2T_{mes}}(x-x_0)^2, \quad (2.25)$$

for small argument[3], approximating the vertical shape of the messenger wire as a parabola is suitable.

Assuming the messenger wire shape limits the ultimate shape of the contact wire without preset dropper lengths, as the parabolic messenger wire shape neglects presag of the contact wire. This can be avoided if the height of the contact wire is set and the dropper lengths are calculated to achieve the desired level of contact wire presag. In [213], the shape of the catenary is derived from explicit expression for the contact and messenger wires, adopting an iterative process to calculate the lengths and therefore the loads in the droppers to produce the correct static equilibrium. Similarly, in [214, 215], an explicit expression for the length of the droppers and presag of the contact wire is derived, giving the contact wire sag (s_c) at the j^{th} dropper location as

$$(s_c)_j=\frac{m_{con}g}{T_{con}}(x_j-l)(L_s-x_j+l), \quad (2.26)$$

where x_j is the location of the j^{th} dropper, L is the span length and l the distance between a support and the first dropper in the span. With the contact wire sag and forces in the dropper

[3]For typical messenger wire tension T, the argument of higher order terms in the expansion of the hyperbolic cosine is of order $10^4/10^{12}=10^{-8}$.

known, the messenger wire sag (s_m) at the droppers is therefore

$$(s_m)_j = \frac{1}{T_{mes}} \left(F_s x_j - \frac{1}{2} m_{mes} x_j^2 - \sum_{i=1}^{j-1} F_i (x_j - x_i) \right), \tag{2.27}$$

where F_s is the reaction force at the support and F_i the force acting on the i^{th} dropper.

The method to generate the shape of the catenary derived using Equations 2.26 and 2.27, is contrasted by the method in [216–219], where a 3D representation of the overhead line is created using the absolute nodal coordinate formulation, which transforms the shape finding problem to the problem of optimizing the shape of the catenary. The optimization of the catenary system height is found to be more accurate in matching the desired catenary shape based on benchmark geometries, however the requirement of higher order derivatives during the optimization process makes the method undesirable compared with analytical techniques, which are found to represent the catenary shape to a good level.

To consider the changes in the unloaded lengths of the contact and messenger wires, [220] adopted a nonlinear model based on flexible cable and truss elements to achieve the target configuration under dead load (TCUD). The TCUD corresponds to the desired static equilibrium of the catenary. The equation of motion for the catenary is derived as

$$d\mathbf{F}_c = \mathbf{K}_c d\mathbf{X} + \mathbf{K}_G d\mathbf{L}_0, \tag{2.28}$$

where $\mathbf{K}_c$ is the stiffness of the incremental coordinate, $\mathbf{K}_G$, the stiffness of the initial lengths and $d\mathbf{X}$ and $d\mathbf{L}_0$ are the incremental and initial lengths respectively. The unbalanced force vector is given by $\mathbf{F}_C$. The design constraints limit the size of the system in Equation 2.28, and the Newton–Raphson iteration optimizes the initial catenary shape. Compared with [215], the TCUD varied by 0.7 mm.

2.6.1 Finite element analysis

In the literature, a common technique for simulating the catenary pantograph interaction is representing the overhead line geometry using finite elements [42, 40, 221, 222] and coupling the resulting geometry with either a lumped–mass or multibody approach to the pantograph.

Solving the structural problem of the catenary pantograph interaction requires reducing the continuum equation for infinitesimally small elements to a set of discrete finite elements to approximate the resultant behaviour. With respect to the use of a commercial package such as ANSYS as used in this thesis, the finite element method is programmed automatically

without the need for user implementation of the method. As an example however, consider the linear equation

$$\frac{\mathrm{d}^2\tilde{u}}{\mathrm{d}x^2} = -\frac{b}{a}, \tag{2.29}$$

for $0 \leq x \leq 2L$, with boundary conditions $\tilde{u}(0) = 0$ and $\tilde{u}(2L) = 0$. The exact solution is given by

$$\tilde{u}(x) = -\frac{b}{2a}x^2 + \frac{1}{a}(R_0 + 2bL)\,x. \tag{2.30}$$

The Galerkin Method [223] provides a means of approximating the solution to Equation 2.29 using finite elements such as those shown in Figure 2.19.

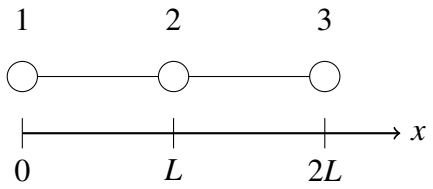

Fig. 2.19 One–dimensional linear elements used to approximate the solution $u(x)$.

The solution $\tilde{u}(x)$ is approximated with $\tilde{u}(x) \approx [\bar{N}]\{\tilde{u}\} = [\bar{N}_1\ \bar{N}_2]^T\ \{\tilde{u}_1\ \tilde{u}_2\}$, where N_i are the shape functions

$$\bar{N}_1 = 1 - \frac{x - x_1}{x_1 - x_2}, \quad \bar{N}_2 = \frac{x - x_1}{x_2 - x_1}. \tag{2.31}$$

The nodal values $\tilde{u}_1$ and $\tilde{u}_2$ are unknown components of the solution $\tilde{u}(x)$. Substituting the nodal values and the shape functions in Equation 2.29, the approximate solution satisfies the equation,

$$a\frac{\mathrm{d}^2}{\mathrm{d}x^2}[\bar{N}]\{\tilde{u}\} + b = \Psi, \tag{2.32}$$

where Φ is the residual due to approximating the solution $\tilde{u}(x)$. Premultiplying Equation 2.32 by $[\bar{N}]$, and integrating over the finite element, minimises the residual Φ and

$$\int_{x_1}^{x_2} [\bar{N}] a \frac{\mathrm{d}^2}{\mathrm{d}x^2}[\bar{N}]^T \{\tilde{u}\}\,\mathrm{d}x + \int_{x_1}^{x_2} [\bar{N}] b\,\mathrm{d}x = 0. \tag{2.33}$$

Integrating the first term in Equation 2.33 by parts, transforms Equation 2.29 into the discrete approximation,

$$\int_{x_1}^{x_2} \frac{\mathrm{d}}{\mathrm{d}x}[\bar{N}]a\frac{\mathrm{d}}{\mathrm{d}x}[\bar{N}]^T\,\mathrm{d}x\{\tilde{u}\} - \int_{x_1}^{x_2}[\bar{N}]b\,\mathrm{d}x \\ - \begin{pmatrix}0\\1\end{pmatrix} a\left.\frac{\mathrm{d}\{\tilde{u}\}}{\mathrm{d}x}\right|_{x=x_2} + \begin{pmatrix}1\\0\end{pmatrix} a\left.\frac{\mathrm{d}\{\tilde{u}\}}{\mathrm{d}x}\right|_{x=x_1} = 0. \quad (2.34)$$

From Equation 2.34, the stiffness matrix $[K]$ is given by

$$[K] = \int_{x_1}^{x_2} \frac{\mathrm{d}}{\mathrm{d}x}[\bar{N}]a\frac{\mathrm{d}}{\mathrm{d}x}[\bar{N}]^T\,\mathrm{d}x, \quad (2.35)$$

and the force vector F, is given by

$$[F] = \int_{x_1}^{x_2}[\bar{N}]b\,\mathrm{d}x + \begin{pmatrix}0\\1\end{pmatrix} a\left.\frac{\mathrm{d}\{\tilde{u}\}}{\mathrm{d}x}\right|_{x=x_2} - \begin{pmatrix}1\\0\end{pmatrix} a\left.\frac{\mathrm{d}\{\tilde{u}\}}{\mathrm{d}x}\right|_{x=x_1}. \quad (2.36)$$

The global equation for the three nodes given in Figure 2.19 after application of the boundary condition $\tilde{u}(0) = 0$, is therefore,

$$\underbrace{\begin{pmatrix}1 & 0 & 0\\ 0 & 2 & -1\\ 0 & -1 & 1\end{pmatrix}}_{K}\begin{pmatrix}\tilde{u}_1\\ \tilde{u}_2\\ \tilde{u}_3\end{pmatrix} = \frac{1}{2a}bL^2\begin{pmatrix}0\\2\\1\end{pmatrix} + \begin{pmatrix}0\\0\\aR/L\end{pmatrix}. \quad (2.37)$$

Premultiplying Equation 2.37, by K^{-1} gives the solution for each of the $\tilde{u}_i$. Figure 2.20 gives the exact solution and the finite element approximation when $a = b = L = R_0 = 1$. The piecewise linear approximation in Figure 2.20 is exact at nodal values for this problem, and accuracy between the nodal points can be improved with increased order elements.

The Galerkin Method is one such method for discretizing the domain of a structural problem. Another method is the variational formulation [224]. Again, considering Equation 2.29, where a is now the stress in a beam and b and R_0 are distributed and concentrated loads respectively. Considering the potential energy of the one dimensional bar with deflection described by Equation 2.29, the problem can be discretized by minimising the energy functional

$$J[\tilde{u}] = \int_L \frac{1}{2}a\left(\frac{\mathrm{d}\tilde{u}}{\mathrm{d}x}\right)^2\mathrm{d}x - \int_L b\tilde{u}\,\mathrm{d}x - R_0\tilde{u}(x = 2L), \quad (2.38)$$

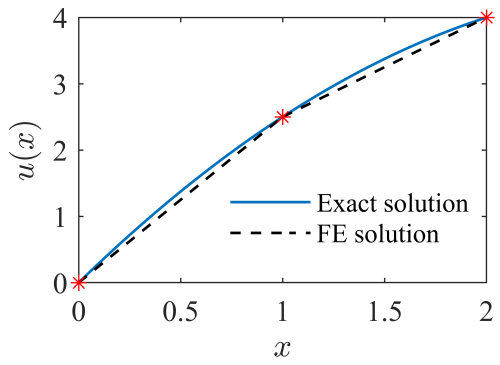

Fig. 2.20 Comparison between the exact solution and approximate finite element solution.

with the boundary condition $u(0) = 0$. The approximate solution for $u(x)$ is again given by $u(x) \approx [\bar{N}]\{\tilde{u}\}$ and the potential energy functional for an element is given by

$$J[\tilde{u}] = \int_{x_1}^{x_2} \frac{1}{2} a\{\tilde{u}\}^T \frac{\mathrm{d}}{\mathrm{d}x}[\bar{N}] \frac{\mathrm{d}}{\mathrm{d}x}[\bar{N}]^T \{\tilde{u}\}\,\mathrm{d}x - \int_{x_1}^{x_2} \{\tilde{u}\}^T [\bar{N}] b\,\mathrm{d}x - \{\tilde{u}\}^T \begin{pmatrix} 0 \\ R_0 \end{pmatrix}. \tag{2.39}$$

Equation 2.39 is minimised when $\partial J[y]/\partial \tilde{u}_i = 0$ for $i \in [1,n]$. Differentiating Equation 2.39 with respect to $\tilde{u}_i$ gives the equilibrium equation for the finite element formulation and is equal to the discretized formulation given by the Galerkin Method in Equation 2.34. More generally, the variational formulization for discretizing the structural dynamics of a body of volume V and boundary $S_{\tilde{u}}$, is given by,

$$\int_V \sigma_{ij} \delta\varepsilon_{ij}\,\mathrm{d}V - \int_V \bar{F}_i \delta\tilde{u}_i\,\mathrm{d}V - \int_{S_{\tilde{u}}} \bar{T}_i \delta\tilde{u}_i\,\mathrm{d}S = 0, \quad \delta\tilde{u}_i = 0 \text{ on } S_{\tilde{u}}, \tag{2.40}$$

where σ_{ij} and ε_{ij} are the stress and strain due to displacements $\tilde{u}_i$ between the i and j^{th} nodes and $\bar{F}_i$ and $\bar{T}_i$ are the body forces and stress vector respectively.

In respect to modelling the overhead line using finite elements, again Euler–Bernoulli beam theory is the prevalent choice. In [211], Timoshenko beam theory is used is place of Euler–Bernoulli beams when modelling the overhead line geometry. Use of Timoshenko beams includes the effects of shear deformation under loading, however in slender beams such as those used to represent overhead line cables, the aspect ratio between the length and diameter of a cable in a span is small (approximately 10^{-4}), so the use of Timoshenko beam elements appears unnecessary in modelling the catenary geometry. Using Euler–Bernoulli beam theory, the global stiffness matrix $\mathbf{K}_g = \sum_m \mathbf{K}_e$, where m corresponds to the order of the elements used in the finite element analysis and $\mathbf{K}_e$ is the element stiffness matrix. For a

third order beam element,

$$\mathbf{K}_g = \mathbf{K}_e^{(1)} + \mathbf{K}_e^{(2)} + \mathbf{K}_e^{(3)}, \tag{2.41}$$

where $\mathbf{K}_e^{(1)}$, $\mathbf{K}_e^{(2)}$ and $\mathbf{K}_e^{(3)}$ are the linear stiffness, stress stiffness and large deformation stiffness matrices respectively. The structural equation of motion can then be written as

$$\mathbf{M}\Delta\ddot{q} + \mathbf{C}\Delta\dot{q} + \mathbf{K}_g\Delta q = \mathbf{F}_g, \tag{2.42}$$

where $\mathbf{M}$ is the element mass matrix, $\mathbf{C}$, the global damping matrix, $\mathbf{F}$ the external force matrix and Δq, $\Delta\dot{q}$ and $\Delta\ddot{q}$ are the displacement, velocity and acceleration vectors respectively. This method of formulating the catenary is adopted in [225–227, 191] to study the dynamics in combination with lumped–mass representations of the pantograph. Since the vertical displacements of the contact wire relative to the span length are small, geometric nonlinearities are typically ignored and $\mathbf{K}_e^{(3)} = 0$. Large deformations of the contact wire such as under high wind load or high train speeds where geometric nonlinearities cannot be neglected, are considered in [214, 217, 228, 229].

Similar to [228], the absolute nodal coordinate is adopted in [230] to effectively deal with large deformations of beam elements, as is also used in [220]. For two points X_0 and Y_0, the equilibrium lengths in the coordinate directions are given by,

$$\ell_1 = \frac{f_1 L_0}{EA} + \frac{f_1}{p}\ln\left(\frac{\sqrt{f_4^2+f_5^2+f_6^2}+F_6}{\sqrt{f_1^2+f_2^2+f_3^2}-f_3}\right) \tag{2.43}$$

$$\ell_2 = \frac{f_2 L_0}{EA} + \frac{f_2}{p}\ln\left(\frac{\sqrt{f_4^2+f_5^2+f_6^2}+F_6}{\sqrt{f_1^2+f_2^2+f_3^2}-f_3}\right) \tag{2.44}$$

$$\ell_3 = \frac{L_0}{EA}\left(f_3 + \frac{pL_0}{2}\right) + \frac{1}{p}\left(\sqrt{f_4^2+f_5^2+f_6^2} - \sqrt{f_1^2+f_2^2+f_3^2}\right), \tag{2.45}$$

where p is the self–weight, L_0 is the unloaded length and F_i are the nodal forces. The stiffness matrix is obtained by differentiation of the equilibrium lengths, to generate the flexibility matrix $\mathbf{G}_e$, then the stiffness matrix is given by

$$d\mathbf{F}_e = \left[\frac{\partial\{\ell_i\}}{\partial f_j}\right]^{-1} d\{\ell_i\} = \mathbf{G}_e^{-1} d\{\ell_i\}, \tag{2.46}$$

where $(i, j) \in [1, 2, 3]$. Equation 2.46 establishes the relationship between the stiffness matrix $\mathbf{G}_e^{-1}$ and the nodal displacements, similar to the ANCF formulation. The nodal forces are then calculated using the Newton–Raphson's method [231].

In [12, 232], the dynamic performance of the catenary pantograph interaction is studied with regards to the use of nonlinear droppers, whilst using the finite element formulation of the messenger and contact wires discussed here. For a train speed that is 50% of the mechanical wave propagation speed, given by Equation 2.19, stiffness variations due to a nonlinear dropper decrease the contact force variation, however at speeds approaching 70% of the wave propagation speed, the contact force variation rises to unacceptable levels due to the reflection of the mechanical waves at supports.

Since the contact point between the pantograph and the contact wire is small, detailed meshing of the contact neighbourhood is necessary for accurate determination of the contact forces. In [233], a moving mesh is implemented to increase the resolution of the meshing elements at the contact point, and compared with static element sizing across the geometry, computational costs are decreased. A moving mesh is also utilised in [234], and a similar reduction in the computation time was found compared with static meshing. Dynamic meshing requires the solving of unbalanced forces at every time step due to changes in the length of the mesh elements. This is not a required step in static mesh analysis.

In general, studies of the overhead line consider idealised conditions with the dynamics of the train body neglected as movement of the base of the pantograph has only a small effect on the contact force variation [235]. In [236], the effect of irregularities in the track are included and found that the effects of wheel–rail dynamics had a small effect (approximately 5%) on the contact force but that a larger uplift in the contact wire height is possible for low quality track. This is consistent with [237, 238], where it was found that due to high frequency irregularities in the track being absorbed by the train body suspension, only low frequency vehicle vibrations were transmitted to the pantograph and therefore had only a slight effect on the contact force. In [239], the contact force was noted to increase due to travel along curved tracks compared with straight track due to the lateral offset of the steady arms located on the inner radius of the curved track.

The computational expense of finite element analysis largely outweighs the modal superposition method, however the finite element approach is more versatile when considering non–standard wire geometries or features such as overlaps.

2.6.2 Modelling the pantograph

Modelling of the pantograph is largely divided into two groups: lumped–mass models [30, 39, 209, 218, 232, 240–243, 20, 244] and general multibody models [135, 221, 225, 237, 245, 246] run in co–simulation with a finite element representation of the overhead line geometry. Typically, lumped–mass models adopt a two or three–mass representation of the pantograph as required by BS EN 50318 [14] for validation purposes, however [247] and [162] propose four or nine mass representations respectively. To account for the transmission of vibrations through the pantograph knuckle, [248] recommend the three–degrees–of–freedom model. Increasing the number of masses increases the fidelity of the model representation, however the increase in computational expense becomes undesirable for large models.

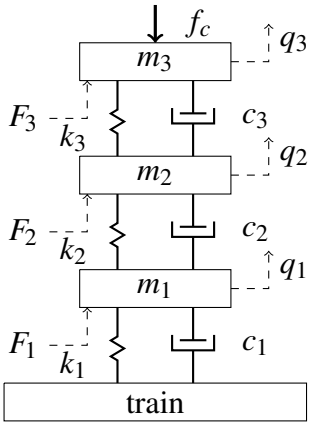

Fig. 2.21 Three degrees of freedom mass-spring representation of a pantograph.

Identification of the lumped–mass parameters are obtained from pantograph test rig experiments such as [249], however the parameters typically do not correspond to specific parts of the pantograph. In the lumped–mass representation, shown in Figure 2.21, the parameters can be distributed and optimised in alternative ways to achieve similar dynamic performance [227, 250]. Indeed, from the equation of motion for a lumped–body representation,

$$\mathbf{M}\{\ddot{q}\} + \mathbf{C}\{\dot{q}\} + \mathbf{K}\{q\} = \{F\}, \tag{2.47}$$

the dynamics of the pantograph are described completely by the eigenvalues and eigenvectors of **M**, **C** and **K**. The lumped–mass representation is attractive due to its simplicity compared with the dynamic equation for the overhead line geometry. In the three–body case, the equation of motion is given by,

$$\begin{pmatrix} m_1 & 0 & 0 \\ 0 & m_2 & 0 \\ 0 & 0 & m_3 \end{pmatrix} \begin{pmatrix} \ddot{q}_1 \\ \ddot{q}_2 \\ \ddot{q}_3 \end{pmatrix} + \begin{pmatrix} c_1+c_2 & -c_2 & 0 \\ -c_2 & c_2+c_3 & -c_3 \\ 0 & -c_2 & c_3 \end{pmatrix} \begin{pmatrix} \dot{q}_1 \\ \dot{q}_2 \\ \dot{q}_3 \end{pmatrix} + \begin{pmatrix} k_1+k_2 & -k_2 & 0 \\ -k_2 & k_2+k_3 & -k_3 \\ 0 & -k_3 & k_3 \end{pmatrix} \begin{pmatrix} q_1 \\ q_2 \\ q_3 \end{pmatrix} = \begin{pmatrix} 0 \\ 0 \\ -f_c(t) \end{pmatrix}. \quad (2.48)$$

From Equation 2.48, it is clear that the eigenvectors are dominated by the leading diagonal due to the zero entries, so changes in the element parameters in the leading diagonal can be compensated for, ensuring similar dynamic performance. In [64], the contact force is shown to be most sensitive to the plunger stiffness (given as k_2 in Figure 2.21) thus ensuring k_2 variations are small, allows for comparison between different pantograph parameters. Damping in the lumped–mass model of the pantograph is approximated by a linear damper, thus only provides unidirectional damping. Real pantographs observe nonlinear damping during raising and dropping of the pantograph to reduce the contact force between the collector head and the contact wire. In [183], a nonlinear damping element is introduced into the catenary pantograph interaction. The damping element observes a damping force proportional to the displacement, giving a high damping when the pantograph reaches the maximum working height, and then observes a low damping as the pantograph returns to the equilibrium position. Use of the nonlinear damper lead to a reduction in the contact force variation compared with a linear damper.

Multibody approaches to the pantograph can improve the fidelity of a catenary pantograph interaction model. The multibody representation is also desirable at the design stage where experimental identification of pantograph parameters for the lumped–mass representations are not available. In the multibody formulation, such as in [135], the pantograph is formed of rigid bodies, kinematic (spherical and revolute) joints, linear force elements and external forces. The four–degree–of–freedom formulation, shown in Figure 2.22 as a 2D representation, accounts for both the vertical displacement of the pantograph as well as angular deflections of the pantograph frame. The 2D representation given in Figure 2.22 neglects the lateral stiffness variation of the collector strips, however in implementing a multibody approach, the model is 3D and as such would include the lateral variations of the collector strips. Physical parameters of the pantograph are derived from the geometry and material properties of the real pantograph and more accurately reflect the pantograph behaviour compared with the

lumped–mass approach. The kinematic joints impose restrictions of the relative displacement of the rigid bodies forming the pantograph components and are expressed as algebraic constraints [251]. The revolute joints, denoted RJ in Figure 2.22 allow rotation between the i and j^{th} bodies, representing mechanical rollers, whilst the spherical joints, denoted SJ in Figure 2.22 constrains the relative motion between the i and j^{th} bodies to spherical rotations [252].

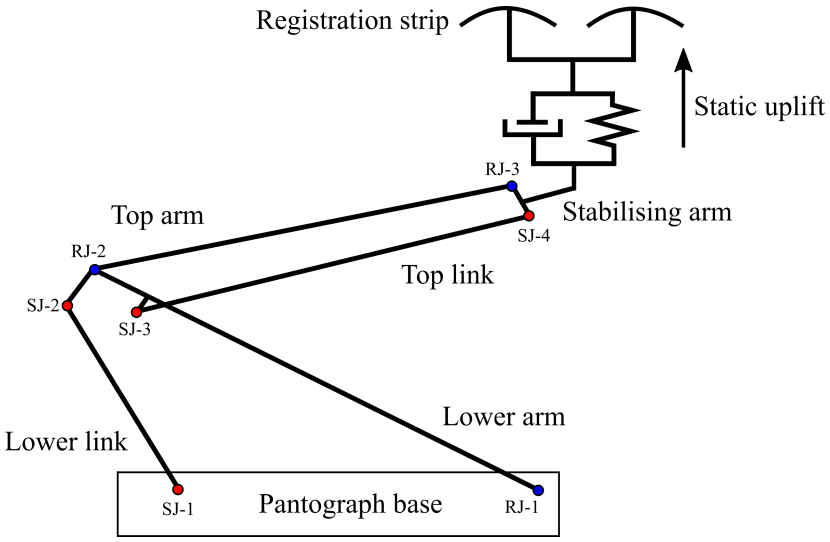

Fig. 2.22 Multibody formulation of a single arm pantograph consisting of rigid bodies and spherical (red circles) and revolute (blue circles) joints.

Linear spring elements placed between the pantograph base and the lower arm, and between the stabilising arm and the collector head, depend on the displacements between the bodies during operation. The undeformed length of the springs are calculated to ensure the pantograph is in static equilibrium before interacting with the overhead line. During the dynamic analysis, the horizontal displacement of the pantograph is described by a reference path, constraining the pantograph motion to a desired path. This is in contrast to the lumped–mass approach, where the horizontal displacement of the pantograph can be constrained by the boundary conditions placed on the masses. The reference path prescribes the position of each of the rigid bodies at each time step [253]. The constraints placed on the motion of the rigid bodies is described by a set of differential algebraic equations. In [246], the Udwadia–Kalaba [254] formulation is adopted to transform the algebraic constraints into ordinary differential equations, reducing the computation complexity. Solver requirements for implementation of multibody models are different from those required by FE/lumped–mass models. Co–simulation between the finite element model and the multibody pantograph is typically adopted in the literature [227].

Analysis of pantograph behaviour is typically limited to behaviour in the 0 – 20 Hz range, however a modal analysis in [255] shows that dynamic behaviours of the pantograph are predicted at frequencies beyond this, that are not captured in existing pantograph models. Excitation modes above the 20 Hz frequency should be considered for stiffer overhead lines, required as train speeds are increased.

2.6.3 Contact methods

Sliding contact between the contact wire and the pantograph is typically considered with respect to the normal component of the contact force with frictional forces neglected. In the simulation of the catenary pantograph interaction, contact is typically approached using two methods: the penalty method or with unilateral constraints applied using Lagrangian multipliers introduced into the system's equations of motion.

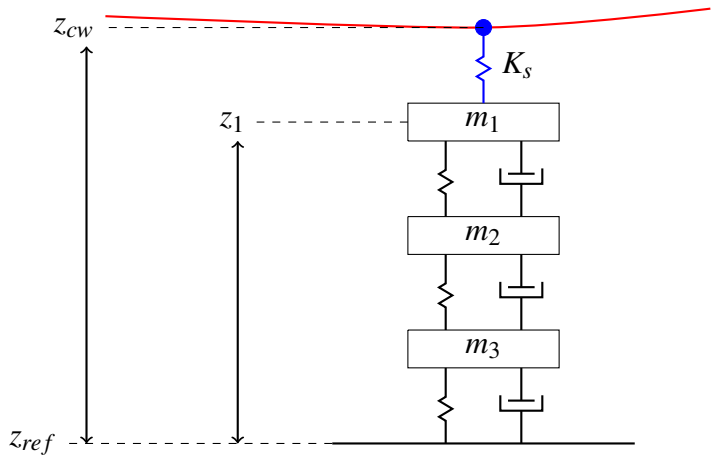

Fig. 2.23 Penalty method formulation for the catenary pantograph sliding contact.

With regards to the penalty method, contact between the pantograph and the contact wire is defined based on the interpenetration between the elements forming the contact wire and pantograph surfaces. To utilise the penalty method, a high stiffness elastic element is introduced between the pantograph head and the contact wire, as shown in Figure 2.23. The stiffness of the elastic element is typically set as given in [14] and is defined as $K_s = 50$ kN/m in tension and zero otherwise, indicating contact loss. From the measure of interpenetration and the contact stiffness, the contact force is then calculated as

$$f_c = \begin{cases} K_s(z_1 - z_{cw}) & \text{if } z_1 > z_{cw}; \\ 0 & \text{if } z_1 \leq z_{cw}, \end{cases} \tag{2.49}$$

where z_{cw} is the contact wire height, z_1 is the vertical position of mass m_1 and z_{ref} is a reference height, typically taken to be the base of the pantograph. In the finite element formulation in ANSYS adopted in this thesis, the contact force is calculated using Equation 2.49 and is automatically generated at each timestep by the solver. In [256], the effect of an increased K_s is considered, and found that for even large K_s, the amplitude of the contact force is reduced in the 0–20 Hz range, but that the contact force variation increased when higher frequencies were considered.

In the Lagrange formulation, the condition that no interpenetration between the pantograph head and the contact wire is imposed, in contrast to the penalty method where interpenetration is required. The no interpenetration condition is given by

$$Z(\mathbf{z}) = z_1 - z_{cw} \geq 0, \tag{2.50}$$

and to satisfy this condition, the Lagrangian constraint is defined by

$$\mathscr{L}(\mathbf{z}, \dot{\mathbf{z}}) = T(\dot{\mathbf{z}}) - V(\mathbf{z}) - \lambda Z(\mathbf{z}), \tag{2.51}$$

where $\mathbf{z} = \mathbf{z}(z_{cw}, z_1, z_2)$ are the generalised coordinates. The functions T and V represent the kinetic and potential energies of the system and are defined by

$$T(\dot{\mathbf{z}}) = \frac{1}{2} m_{con} \dot{z}_{cw}^2 + \frac{1}{2} \sum_{i=1}^{2} m_i \dot{z}_i^2, \tag{2.52}$$

$$V(\mathbf{z}) = \frac{1}{2} k_{con} z_{cw}^2 + \frac{1}{2} \sum_{i=1}^{2} k_i z_i^2 - \frac{1}{2} k_1 \sum_{\substack{i,j=1 \\ i \neq j}}^{2} z_i z_j, \tag{2.53}$$

where m_i, k_i and z_i represent the mass, stiffness and vertical position of the i^{th} mass. Non–conservative forces $\mathbf{F}$, such as aerodynamic lift, are viscously damped and so the dissipation of energy is given by

$$D(\mathbf{z}) = \frac{1}{2} c_{cw} \dot{z}_{cw}^2 + \frac{1}{2} \sum_{i=1}^{2} c_i \dot{z}_i^2 - \frac{1}{2} k_1 \sum_{\substack{i,j=1 \\ i \neq j}}^{2} \dot{z}_i \dot{z}_j, \tag{2.54}$$

Then by Lagrange's equation, the equations of motion are

$$\frac{\mathrm{d}}{\mathrm{d}t} \left(\frac{\partial \mathscr{L}}{\partial \dot{\mathbf{z}}} \right) - \frac{\partial \mathscr{L}}{\partial \mathbf{z}} + \frac{\partial D}{\partial \dot{\mathbf{z}}} = \mathbf{F}. \tag{2.55}$$

In [237], the contact force is represented by the Hertzian contact equation

$$F_N = K'\delta^n \left[1 + \frac{3\left(1-e^2\right)}{4}\,\frac{\dot{\delta}}{\dot{\delta}^{(-)}}\right]. \tag{2.56}$$

where e is the restitution coefficient, $\dot{\delta}$ and $\dot{\delta}^{(-)}$, the penetration and impact velocities respectively and K' a generalised stiffness coefficient determined by the contact between two cylinders. If the penetration or impact velocity is taken to be zero, then Equation 2.56 reduces to Equation 2.49. The calculation of the contact force during sliding contact was proposed by [257] based on [258] and proposed as a model of the contact between a pantograph and contact wire in [259]. Equation 2.56 includes damping during the contact time, compared with Equation 2.49. In [221], the penalty method is extended to include damping in the calculation of the contact force, given by

$$f_c = \begin{cases} K_s(z_1 - Z_{cw}) - C_{\text{con}}(\dot{z}_1 - \dot{Z}_{cw}) & \text{if } z_1 > Z_{cw}; \\ 0 & \text{if } z_1 \leq Z_{cw}, \end{cases} \tag{2.57}$$

where $Z_{cw} = z_{cw} - z_{wear}$ is the worn radius of the contact ($z_{wear} = 0$ when the wire is intact) and C is the damping coefficient of a possible damper between the pantograph and contact wire. The contact force given by Equation 2.57 is no longer proportional to the interpenetration of the contact surfaces due to the addition of the velocity of the pantograph and contact wire components, thus the contact force given by [221] is nonlinear.

Compared with the penalty method, the Lagrangian formulation includes the addition of extra terms due to the Lagrange multiplier constraint. In large models, the addition of the constraint can lead to an increased computation time, thus the penalty method appears to the favoured option.

2.7 Damping

The overhead line is known to be lightly damped [240] and vibrates at low frequency (typically 1 Hz [13]), thus small effects are likely to degrade the current collection quality during train operation. The lightly damped equipment allows transmission of oscillations across a wide distance both in front of and behind the contact point between the contact wire and the pantograph [162]. In the case of compound catenary systems, the damping of the overhead line is reinforced by tuned dampers installed between the contact wire and the auxiliary messenger wire. Since the magnitude of the structural damping determines the amplitude of

equipment vibrations, the contact quality is highly sensitive to the damping of the system [162]. Determination of the structural damping of the overhead line equipment has been determined with both experimental and numerical techniques. In [260], the damping ratios of the overhead equipment were found to be in the range 0.01 to 0.04 by applying wavelet transforms to measured test track data. Wavelet transforms are also used in [199], estimating that the damping ratio for the overhead equipment is approximately 1%. Estimation of the damping characteristics of the overhead line due to observed noise in acceleration measurements of the equipment is given in [261]. The damping ratio is also sensitive to stiffness changes in the equipment due to increasing train speed [203]. Modal analysis of measured track data in [261] identified the damping ratios of the overhead line for both pre– and post–train passage for three existing systems.

In modelling the catenary pantograph dynamics, Rayleigh damping [262] is a popular choice for the application of viscous damping [211, 240, 221, 222, 241]. The viscous damping is expressed as a linear combination of the mass and stiffness matrices, that is

$$\mathbf{C} = \nu\mathbf{M} + \eta\mathbf{K}, \tag{2.58}$$

for α and β real scalars. Using this form of structural damping, the structural equation of motion given by Equation 2.42 can be written as,

$$\mathbf{M}\Delta\ddot{q} + (\nu\mathbf{M} + \eta\mathbf{K})\,\Delta\dot{q} + \mathbf{K}\Delta q = \mathbf{M}\,(\Delta\ddot{q} + \nu\Delta\dot{q}) + \mathbf{K}\,(\eta\Delta\dot{q} + \Delta q) = \mathbf{F}. \tag{2.59}$$

Usage of frequency response functions applied to measured accelerations of the overhead equipment in [263] allowed for determination of the damping coefficients. The scalars ν and η are then related to the damping ratio of the n^{th} mode ξ_n by

$$\xi_n = \frac{\nu}{2\omega_n} + \frac{\eta\,\omega_n}{2}, \tag{2.60}$$

Throughout the literature, various ν and η are used to approximate the magnitude of the viscous damping of the system. Table 2.3 gives examples of the coefficients identified in the literature. The damping factors presented in [217] are distinct in that different damping factors are identified for the contact and messenger wires compared with the others where ν and η are given and are equal for both the contact and messenger wires. Table 2.3 also highlights the large spectrum of overhead line damping factors matched to the specific system for which they are measured from or applied to in the case of dynamic models. This variation

in the damping factors represents difficulty when optimising pantographs for interoperability due to the requirement to satisfy a range of systems with varying damping properties.

Table 2.3 Scalar values for ν and η presented in the literature where ν and η correspond to the mass and stiffness proportional damping factors, and ξ is the damping ratio. Subscripts $_{cw}$ and $_{mw}$ correspond to contact and messenger wires respectively.

Study	ν_{cw} (10^{-2})	ν_{mw} (10^{-2})	η_{cw} (10^{-3})	η_{mw} (10^{-3})	ξ_{cw}	ξ_{mw}
Zhang et al. [209]					0.01	0.01
Jung et al. [214]					0.01	0.05
Cho [232]					0.01	0.05
Ambrósio et al. [227]	0	0	2.7-27	2.7-27		
Seo et al. [217]	1	5	0.1	0.1		
Bruni et al. [240]	1.125	1.25	1	1		
Zou et al. [199]	2.2845	2.845	2.74	2.74		
Nåvik et al. [261]	6.2	6.2	6.13×10^{-3}	6.13×10^{-3}		
Beagles et al. [241]	0.55	0.55	11	11		

More comprehensively the damping of the overhead line equipment can be described with modal damping across a larger frequency range than would be valid for Rayleigh damping [264]. In [264], the damping of a structure with complex mode shapes is identified by

$$\mathbf{C} = [\mathbf{M}\Phi]_{N\times N_m} \operatorname{diag}\left[2\xi_j\omega_j\right]_{N\times N_m} [\mathbf{M}\Phi]^T_{N_m\times N}, \tag{2.61}$$

where $\mathbf{M}$ is the mass matrix, ξ_j and ω_j correspond to the damping and frequencies of the j^{th} mode and Φ gives the mode shapes solution to the eigenvalue problem

$$\left(\mathbf{K} - \omega_j^2\mathbf{M}\right)\Phi = \{0\}. \tag{2.62}$$

Equation 2.61 more accurately reflects the structural damping of the overhead equipment, however is computationally expensive compared with linear viscous damping modelled by Equation 2.58, thus Rayleigh damping has remained an attractive choice for modelling of viscous effects during the catenary pantograph interaction.

2.8 Hybrid Simulation

Recent developments in the modelling of the interaction between a pantograph and the contact wire is the adoption of hybrid simulations, whereby a physical pantograph rig interacts with

a dynamic simulation of the overhead line geometry. The method has become attractive since being proposed by [119, 210], with the advent of real–time simulation techniques. Figure 2.24 shows a schematic of the hybrid simulation methodology. In the hybrid simulation, the displacement of the catenary geometry is applied to the pantograph head by actuators and the resultant force caused by the displacement of the pantograph components is transmitted back into the numerical simulation of the flexible catenary geometry. Hybrid simulations are advantageous over pure numerical simulations as nonlinearities (e.g., friction, damping) and flexibility in the pantograph are included in the analysis. Large scale adoption of the technique is limited due to requirements of suitable apparatus.

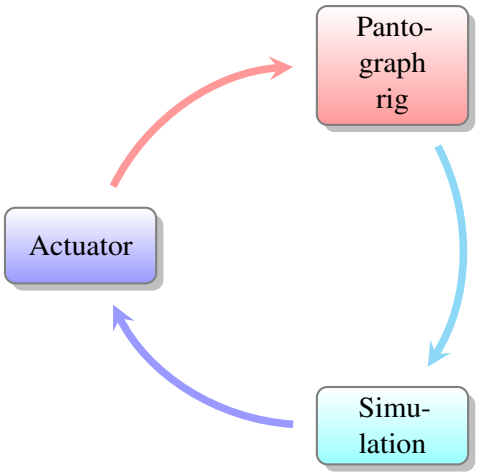

Fig. 2.24 Hybrid simulation schematic.

The method of [210] was refined by [265] with the introduction of dropper slackening, a significant cause of dynamic effects [232], before the method was refined even further by [266] with the adoption of independently excited, sprung collector strips. In [81], the hybrid simulation output is compared with purely numerical and line test data, and good correlation between each data source was presented, validating the methodology. Similar to real–time simulation hybrid simulations, [267] presents the “offline” and “online” method for numerical integration of the catenary equations of motion. In the offline stage, the response to unit loads of the contact and messenger wires is stored and used in the online stage to reduce the order of the dynamic matrix, reducing computational time to that comparable with real time simulations. Adoption of the “fast” simulation method in [267] into a hybrid simulation has so far not been presented.

Hybrid simulation of the catenary pantograph interaction is adopted in [268] based on the dynamically substructured system (DSS) presented in [269] utilising a multiple degree–

of–freedom representation of the catenary to reduce the deviation between hybrid simulation and pure numerical modelling.

Hybrid simulations have been adopted as the use of real–time simulations have become more readily available. In [270], a modal method approach is used to generate a diagonal matrix at each time step. Since the matrix is diagonal, computation time is reduced and has been adopted in hardware–in–the–loop simulations for real–time simulations. A proposed DSS in [271] is used as an alternative to traditional hybrid simulation, opting to represent the overhead line as a linear system with time–dependent stiffness, coupled with a physical DSS of the pantograph.

2.9 Review of the existing overhead line dynamic model

The model of the catenary pantograph interaction presented in [241] is a finite element representation of an overhead line geometry coupled with a lumped–mass representation of a pantograph. In this section a review of the existing model is presented, and the limitations of the model are discussed and the work performed to enhance the model to answer the research aim stated in Chapter 1.

Overhead line model

The simulation method implemented using the APDL language in ANSYS is defined using tensioned Euler–Bernoulli beams to represent the messenger and contact wires, and concentrated masses representing the registration arms. Use of Euler–Bernoulli beam elements neglect shear deformation which can be overcome by adopting Timoshenko beam elements. However since the shear deformation of the contact and messenger wires is small [245], it is appropriate to model the contact and messenger wires as Euler–Bernoulli beams. The use of Euler–Bernoulli beam elements is similar to the methods adopted in other existing catenary pantograph simulations such as [40]. In contrast to [40], discrete features such as stitched catenaries or conductor bars are not included in the existing model. Nonlinear beam elements are used to represent the messenger and contact wires with two degrees of freedom at each nodal point of the element. The degrees of freedom of the elements are translations in the horizontal and vertical deflections. Models such as [43] allow for rotations of the beam elements, however since no rotations are expected to occur, in [241] this behaviour is neglected for an improvement in the computational speed of the simulations. The model representation is constrained to the 2D plane, as are the models presented in [42, 196, 221],

however this restricts investigation of dynamics that occur only in the vertical plane of the system, thus situations such as aerodynamic loading or transitions along curved track and stagger are not possible. Models that adopt a 3D representation include [43, 212]. Nonlinear deformation of the overhead line is assumed in accordance with other finite element models

Registration arms are represented by lumped–masses so that all of the mass of the registration arm is concentrated at the support location where they meet the contact and messenger wires. Other models adopt this approach, however this has the effect of concentrating the inertia of the registration arm at the point where the arm supports the contact wire, which potentially leads to an increased contact force at this point, compared with the contact force that occurs when a more complex representation of the registration arm is used.

Dropper behaviour is approximated using nonlinear spring–dampener models with stiffness curves defined for both stiffness and compression of the droppers. As the pantograph passes a dropper, the dropper is compressed and the relative displacement between the nodes at each end of the dropper is negative and the stiffness of the dropper is zero. For a dropper in tension due to supporting the contact wire, the stiffness value is non-zero as the relative displacement between the nodes is positive. This accurately reflects the dropper behaviour of a real system.

Pantograph model

The pantograph model is derived from experimental testing of in use mainline pantographs with the mechanical parameters determined by the frequency response of the pantographs tested [249]. The model is equipped with both 2– and 3–mass representations of pantographs and the lumped–mass representation adopted in [241] is formed of spring–mass–damper elements, consistent with the models adopted in [42, 196, 272], although unlike the pantograph model presented in [42], the existing pantograph model does not account for rolling of the pantograph head, and constrains the pantograph elements to be in the vertical plane. Removing this constraint allowed for the investigation of sidewinds in Chapter 7. The use of a lumped–mass representation is likely the most significant difference from other models of the catenary pantograph interaction. Whilst the use of lumped–mass representations is well documented and widely used, the adoption of more comprehensive 3D multibody models is becoming increasingly popular. The more comprehensive representation of the pantograph allows for the integration of nonlinear dynamics not readily available to equivalent lumped–mass models. These include the use of bumpstops and the orientation of the pantograph knuckles. Since the dynamic response of a multibody pantograph compared with

a lumped–mass approach appears to have only a small effect on the contact force [273], the pantograph model was not updated to a full multibody model.

A static uplift force is applied to the bottom pantograph mass to ensure good contact between the pantograph collector head and contact wire and aerodynamic force is applied to the pantograph collector head that is proportional to the square of the velocity applied to the pantograph. Since the pantograph model does not account for the pantograph knuckle direction, the model neglects the aerodynamic effects which are influenced by the knuckle direction. In the knuckle trailing position, the aerodynamic uplift causes the pantograph to "open" thus inducing a larger uplift at the contact point that is therefore, not measured in the model.

Simulating the dynamic contact

Meshing of the overhead line model is performed prior to the application of gravitational and tensioning loads with an element size of 0.5 m and the timestep of the model was set to 0.05 s, or equivalently data collection was performed at 200 Hz. This was ten times the frequency performed in the data analysis so all necessary behaviour was captured by this frequency. The data collection frequency also matched the data collection frequency used during track tests, thus behaviour captured by the test train would be accurately reflected in the simulation output. Few models consider a frequency higher than this as high frequency dynamics such as the effect of dropper clamps require a data collection frequency greater than 2 kHz, thus for analysis of the bulk catenary pantograph behaviour, the considered frequencies are kept below 200 Hz.

Initialisation of the model is performed in a static state. In this step, gravitational and tensioning loads are applied, and the overhead line geometry deflects vertically. The geometry after the loads have been applied is considered the static equilibrium of the overhead line. The model in [241] requires the knowledge of the dropper lengths to calculate the contact wire height based on the messenger wire height at supports. This differs from other models where the dropper lengths are typically not known and an iterative procedure determines the dropper lengths to ensure a correct overhead line geometry.

Using the static equilibrium geometry, the sliding contact between the contact wire and pantograph is simulated. The finite element model and lumped–mass pantograph model are run simultaneously in the time domain according to a Newmark–β method [274], where the

discretised structural equation describing the dynamics is given by

$$\dot{q}_{n+1} = \dot{q}_n + (1-\gamma_N)\ddot{q}_n + \gamma_N \Delta t \ddot{q}_{n+1}, \tag{2.63}$$

$$q_{n+1} = \dot{q} + \Delta t \dot{q}_n - (\Delta t)^2 \left(\beta_N - \frac{1}{2}\right) \ddot{q}_n + (\Delta t)^2 \beta_N \ddot{q}_{n+1}, \tag{2.64}$$

where γ_N and β_N are the Newmark parameters. The Newmark method appears to be the most widely adopted numerical procedure for simulating the catenary pantograph interaction, though methods such as the Runge–Kutta method are also used.

The contact method adopted in [241] is the penalty method with a contact stiffness between the contact wire and pantograph collector head of 50 kN, and based on the contact stiffness, the contact force is calculated according to Equation 2.49. This contact method is widely used, however differs from the penalty method in [221], where the velocity of the penetration between the two contact surfaces is also considered. As the penalty method is specified for the method of contact between the two surfaces in BS EN 50318, further methods of contact were not investigated in this work.

Viscous damping is applied using a Rayleigh damping representation, given by Equation 2.58 with damping factors $\nu = 0.55$ s^{-1} and $\eta = 0.011$ s. This form of damping is used in a wide range of models of the catenary pantograph interaction, including the five given in Table 2.3. For this reason, Rayleigh damping appears to be an appropriate method to approximate the light damping of the overhead system and different methods of representing the structural damping were not considered.

Further details of the geometry creation and the simulation process of the contact between the overhead line and pantograph are presented in Chapter 3.

2.9.1 Limitations and model enhancements

The model presented in [241] is well suited to modelling cases where mechanical properties of the overhead line are assumed to be identical across all spans modelled. To extend the model to consider cases where the mechanical parameters may differ, such as individual droppers having differing stiffnesses in tension, modular functions can be implemented in the ANSYS framework. This allows for the separation of the spans and consider differences beyond just the geometry. As an example, in the case of individual dropper stiffnesses, the following pseudocode was implemented:

```
for i = 1:number of spans
        for j = 1:number of droppers
```

```
                if j = a mod n
                        k_T = k_(T,1)
                elseif j = b mod n
                        k_T = k_(T,2)
                endif
        end
end
```

This procedure can be iterated for each parameter under consideration using a vector of each parameter value. Using the modular function, each element of the vector containing the parameter values and be related to a component in the model in ANSYS. This procedure was adopted when a distributed registration arm rather than a concentrated registration arm was considered. The masses representing the registration arms were defined in the typical manner, however using the modular approach, the mass at the location where a distributed registration arm was implemented was set to zero and the mass was distributed along the more comprehensive representation of the registration arm. That is, when the position of the registration arm $x \equiv L_w/n \pmod{L_w}$, then $m_{\text{reg}} = 0$ and $m_{\text{reg}} \neq 0$ elsewhere, where n is the number of the span in which the distributed registration arm occurs, m_{reg} is the concentrated mass of a registration arm and L_w is the wire run length.

A further limitation of the existing model is the lack of 3D behaviour as all dynamics are constrained in the vertical plane. This makes the simulation of the catenary pantograph interaction under aerodynamic loads out of the plane impossible to model. For this reason, the model was extended to a fully 3D structure as described in Section 4.1, to consider dynamic effects from loads beyond those of the sliding contact. To apply the aerodynamic loads the constraints applied to the nodal coordinates corresponding to the messenger and contact wires and droppers were relaxed to allow for deflections in the lateral plane, orthogonal to the vertical plane of motion the system was originally constrained to. The use of a distributed registration arm orthogonal to the plan of the overhead line geometry also extended the model from a 2D representation to a fully 3D system. Stagger was not introduced when enhancing the model to a 3D structure as the effects on the catenary pantograph interaction are expected to be small as shown in Section 3.2.4.

The adopted pantograph model in [241] was initially a two–mass representation in accordance with the validation process given in BS EN 50318. This was updated to a three–mass representation for the validation process against the test track data and also to investigate the dynamic effects due to large–scale wire height variations. Under contact wire

height variations, a two–mass model is insufficiently sophisticated to represent the behaviour that occurs as the pantograph is compressed.

Frictional behaviour between the pantograph and contact wire was not included in the existing model, consistent with the models presented in [240], considering only the normal component of the contact force. This was implemented to assess the sensitivity of the model to frictional behaviour as discussed in Section 4.1.1. Coulomb friction was the model of friction implemented in the model with a single coefficient of friction μ. Whilst the frictional forces are predicted to be small compared with the applied line tension of 16.5 kN (an uplift of 200 N and a coefficient of friction of 0.5 would provide a force parallel to the contact wire of 100 N), this addition enhances the model by considering the nonlinear effects due to the sliding contact in a way that was previously neglected.

2.10 Conclusions

In this Chapter, a comprehensive overview of the current state of the art of the catenary pantograph interaction has been presented, which can be summarised as

- The field of numerical simulations of the catenary pantograph interaction can be considered to have matured in recent years, not least due to the large number of commercial and academic simulation methodologies that currently exist [40, 42, 43, 196, 211, 212, 221, 222, 245, 272]. The existing numerical simulations have typically focused on conventional catenary, largely without discrete irregularities or otherwise abnormal features, thus future developments in the field should begin to adopt discrete features such as overlaps. This is likely to become a focus with the addition of overlaps to the numerical validation standard BS EN 50318 [14]. The majority of numerical methodologies also neglect large scale height variations due to low clearances and only consider the small–scale height changes due to wire sag. Thus a greater focus on the variation due to large scale height changes is expected to develop, particularly with respect to the pantograph vertical transitions, which thus far appears to have been subject to very limited investigation.

- New approaches of the catenary pantograph interaction have been developed due to progress in real–time simulations allowing for hybrid simulations between numerical models of the overhead line and physical pantographs. Hybrid simulations have been shown to provide accuracy comparable to purely numerical solutions and are likely to become more prevalent with advances in real–time computing efficiency.

- Damping of the overhead line is typically represented by proportional damping, largely due to the attractiveness of linear damping in numerical simulations. Damping representations have been advanced in [264], however the representation of damping presented is not well suited to other simulation methodologies of the catenary pantograph interaction. Thus further research on the catenary damping will possibly provide more accurate predictions of the dynamic contact force, particularly when discrete features such as overlaps and conductor bars are included.

- Aerodynamic effects on both the catenary and the pantograph are well–documented in the literature, however validation between wind tunnel tests and computational fluid dynamics (CFD) simulations is limited. The characteristics of the wind are typically related to unidirectional flow and whilst static and turbulent wind conditions are studied, further enhancements to CFD techniques are required and the adoption of large–scale fluid interaction models are likely to be adopted as computing power continues to increase. At present no fluid–structure interaction between aerodynamics and the catenary pantograph interaction have been presented. Wind tunnel experiments are often scaled to be viable in existing wind tunnels and full–scale aerodynamic tests of pantographs are not yet a mature research focus, and much of the focus on aerodynamics is related to the train body in the absence of either the pantograph or the overhead line. With line speeds continuously increasing, the aerodynamic effects become large, thus further research into the pantograph dynamics under aerodynamic load is vital to understanding high speed contact dynamics.

- Contact wire irregularity can be assessed in terms of its effects on the dynamic characteristics of the catenary pantograph interaction, and the focus has largely been on the characteristic effects of contact wire wear on the dynamic performance. Less well assessed is the contact wire irregularity caused by variations in other components of the overhead line equipment, e.g., the messenger wire tension. A more comprehensive assessment of the effects of each of the system parameters will indicate failure modes in measured contact forces.

- The majority of focus on the catenary pantograph interaction has been performed on straight track, with only a few presentations of work assessing the effects of track dynamics and curved track. Given the increases in dynamic contact force predicted in [239] due to registration arms on the inner radius of curved track, further research requirements would include an assessment of the locations of supports or radius of

curvature of the overhead line with respect of the track to highlight contact force variations throughout the curve.

- Measurements of the contact force are currently limited to a frequency range of 0–20 Hz. It has been demonstrated in [132] that vertical motion occurs at frequencies above 20 Hz thus will directly affect the dynamic contact force. Measurement of the contact force at higher frequencies will detect the dynamic behaviour. With respect to condition monitoring, knowledge of high frequency behaviour allows for better predictive maintenance compared with reactive maintenance.

- Active pantograph control has been shown to actively improve the catenary dynamics during train operation, for example at higher line speeds than the existing systems are optimized for, however few examples exist demonstrating that active pantographs have moved past the design and prototyping stage, and into active usage on rail networks. Going forward the research focus appears to be developing methods of pantograph actuation and control strategies.

Based on the literature presented, Chapters 5–8 seek to answer four identified open problems:

1. Experimental and computational determination of aerodynamic forces on railway contact wire, using experimental measurements as validation of a numerical fluid simulation,

2. The effects of contact wire irregularity not associated with the wear characteristics of the contact wire such as messenger and contact wire tensions, missing droppers and speed variations,

3. Dynamics of an overhead line under wind load considering cases where the aerodynamic loading will change abruptly,

4. Effect of large–scale wire height changes on the dynamic contact force.

Chapter 3

Methodology

In the previous Chapter, four open problems were stated. In this Chapter, the methodological approaches adopted to answer each of the research questions are presented. For each of the Chapters 5–8, the corresponding experimental methodology and plan is discussed, and how the approaches adopted seek to answer the open problems identified in Chapter 2.

3.1 Determining aerodynamic loads on a railway contact wire

The interaction between an aerodynamic flow and a surface causes aerodynamic drag and lift forces. For a railway contact wire, the aerodynamic loads on slender cables cause vibrations of the system leading to damage and dewirement, as such quantifying these aerodynamic forces is an important area of research. Here, experimental and computational approaches have been used to determine the aerodynamic loads present on a single contact wire placed in an incident flow. Both approaches were adopted as simulation methods are able to predict aerodynamic forces at wind speeds well beyond those possible in a wind tunnel, whilst the experimental approach provides a method of validation for the predicted aerodynamic forces.

The purpose of determining the aerodynamic loads on components of the overhead line system is to provide input to an overhead line model to determine the effects aerodynamic loads have on the catenary pantograph interaction. Drag forces contribute to excessive blow–off, increasing the risk of dewirement. These events cause catastrophic damage to both the pantograph and overhead line [89]. Similarly, lift forces alter the contact wire height away from the design position increasing the variation in the contact force. Increased oscillations in the contact wire also raise the risk of contact loss between the pantograph and contact wire.

This separation leads to arcing at the contact interface degrading the surfaces and hastening fatigue. By quantifying aerodynamic forces, the dynamic response of the overhead line can be predicted, identifying areas of concern such as undesirable contact wire deflections and contact force variation.

3.1.1 Experimental determination

The Large Scale Sheffield Wind Tunnel, described also in [275, 276], was used to determine the aerodynamic forces acting on a 720 mm length of AC–120 railway contact wire. The air flow was assumed to be without the dynamic effects of a passing train, thus turbulence caused by the train body movement was neglected here. With respect to BS EN 50119, this situation would be considered the static state due to no train passage. The wind tunnel schematic and the experimental arrangement is given in Figure 3.1. The wind tunnel is an open-circuit wind tunnel with an axial fan placed at the outlet. The fan generates negative pressure downstream of the samples placed in the working section and the pressure gradient generates the air flow. The wind tunnel is 8.5 m long and the working section is 3 m long with a cross–sectional area of 1.2 m $\times$ 1.2 m. A honeycomb mesh straightens the inlet flow and dissipates any large scale structures in the flow that would lead to turbulent flow upstream of the wire sample. Further fine meshes dissipate any turbulence and non-uniformities in the flow before the working section.

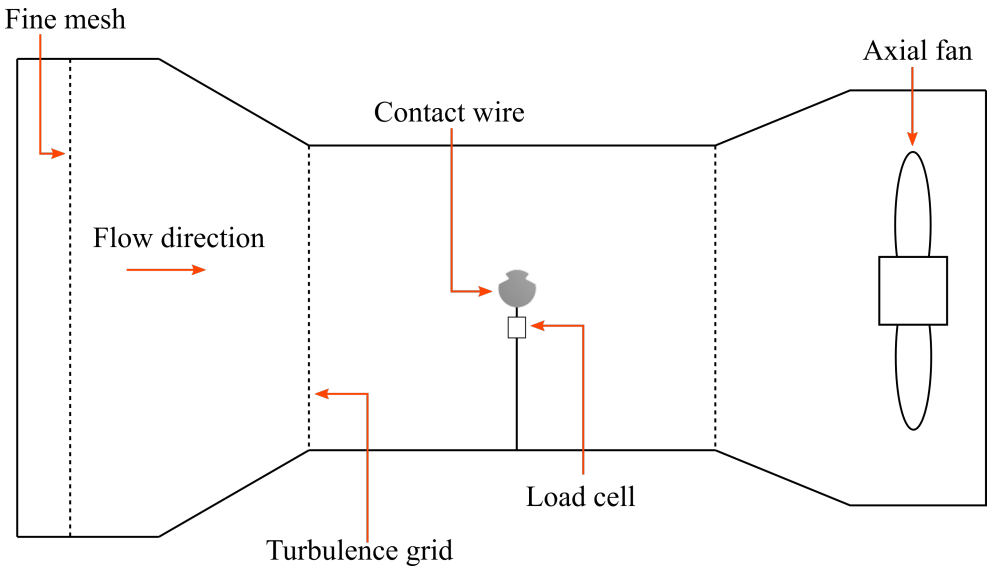

Fig. 3.1 Wind tunnel schematic and experimental arrangement.

During the experimental cases, consideration was given to the variations in the air pressure, density and temperature. In comparison to the simulation cases where the atmospheric conditions can be kept constant according to,

$$P = \rho R \mathscr{T}, \tag{3.1}$$

where ρ is the air density, $\mathscr{T}$, the air temperature, P, the air pressure and the ideal gas constant $R \approx 8.31446$ J/Kmol, fluctuations in the air temperature were recorded during each of the experimental cases. With repeated use, the air temperature inside the wind tunnel was found to increase, for example during the first test, the recorded temperature was 18.5 °C and for the final test, the recorded temperature was 22.6 °C. These fluctuations were taken into account according to Equation 3.1 when calculating the aerodynamic coefficients.

Aerodynamic instability of railway overhead line conductors is driven by a combination of wind speed, wire wear and the angle of attack [174], thus these were chosen as the variables investigated during the experimental procedure. Table 5.1 gives the test cases used. The air speed and pressure was measured using an FC0510 micromanometer, as shown in Figure 3.3, connected to a pitot tube mounted in the wind tunnel. Due to fluctuations in the air flow inside the wind tunnel, ten measurements were taken to give an average air speed for each case. The air speed values given in Table 5.1 are the averaged air speeds.

In the cases where wear was considered, only substantial wear was considered rather than surface defects such as scratches. The angle of attack was achieved through the use of a pivot mounted at the base of the rod onto which the contact wire sample and load cell were affixed. The arrangement of the contact wire and load cell atop the sting are shown in Figure 3.2.

Experiment parameters

The wind tunnel allows for the wind speed and angle of attack to be varied. The wind speed is controlled by the axial fan at the outlet of the wind tunnel, whilst the angle of attack is controlled by a pivot placed at the base of the sting upon which the contact wire and load cell are mounted. This is shown in Figure 3.2. The angle of attack can be varied up a maximum of $\pm 50^\circ$, however only angles up to $\pm 30^\circ$ were considered as angles beyond this were assumed to be unrealistic as rotations of the contact wire are restricted by the dropper clamps and supports. Safety restrictions placed on the wind tunnel due to the wind tunnel being located in a working laboratory restricted the magnitude of the air speeds considered, thus wind speeds were kept below 10 m/s, despite the wind tunnel providing the possibility of wind

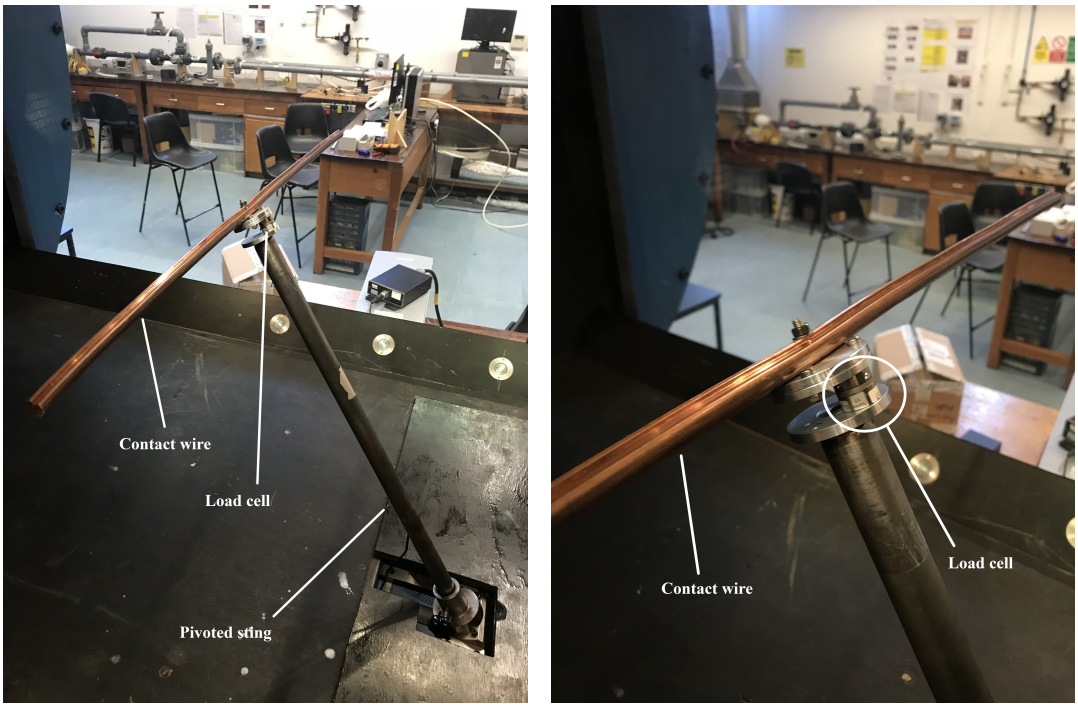

Fig. 3.2 Contact wire experimental arrangement in the wind tunnel. The contact wire is mounted on a pivoted sting that allows for variation of the angle of attack as shown.

speeds up to 22 m/s. Higher wind speeds are considered in the computational cases given in Section 3.1.2. Table 3.1 show the experimental variables used throughout the experiments.

Table 3.1 Independent variables used during the experimental determination of aerodynamic forces.

Air speed (m/s)	Angle of attack (°)	Wire wear (mm)
3.99	-30	0
4.93	-20	2
6.01	-10	4
7.02	0	6
8.15	10	
9.11	20	
	30	

Each of the experiment variables were chosen to reflect the environmental conditions that occur during the lifetime of an overhead line system. Variations in the angle of attack were considered to represent the directions of incident wind flows, and also to represent movement in the supports over the lifetime of the equipment which would cause twisting of the contact wire relative to the design position. Since the sliding contact between the pantograph and

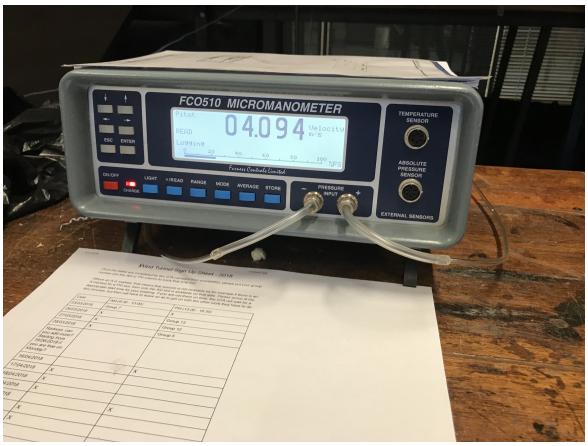

Fig. 3.3 FC0510 micromanometer used to measure the air speed and pressure inside the wind tunnel.

contact wire induces wear, different wear states of contact wire were used to represent the contact wire over its lifetime, to determine the effect of wear on the aerodynamic response of the contact wire.

Data collection

The aerodynamic drag and lift forces due to the incident air flow were measured during each experiment. Data was collected from the load cell at a frequency of 1 kHz for 10 s giving 10^4 data points for each case. The forces were measured using a a load cell mounted beneath the contact wire. The load cell used during the experiments is an ATI Nano 17 [277], a six–axis transducer with a maximum loading force of 17 N. Table 3.2 gives the load cell specification and measurement resolutions.

Table 3.2 Nano–17 load cell specification. The loading range and resolutions for the measured force, F (N), and torques, τ (N mm), are given. Subscripts denote the measured axis with x denoting the direction parallel to the flow and z denoting the direction perpendicular to the flow.

	F_x, F_y	F_z	τ_x, τ_y, τ_z
Load range	12	17	120
Resolution	1/320	1/320	1/64

The load call can exceed the load ranges given in Table 3.2, however the measurement resolution drops accordingly. For each doubling of the load, the resolution drops by half, i.e., for $F_z \in (17, 34]$ and $\tau \in (120, 140]$, the measurement resolution is 1/160 and 1/32

respectively. Initial numerical predictions indicated that the aerodynamic loads during the wind tunnel experiments were not expected to exceed the 17 N load so the resolution was not likely to be reduced below the initial 1/320.

As well as consideration given to fluctuations in the environmental conditions inside the wind tunnel, variations in the recorded measurements of the load cell were also considered. Before each test, the force on the load cell was recorded and if non-zero, was subtracted from the measured results. For example, during the case of the contact wire sample with 4 mm wear, the load cell recorded a lift force of -0.01 N before the wind tunnel was switched on and so this measurement was deducted from each of the tests. This check was performed for each respective test.

To ensure a steady state had been achieved due to the steady load, measurements of the aerodynamic loads were recorded only after 10 s had elapsed. This ensured transient behaviour due to the aerodynamic loads being first applied to the contact wire were not recorded and only the steady state behaviour was measured.

3.1.2 Computational determination

Restrictions placed on wind velocity in the wind tunnel, required the use of a computational method to investigate the aerodynamic forces at wind velocities greater than 10 $\mathrm{m/s}$. The simulations were performed using the ANSYS Fluent 17.0 package and generation of the geometry and mesh was performed using the packages provided by ANSYS 17.1. The use of simulations of the fluid flow around the contact wire also allow for greater reproducibility of each experiment. In the experimental case, each wire has to be machined to achieve the desired wear amount. The machining process can lead to small surface defects that affect the air flow. Computational efforts also offer greater granularity of the independent variables that are not easily achieved in the experimental case. For example the angle of attack was set according to $\pm 2^{\circ}$, whilst the angle of attack can be chosen arbitrarily in the computational case. Since validation of the modelling predictions was required, the independent variables in the simulations were chosen to match those of the wind tunnel.

Model setup

Initial conditions such as air density, pressure and temperature were be kept constant throughout each simulation. This was in contrast to the wind tunnel experiments, where the pressure and temperature varied as detailed in Section 3.1.1. The simulation environmental conditions were:

- air density, $\rho = 1.225$ kg/m^3,
- temperature, $T_1 = 15$ °C,
- pressure, $p = 101.325$ kPa, and
- viscosity, $\mu_0 = 1.7894 \times 10^{-5}$ kg/ms.

The computational domain for the simulation of air flow around a railway contact wire is given in Figure 3.4. The contact wire centre, represented by a circle in the schematic, was placed at the origin of the domain, and the domain height L_{dom}, was taken to be $20D$ to ensure boundary effects did not influence the fluid regime around the contact wire. Similarly, the longitudinal domain was split into $L_1 = 20D$, giving sufficient longitudinal distance for the flow regime to be fully established and $L_2 = 30D$, allowing sufficient distance for the effect of the contact wire boundary on the flow to be fully realised.

The characteristic length of the domain is the contact wire diameter $D = 13.2$ mm, giving a characteristic Reynolds number (Re_x) of

$$\text{Re}_\text{x} = \frac{\rho U D}{\mu_0} \approx 904U, \tag{3.2}$$

where U is the flow speed given in Table 3.3. At the inlet, the free stream Reynolds number (Re) is given by

$$\text{Re} = \frac{\rho U L}{\mu_0} = \frac{20\rho U D}{\mu_0} \approx 1.8 \times 10^4 U, \tag{3.3}$$

where $L_{\text{dom}} = 20D$, as in Figure 3.4.

For the velocities considered, Equation 3.2 gives $9 \times 10^2 < \text{Re}_\text{x} < 4 \times 10^4$ and Equation 3.3 gives $1.8 \times 10^4 < \text{Re} < 5.5 \times 10^6$. From [278], it is expected that since the contact wire boundary is approximately circular, the flow regime will involve a laminar boundary layer and a turbulent wake.

The boundary of the contact wire is shown in Figure 3.5a and the entire domain is shown in Figure 3.5c. The boundary of the contact wire was taken to be fixed in the flow, allowing for the determination of solely the aerodynamic forces on the contact wire, rather than changes in the fluid due to motion of the contact wire itself.

Table 3.3 gives the different cases considered during the simulation process. The fluid speed U given in Table 3.3 is the free stream velocity. For simplicity, to achieve an angle of attack, the free stream velocity was decomposed into horizontal and vertical components corresponding to the required angle rather than rotating the geometry and leaving the velocity

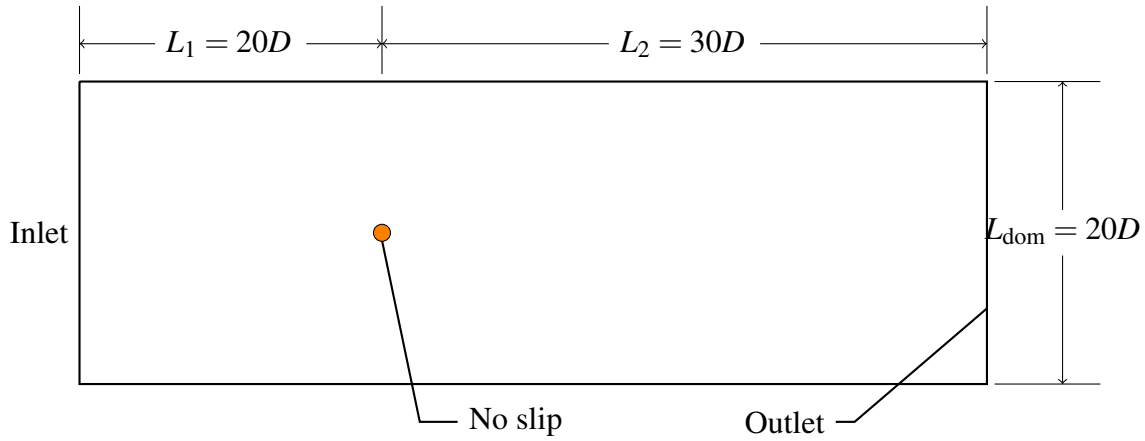

Fig. 3.4 (Not to scale) Schematic of the computational domain. The boundaries of the domain are scalar multiples of the contact wire diameter (also the characteristic length scale) $D = 13.2$ mm, shown here by the orange circle. The fluid flows through the domain from left to right.

unchanged. For example, to achieve an angle of attack of θ, the free stream velocity $U = (u, v)$ was decomposed into the components

$$(u, v) = (|U| \cos\theta, |U| \sin\theta), \tag{3.4}$$

and by the parity of the circular functions, an angle of attack $-\theta$ is achieved with velocity components

$$(u, v) = (|U| \cos\theta, -|U| \sin\theta). \tag{3.5}$$

The fluid velocity components given by Equations 3.4 and 3.5 correspond to the orientations of the contact wire given in Figure 5.2a for a positive angle of attack and Figure 5.2b for a negative angle of attack respectively.

The wear parameter was achieved by reducing the vertical diameter of the contact wire. The maximum reduction was 6 mm, giving a contact wire vertical diameter of 7.2 mm. This case is shown in Figure 3.5b and the other wear cases are similar.

The mesh was divided into discrete sections allowing for a greater mesh density around the contact wire boundary without a large increase in computational time. Figure 3.6 shows the mesh used throughout the simulation process. The mesh is split into different regions of varying mesh density: A denotes the coarse mesh used in regions away from the contact wire boundary where the fluid behaviour is of little interest, B a denser mesh directly in the path of the contact wire. This region has an increased density to properly resolve the fluid flow prior to the interaction with the contact wire boundary and also to accurately resolve the

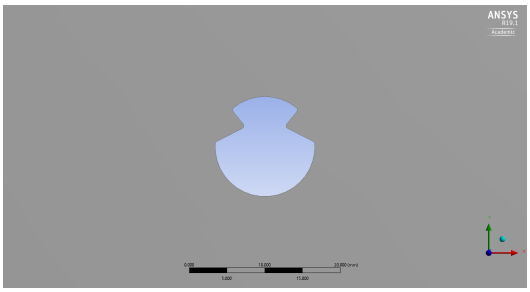

(a) Cross-sectional geometry of an AC-120 railway contact wire.

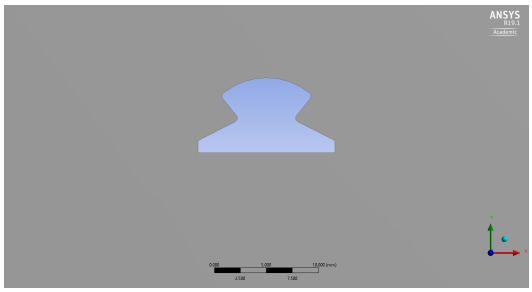

(b) Contact wire profile with a vertical wear of 6 mm applied.

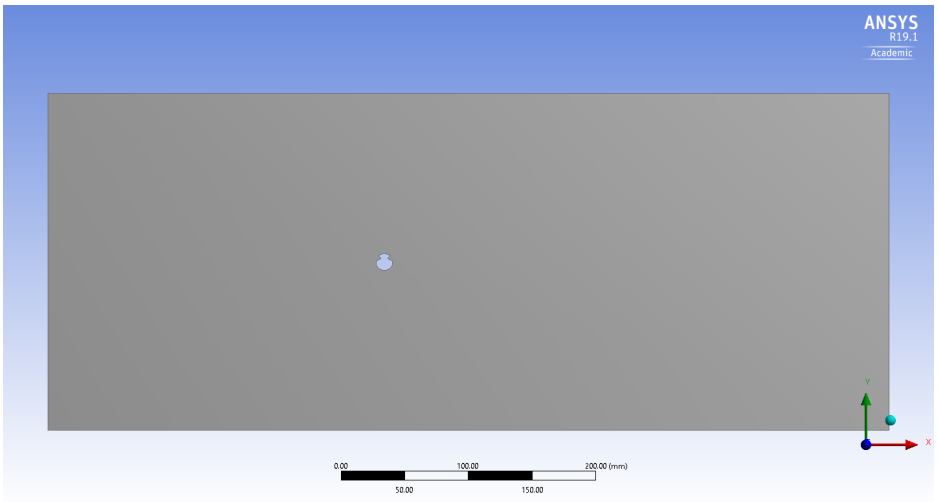

(c) Flow domain showing the geometry of the model when the wire wear is zero.

Fig. 3.5 Contact wire boundary and the flow domains generated in the ANSYS software.

wake downstream from the contact wire. The region C is the region with the highest mesh density, surrounding the contact wire where the fluid behaviour is most of interest.

Along the contact wire boundary, a boundary layer will form and so the dense mesh is extended beyond the boundary layer thickness to properly capture the behaviour within this layer. Along the leading edge of the contact wire, for small lengths, the boundary layer thickness can be approximated by

$$\delta_l = \frac{5x}{\sqrt{\mathrm{Re_x}}}, \qquad \text{and} \qquad \delta_t = \frac{0.37x}{\sqrt[5]{\mathrm{Re_x}}}, \tag{3.6}$$

where δ_l and δ_t correspond to laminar [279, pg. 140] and turbulent [279, pg. 638] boundary layer thicknesses respectively and x is the length along the leading edge of the boundary as shown in Figure 3.6b. For the minimum free stream Reynolds number considered (Re =

Table 3.3 Flow conditions used in the simulation cases. For each velocity in column 1, each of the angles and wear amounts in columns 3 and 4 respectively, were considered.

Fluid speed (m/s)	$\mathrm{Re_x}$	Angle of attack (°)	Wire wear (mm)
1	904	-30	0
2	1,807	-20	2
3	2,711	-10	4
4	3,615	0	6
5	4,518	10	
6	5,422	20	
7	6,326	30	
8	7,229		
9	8,133		
10	9,037		
15	13,555		
20	18,073		
25	22,591		
30	31,628		

1.8×10^4), the hydrodynamic entry length [280] L_e, given by,

$$L_e = 4.4\sqrt[6]{\mathrm{Re}} \approx 23\,\mathrm{m}, \tag{3.7}$$

indicates that the fluid flow is laminar when it reaches the leading edge of the contact wire. Thus, we can take the boundary layer thickness to be given by δ_l. Since L_e is monotonically increasing, the flow is always laminar when reaching the contact wire for the cases considered here.

Mesh independence was achieved with a mesh independence study until the variation in the drag and lift coefficients was below 0.5%. The initial number of elements used was approximately $250,000$ and Figure 3.7 shows the number of elements required to achieve the mesh independence. The large number of elements required is in contrast to studies focusing on a circular boundary in a flow such as [281], where only approximately 436,000 elements were required. This is likely due to the significant number of smaller elements with length scales of 10^{-4} m needed to mesh around the grooves of the contact wire on each side.

Since the time step size and the mesh size are related through the one-dimensional Courant number [282],

$$C_n = \frac{U\Delta t}{\Delta x}, \tag{3.8}$$

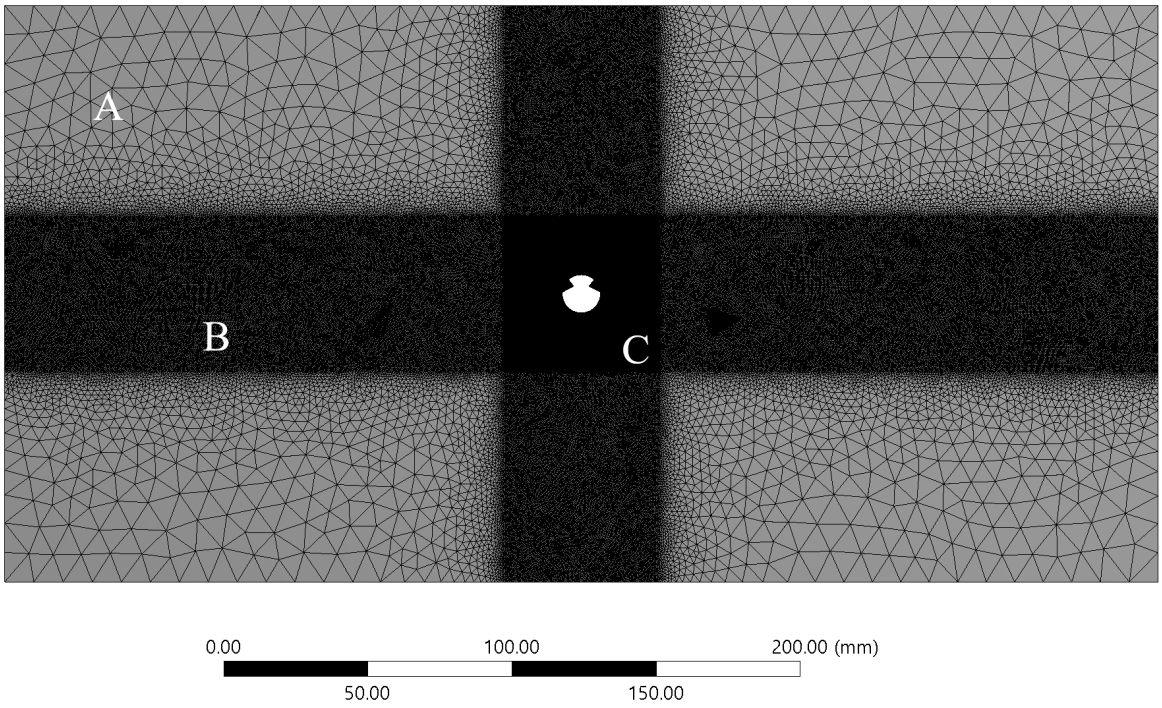

(a) Mesh generated for the fluid domain.

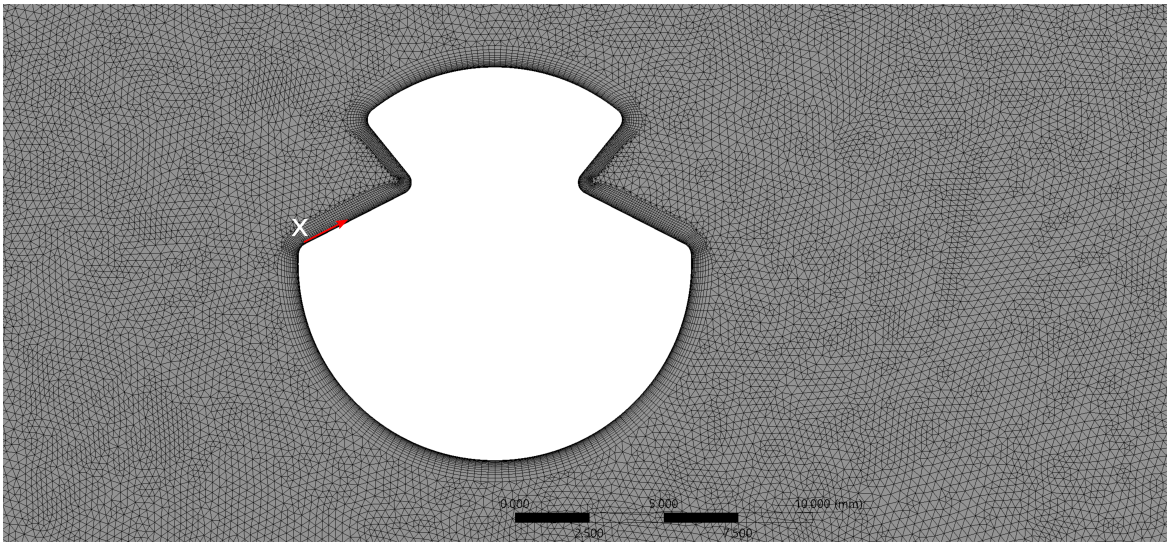

(b) Meshing applied to the domain close to the contact wire boundary indicating the large number of elements.

Fig. 3.6 Meshed domain used throughout the simulation process achieved using the mesh independence study shown in Figure 3.7. Letters used in the figures are referred to in the text and the scale indicates the size of the elements required when meshing in a neighbourhood of the contact wire boundary.

where Δt and Δx are the time and spatial element sizes respectively, the time step size was chosen such that $C_n \leq 1$ to ensure the information encoding the behaviour of the fluid in each time step was strictly constrained to an individual element size during that time step. For the case where the simulation was found to be independent of the mesh sizing, the smallest mesh element was found to have a length scale of approximately 4×10^{-4} m. This meant the smallest time step size required to satisfy $C_n \leq 1$ was

$$\Delta t \leq \frac{\Delta x}{U} \approx \frac{4 \times 10^{-4}}{30} = \frac{4}{3} \times 10^{-5}\text{s}, \tag{3.9}$$

when a wind speed of $U = 30$ m/s was used. However, in order to correctly resolve the boundary layer which becomes increasingly thin as the characteristic Reynolds number increases, a smaller time step than the one given by Equation 3.9 is required. To achieve a dimensionless wall distance $y^+ < 1$, a time step of approximately 9×10^{-6} was required. Since $9 \times 10^{-6} < 4/3 \times 10^{-5}$, the condition imposed by C_n is still satisfied.

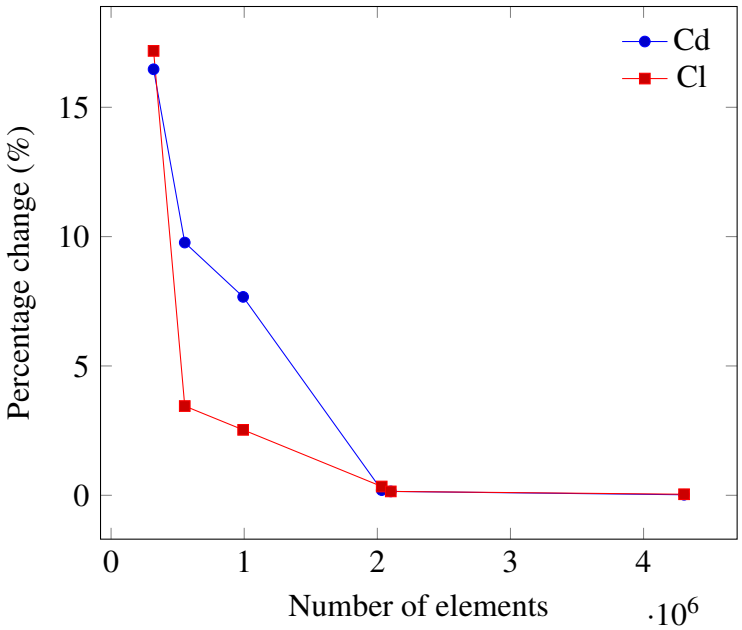

Fig. 3.7 Mesh independence study demonstrating that mesh independence is achieved with less than 0.5% change in the drag (Cd) and lift (Cl) coefficients with 2,101,041 elements.

Throughout the simulation process, the flow was taken to be incompressible, as the maximum serviceable wind speed for UK railway overhead lines is 37 m/s [283], giving a maximum Mach number M_{max} of 0.109. As $M_{\text{max}} < 0.3$, application of the incompressibility condition was valid [284]. In fact, for the wind velocities considered here, the variation in the density of the fluid is approximately 1%. The flow was also taken to be isothermal

throughout in contrast to the experimental case (the air temperature in the experimental case varied due to changes in air pressure caused by the rotating fan) and to ensure a pressure gradient across the contact wire, viscous flow was used. Single phase flow was appropriate since the only fluid in the domain was air.

In the computational cases, the flow was considered to be 2D. This gave the idealised flow regime under the assumption that the fluid flowed parallel to the boundaries of the domain rather than replicating the exact cases in the wind tunnel where 3D effects would be encountered. This in particular discounted any torque on the contact wire length due to pressure from the air flow that would have occurred in the experimental case. Transient effects due to changes in the fluid velocity were considered to capture the vortex shedding behaviour downstream of the contact wire.

The no slip condition was applied to the contact wire boundary which was defined as a static wall. The no slip condition specified that fluid at the solid boundary would have zero velocity. Since only single phase fluids were considered, this was considered a valid condition. The static wall condition specified that the contact wire was fixed in the domain and only the effect of the fluid interaction on the wall was recorded in the calculation of the aerodynamic forces rather than the response to a moving boundary affecting the flow regime. The leftmost region of the computational domain was designated the inlet and similarly the rightmost region of the domain was specified as an outlet. These are shown in Figure 3.4. The horizontal extremes of the domain were set as pressure outlets to correctly represent the free air surrounding a contact wire, particularly when non-zero angles of attack were considered. Setting the horizontal edges of the domain as walls would have introduced undesirable reflections in the fluid.

The data collected in each of the simulations was the same as the data collected in the experimental case, that is the aerodynamic drag and lift forces. Since the required time step of the simulations was 9×10^{-6} s, each simulation case provided approximately 100 times more data points than the experimental case.

3.1.3 Data analysis methods

The maximum drag forces in each case was recorded and the arithmetic mean of the lift forces were chosen to highlight the core aerodynamic loads on the contact wire in both the experimental and simulation cases. This allowed for prediction of the dynamic response of the overhead line in Chapter 7. To determine the frequency of the oscillating aerodynamic lift force, a discrete Fourier Transform was applied to the data. In each case, the first fundamental

frequency was identified as the dominant driver of oscillatory behaviour. Lower fundamental frequencies indicate the possibility of conductor gallop, whilst high frequency behaviour is characteristic of contact wire resonance. From either the time–varying or static aerodynamic forces the drag and lift ratios can be determined according to

$$F_{\text{Drag}} = \frac{1}{2} C_d \rho U^2 A, \tag{3.10}$$

$$F_{\text{Lift}} = \frac{1}{2} C_l \rho U^2 D. \tag{3.11}$$

From the drag and lift ratios, a comparison across all the independent variables used can be made to quantify the aerodynamic response as the wear state and the angle of attack is varied.

3.2 Sensitivity of the catenary pantograph interaction to mechanical parameter variation

In Chapter 2, it was identified that much focus has been given to contact wire irregularity with respect to the contact wire wear. The work presented in this thesis considers contact wire irregularity beyond the wear state of the contact wire. By considering mechanical parameters of the system such as line tension, or contact wire mass, the effects of alterations to the system can be predicted and quantified potentially leading to cost effective improvements of the catenary-pantograph dynamics, for example, avoiding the need for expensive system redesigns to achieve increases in the line speed. In this section, the modelling methodology for analysis of the catenary pantograph interaction is presented, with focus given to the creation of a finite element representation of the overhead line equipment. The output provided by numerical modelling of the catenary pantograph interaction is also discussed, with the methods used to analyse the output given.

3.2.1 Modelling process – Inputs

The modelling process to simulate the catenary pantograph interaction is shown in Figure 3.8.

Creation of the input file from which simulation of the interaction between the contact wire and pantograph can be investigated is handled with a user–defined interface. The required geometry and pantograph inputs are exported using this to a text file that can be read using the ANSYS scripts.

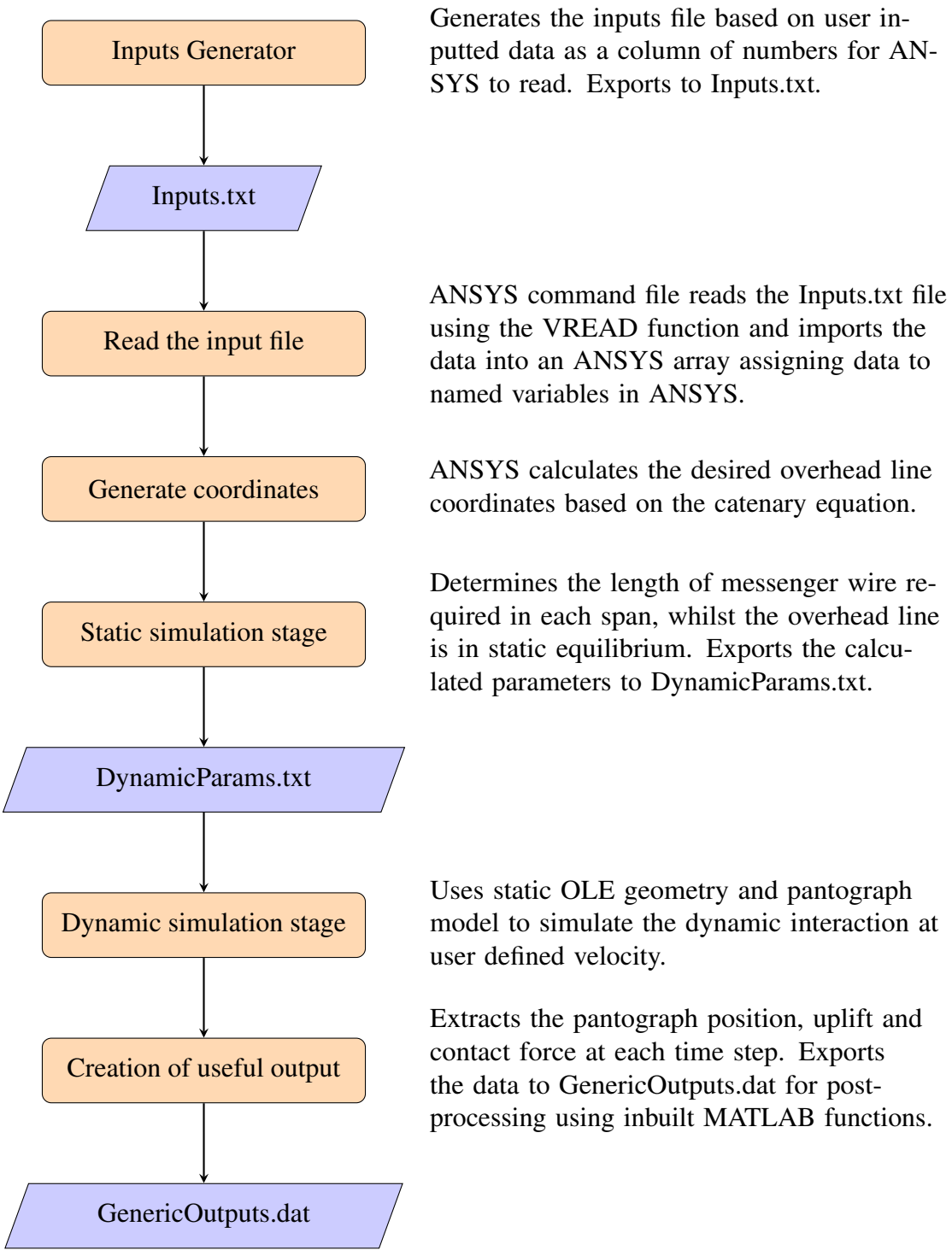

Fig. 3.8 Flowchart of the modelling process.

The input processing file is separated into seven packages, four allowing for data input and three for processing the data into an exportable format. The data input packages are comprised of:

- Overhead line parameter inputs,
- Overhead line geometry inputs,
- Pantograph parameter inputs, and
- ANSYS modelling inputs.

The data processing packages are comprised of:

- A compilation of the data inputs from the previous four packages,
- a single column of all modelling inputs ready for exporting, and
- a count of the number of inputs to be exported.

Physical parameters of the overhead line geometry

Inputs required in this package include the physical properties of the overhead line consisting of the messenger and contact wires and the droppers. As such the required properties for the messenger and droppers wires are:

- wire tension,
- cross–sectional area,
- mass per unit length, and
- Young's modulus and Poisson's ratio.

For the droppers, the following parameters are required:

- the mass per unit length,
- the masses of the clamps at each end connecting the droppers to the messenger and contact wires, and
- the dropper stiffness in both tension and compression.

The final two parameters required here are the mass of the registration arms and the required amount of pre-sag as a fraction of the span length if chosen, otherwise pre-calculated dropper lengths are used. The registration arms are presented by point masses capturing the total mass of the registration arms as point additions to the overhead line geometry at the mast locations.

Span geometry

To represent the overhead line geometry, inputs required include the mast locations, the span lengths and the number of droppers in each span. To calculate the contact wire height in each span, the messenger wire height at each support is required. From the messenger wire height, the inclusion of the dropper lengths and positions determine the contact wire height. The adopted method for determining the contact wire geometry differs from conventional methods for designing the equipment geometry during electrification projects. In design projects, the contact wire height is given and the messenger wire height is determined by the available vertical space, i.e., at bridges or tunnels, the messenger wire height is dropped. The dropper lengths are then determined based on the desired presag of the contact wire and the messenger wire vertical profile.

Lumped-mass pantograph inputs

Options available with respect to pantograph modelling include the option to investigate the dynamics of two– and three–lumped mass pantographs, including the mass, stiffness, viscous damping and horizontal velocity of the associated pantograph components.

Simulation parameters

Simulation parameters set by the user input directly affecting the performance of the ANSYS simulations include:

- messenger wire tensioning spring length (Section 3.2.3),
- overhead wire mesh lengths,
- contact stiffness for use in the penalty method during contact between the contact wire and pantograph, and
- damping coefficients α and β used to apply global Rayleigh damping to the system.

3.2.2 Functionality options

The work packages that generate the input files required by the ANSYS scripts, allow for different functionality options to be built into the model easily and efficiently.

Pantograph type

Generic two- and three-lumped mass models as discussed in Chapter 2.6.2 are functional within the model. The full set of parameters are required for these models, including the static and aerodynamic uplift forces acting on them. The included models do not support nonlinearities such as frictional elements or bump-stops designed to limit pantograph component displacement.

Wear/Ice loading

Ice loading of wires can be introduced into the simulation by introducing a mass addition. This mass addition requires the cross–sectional area of the wire to be altered in turn. To calculate the resultant cross-sectional area of a wire, $A_{c,\text{ice}}$, consider a mass addition m_{ice} to the original wire mass, then the resultant cross–sectional area is simply

$$A_{c,\text{ice}} = \frac{m_{\text{con}} + m_{\text{ice}}}{\rho_{\text{con}}}, \tag{3.12}$$

where ρ_{con} is the wire density.

Contact wire wear is typically considered in terms of vertical wear depth, relative to the edge of an unworn contact wire, as shown in Figure 3.9. By adjusting the cross–sectional area of the contact wire, wear can also be introduced into the simulation. Reducing the cross–sectional area to create an equivalent mass per unit length to a worn contact wire decreases the contact wire sag. The contact force statistical output shown in Table 3.4 shows that altering the contact wire mass or area to create a contact wire with an equivalent density achieves the same dynamic response.

Table 3.4 Statistical output for the catenary pantograph interaction when either the contact wire cross–sectional area of mass per unit length are changed to achieve equivalent dynamic performances. All results in N.

	F_m	σ	$F_{D_{\max}}$	$F_{D_{\min}}$	$F_{S_{\max}}$	$F_{S_{\min}}$
Increased cross–sectional area	105	12.6	149	83	143	67.2
Increased mass per unit length	104	13.1	149	82	143	64.7

The resultant cross-sectional area of a worn wire can be calculated from the original wire cross-sectional area. Given the unworn area is $A_{\text{con},0} = \pi R_{\text{con},0}^2$, the area of the worn contact wire is given by

$$A_{c,\text{wear}}(\phi) = R_{\text{con},0}^2 \left(\pi - \frac{\phi}{2} + \sin\phi \right), \tag{3.13}$$

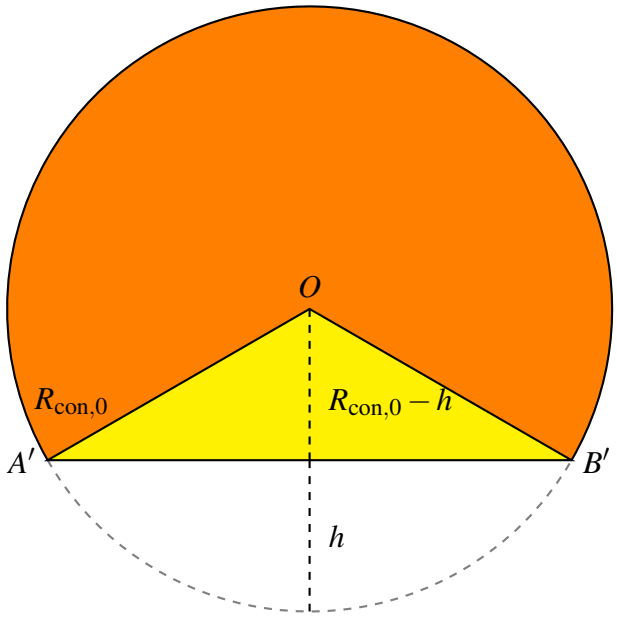

Fig. 3.9 Wire cross section approximated as a circle with a wear flat.

where $\phi \in [0, \pi]$ is the angle $A'OB'$ in Figure 3.9 and is given by

$$\phi = 2 \arccos\left(1 - \frac{h}{R_{con,0}}\right). \tag{3.14}$$

Multiple pantographs

The interaction between multiple pantographs and the overhead line is frequently of interest when investigating catenary dynamics as the performance of the trailing pantograph is typically worse than that of the leading pantograph [68, 69], particularly as the train speed is increased. As such this option is included in the model allowing for up to three pantographs to be included. Both the pantograph types and spacing between can be changed independently allowing for a large range of system setups to be considered.

Implementation of trailing pantographs is the same as for the leading pantograph with the input processing and solution files being replicated from the files for the leading pantograph with the boundary conditions for the trailing pantographs applied by the user. The use of multiple pantographs in this model as thus far not been validated and is left to further work.

Variable wire heights

The implementation of varying wire heights in simulations of the catenary pantograph interaction can be achieved by altering the wire support heights and the length of the droppers. Alteration of these two parameters effects a change in the contact wire height and thus any configuration of a standard overhead line can be investigated. Using this method is the core to the investigation of the effects of wire height changes in Chapter 8. In this study, the dropper lengths used were taken from measurements of the overhead line geometry at Network Rail's Rail Innovation & Development Centre (RIDC) [285, 286].

3.2.3 Modelling process – Creation of the wire geometry

To generate the overhead line geometry, the wire heights at supports and span lengths are typically the only known parameters and the full geometry is otherwise unknown. In this section, the methodology for creating the overhead line geometry is described and shown in Figure 3.10.

The messenger wire geometry can be predicted using the catenary equation [13, p. 276] given by,

$$y(x) = \frac{T_{\text{mes}}}{mg}\cosh\left(\frac{mg}{T_{\text{mes}}}(x-x_0)\right)+C, \tag{3.15}$$

where the height $y(x)$ at location x, as shown in Figure 3.11, is a function of the messenger wire tension, T_{mes} and the total mass supported by the messenger wire per unit length, $m = m_{\text{mes}} + m_{\text{con}}$.

Equation 3.15 gives the general shape of the messenger wire when the support heights are not constant and thus the low point of the catenary is offset by x_0. When the support height is constant, x_0 vanishes and Equation 3.15 becomes

$$y(x) = \frac{T_{\text{mes}}}{mg}\cosh\left(\frac{mg}{T_{\text{mes}}}x\right)+C. \tag{3.16}$$

The constants x_0 and C are uniquely determined by the wire heights at supports at either end of a span. Given the two coordinates at the end of each span, this gives two catenary equations in two unknowns which give,

$$x_0 = \frac{1}{2}(x_1+x_2)+\frac{T_{\text{mes}}}{mg}\operatorname{arcsinh}\left(\frac{mg}{2T_{\text{mes}}}(y_1-y_2)\operatorname{csch}\left(\frac{mg}{2T_{\text{mes}}}(x_2-x_1)\right)\right), \tag{3.17}$$

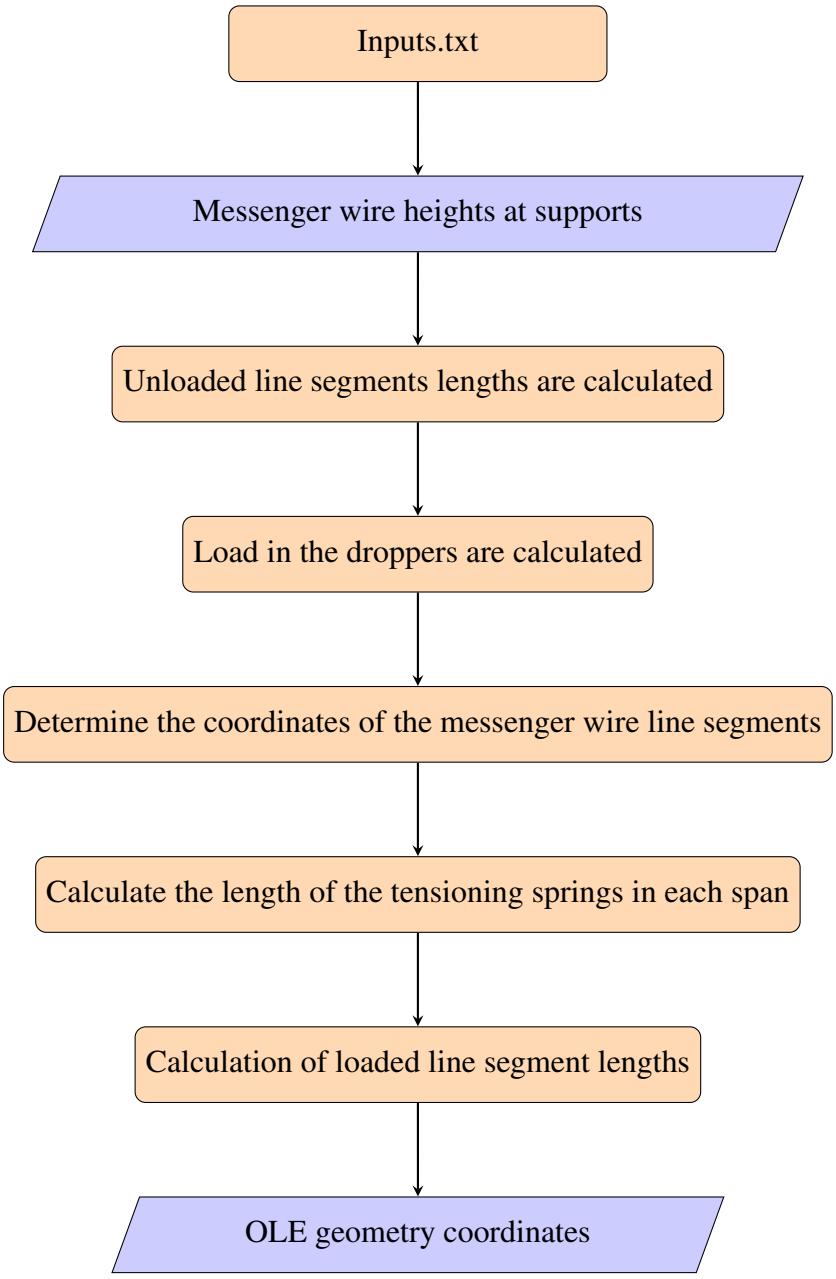

Fig. 3.10 Flowchart of the process to create the overhead line coordinates.

and

$$C = y_1 - \frac{T_{\text{mes}}}{mg}\cosh\left(\frac{mg}{2T_{\text{mes}}}(x_1 - x_2) - \operatorname{arcsinh}\left(\frac{mg}{2T_{\text{mes}}}(y_1 - y_2)\operatorname{csch}\left[\frac{mg}{2T_{\text{mes}}}(x_2 - x_1)\right]\right)\right). \tag{3.18}$$

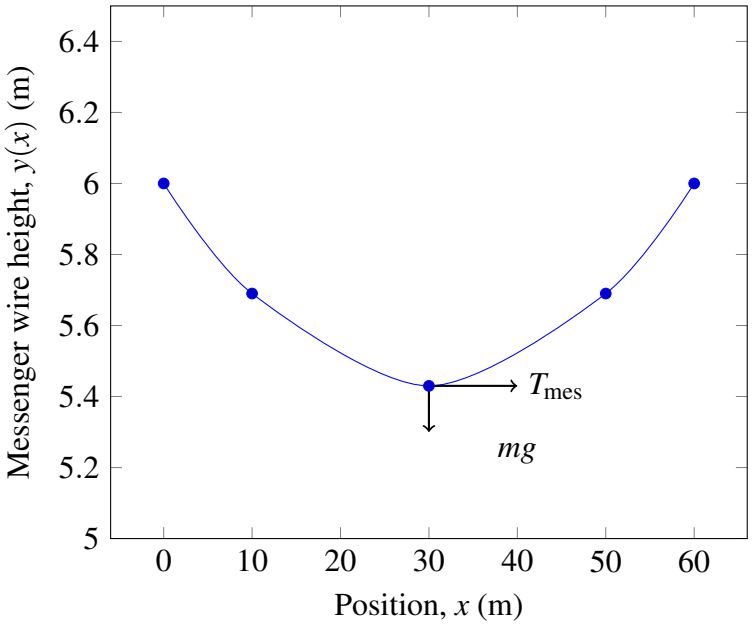

Fig. 3.11 Typical messenger wire height due to self–weight mg, and horizontal tension T_{mes}.

In the absence of non-uniform loads and droppers, Equation 3.15 describes the shape of a tensioned messenger wire, however in reality this is an approximation to an installed messenger wire as the addition of droppers and non-uniform loads distort this shape.

Pre-tensioned coordinates

An initial geometry is created using Equation 3.15 together with the constants given by Equations 3.17 and 3.18. This geometry is used as a 'pre-tensioned' geometry as an input for the static simulation.

Considering the overhead line geometry as a system of straight lines between the masts and droppers of the tensioned geometry, as shown in Figure 3.12, the tensioned lengths L_t of each of the straight lines are given by

$$L_t = \sqrt{(x_2 - x_1)^2 + (y_2 - y_1)^2}. \tag{3.19}$$

This length L_t, consists of the unloaded natural length L_0 and the extension due to the load forces δL_t.

In the case of the contact and messenger wires, the material properties and cross-sectional areas are known, and an application of Hooke's Law,

$$\sigma_s = E\varepsilon_s, \tag{3.20}$$

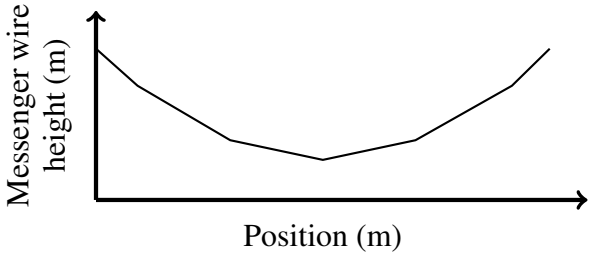

Fig. 3.12 Straight line segments L forming the messenger wire.

gives the initial unloaded length of each line segment. To determine the unloaded length, replace the tensile stress σ with T_{mes}/A_c and strain ε with $\delta L_t/L_0$. Then the unloaded length is given by

$$L_0 = \frac{LEA_c}{T_{\text{mes}} + EA_c}. \tag{3.21}$$

Gravitational effects act to increase the axial tension on sections of wire not parallel to the ground, however these effects are small compared with the applied tension and are neglected. Axial loads in the wires are assumed to be constant and equal to that off the applied tension at the end of the wire runs.

As the droppers are represented in the model by nonlinear spring elements, specific material properties are not defined. The extension of the droppers under loading is governed by the tension stiffness k_T. The unloaded length of the droppers can therefore be found by the alternative form of Hooke's Law, $F_T = k_T \delta L_t = k_T(L - L_0)$, giving

$$L_0 = L - \frac{F_T}{k_T}. \tag{3.22}$$

The tensile force F_T in each of the droppers varies in contrast to the messenger and contact wires, where the tensile force is constant. It is assumed that each dropper supports the contact wire load from halfway between the preceding and successive droppers as shown in Figure 3.13 as well as the weight of the dropper clamp connecting the droppers to the contact wire. The first and last droppers in each span also support half the mass of the registration arm between them.

Thus the approximation to tensile load F_T in the i^{th} dropper can be written as

$$F_{T,i} = m_{\text{con}} g \left(\frac{x_i - x_{i-1}}{2} + \frac{x_{i+1} - x_i}{2} \right) + M_{\text{s}} g = m_{\text{con}} g \left(\frac{x_{i+1} - x_{i-1}}{2} \right) + M_{\text{s}} g, \tag{3.23}$$

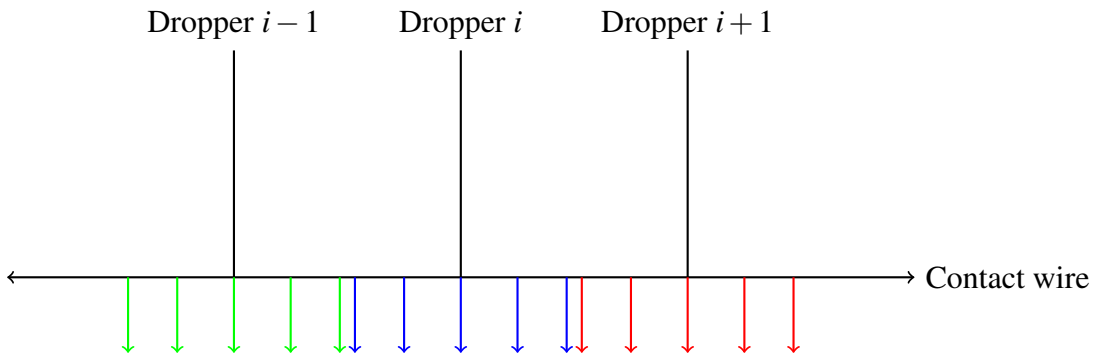

Fig. 3.13 Approximating the tensile force in each dropper supporting the contact wire from half way between the preceding and successive dropper. The load in each dropper due to supporting the contact wire is indicated by the colour arrows.

where M_s is the mass of the clamps and the registration arm where appropriate. Substituting the approximation $F_{T,i}$ into Equation 3.22, the unloaded dropper lengths can be written as

$$L_0 = L - \frac{1}{2k_T}\left[m_{\text{con}}g(x_{i+1} - x_{i-1}) + 2k_T M_s g\right]. \tag{3.24}$$

From Equations 3.21 and 3.24, the unloaded lengths of the messenger and contact wires and droppers are known and from these, the unloaded overhead line geometry can be created.

To generate the coordinates required to create the overhead line geometry, in each span, a quadrilateral can be formed between two successive droppers and the contact and messenger wires. To do this, the contact wire is fixed in a straight line, this need not be horizontal in the case of unequal support heights for the required span, and an unloaded dropper at the centre of the span is also fixed, as shown in Figure 3.14a. Then the dropper preceding the one already fixed is centred on the next point in the contact wire determined by the dropper horizontal location. Given the stated length of the dropper, a circle can be formed with dropper length as the radius. In a similar way, the length of the next section of messenger wire forms a radius of a second circle. The coordinate locating the intersection of the dropper and messenger wire is the intersection of these two circles. This is demonstrated in Figures 3.14b and 3.14c. This process is repeated for all droppers in the span to create the unloaded geometry as in Figure 3.14d.

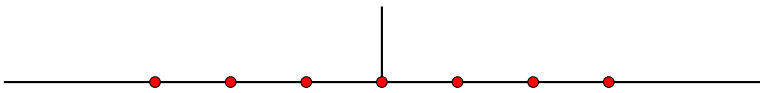

(a) Step 1 in establishing the 'pre-tensioned' coordinates. The contact wire is fixed in a straight line and a dropper in the centre of the span is fixed.

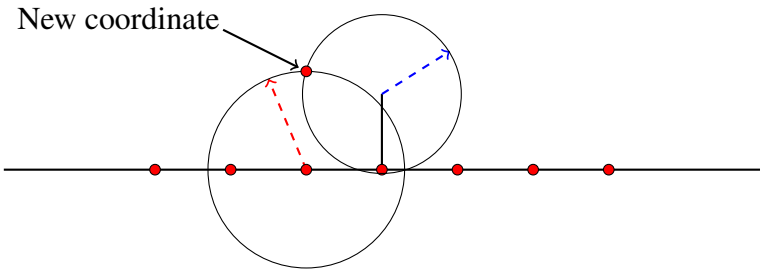

(b) Step 2 in establishing the 'pre-tensioned' coordinates. The next messenger wire coordinate is calculated from the intersection of two circles with radii equal to the next dropper length and next messenger wire segment length respectively.

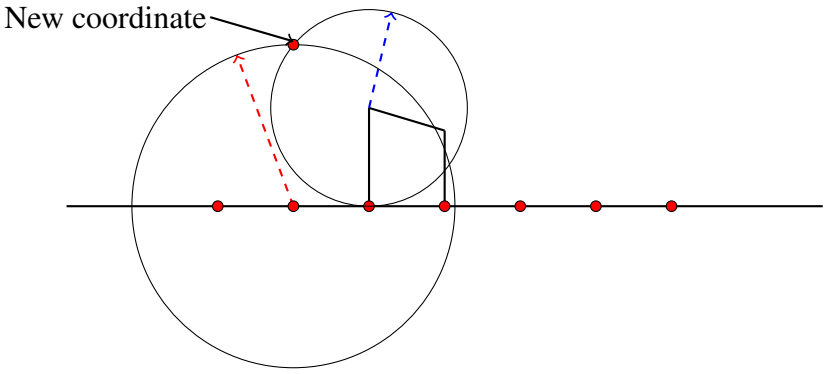

(c) Step 3 in establishing the 'pre-tensioned' coordinates. The previous step is iterated for the remaining droppers until the entire span is completed.

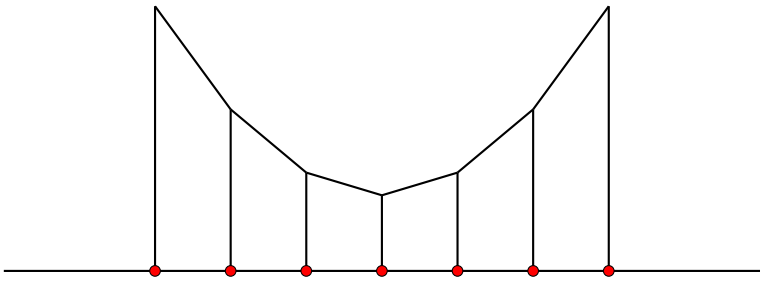

(d) Step 3 in establishing the 'pre-tensioned' coordinates. The previous step is iterated for the remaining droppers until the entire span is completed.

Fig. 3.14 Steps in creating the unloaded overhead line geometry.

In the global coordinate system the intercept of the two circles and thus the next geometry coordinate is the solution to

$$(x-x_1)^2+(y-y_1)^2=R_1^2, \tag{3.25}$$

$$(x-x_2)^2+(y-y_2)^2=R_2^2, \tag{3.26}$$

however, a translation of the coordinate axes to centre the origin on one of the known coordinates simplifies finding the next coordinate to solving

$$X^2 + Y^2 = R_1^2, \tag{3.27}$$

$$(X - \bar{x})^2 + Y^2 = R_2^2. \tag{3.28}$$

Thus the successive coordinates are given by,

$$(X,Y) = \left(\frac{R_1^2 - R_2^2 + \bar{x}^2}{2\bar{x}}, \pm\sqrt{R_1^2 - \left(\frac{R_1^2 - R_2^2 + \bar{x}^2}{2\bar{x}} \right)^2} \right), \tag{3.29}$$

where the sign of the Y coordinate is determined by the orientation of the translated coordinate axes relative to the global coordinate system. Transforming back into the global coordinate system gives the unloaded overhead line geometry for each span.

Whilst the unloaded geometry has been created, each geometry is specific to the span in which it was created as the coordinates are relative to the central dropper. In each individual span, this presents no issues. However, since the lengths calculated are unloaded, they are shorter than the tensioned coordinates and shift towards the fixed dropper at the centre of each span when under tension and gravitational loads. Since a continuous wire is required, a node is shared between each span. To overcome this, introducing a linear spring element ensures the messenger wire is the correct length when tensioned at the mast location, ensuring a continuous wire at the support nodes.

To determine the spring length, ℓ, consider

$$\ell = \frac{1}{2}\left(\mathscr{L} - L_0\right), \tag{3.30}$$

where $\mathscr{L}$ is the required length of the messenger wire after loads are applied, and L_0, the unloaded lengths, calculated using Equation 3.21. Then the loaded lengths $\mathscr{L}$ can be calculated numerically. The numerical calculation is chosen over using the catenary equation in Equation 3.15, as due to non-uniform loading of the messenger wire at dropper locations, 'pinching' of the wire profile occurs. These deviations from a true catenary are large enough that arc lengths calculated from the catenary equation are significantly inaccurate.

Using the unloaded coordinates generated using Equations 3.21, 3.24 and 3.29, beam elements are created in straight lines between mast locations. Loads at the dropper locations are applied as well as gravitational and tensile loads deforming the straight lines forming the messenger wire into the loaded catenary shape. This deformation changes the span

length, displacing the sections of the messenger wire away from the mast locations. These displacements are shown in Figure 3.15. With each subsequent span, these displacements grow larger, that is $0 = d_1 < d_2 < d_3 < \ldots < d_n$.

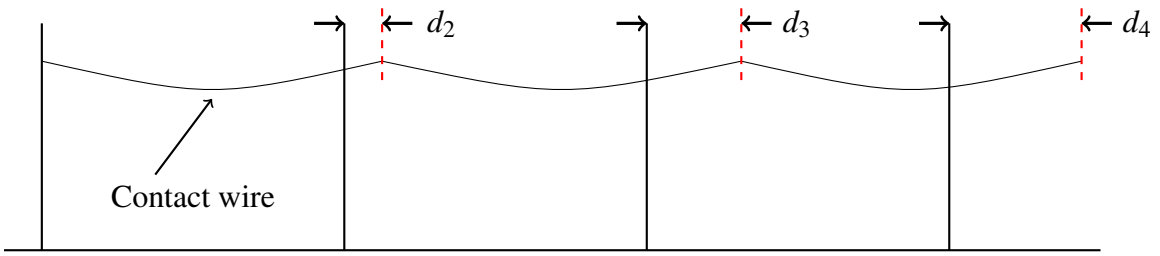

Fig. 3.15 Displacements of the support locations due to a shortening of the messenger wire due to loading. Diagram not to scale and displacements are exaggerated. Mast locations indicated by the vertical lines.

The displacement d_i of the i^{th} mast point and the unloaded length $L_{0,_i}$ of the i^{th} span, is used to calculate the strain in the x-direction for each span using

$$L_{0,i}\varepsilon_{x,i} = d_{i+1} - d_i, \qquad i \in \big[1, \text{number of spans}\big]. \tag{3.31}$$

From the strain, calculated in Equation 3.31, the tensioned lengths L calculated using Equation 3.19 and the mast coordinates, the loaded length $\mathscr{L}$ is given by

$$\mathscr{L} = \frac{L}{1+\varepsilon_x}, \tag{3.32}$$

which can be substituted into Equation 3.30 to determine the initial spring length ℓ.

Once the spring length is known, the spring stiffness is fixed to match the material properties of the messenger wire that the spring element is representing. Considering Hooke's Law once again, the spring stiffness k is given by EA_c/ℓ, where ℓ is given by Equation 3.30. Given each ℓ varies from span to span, the spring constant in each span varies in the same way.

This completes the process required to generate the correct coordinates and line lengths to create the overhead line geometry, an example of which is shown in Figure 3.16.

Once the geometry discussed in this section has been created, the interaction between them and a moving train pantograph can be studied. The process used to do this is discussed in the following Section.

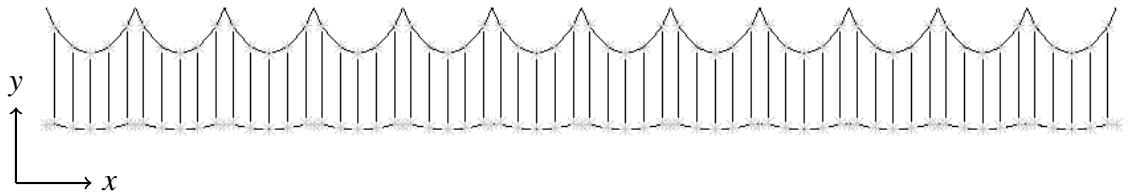

Fig. 3.16 Overhead line geometry example generated using the described method.

3.2.4 Modelling process – Simulating the catenary pantograph interaction

Throughout the simulation of the catenary pantograph interaction, the simulation is split into distinct stages so as to allow for the manipulation of the forces and boundary conditions applied to the model. At the end of each load step, the forces and boundary conditions are retained to act as the initial state for the subsequent load step. As well as the forces and boundary conditions, the initial conditions retained also include the nodal positions, velocities and accelerations. In this instance, the model is split into three load steps:

1. The static load step where the wires are tensioned, and gravity is applied, pulling the OLE into the correct geometry.

2. The 'settling' step whereby all vibrations caused by applying tension and gravity to the OLE are allowed to decay, leaving the geometry in static equilibrium.

3. The dynamic load step where the catenary pantograph interaction is simulated.

Within each load step, a number of sub–steps are used to apply external forces to the OLE. This aids in the convergence of the model as changes between each sub–step are small.

Static wire equilibrium and imposition of the boundary conditions

Using the coordinates generated using the process described in Section 3.2.3, the OLE geometry is created and meshed based on the element size chosen during the data input process.

Tension and gravitational loads are applied to the OLE during this load step, giving the OLE the correct shape. The result of this load step is an OLE geometry in static equilibrium. As well as gravitational and tensile loads being applied to the overhead line, sufficient boundary conditions are also applied to the OLE to constrain the system. Whilst

the boundary conditions and constraints are also applied to the pantograph in this load step, discussion of those is given in Section 3.2.4.

Globally, the system is constrained against any displacements in the lateral z-direction and rotations about the horizontal x- and vertical y-directions are also constrained. These constraints result in a 2D representation of the overhead line, and also reduces the degrees of freedom of the system, significantly reducing the number of calculations required. By constraining the OLE geometry to the xy-plane, the length of the contact wire in each span has been shortened relative to the true wire length when the wire is staggered. In the xy-plane, the difference between the contact wire length and the true staggered length is small and can be calculated using

$$F(x;s_0) = \left(\sqrt{1+\left(\frac{s_0}{x}\right)^2} - 1\right), \tag{3.33}$$

where x is the span length and s_0 is the stagger amount. Since the derivative

$$F'(x;s_0) = -\frac{s_0^2}{x^2\sqrt{x^2+s_0^2}}, \tag{3.34}$$

is negative definite away from the origin, this difference decreases with the cube of the span length. The magnitude of the difference can be seen in Figure 3.17 when a maximum stagger of 400 mm is used.

The messenger wire is constrained against all displacements at the first mast location and displacements in the vertical direction at subsequent mast locations are constrained, replicating support provided by the registration arms at each mast. The transmission of mechanical waves between spans is permitted by leaving the wire at the subsequent supports free. Tension is applied in the longitudinal x-direction at the final messenger wire node.

The contact wire is constrained against x-direction displacements at the first node only, in contrast to the messenger wire and is constrained against rotations about the z-axis at the end points. Tension is applied in the x-direction in the same manner as the messenger wire.

Settling step

Once the first load step is complete, nodal positions and applied boundary conditions are retained as the initial conditions for the settling step. During the first load step, nodal accelerations are incurred during the sagging of the overhead line. This is rectified by maintaining the boundary conditions from the previous load step and the residual accelerations are allowed to decay. Since this load is static, time integration effects are turned off ensuring the effects

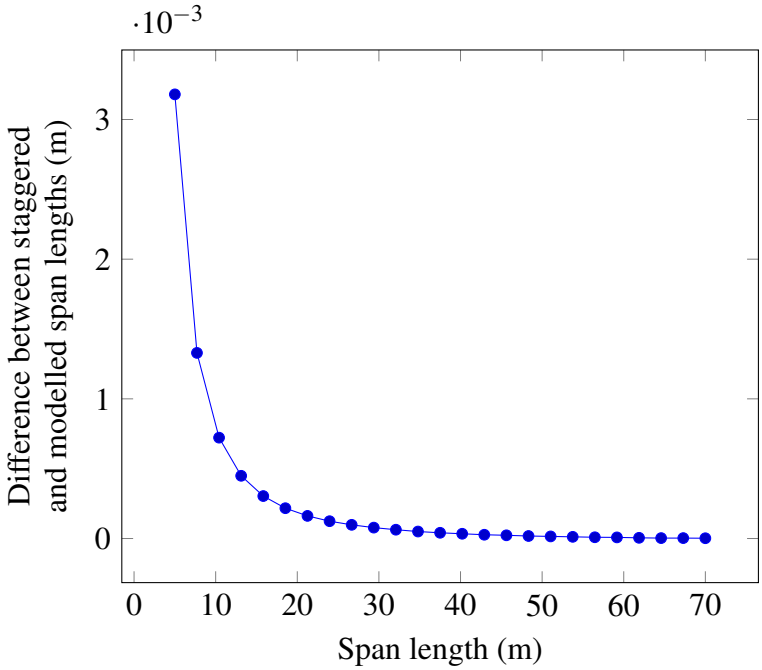

Fig. 3.17 Difference between the length of a contact wire in the plane and a staggered contact wire with increasing span length.

of removing residual accelerations don't affect the subsequent load step. No displacements of the OLE geometry are applied in this load step so the desired geometry from the previous load step is maintained.

Pantograph model

Once the overhead line geometry is created, the model of the pantograph is introduced. The process to create the pantograph model is substantially more straightforward than creating the overhead line geometry. A lumped–mass representation of the pantograph, shown in Figure 3.18a and keypoints are created in a 'T'–shape to represent each of the lumped masses as shown in Figure 3.18b. A 'T'-shape is used rather than a single vertical line of keypoints to ensure contact between the pantograph and the contact wire in the lateral direction. A single vertical line of keypoints would allow for the contact wire to 'fall off' the node representing the pantograph. The parameter values used for each element of the pantograph are given in Table 3.5.

The three-mass representation was chosen over the simpler two-mass to be able to represent the pantograph arm opening and closing at the knuckle. Whilst the two-mass model was sufficient for performing simulations with a level contact wire where the change in the

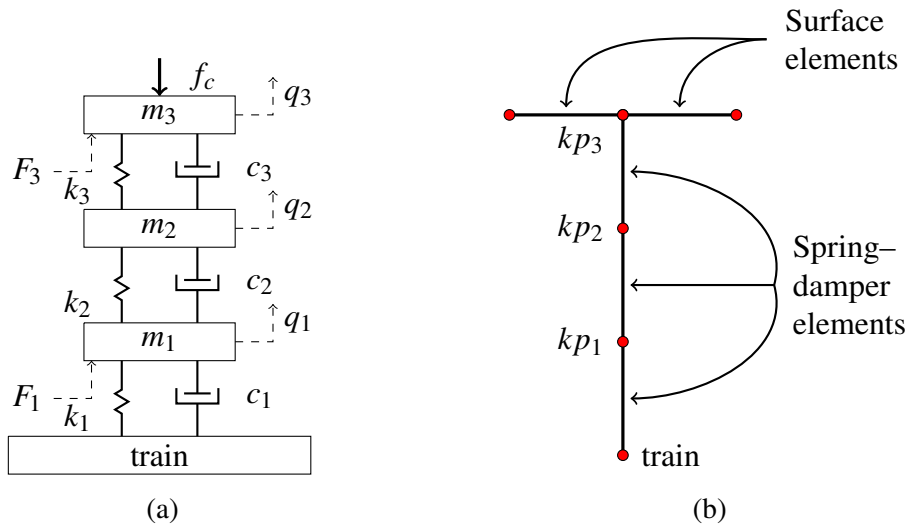

Fig. 3.18 (a) Three degrees of freedom lumped mass-spring representation of the pantograph. The displacement of mass i is given by q_i, and the force F_1 is the static uplift force taken to be 70 N. The aerodynamic force F_3 in this case is given by $0.01031v_p^2$ N. (b) The element representation of the lumped mass model created in ANSYS. Each of the keypoints kp_i, correspond to mass i of the lumped mass model with the bottom keypoint taking the place of the train roof where the pantograph is mounted.

contact wire height due to presag (60 mm) is small relative to the span length ($\sim 0.1\%$), the lack of a third mass caused breakdowns in the simulation when the contact wire height change was much larger ($\sim 10\%$ of the span length).

As with the overhead line model, constraints are applied to the pantograph model to ensure the correct dynamic behaviour during the dynamic simulation. During the static load step, all lines and keypoints of the pantograph are constrained against rotations in the lateral z-direction ensuring the pantograph remains upright and all accelerations are in the vertical direction. The bottom keypoint is constrained against displacements in the y-direction as displacements of the pantograph mounting due to vibrations from the train suspension are small relative to the vertical displacements of the pantograph head.

During this load step, gravity brings the contact wire into contact with the collector head of the pantograph. Temporarily constraining the collector head keypoints against displacements in the vertical direction allows the contact wire sag to bring the contact wire into contact with the collector head rather than the uplift forces of the pantograph pushing up against the contact wire reducing the initial contact force and pantograph uplift prior to simulations of the dynamic interaction.

Table 3.5 Parameter values for the lumped-mass model of the pantograph.

Mass (kg)	Damping (N s/m)	Stiffness (kN/m)
$m_1 = 3.53$	$c_1 = 32.6$	$k_1 = 0$
$m_2 = 7.5$	$c_2 = 0$	$k_2 = 5$
$m_3 = 5.3$	$c_3 = 70$	$k_3 = 6.3$

No changes are made to the constraints applied to the pantograph model during the settling step and similar to the contact wire, no changes in the geometry are made during this step. Once this step is complete all residual velocities and accelerations of the pantograph caused by bringing it into contact with the contact wire have decayed to zero.

The outcome of the previous static and settling load steps are an overhead line geometry correctly tensioned and fully settled, in contact with the pantograph collector head ready for the dynamic load step.

Dynamic load step

The two previous steps generate a tensioned and settled overhead line system ready for a velocity to be applied to the pantograph and for the interaction between the pantograph and catenary to be simulated. The third load step occurs from the time the previous load step finished to the time the pantograph reaches the final span in the working section, thus each simulation had a different end point. This was chosen to avoid simulating an extensive number of spans, such as those in Figure 3.23a, when the output from them would be unused. Thus the time required is given by

$$T_{\text{tot}} = t_{\text{end}} + \frac{L_{\text{con}} - P_{\text{sep}}}{v_{\text{p}}}, \tag{3.35}$$

where L_{con} is the end of the working section of the model and v_{p} is the pantograph velocity. In the case of multiple pantograph operation, P_{sep} gives the pantograph separation.

A transient analysis of the catenary pantograph interaction is performed with a fixed time step determined by the frequency of the data collection. Typically the frequency of interest is 20 Hz as required by BS EN 50318 [14], however to better understand the high frequency dynamic effects, frequencies up to 80 Hz are considered in Chapter 8. Data collection was performed at a frequency of 200 Hz giving a time step of 0.005 s, more than double the frequency of interest, and was chosen to match the data collection frequency of the test track measurements used in the validation step. Given the pantograph velocity was taken to be

200 km/h, the time step size corresponded to a pantograph translation of 0.278 m during each time step, smaller than the 0.5 m mesh element size. This was chosen to ensure that during each time step, the elements forming the pantograph carbon followed the elements forming the contact wire during the height transition. Figure 3.19 shows the displacement of the pantograph during each time step relative to the mesh sizing of the contact wire.

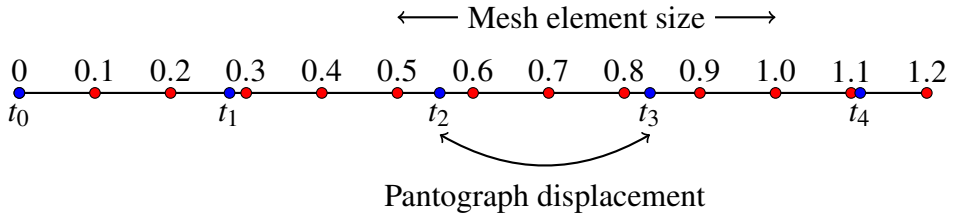

Fig. 3.19 Mesh element sizing and pantograph displacement during each time step. During each time step, the displacement of the pantograph is less than the mesh element size.

Damping of the overhead line is applied globally using Rayleigh damping of the form

$$\mathbf{C} = \nu\mathbf{M} + \eta\mathbf{K}, \tag{3.36}$$

where $\nu = 0.0055$ s^{-1} and $\eta = 0.011$ s, are the mass and stiffness proportional damping factors respectively [241].

During the simulation of the catenary pantograph interaction, six of the pre-defined element types in ANSYS are used. These are:

- BEAM189: A three–node Timoshenko beam element, used to represent the messenger and contact wires. The three–node element is defined by a quadratic shape function allowing for nonlinear deformation of the elements between nodal points. Two of these elements are also used to model the contact strips on the collector head. By using a pair of beam elements, contact between the contact wire and pantograph can be modelled as the contact between two crossed beams.

  Material properties required by the BEAM189 element include the Young's Modulus, E, Poisson's ratio, ν and the material density ρ. These are defined by the inputs provided by the user in the inputs package. The contact strips on the collector head are given the default values for E and ν, and the density is set to zero as lumped-masses are used in the pantograph model.

- COMBIN14: A linear spring-damper, used for the tensioning springs applied to the messenger wire at the ends of each span. The spring stiffness, k, and the initial length,

ℓ, are defined by the process given in Section 3.2.3. As well as being used for the tensioning springs in each of the overhead line spans, the COMBIN14 element is also used to represent the spring-dampers in the pantograph where the required real constants are the spring stiffnesses, k, and damping coefficients, c, given in Table 3.5.

- COMBIN39: A nonlinear spring is used to model the droppers allowing for different behaviours to be determined based on the dropper being in compression or under tension. Typically a dropper is under tension due to the droppers supporting the weight of the contact wire, but during train passage, uplift caused by the pantograph causes the droppers to buckle thus the element is required to satisfy both these behaviours.

  Real constants required include a pair of coordinates to define the force-extension curve. Given the two different behaviours, two different dropper stiffnesses are required, k_{tens} and k_{comp}. Under compressive load, a dropper provides no resistance to vertical uplift and buckles. This behaviour can be represented using the COMBIN39 element option to set the dropper compressive stiffness to zero.

- MASS21: Structural mass elements are used for all elements of the model represented by lumped masses. These include the registration arms, dropper clamps and the lumped-masses of the pantograph model. The material properties required by the element are given by the initial data inputs.

- CONTA176/TARGE170: Line-to-line 3D contact elements and 3D target elements are paired together to allow for the interaction between the contact wire and pantograph to be modelled. The elements are used to detect contact between the respective surfaces and are overlaid onto the BEAM 189 elements sharing the same nodes. Contact is defined using the penalty function algorithm with a contact stiffness of 50 kN [14] between the CONTA176 and TARGE170 elements. They are also given a common radius which is taken to be the contact wire radius for simplicity.

The full list of physical constants (referred to as 'real constants' in the ANSYS literature) given for the element types described above are given in Table 3.6.

Having defined the element types and the required physical constants for each of them, the 'pre-tensioned' coordinates generated in Section 3.2.3 are used as coordinates for the keypoints in ANSYS. Beginning with the messenger wire, and then the contact wire, the keypoints are ordered sequentially in the positive x-direction, with a keypoint located at each end of a dropper and for the registration arms between each span. Further keypoints are created between the messenger wire and the messenger wire tensioning springs. The

Table 3.6 Parameter values for the finite element representation of the overhead line equipment.

Application	Element type	Physical constant
Contact wire	BEAM189	Young's Modulus, $E = 117$ GPa, Poisson's ratio, 0.33, Mass per unit length, 1.07 kg/m
Messenger wire	BEAM189	Young's Modulus, $E = 100$ GPa, Poisson's ratio, 0.34, Mass per unit length, 0.6 kg/m
Droppers	COMBIN39	Stiffness in tension, 1260 kN/m
Clamps	MASS21	Dropper mass, 0.093 kg/m, Contact and messenger wire clamps, 0.15 kg, Registration arms 0.924 kg
Contact elements	CONTA176, TARGE170	Contact radius, 13.2 mm

pantograph keypoints are created in the positive y-direction after the overhead line keypoints are created.

Connecting the keypoints of the contact wire and messenger wire are straight lines, that are also numbered sequentially beginning with the messenger wire, the contact wire, the droppers and finally the pantograph. These nominally straight lines under load deform quadratically according to the defined behaviour of the BEAM189 element, generating the correct overhead line curvature. Each of the straight lines represents a single element. Meshing of the created straight lines is performed and the element types and physical constants are assigned to the appropriate lines and lumped-masses and CONTA176 elements are overlaid on the pantograph collector head, whilst TARGE170 elements are overlaid on the contact wire.

The boundary conditions maintained from the previous load step are altered to allow for the interaction between the pantograph and contact wire. To allow this, the constraint against y-direction displacements of the collector head is removed and the constraint against x-direction displacements of all pantograph keypoints is removed. Finally an x-direction velocity is applied to each of the pantograph nodes.

The outcome of this load step is a transient analysis of the catenary pantograph interaction for a given train velocity. Dynamic behaviour is recorded at each sub-step and the nodal and element data for both the pantograph and overhead line is retained for data post-processing.

Mechanical parameters investigated

To investigate the dynamic response of the catenary pantograph interaction to mechanical parameter variation, the varied parameters were split between those of the overhead line equipment and those of the pantograph. With respect to the overhead line equipment, the chosen parameters were:

- Messenger and contact wire tensions, to assess the effects of either increased wire sag when the tension is reduced (this situation represents thermal expansion or loss of effective tension over the system life), or decreased wire sag as an approach to improve the dynamic performance.
- Contact wire mass, to represent (i) the wear state of the contact wire over the lifetime of the equipment, and (ii) the response to an increase in the contact wire mass to increase the system resilience to wear, thus prolonging the system life.

Parameters varied with respect to the pantograph include:

- The mass of the pantograph collector head to demonstrate the requirement that the pantograph head should be minimised to ensure good dynamic performance.
- The mass of the frame supporting the pantograph collector head.
- The stiffness of the bar connecting the pantograph collector head to the pantograph collector frame.
- The static uplift applied at the base of the pantograph necessary to ensure good contact at the contact interface.

Parameters such as the dropper clamp mass can be investigated, however to correctly assess the dynamic response for a train speed of 200 km/h, the required simulation time step would be approximately 0.5 ms, or equivalently a data collection frequency of approximately 2 kHz. Since the mass of the clamps is small (150 g) relative to the mass of the contact wire and the pantograph collector head, it is unlikely that the mass of the dropper clamps has a significant effect on the dynamic response of the system. As such, dropper clamp mass was not investigated here.

The geometry of the overhead line can also be configured. In this regard, a dropper was removed to represent the system response to a dropper failure (either due to the dropper buckling or breakage), and also the number of droppers in each span was increased to determine if the contact force variation as the line speed increases can be improved by reducing the unsupported contact wire lengths.

Data post-processing and generation of outputs

Due to recording the nodal and element solutions at each sub-step during the dynamic step, a substantial results file is created, typically of order 300 GB. Outputs were generated from this data file using the ANSYS GUI or through the use of a macro to generate useful outputs such as the contact force at each time step.

Data towards the end of a wire run is not included in the data analysis due to end effects. At the beginning of a simulation, due to the change in the pantograph boundary conditions as the dynamic load step begins, settling occurs between the pantograph and contact wire before the interaction becomes fully realised. Towards the end of the simulation, mechanical waves reflected back from the final support interact with the waves sent out from the point of contact. To avoid this, the substantial number of spans after the working section, as shown in each of the geometries in Figure 3.23 for example, are used to allow the pantograph to reach the end of the working section before the reflected wave. This differs from a real system where the length of the wire run is limited and therefore the catenary pantograph interaction would be affected by the reflected wave from the support at the end of the wire run. The calculation to determine the required number of spans depends on the wave propagation speed in the contact wire given by

$$c_s = \sqrt{\frac{T_{\text{con}}}{m}}, \tag{3.37}$$

where T_{con} is the contact wire tension and m, the mass per unit length.

Manual post–processing of the results was initially performed using the ANSYS GUI. The results displayed using this method allow for the results of the full finite element model to be displayed at each time step. Whilst this method is useful for considering the results in each time step, given the significantly large number of time steps used during each simulation, it came apparent that traversing each time step and recording the necessary data to predict the dynamics over time is prohibitively time consuming.

Collecting useful data from the results file

To generate data outputs for the entire time of the simulation, macro–based post–processing was used to export useful results such as the contact force and pantograph uplift at each time step. The contact force can be derived from the penetration between the CONTA176 and TARGE170 elements at each time step, which together with the contact stiffness between the elements gives the contact force using Hooke's Law. Whilst ANSYS records the contact force at each time step despite the contact force equalling zero everywhere away from the

point of contact, the maximum contact pressure, at the contact point, can be extracted from the data and recorded using an Element Table. The vertical position of the pantograph head was recorded at each time step, and was extracted during the post–processing step to allow the contact wire uplift to be observed. At each time step, the vertical nodal displacements of the nodes representing the contact wire supports were extracted to examine the contact wire support uplifts as the pantograph passed each location.

Filtering the data

Data collection during the simulation is performed at a frequency of 200 Hz. This is done to keep the simulation sub-steps small and to aid in the convergence of the simulation at each time step. Collecting data at a high frequency also captures high frequency behaviour in the model such as sudden shocks due to overly stiff registration arms for example. Typically however, the data is filtered using a low-pass filter with a cut-off frequency of 20 Hz, during the validation process. This attenuation of higher frequencies causes high frequency behaviour to be lost during the filtering process, so analysis of the contact force at frequencies up to 80 Hz is performed in Chapter 8.

To perform the low-pass filter, a digital finite impulse response (FIR) filter is implemented in MATLAB using the 'designfilt' procedure. Alternative methods including the use of the Fast Fourier Transform in Excel were considered however the Excel procedure limits the number of datum points to be transformed to a power of two. This restricts the amount of data to be considered. For example, a contact force output with, say 3000 entries, only the first $2^{11} = 2048$, or 68.3% of the data can be transformed. The filter procedure in MATLAB does not have this limitation and also requires less user input during the filtering process.

The sampling frequency used was 200 Hz to match the frequency of the data collection and the cutoff frequency was 20 Hz. To achieve the required level of performance, a filter order of 300 was used and the filter length was 301 samples. Since the filter order was 300, this corresponded to a group delay of 150 samples which was accounted for by a shift of the transformed data. The linear group delay was a major factor in the choice of a FIR filter over an infinite impulse response filter (IIR) which display nonlinear group delay. The magnitude response for the low-pass filter is given in Figure 3.20.

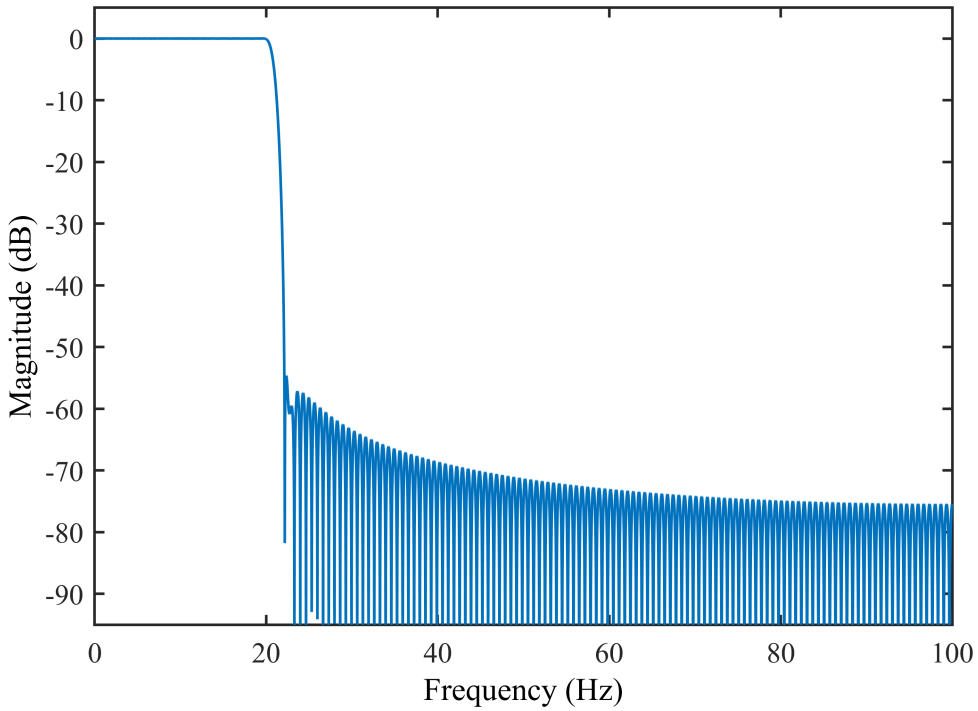

Fig. 3.20 Magnitude response function for the low-pass filter used.

3.3 Aerodynamic loading of a railway overhead line system

In Section 3.1, a description of the methodology to determine the aerodynamic forces on a contact wire in an incident flow was described. In this section, the methodology to apply those aerodynamic loads to a model of the overhead line system is discussed. The proposed method also seeks to predict what effects may be caused by an incident wind flow on the catenary pantograph interaction. Identification of the possibility of unwanted dynamic effects would suggest more research is necessary in this area as it currently a not well researched topic.

To allow for the effects of aerodynamic loading on an overhead line system to be investigated, building upon the finite element model presented in the previous section, modifications are made to allow for 3D behaviour. To allow for this behaviour, constraints applied to the pantograph and overhead line that fix the dynamics in the plane are removed. This allows for displacement of the contact wire and pantograph components in the lateral direction orthogonal to the motion of the pantograph. Since lateral displacements of a train are small relative to the lateral deflections of the contact wire, the boundary condition placed

on the base of the pantograph is maintained, as are the boundary conditions fixing the lateral position of the overhead line supports. This was done as lateral deflection of a rigid support is similarly small to the deflection of the train body under sidewinds.

On open areas of the network, the entire system can be considered to be under the influence of the aerodynamic flow. However, sections of the network are protected from sidewinds, either by tunnels, embankments or bridges. For this reason, two cases studies are considered: the effect of sudden aerodynamic loads on an overhead line leaving a tunnel, and when a small section of an overhead line is protected by the supports of an overbridge. Both of these cases are considered to extend the applicability of the predicted dynamics, as well as to identify what effects and degradation of the catenary pantograph interaction, if any, may occur due to sidewinds.

3.3.1 Simulation parameters

To assess the effect due to aerodynamic loads on the catenary pantograph interaction, the geometry and mechanical parameters of the overhead line and pantograph are fixed in each simulation whilst the variables altered are:

- The magnitude of the aerodynamic load, and
- The frequency of the oscillations of the aerodynamic lift force.

Each of the these were calculated from the simulations of the flow around a contact wire. The magnitude of the aerodynamic load was considered to predict the dynamic response of the system as the wind speed increases. With increasing wind speed, the aerodynamic pressure on the contact wire increases, thus increasing the magnitude of the resultant force on the system. A larger drag force is predicted to increase the contact wire deflection, and lead to a larger risk of dewirement. Similarly, the increased wind speed increases the magnitude of the aerodynamic lift which is likely to cause high frequency oscillations of the contact wire resulting in contact loss. This contact loss causes arcing at the contact interface degrading the contact surfaces hastening the onset of fatigue.

To apply the wind load to the overhead line, a sinusoidal function is applied to the nodal points of the model components representing the contact wire, messenger wires and the pantograph. This sinusoid has amplitude and frequency derived from the methodology presented in Section 3.1, with the frequency taken to be zero in the case of aerodynamic drag, i.e., aerodynamic drag was considered a static load on the system, whilst aerodynamic lift was taken to be a dynamic behaviour.

The output generated in the previous section, contact force and uplift of the contact wire at supports, is also the generated output here. The resultant contact force of a catenary pantograph interaction is predicted to experience a larger variation due to the incident flow, degrading the contact performance of the system. The uplift at the supports is also of value as an increase in the wire uplift risks breaching the electrical clearances between the contact wire and civil structures such as bridges and tunnels. Breaching these clearances poses a risk of arcing to structures. Since the model is also unconstrained to exhibit behaviour in the lateral direction, the lateral displacements of the node corresponding to midspan is also recorded to measure the greatest blow–off due to aerodynamic drag.

3.4 Effect of contact wire height variation on the catenary pantograph interaction

The previous sections considered an overhead line with a constant wire height, that is the wire height at the supports was constant, whilst height variations due to were wire sag were small relative to the span length. In this section the methodology with respect to investigating the effect of introducing large scale wire height changes, and thus inducing a gradient in the contact wire, is presented.

3.4.1 Overhead line geometries used

Three models are adopted to assess the effect of wire height changes on the dynamic catenary pantograph interaction, whilst a level wire height model with a varying system height is used to highlight core effects due to dropper height changes. In this section, the models used are presented.

Model 1

Before investigating the influence of gradients on the catenary pantograph interaction, validation of the model for changing wire heights was performed. This was performed using data provided by track tests using a British Rail Class 395 high speed electric multiple unit at Network Rail's Melton Rail Innovation and Development Centre (RIDC).

Using data provided from track tests at the RIDC was advantageous as the full overhead line geometry is known in contrast to OLE installed on the mainline where typically wire heights and locations are only known at supports. As such a finite element representation of

the overhead line was created using the method described in the Section 3.2.3 and is shown in Figure 3.21.

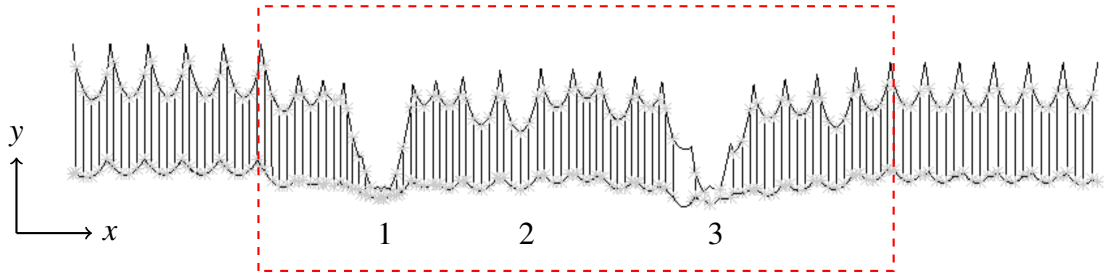

Fig. 3.21 Vertically exaggerated and horizontally compressed test track overhead line geometry created in ANSYS. Here, 1 m vertically corresponds to 120 m horizontally. The dashed box indicates the section of overhead line data analysis was performed over. The spans not included in the box were included to account for end effects.

The wire run used in the validation consisted of 22 spans over a length of 826 m and the contact wire height ranged from a maximum of 4.46 m down to 4.08 m. As evident from Figure 3.21, span lengths were inconsistent with the longest a span of 65 m (location 2) and a smallest of 9 m (location 1) where registration arms were fixed either side of a bridge to better resist dynamic uplift in the wire during train passage.

Given the nature of the overhead line being used primarily as a test line, dropper spacing is also inconsistent, most evident before the second bridge location, shown as location 3 in Figure 3.21. Here, a dropper had been removed to investigate the effect of missing droppers in an otherwise conventional overhead line, thus causing the contact wire to sag further than usual. This had the advantage of providing a larger change in contact wire height than would otherwise have been expected, useful for validating the model over bigger changes in contact wire height.

Model 2

Whilst model 1 was used only for the validation case against test track data, model 2 was used to investigate a range of different wire gradients in otherwise identical spans of overhead line. In this model, the span length was taken to be 60 m, and the total wire height change was 1.2 m. To achieve the wire height change, only the messenger wire support height was changed, and the lengths of the droppers were unaltered. The lengths and dropper spacings are given in Table 3.7. The aim was to allow study of the core dynamic effects due to different

wire gradients while avoiding the complexity of the more realistic geometries in models 3 and 4.

Table 3.7 Dropper locations and their lengths used in model 2. All entries given in m.

Dropper	1	2	3	4	5
Location from start of span	5.5	17.75	30	42.25	54.5
Length	1.09	0.94	0.845	0.94	1.09

In this model, the messenger wire support height was chosen to induce a gradient in the contact wire exceeding the current maximum permitted wire gradient of 1:500 according to BS EN 50119 [26]. A schematic showing the contact wire height in the case of a wire gradient of 1:100, is shown in Figure 3.22 indicating the level, and gradient spans. In each gradient case, the schematic is similar, but with the 'gradient studied' section extended over sufficient spans to achieve the required height change of 1.2 m.

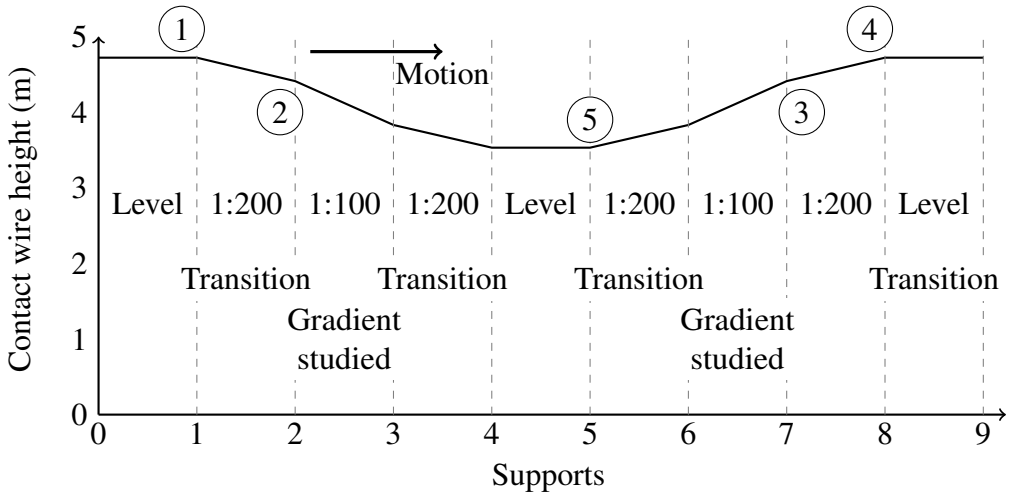

Fig. 3.22 Wire schematic indicating the contact wire height when the wire gradient is 1:100. Mast locations are indicated by dashed vertical lines, and the contact wire gradient in each span is given. Each of the gradients studied has a similar schematic, with an increased number of 'Gradient studied' spans used in each case. Sharp transitions are exaggerated by the scaling (120:1 between horizontal and vertical scales) and were not present in reality.

Within each wire run, a transition span between the level spans and the maximum gradient span is used. In these spans, the wire gradient is half that of the maximum wire gradient as required by BS EN 50119 [26], e.g., when the maximum wire gradient was 1:200, the gradient in the transition span was 1:400. In each simulation, there are four of these transitions, as

shown in Figure 3.22. Table 3.8 gives the gradients used throughout as well as the total length of each wire run for each simulation.

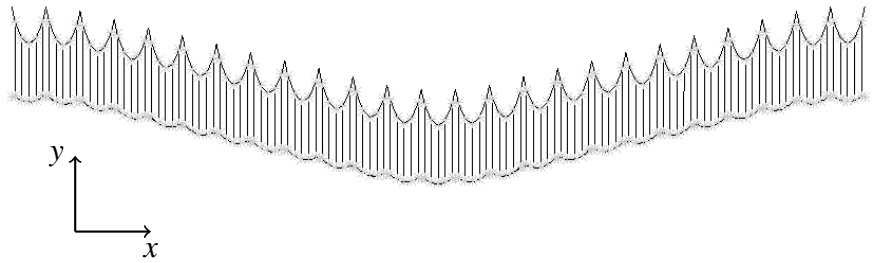

(a) Wire geometry when the wire gradient is 1:500.

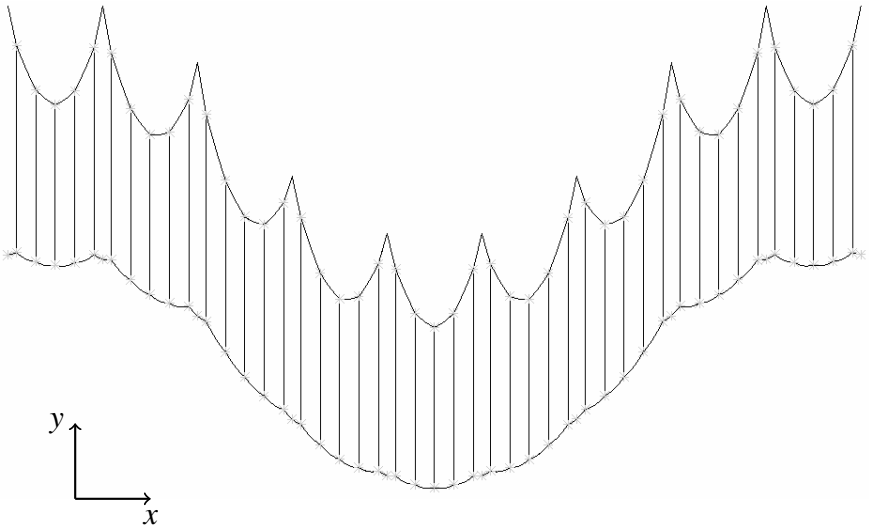

(b) Wire geometry when the wire gradient is 1:100.

Fig. 3.23 Two of the wire geometries used representative of the different geometries considered. The vertical scale is exaggerated relative to the horizontal scale with 1 m vertically corresponding to 120 m vertically.

Figures 3.23a and 3.23b show the geometries for the cases where the wire gradient was 1:500 and 1:100 respectively. The necessary spans following the height variation to account for any end effects are clearly shown to become significant as the gradient is increased. Due to these spans only being included to avoid unwanted boundary effects caused by wave reflections at the end of the wire run, simulations were halted once the height change section had been completed to avoid unnecessary computational time.

Table 3.8 Maximum gradient, number of spans, total wire length, and working section ends used for model 2. The working section begins at 300 m in each case.

Maximum gradient	Number of spans at maximum gradient	Number of spans used in simulation	Total length of wire run (km)	Working section end (m)
1:500	9	46	2.76	1800
1:400	7	40	2.40	1560
1:300	5	34	2.04	1320
1:200	3	28	1.68	1080
1:100	1	22	1.32	840

Model 3

Model 2 introduced variable wire heights in otherwise identical spans of overhead line. In model 3, a reduction in the dropper lengths and thus the system height is introduced. Figure 3.24 shows the wire profile when the contact wire gradient is 1:100 and is designed to be consistent with the contact wire profile presented in model 2. The dropper lengths are reduced to allow the messenger wire to drop down further than the contact wire. The reduced dropper lengths in the central level span are approximately 50% of those in the corresponding level span in model 2 and represent a more realistic installation where best use of the available space is made by using appropriately sized droppers.

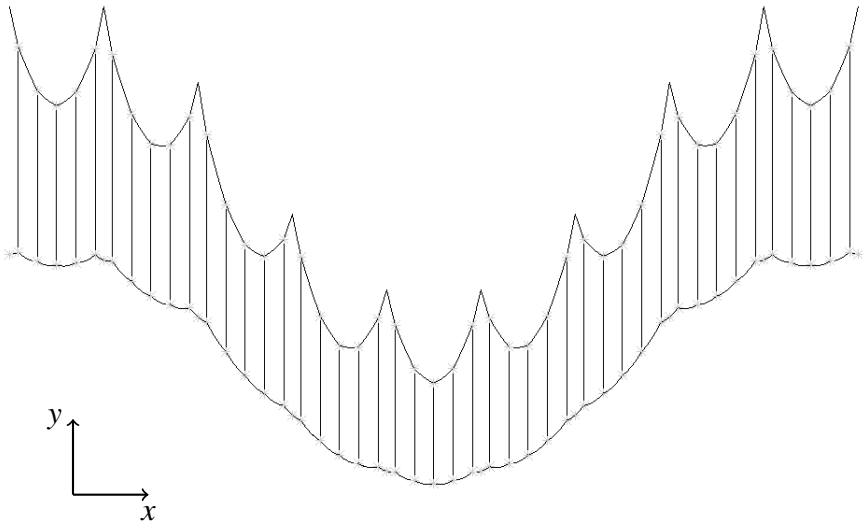

Fig. 3.24 Overhead line geometry with a reduction in the system and contact wire heights.

Model 4

The final overhead line geometry considered here is a reduction in the system height but maintaining the contact wire height. Using the geometry shown in Figure 3.25, the influence of the dropper lengths can be determined.

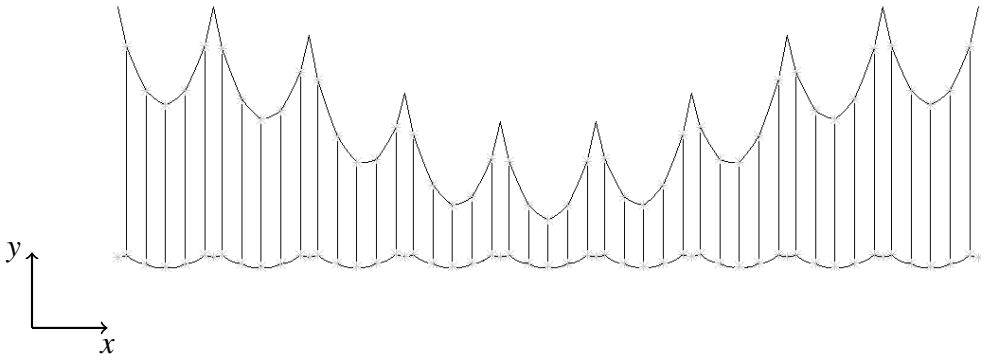

Fig. 3.25 Overhead line geometry with a reduction in the system height only.

Aside from the lengths of the droppers in models 3 and 4, the parameters from model 2 such as wire tension or material properties were left unchanged.

Data analysis

Data analysis of the output generated for each of the four models presented in this section is performed in the same manner as that discussed in Section 3.2.4, however a new technique is introduced to study the dynamics due to wire gradients. Since a large number of spans are required to achieve the necessary gradients, core dynamic behaviours are masked when applying the usual statistical analysis. As such, a windowing technique is adopted. The windowing technique is used to analyse the data over smaller lengths than used in the previous analysis. Since the length of all of the spans used in models 2,3 and 4 was 60 m, the window length was set to cover the corresponding number of data samples. This was 216, since each time step corresponded to a pantograph travel distance of 0.278 m. The window was also allowed to 'slide' over every datum point rather than just consider each individual span allowing for closer analysis of the behaviour of discrete sections of the overhead line. The windowing technique is demonstrated in Figure 3.26 using a data set containing 7 elements and a window of length 3.

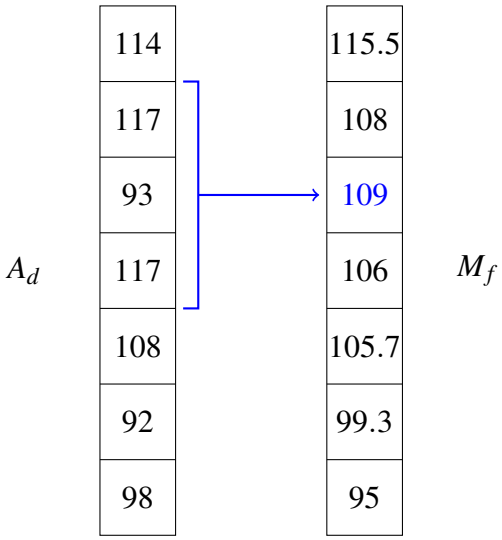

Fig. 3.26 Example of the windowing technique with window length 3. The window averages the data set A_d over three datum points to create the data set M_f. The method is used to analyse discrete behaviours during the catenary pantograph interaction.

3.5 Research work flow

Figure 3.27 gives the workstream adopted throughout this project.

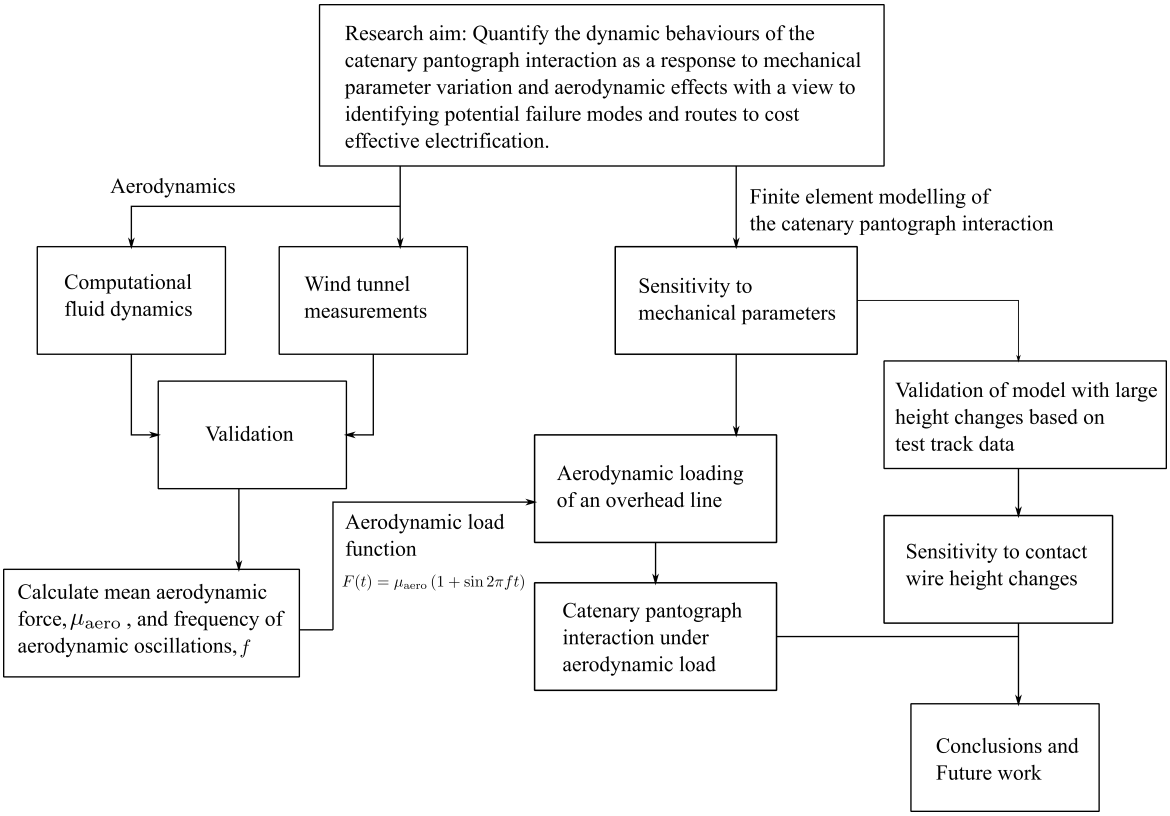

Fig. 3.27 Workstream highlighting the key areas of work performed.

Chapter 4

Dynamic overhead line modelling

4.1 Model development

The research in this thesis builds upon a previously validated and published model in [241] and extends the model in two way:

1. New wire configurations are explored, particularly inclines, using the originally adopted physics model of the pantograph to overhead line system.

2. The model is transitioned from a 2D to a 3D system with the addition of side loading from the wind.

This Chapter describes the addition of specific new features. In addition, some of the original modelling assumptions such as neglection frictional forces at the contact interface are explored to ensure their validity for the more demanding modelling reported in this thesis.

4.1.1 Addition of friction between the pantograph and contact wire

The previous model, developed in [241], included no friction between the contact wire and pantograph. Friction may have a greater effect on the inclined wires explored in the current research than in the previous level wire configurations, so to determine the effect friction has the on the catenary pantograph interaction, the model was updated to allow for this. The frictional model adopted represents Coulomb friction with a single coefficient of friction μ as the friction is assumed to be isotropic, that is friction between the contact surfaces would be equal irrespective of the direction of travel. Implementation of the model in ANSYS is provided using the `TB` command along with specification of the coefficient of friction after

the contact surfaces have been specified. Section 4.3.3 discusses the sensitivity of the finite element model to various non-zero friction coefficients.

4.1.2 Aerodynamic load input to a dynamic finite element model

The aerodynamic load on an overhead line is quantified in Chapter 5 and to implement the aerodynamic forces into the overhead line model in Chapter 7, the existing model was developed to allow for this functionality extending it from consideration of pantograph loads alone.

The aerodynamic force was applied using a transient function, given by Equation 4.1, which defines a value at each time step of the simulation based on the mean aerodynamic lift and drag forces and the relevant frequency of the aerodynamic oscillations as calculated in Chapter 5. This method was adopted to avoid requiring the definition of individual aerodynamic loads at each time step of the simulation in the model input file. The aerodynamic load function can then be applied to the desired nodal coordinates of the model before the transient simulation of catenary pantograph interaction is performed. The function can also define different regimes with different behaviour, for example gusting can be implemented with a Gaussian of small variance superimposed on the sinusoid approximating the aerodynamic force, given by

$$F(t) = \mu_{\text{aero}} \left(1 + \sin(2\pi f t)\right), \tag{4.1}$$

where μ_{aero} was the mean aerodynamic force and f is the oscillation frequency for the corresponding lift force, as calculated in Chapter 5. The form of Equation 4.1 was chosen to represent the sinusoidal lift force shown in Figure 5.14 in Chapter 5. In the case of the drag force, the oscillation frequency was zero and the drag load can be taken to be static.

To reduce the number of degrees of freedom in the previous simulations, lateral deflections of the overhead line in the original model were constrained so that all motion occurred in the vertical plane. To account for deflections due to aerodynamic drag, the constraints are relaxed and away from the supports at mast locations, the geometry is now free to displace in all directions as a fully 3D structure. The aerodynamic force was modelled in this way using the function editor application in ANSYS rather than creating a load step for a new aerodynamic load to be applied at every time step, drastically reducing the computation time. The aerodynamic force is applied to the contact wire nodes in the lateral z–direction across the track in the case of the drag force and in the vertical y–direction in the case of the lift force, as shown in Figure 4.1. No aerodynamic loads along the track (i.e., in the x–direction) were considered.

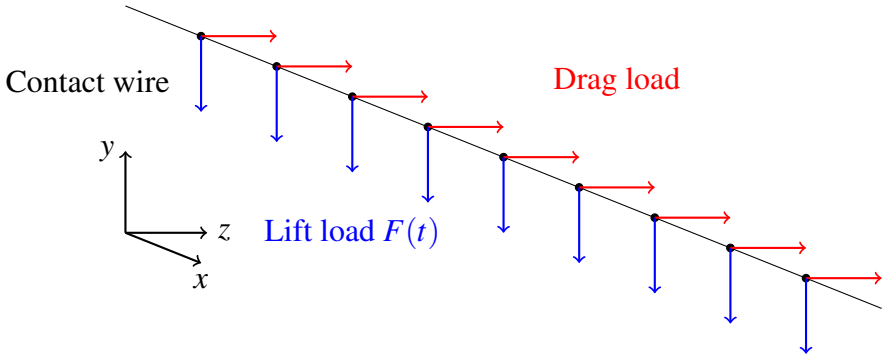

Fig. 4.1 Schematic of aerodynamic loads applied to the contact wire nodes to represent the lift and drag forces calculated in Chapter 5.

4.2 Validation process

Model validation is performed in accordance with the methodology described in BS EN 50318 [287]. According to BS EN 50318, model validation is performed in two steps:

Step 1: Analysis of the predicted overhead line dynamics of a reference model with a given overhead line geometry and pantograph model.

Step 2: Comparison of modelling predictions against test track data measured in accordance with BS EN 50317 [10].

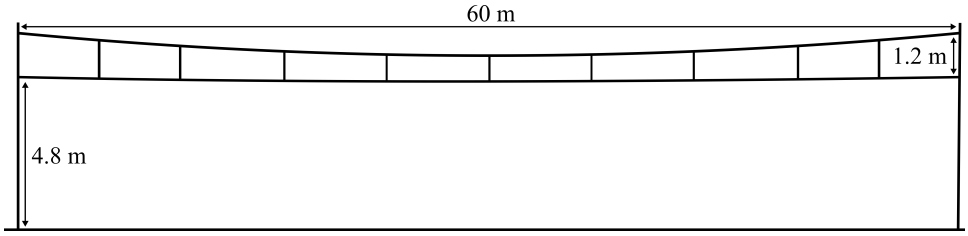

Fig. 4.2 A representative span of the reference geometry used for Step 1 of model validation where the dropper positions and lengths are given in Table 4.1. Components such as registration arms and supports are omitted here for clarity.

The validation reference model used in Step 1 considers an idealised overhead line geometry consisting of ten identical 60 m spans under which a single pantograph passes, and statistical analysis is then performed over the central two spans to discount unwanted end effects, such as reflected wave behaviour. Figure 4.2 gives the idealised geometry used for each span in the reference model. Each of the ten spans are identical, and the positioning of the droppers in each span are given in Table 4.1.

Table 4.1 Dropper positions and lengths as described in the reference model in BS EN 50318. All values given in m.

Dropper	1	2	3	4	5	6	7	8	9
Position	5	10.5	17	23.5	30	36.5	43	49.5	55
Length	0.986	0.805	0.648	0.554	0.523	0.554	0.648	0.805	0.986

Throughout the reference case, the standard specifies that the contact wire has a mass per unit length of 1.35 kg/m and is tensioned with an axial load of 20 kN. Similarly, the messenger wire has a mass per unit length of 1.07 kg/m and is tensioned with a load of 16.5 kN. Self–weight of the droppers and clamps connecting the droppers to the messenger and contact wires is neglected, however the droppers do have a stiffness of 100 kN/m in tension and has zero stiffness in compression, to accurately represent dropper buckling during pantograph passage.

To assess the accuracy of the modelling predictions, the following statistical parameters are compared between the BS EN 50318 reference model and the model predictions:

- The arithmetic mean of the contact force, F_m.
- The contact force standard deviation, σ.
- Discrete maxima and minima of the contact force, $F_{D_{\max}}$, and $F_{D_{\min}}$ respectively.
- Statistical maxima, $F_{S_{\max}}$, and minima, $F_{S_{\min}}$, of the contact force given by $F_m \pm 3\sigma$.

For each of the above quantities, BS EN 50318 defines an acceptable range of for which the output can be considered valid when the train speeds are either 250 or 300 km/h. The raw modelling output is then passed through a minimum sixth–order 20 Hz low–pass filter to remove high the high frequency behaviour. To ensure that end effects due to reflected mechanical waves and the pantograph coming into contact with the contact wire are not included in the analysed data, only the fifth and sixth spans are used for data analysis.

For comparison against the reference model, the specifications for the pantograph model are also given in BS EN 50318. In this case, the pantograph is represented by a mass–spring–damper system, given in Figure 4.3. The standard specifies that aerodynamic loads on the pantograph are assumed to be zero and the uplift force applied by the pneumatic actuator at the base of the real pantograph is represented by the 120 N load applied to the bottom mass. The base of the pantograph is assumed to be fixed and that vertical vibrations caused by movement of the train body on its suspension is small relative to the available displacement

of the pantograph (typically 2 m) and thus has little effect on the dynamics of the pantograph, as discussed in Section 2.6.1. The contact stiffness between the pantograph and the contact wire is 50 kN/m as specified in the reference model. For work with significant wire height variation, the alternative pantograph model shown in Chapter 2.6.2 is adopted.

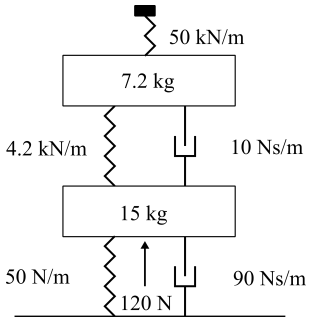

Fig. 4.3 Lumped–mass representation of the pantograph used to compare modelling predictions against the BS EN 50318 reference model. The value of the physical characteristic of each of the pantograph element's are also given.

For Step 2 of the validation, the measured data required was obtained from line tests performed at Network Rail's Innovation and Development Centre (RIDC) using a British Rail Class 395 train. The test track overhead line geometry consisted of 12 non–identical spans with spans ranging between 46 and 65 m, with four or five droppers in each span. Mechanical properties of the overhead line system were given as: messenger and contact wire tensions of 13 and 16.5 kN respectively, and cross–sectional areas of 65 and 120 mm^2. The train speed used during the test was 185 km/h.

From both the test track data and the modelling predictions BS EN 50318 requires that,

1. the standard deviation of the contact force,
2. the maximum wire uplift at the supports, and
3. the range between the wire uplift maxima and minima,

are compared before a model can be considered validated. The standard allows a validated model to show up to $\pm 20\%$ variation between the modelling output and test track data. This band for which comparisons between test track data and modelling predictions can be made is due to the difficulty in completely capturing the environment in which the test data was collected in a simulated model. Two examples would be,

1. Ground movements over time (e.g, due to unstable embankments) cause shifting of the position of the masts with respect to the track, altering the overhead line geometry

from the original installed design contributing to variations in the contact force during operation, and

2. Poor quantification of the wear state of the contact wire, leading to reductions in the effective inertia of the contact wire during train operation.

In the reference cases used in the validation methodology provided by BS EN 50318, the contact wire can be considered level, that is the height of the supports at each and of a span is equal and the only height variation in the contact wire is due to a designed pre–sag or the natural sag of the wire under gravitational loading. In the test track case, the changes in the support heights were small (the root–mean square height change between supports was 20 mm with the largest, a decrease of 56 mm) and therefore could be considered to be a good approximation to a level contact wire.

4.2.1 Validation of a flat wire arrangement

Validation of the flat level wire arrangement was performed in [241], however was repeated as a test case to assess the model viability after the development process as described in Section 4.1. The statistical comparison between the model predictions and the acceptable ranges of pantograph to wire contact force in BS EN 50318 are provided in Table 4.2 and Figure 4.4 shows the maximum wire uplift at a support for the two reference cases when the train speeds were 250 and 300 km/h. The permissible range for the contact wire uplift prediction when a train speed of 250 km/h is given as 48–55 mm, and the maximum uplift predicted by the model is 51 mm. For a train speed of 300 km/h, the permissible range is 55–65 mm, whilst the maximum simulated uplift is 60 mm.

Table 4.2 Model statistical output for the two references cases and the allowable range provided by BS EN 50318. All values given in N.

(a) 250 km/h

Parameter	EN 50318	Model
F_m	110 – 120	115
σ	26 – 31	29.8
$F_{D_{\max}}$	175 – 210	188
$F_{D_{\min}}$	50 – 75	52.7
$F_{S_{\max}}$	190 – 210	204
$F_{S_{\min}}$	20 – 40	25.8

(b) 300 km/h

Parameter	EN 50318	Model
F_m	110 – 120	116
σ	32 – 40	37.9
$F_{D_{\max}}$	190 – 225	207
$F_{D_{\min}}$	30 – 55	33.9
$F_{S_{\max}}$	210 – 230	230
$F_{S_{\min}}$	−5 – 20	2.27

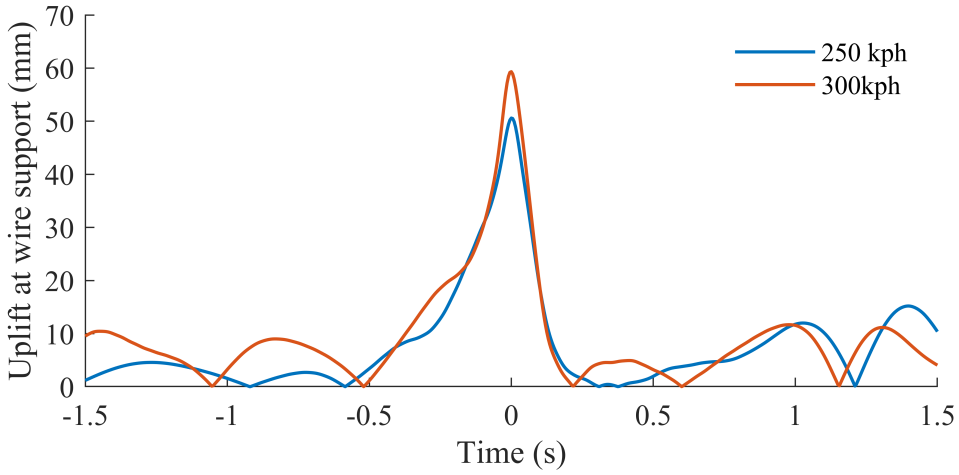

Fig. 4.4 Predicted maximum contact wire uplift at a support for the overhead line geometry specified in standard BS EN 50318. Zero time corresponds to the time the pantograph passed the support. Legend indicates the train speed used in each case. These are modelling predictions for each of the two train speeds, not comparisons with measured wire uplifts.

The contact force trace comparison is not required according to BS EN 50318, however the force trace was compared with the published force trace in [241] and was identical indicating that the model development described in Section 4.1 left the previous modelling predictions unchanged. The required output is given in Table 4.3 and it is noted that each of the outputs is typically towards the lower bound of acceptable output. This is likely due to the noise inherent in the measured data that is not included in the 'idealised' overhead line model e.g. localised wear of the contact wire.

Table 4.3 Comparison between test track data and model predictions.

	Measured -20%	Model	Measured +20%
Contact force standard deviation (N)	18.5	18.6	27.8
Maximum wire uplift (mm)	37	41	56
Range of vertical displacement (mm)	57	61	85

4.2.2 Validation of a model with large scale height variations

Since no reference models exist for non–level wires, comparison with test track data is the method adopted for validating extensions of the existing model when large–scale height

changes such as those considered in Chapter 8 are introduced. Two comparisons against test track data have been adopted in this validation process:

1. Comparison between the test track data from Network Rail RIDC as in the methodology given in BS EN 50318, and

2. Comparison against a range of pantograph height variations with measured contact force data obtained from tests performed on the Great Western Mainline.

Validation of the updated model was achieved using measured data from the Network Rail RIDC, previously described in Section 3.4.1. The test track overhead line geometry used is presented in Figure 3.21 and the pantograph model parameters are those given in Table 3.5.

The output required by BS EN 50318 is given in Table 4.4. All of the results were within the allowable $\pm 20\%$ band, however the vertical displacement of the contact point was only marginally lower than the allowable maximum. The larger range of vertical displacement was due the contact wire model sagging further than the corresponding section of the installed overhead line. Since the wear state of the contact wire was poorly quantified, it is likely that since the corresponding location was under an overbridge, localised wear may have reduced the sag of the installed system, thus reducing the range of vertical displacements. As can be seen from Table 4.5, statistical output for the simulated data fell within the allowable $\pm 20\%$ band defined by BS EN 50318 [287] and the simulated output was in good agreement with the measured data. The largest outlier was peak contact force, which was predicted to be 14.3% higher than measured during the track tests. The peaks in the contact force are observed when the pantograph moves from an upward sloping section to a level contact wire and reflects the necessary force required to generate the acceleration to change the pantograph's direction.

Comparison was made between the force traces of both the simulated and measured catenary pantograph interactions. There was considerable variation in the span lengths used in the test track case, ranging between 9 and 65 m. This variation in the span lengths causes the repeating contact force pattern found on more uniform installations to be lost. Despite this, the modelling predicted the peak forces typical of support locations due to the increased vertical stiffness caused by registration arms, and large scale patterns such as lower contact forces at midspan where the vertical stiffness is reduced were also observed.

Deviations between the modelling predictions and the measured data were likely as the model did not attempt to model every feature of the real world installation. For example, whilst the condition of the wire wear was known from the test track measurements, to

generate a tractable computational model, its variation along the line was not included. For reasons such as this the large ±20% band of allowable statistical output is given.

Table 4.4 Comparison between test track data and model predictions for a model considering large scale contact wire height variations.

	Measured -20%	Model	Measured +20%
Contact force standard deviation (N)	19.6	27.0	29.4
Maximum wire uplift (mm)	40	54	60
Range of vertical displacement (mm)	256	383	384

Table 4.5 Model results for the test track and model predictions for the entire OLE length. All values in Newtons. See nomenclature for definition of statistical terms.

Statistical parameter	Measured contact force -20%	Measured contact force	Simulated contact force	Measured contact force +20%
F_m	82.5	103	105	124
$F_{D_{\max}}$	140	175	200	210
$F_{D_{\min}}$	23.9	29.8	29.2	35.8
$F_{S_{\max}}$	141	177	186	212
$F_{S_{\min}}$	23.8	29.8	24.3	35.7

Figure 4.5 show the histograms for the measured and simulated contact force respectively. Both the measured and simulated data show similar distributions with the contact force mean varying by approximately 2% and the standard distributions differing by less than 10%. The largest deviation between the measured and simulated data occurs at the extremes of the distributions, where the model predicts 1.2% of the contact force is below 70 N compared with the measured data where 3.3% of the measured contact force was below 70 N. The model also overpredicts the contact force maxima compared with the measured data. For the simulated case, approximately 7% of the contact force was above 160 N compared with 3% of the measured data. Considering $F_m \pm 2\sigma$, into which approximately 95% of the data falls, the variation between the measured and simulated data was approximately 5% indicating good agreement for a majority of the data. For the remaining 5% where the variation was greater, the data represents only a small proportion of the contact force.

The new adopted validation process for non–level contact wires makes comparison between the measured and simulated contact force as the pantograph is compressed as the contact wire height is reduced. In this way, the predictions using the lumped–mass model can be assessed in a way that thus far has not been presented in the literature. The measured

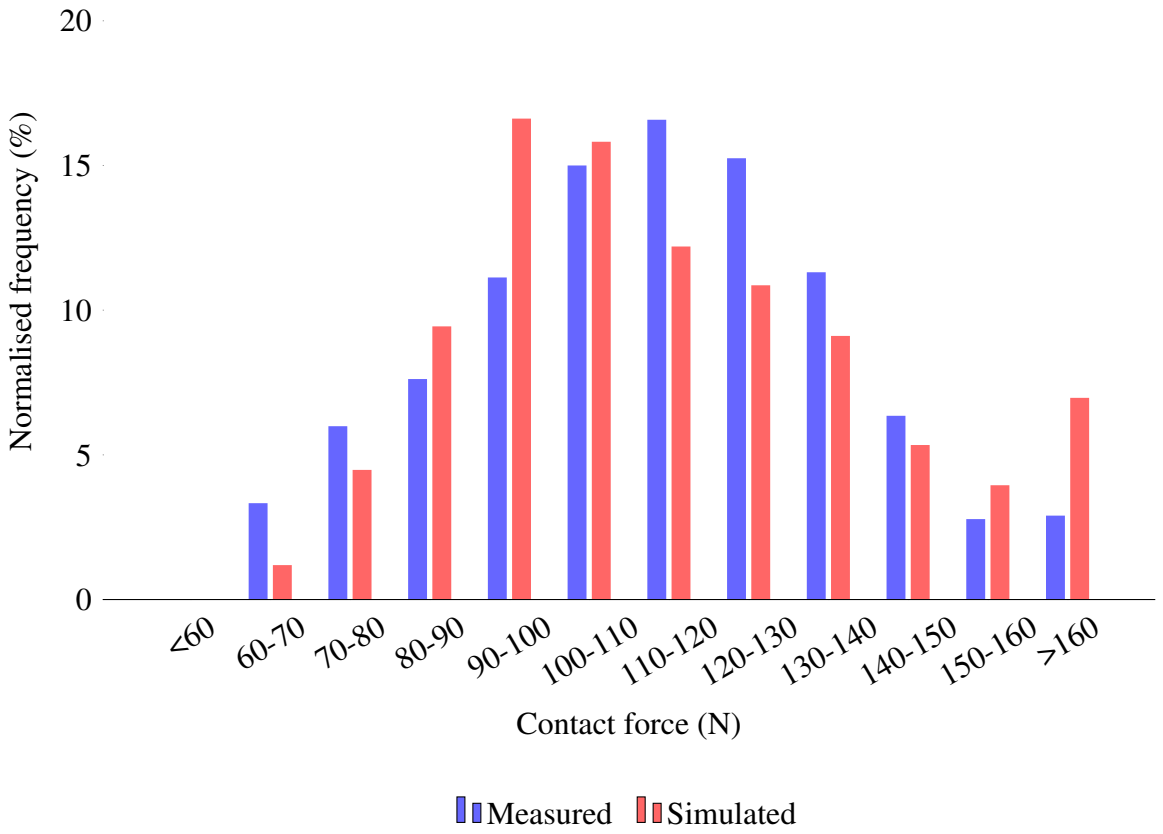

Fig. 4.5 Histogram of predicted and measured contact force for the validation case. The normalised frequency indicates the percentage of data falling within each bin.

contact force from the Great Western Mainline corresponded to a track length of 80 km and the compression of the pantograph due to decreasing wire heights was up to approximately 1.5 m. The pantograph height over the entire track length is given in Figure 4.6a, and Figure 4.6b and Figure 4.6c show detailed views of the pantograph head height at locations 4 and 6 respectively.

For the test data obtained from the Great Western Mainline, the train speed varied with a mean of 150 km/h compared with the 185 km/h used in the test cases performed at the RIDC. To account for the variation in train speed, the mean contact force was normalised by dividing the mean contact force by the square of the train speed to give mean contact force per unit speed squared (i.e., $\mathrm{N s^2/m^2}$). The square of the train speed is used since the mean contact force is proportional to the square of the train speed [61].

Figure 4.7, shows the comparison between the measured contact force data obtained from the Great Western Mainline and the predicted contact force using the finite element

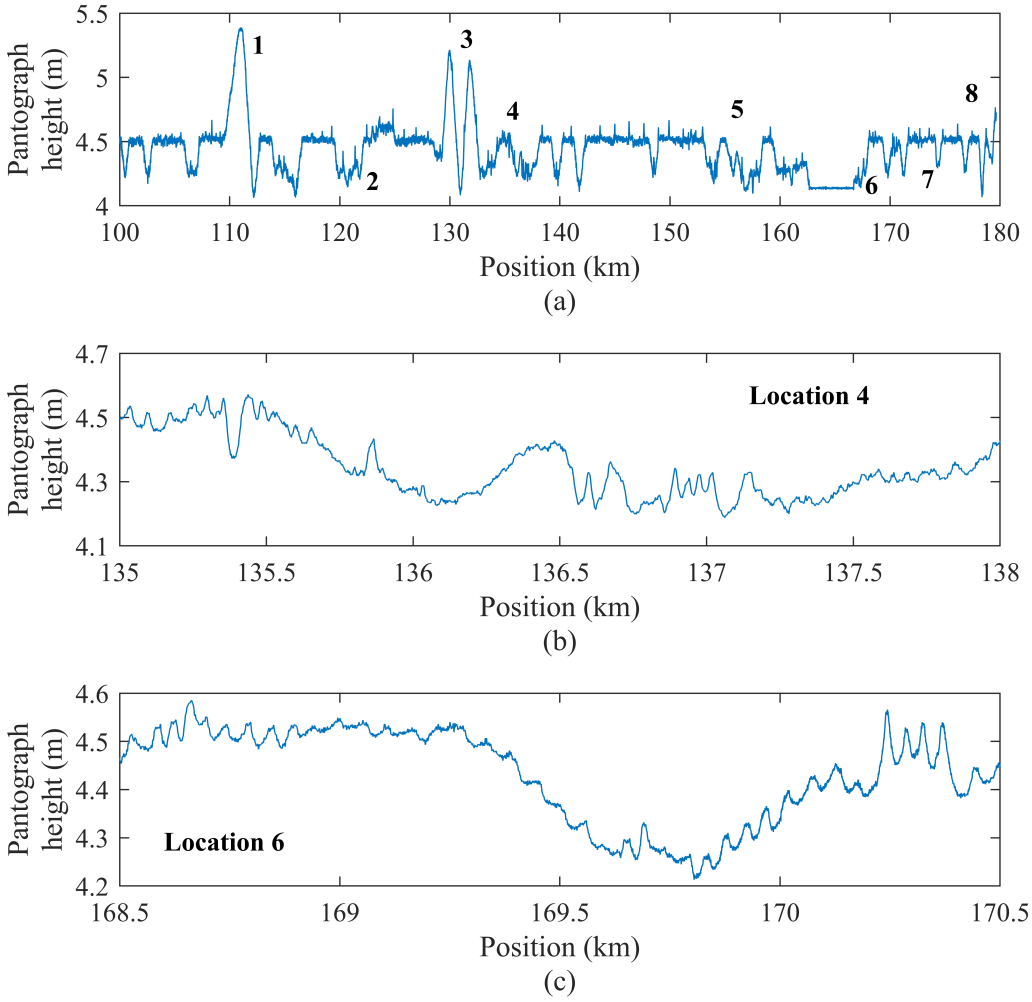

Fig. 4.6 Pantograph height as measured on test runs on the Great Western Mainline. The pantograph for the entire track length of 80 km is shown in (a), and (b) and (c) show a detailed view of the pantograph height transition for selected sections of the track length. Locations specified in Figure 4.7 are labelled in the figure.

representation of the Network Rail RIDC overhead line system. It can be seen that for pantograph collector head heights between 4.4 and 4.7 m, the mean contact force grows slowly as the pantograph is compressed due to a decreasing wire height. As the pantograph head is compressed further, the growth of the mean contact force grows more rapidly, and then grows most sharply for pantograph collector head heights below 4.2 m. Outliers are Locations 5 and 7 compared with the other cases. At these locations, sharper wire gradients

are observed indicating that the more rapid change in pantograph height induces a greater force as the pantograph experiences a greater acceleration.

The predicted mean contact force follows the same trend as each of the each of the measured cases in Figure 4.7. For small compressions of the pantograph from the level wire working position, the predicted mean contact is also expected to see similar increases and as the pantograph is compressed further, the rise in the mean contact force becomes greater.

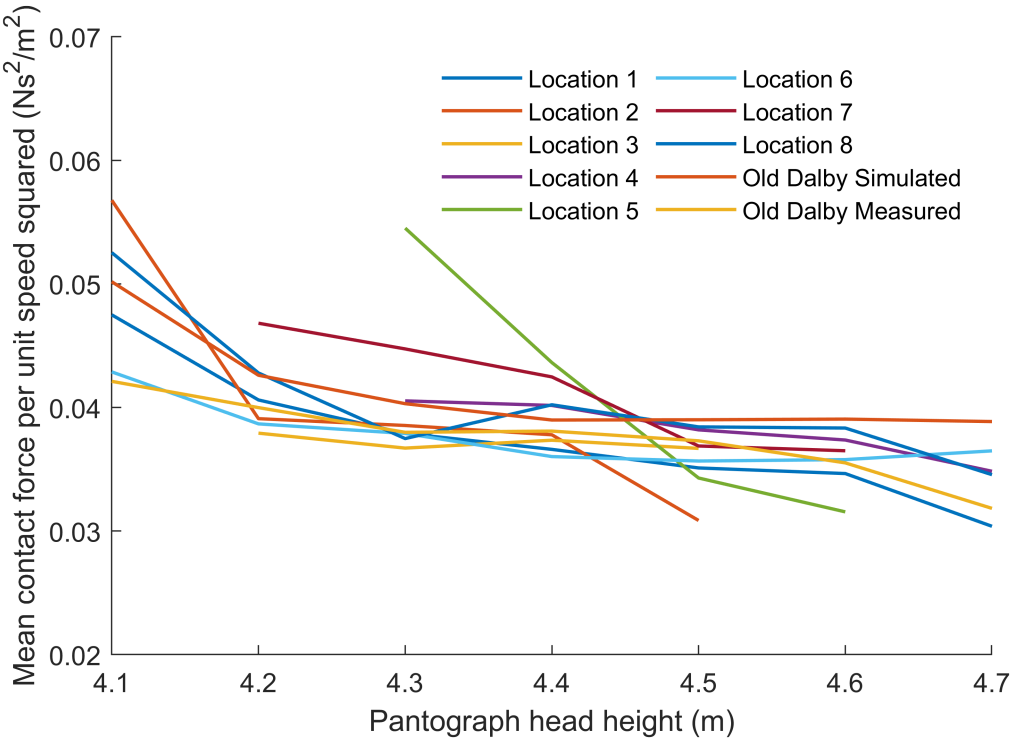

Fig. 4.7 Comparison between the the predicted mean contact force based on the Network Rail RIDC overhead line geometry as the pantograph height is reduced, and the measured contact force for a pantograph at the same operational height as measured on the Great Western Mainline.

4.3 Modelling assumptions and their sensitivity

To generate a tractable model, assumptions to simplify the real system have been made. In this section, those assumptions are discussed and the sensitivity of the modelling output to these assumptions is assessed.

4.3.1 Stranded messenger wires

For simplicity it is assumed that the stranded messenger wire can be approximated by a cylinder of equal cross–sectional area, where the empty space between individual strands can be neglected, with equivalent mechanical properties, e.g., Young's modulus and linear density. Compared with a truly solid wire such as the contact wire, for stranded cables, each strand undergoes small displacements relative to each other under axial tensioning [288–290]. Due to being composed of multiple strands, stranded wires of equivalent metal cross–sectional areas to a single stranded wire demonstrate differing flexural rigidities. To assess the effect of differing flexural rigidities, the cross–sectional area of the single stranded messenger wire was varied. Table 4.6 gives the Young's modulus and cross–sectional area and the corresponding flexural rigidity in each case, where the flexural rigidity is calculated using,

$$\frac{\pi}{4}Er^4 = \frac{1}{4\pi}EA^2. \tag{4.2}$$

Visual inspection of the vertical deflection of the overhead line indicates that the messenger wire deflection is smaller than the uplift of a contact wire due to the flexible dropper buckling as the pantograph passes, thus dynamic behaviour of the messenger is unlikely to have a large effect on the dynamics at the contact interface.

Table 4.6 Messenger wire flexural rigidities used to assess the effect on the overhead line dynamics. The base case is when $EI = 33.6$ Pa m^4.

Cross–sectional area, [mm^2]	71	69	68	65	61	52	40
Flexural rigidity, EI, [Pa m^4]	39.8	37.8	36.6	33.6	30.0	21.4	12.6

Figure 4.8 gives the mean contact force for the catenary pantograph interaction as the messenger wire flexural rigidity varies and the fitted curve for each of the mean contact forces. As EI increases, it can be seen that the mean contact force also increases, however this increase is small. Compared with the mean contact force in the base case, for the maximum $EI = 39.8$ Pa m^4, the increase in the mean contact force was only 0.7%, compared to the approximately 18% increase in the flexural rigidity. Similarly, as EI decreased, so too did the mean contact force. When EI was a minimum at 12.6 GPa, the mean contact force was 103 N. This was 1.1 % smaller than the base case of 104 N, despite the 63% decrease in the flexural rigidity. The equation for the fitted curve in Figure 4.8 is given by,

$$g_{F_m}(EI) = 2.86 \times 10^{-3}(EI)^{1.77} + 103, \tag{4.3}$$

where g_{F_m} denotes the fitted polynomial g for the mean contact force as a function of EI. Equation 4.3 indicates that the mean contact force grows slowly as a response to increasing flexural rigidity. The small dependence of the mean contact force on the flexural rigidity of the contact wire indicates that approximating the messenger wire as a single cylinder, rather than a stranded conductor, has little overall effect on the dynamic behaviour of the system. This was expected since the deflection of the messenger wire is small.

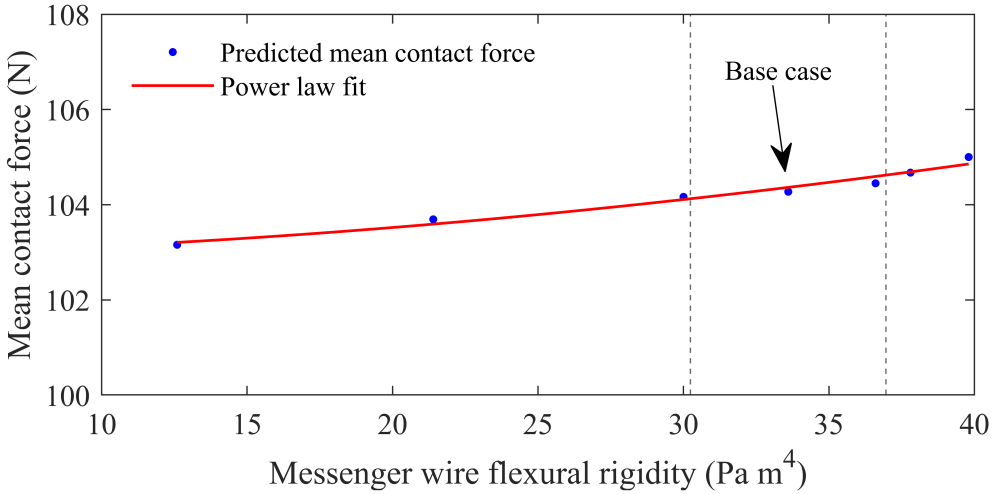

Fig. 4.8 Mean contact force in response to varying the flexural rigidity of the messenger wire. The base case when $EI = 33.6$ Pa m^4 is indicated and the dashed lines indicate values of flexural rigidity up to $\pm 10\%$ of the base case.

The contact force standard deviation is given in Figure 4.9, and the equation of the fitted curve is given by,

$$g_\sigma(EI) = 1.44 \times 10^{-8}(EI)^{5.43} + 11.6. \tag{4.4}$$

In contrast to the mean contact force, the standard deviation grows faster due to the larger exponent, suggesting that the reduced flexural rigidity contributes to a greater variation in the contact force thus reducing the current collection quality. For small increases in the flexural rigidity (i.e., less than 10% as shown in Figure 4.9), the increase in the contact force variation is limited at approximately 8%. Similarly, a decrease in EI of approximately 10% leads to a predicted reduction in the contact force standard deviation of 6%, indicating that for this range of input, the variation of the contact force with respect to changes in the flexural rigidity is small. Increasing the flexural rigidity to the maximum investigated here, the contact force standard deviation increased by approximately 47% and decreasing EI to

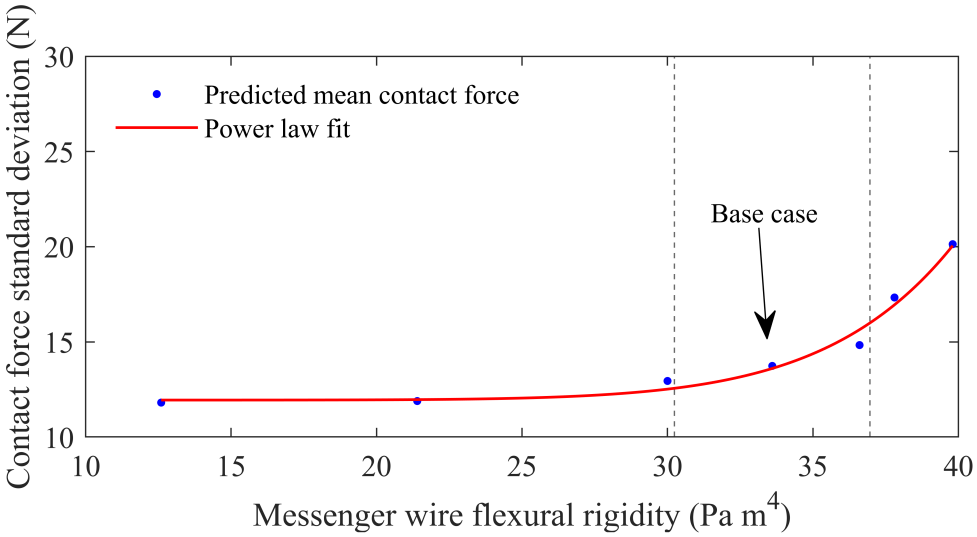

Fig. 4.9 Contact force standard deviation as the flexural rigidity is varied. The base case when $EI = 33.6$ Pa m^4 is indicated and the dashed lines indicate values of flexural rigidity up to $\pm 10\%$ of the base case.

its minimum decreased the contact force deviation by approximately 14%, however these were the extreme cases considered.

4.3.2 Point-mass registration arms

In this work, the registration arms that support the contact wire at the end of each span are assumed to act as point masses. In an installed system, the registration is arm is formed of a cylindrical rod that is mounted to lineside masts and experiences vertical deflections during pantograph passage. To assess the sensitivity of using point masses in contrast to a rod to support the contact wire at masts, a more complex representation of the registration arm was introduced at the central support in the overhead line geometry. The mechanical properties of the registration arm used are given in [240] and are also given in Table 4.7.

To simulate the behaviour of the registration arm, the arm was represented using a nonlinear beam element with properties corresponding to those given in Table 4.7 and the boundary conditions were set such that the contact point between the registration arm was allowed to deflect in the vertical direction during pantograph passage but was fixed in all directions at the end point where the arm would be fixed to the mast. This correctly allowed the registration arm to pivot under vertical loading. The registration arm arrangement with respect to the contact wire is shown in Figure 4.10. The registration arm is orthogonal to the contact wire and supports the wire at the design height.

Table 4.7 Distributed mass registration arm material properties used to assess the effect of using a concentrated mass to represent the registration arms.

Property	Value	Units
Linear density	0.73	kg/m
Axial stiffness	17000	kN
Bending stiffness	1100	$\mathrm{N\,m^2}$
Length	1200	mm
Diameter	50	mm

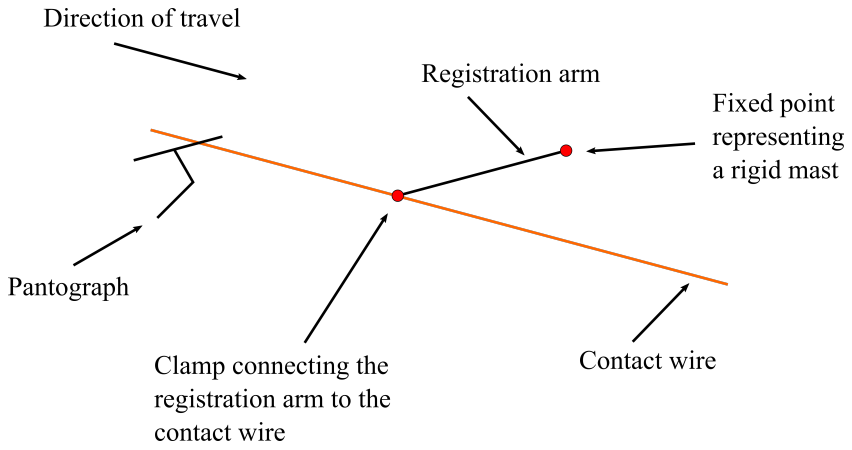

Fig. 4.10 Schematic of the arrangement used to support a contact wire using a registration arm. For clarity the droppers have been omitted.

Figure 4.11 gives the force trace during the catenary pantograph interaction for both the point mass registration arm and when the arm was more comprehensively represented. The registration arm was placed at the mast at 180 m and from the force trace, it can be seen that adopting a point mass representation of the registration arm has little effect on the contact force during the catenary pantograph interaction. Towards the ends of the spans, the concentrated mass causes a small increase in the contact force likely due to the point mass concentrating the vertical stiffness caused by the registration arm at the contact point between the pantograph, contact wire and contact wire support. By distributing the mass along the length of the registration arm, the vertical stiffness created by the registration arm is also distributed. In the centre of the spans, away from the supports, the deviation between the force traces is minimal as the effect of the registration arm on the overhead line dynamics is reduced. Table 4.8 gives the statistical output for each of the cases considered here. Coupled with the force trace, the statistical output highlights the minimal effect distributing the mass of the registration arm has on the dynamic behaviour. Since the mass of the registration

arm relative to the total mass of the contact wire and tha pantograph is small (taking the total mass of the contact wire 5 m either side of the support and the mass of the pantograph head, the mass of the registration arm is approximately 5% of the combined contact wire and pantograph head mass), the increased inertia placed at the support for the contact wire by concentrating the mass has little overall effect. Considering that half the total mass of the contact wire in the spans either side of the support are supported by the registration arm, the ratio between the supported mass and the contact wire to the registration arm mass drops to approximately 1%.

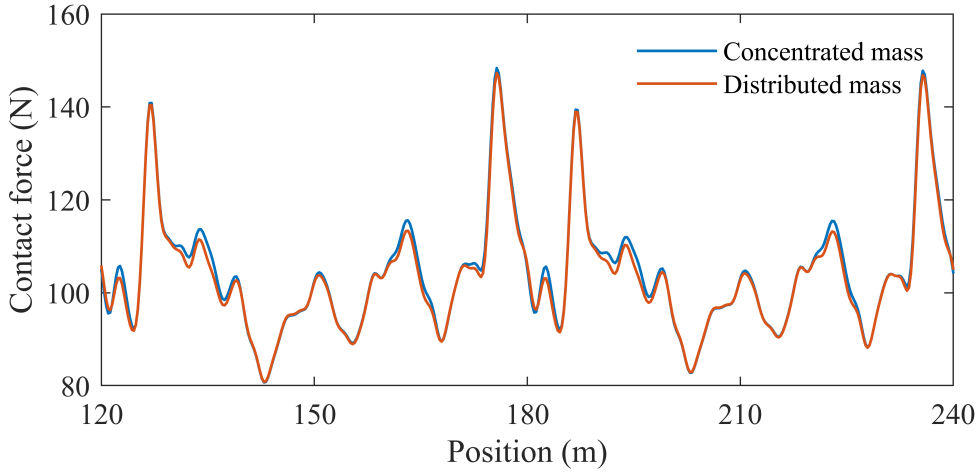

Fig. 4.11 Contact force trace for the cases where either a concentrated mass representation of a registration arm is used or a distributed mass registration arm. The legend indicates which type of mass was used.

Table 4.8 Statistical output comparing the concentrated and distributed mass representations of an overhead line registration arm. All results in N.

Mass type	F_m	σ	$F_{D_{\max}}$	$F_{D_{\min}}$	$F_{S_{\max}}$	$F_{S_{\min}}$
Lumped	104	12.7	148	80.7	142	66.3
Distributed	104	12.4	147	80.8	141	66.4
Difference (%)	-0.6	-2.4	-0.7	+0.1	-0.7	+0.2

4.3.3 Friction

Previous experimental studies of the sliding contact between the pantograph carbons and contact wire in [103, 291], indicate that the frictional coefficient varies relative to the train

running speed and is given as $0.24 \leq \mu \leq 0.35$ when the running speed is between 140 and 170 km/h. The coefficient is also estimated in [292] to be between 0.1 and 0.28. Given the contact force is of the order of 100 N, this would correspond to an additional force parallel to the wire of between 10 and 28 N (i.e., approximately 0.2% of the applied wire tension of 16.5 kN). To assess the sensitivity of the simulations to frictional behaviour, Coulomb friction was implemented between the pantograph carbons and the contact wire with coefficients given by

$$\mu \in \{0, 0.01, 0.5, 0.1, 0.2, 0.3, 0.4, 0.5\}. \tag{4.5}$$

The mean and standard deviation of the contact force for each of the μ_i are shown in Figure 4.12. In each of the cases, the static uplift force applied to the pantograph was 70 N and the train running speed was 200 km/s. From Figure 4.12a, it can be seen that the variation in the mean contact force is small despite the increasing friction between the two contact surfaces. When friction is neglected, the mean contact force is approximately 104 N, and increases to approximately 105 N when $\mu = 0.5$. This represents a less than 1% increase in the mean contact force. The variation in the total contact force is given by the standard deviation in Figure 4.12b. The standard deviation grows more as μ increases compared with the growth in the mean contact force. Comparing the cases when $\mu = 0$ and $\mu = 0.5$, the standard deviation of the contact force increased by less than 0.05 N (less than 0.3%), indicating that the frictional contribution also has little greater effect on total force variation. The range of contact force when friction is neglected is approximately 74.5 N whilst when $\mu = 0.5$, the contact force range is approximately 75 N. Thus, the addition of frictional behaviour increased the contact force range by just under 1%. These results indicate that the effects of Coulomb friction on the dynamic characteristics of the catenary pantograph interaction under consideration in this work are minimal and therefore the neglection of friction (i.e., taking $\mu = 0$) will have little effect on the modelling output.

Since the variation in the contact force when frictional forces are included is minimal, frictional behaviour for train speeds up to 200 km/h can be neglected. For train speeds above this, for which no validation has been made as current UK test tracks are not capable of such line speeds, the inclusion of friction may be necessary. In [293], the effect of friction on the catenary pantograph interaction is analysed for a pantograph uplift force of 152 N and a train running speed of 300 km/h. The frictional effects on the catenary pantograph interaction were found to be larger than those described above. However, the model in [293] makes use of a frame model of the pantograph, and includes the knuckle direction of the pantograph that affects the dynamic uplift force. Thus, no direct comparison to the data presented here can

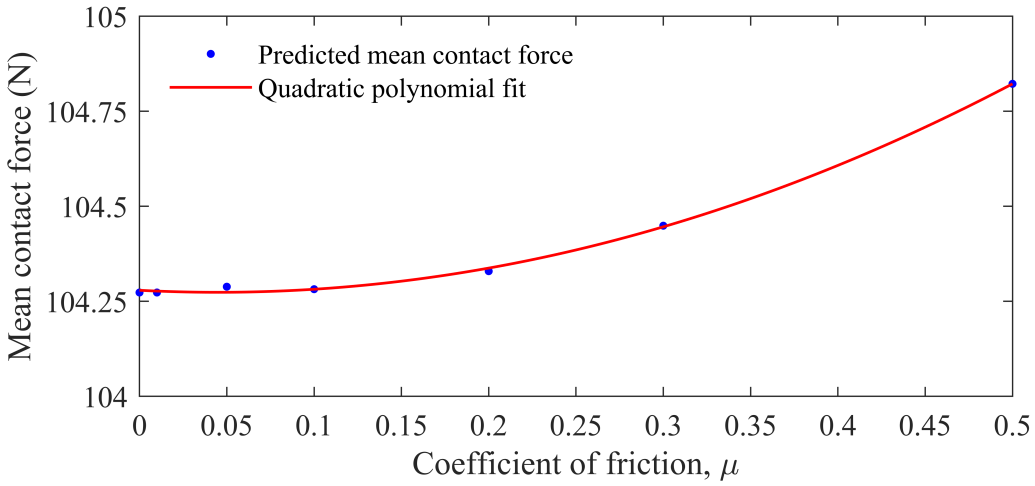

(a) Mean contact force as the coefficient of friction between the pantograph carbons and the contact wire is increased.

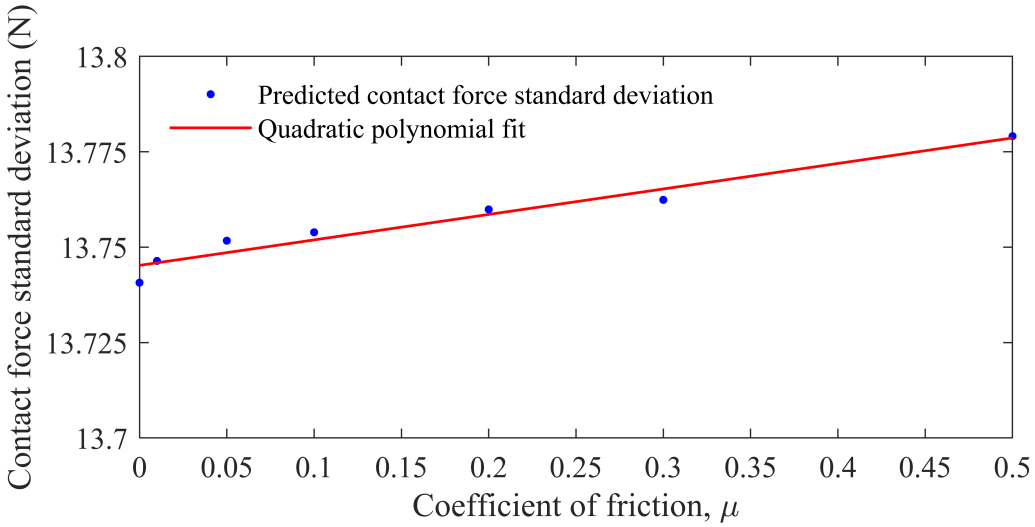

(b) Contact force standard deviation as the coefficient of friction between the pantograph carbons and the contact wire is increased.

Fig. 4.12 Statistical output for the catenary pantograph interaction for varying levels of contact friction.

be made, however it highlights that at increased train speeds, the dynamic effects of friction between the contact surfaces may become a significant.

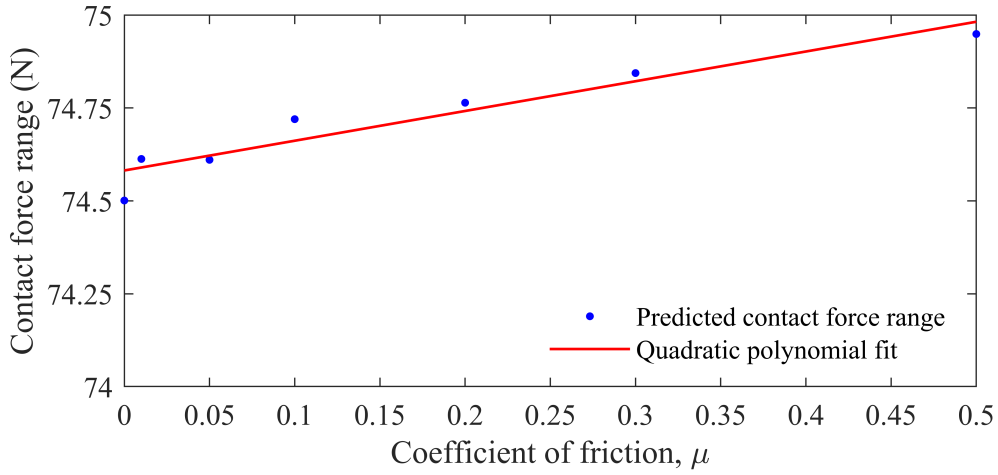

Fig. 4.13 Range of the contact force as the coefficient of friction is varied.

4.3.4 Neglecting reflected mechanical waves

Since the length of an installed wire run is limited, as discussed in Section 2.1.2, mechanical waves caused by contact between the pantograph and the contact wire are reflected back from the supports at the end of the wire and transmit back towards the contact point. The time the pantograph meets the reflected wave is given by $t_p = x/v_p$, and the time the reflected wave meets the pantograph is

$$t_w = \frac{L_w}{c_s} + \frac{L_w - x}{c_s}, \tag{4.6}$$

Since $t_p = t_w$, it follows that

$$\frac{2L_w}{c_s} = x\left(\frac{1}{c_s} + \frac{1}{v_p}\right). \tag{4.7}$$

and the point at which the pantograph meets the reflected mechanical wave is given by,

$$x = \frac{2v_p L_w}{c_s + v_p}, \tag{4.8}$$

where c_s is given by Equation 2.19, v_p is the pantograph speed and L_w is the length of the wire run.

The reflected mechanical wave interferes with the dynamics at the contact point increasing the contact force variation during operation [294] reducing the current collection quality. To account for this, the wire run length adopted in the model with respect to the pantograph is assumed to be an 'infinite' string, that is, the wire run length is chosen to be such that the reflected wave cannot reach the contact point for any areas in which analysis is undertaken.

If the desired pantograph translation length is given by x, then rearranging Equation 4.8 gives the required wire run length necessary to ensure no wave interference at the contact point. Thus the required wire run length is given by

$$\text{ceil}\left[\frac{1}{2}x\left(1+\frac{c_s}{v_p}\right)\right] \leq L_w, \tag{4.9}$$

where ceil$[\cdot]$ is the ceiling function (i.e., the greatest integer less than or equal to L_w). From [294], the reflected wave can cause up to 25% variation in the contact force standard deviation, thus to assess the core dynamic behaviours at the contact point, it is key to ensure that reflected waves are neglected.

4.3.5 Lumped-mass pantograph representation

Throughout this work, it is assumed that the train–mounted pantograph can be reasonably well approximated by a lumped–mass representation with the dynamic behaviour of the pantograph captured accurately as adopted in [191, 240, 295]. In [273], a comparison between lumped-mass representations of the pantograph and a 3D–multibody representation was made. It was found that deviation between the mean contact force between the two pantograph types was less than 1%, whilst the variation between the contact force standard deviations was marginally higher at 1.3%. The largest deviation between the lumped–mass and multibody models was predicted to occur for the predicted contact force maxima, where the multibody formulation predicted a 3.9% lower contact force maxima. The comparisons were performed using a train speed of 300 km/h and a static upload force of 120 N, suggesting that variations between the two pantograph representations will be reduced for lower train speeds. Throughout much of the work that follows, the static preload applied to the pantograph is 70 N and the train speed is 200 km/h.

4.4 Mesh independence

To assess mesh independence of the finite element model of the overhead line dynamics, the following procedure was used:

1. Fix element sizes for the contact and messenger wires given by (s_{c_0}, s_{m_0}), where s_c and s_m denote the mesh element size of the contact wire and messenger wire respectively in metres.

2. Reduce s_{m_0} until the variation in the mean contact force is below 0.5% and denote this element size as s_{m_1}. The new size pair is then (s_{c_0}, s_{m_1}).

3. Fix s_{m_1} and reduce s_{c_0} until the variation in the mean contact force is again below 0.5%. This gives another size pair (s_{c_1}, s_{m_1}).

4. Iterate this procedure to generate the final size pair (s_{c_k}, s_{m_k}), so that no further reductions in either s_c or s_m generate a variation greater than 0.5%.

The initial mesh size pair was chosen as $(s_{c_1}, s_{m_1}) = (5,5)$ and Figure 4.14 shows the reduction in the mesh element sizing required to establish mesh independence of the finite element model. Using the iterative procedure the following size pairings were produced,

$$(s_{c_0}, s_{m_0}) = (5,5) \rightarrow (5,2) \rightarrow (1,2) \rightarrow (1,0.5) \rightarrow (0.75,0.5) \rightarrow (0.5,0.5) = (s_{c_k}, s_{m_k}) . \tag{4.10}$$

From the iterative procedure, a mesh element size of 0.5 m was adopted in the finite element model. Figure 4.14 shows the mean contact force convergence as the mesh element size is decreased. From the convergence plot, it is clear that since the messenger wire is away from the contact point, the contact force variation convergence is largely dependent on the mesh size of the contact wire.

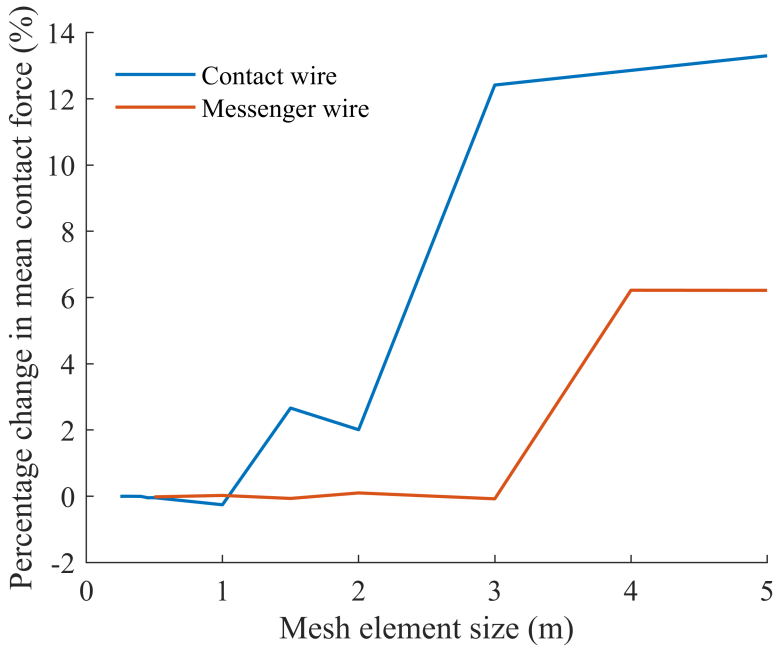

Fig. 4.14 Mesh independence study demonstrating that convergence of the mean contact force is achieved when the mesh element size is 0.5 m.

4.5 Conclusions

In this Chapter, an overview of the modelling developments required to perform the work in later chapters has been given. The critical model development was the introduction of aerodynamic loads to an otherwise purely mechanical model. By adopting a functional representation of the aerodynamic load, a convenient method of imposing transient loads has been implemented in a finite element model. This method also has the advantage of being able to represent further forms of aerodynamic effects such as gusting. An addition to the conventional validation method for modelling overhead lines is proposed when considering overhead lines that undergo large scale height changes. The proposed method allows for the comparison of different system types and line speeds that undergo height variations by assessing the resultant contact force as the pantograph collector height is reduced, i.e., when the pantograph is compressed. From measured data from Network Rail's RIDC and tests performed on the Great Western Mainline, the modelling predictions have been validated for both level wires where the support height remains constant, and also for cases where there are large scale height transitions. The comparison against the two sets of measured data

indicate that a lumped–mass representation of the pantograph is suitable for investigated the effect of contact wire height changes on the dynamic catenary pantograph interaction.

This Chapter also presents the results of the sensitivity of the model to a range of modelling assumptions. Assuming that the messenger wire was a solid cylinder rather than a stranded conductor was found to have little effect on the dynamics (approximately 1%), likely due to being away from the contact point with the pantograph, thus a cylinder of equal mass to that of a stranded wire provided little variation in the contact force. Similarly, the model was found to be mesh independent by iteratively determining a maximum element size. The mesh elements after the iterative process have a length of 0.5 m for both the messenger and contact wires. This element size was found to cause less than 0.5% variation in the mean contact force. It was also found that the modelling assumptions directly affecting the contact point had a greater sensitivity, however this sensitivity was still minor. Representing the registration arms as point masses rather than distributed elements acted to increase the variation in the contact force by up to 2.4%, whilst the implementation of friction caused a less than 1% increase in the mean contact force, when a realistic value of $\mu = 0.5$ was used. Since the variation due to the inclusion of friction was minimal, the computational expense of its inclusion in further modelling for the speeds and static uplift forces of relevance to the work in this thesis was not justified.

The largest sensitivity of the model is related to the pantograph representation chosen. In [273], the contact force standard variation is predicted to increase by 3.6% when adopting a lumped–mass model compared with a flexible multibody representation of the pantograph. Since this variation was predicted for a train speed of 300 km/h, it is likely that this variation is an upper bound when lower train speeds are used, such as those used in the majority of the work in this study. From the various assumptions assessed in this Chapter, the worst case is that the model will have a sensitivity that is of the order 10%. In [296], an accuracy of 15% is presented as an improvement over previous methods suggesting that the methods presented here provide an accurate method for predicting the contact behaviour between the pantograph and overhead line system.

Having assessed the sensitivity of the model, and determined that the results are independent of the mesh sizing used, the following Chapters make use of the developed model to quantify the catenary pantograph interaction under a range of different conditions such as, mechanical parameter variation, aerodynamic loading and the effects of contact wire gradients.

Chapter 5

Determination of aerodynamic forces on a railway contact wire

5.1 Introduction

Knowledge of aerodynamic forces on a railway contact wire is important for the safe operation of the railway. Lateral deflections due to sidewinds are a known cause of overhead line dewirements leading to damage to both the overhead line and the train mounted pantograph. This damage causes delays and disruption to the rest of the network. In the case of a railway overhead contact line, Figure 5.1 gives the free stream direction around the contact wire and the angle of attack and the aerodynamic drag and lift coordinates are denoted x and z respectively. In this Chapter, only sidewinds are considered with no aerodynamic load along

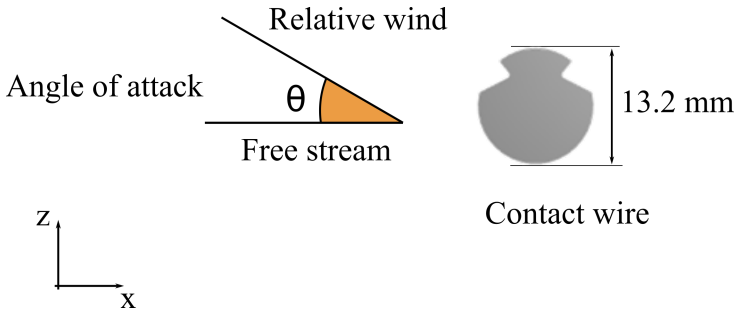

Fig. 5.1 A 2D representation of a typical contact wire cross section and the free stream direction. The angle of attack θ is shown and wear considerations will be made by reducing the vertical diameter of the contact wire from 13.2 mm.

the direction of the track, reducing the region of interest to the 2D plane perpendicular to the track level. Considering only the 2D behaviour neglects the flow parallel to the track,

i.e. flow moves the around the contact wire boundary only, with no flow moving along the length of the contact wire. The effect of the contact wire wear on the aerodynamic loads is also considered by reducing the contact wire cross–sectional area, by reducing the vertical diameter of the contact wire. This has the effect of changing the circular cross–section along the bottom half of the contact wire, to become similar to an aerofoil.

To determine the aerodynamic forces present on a railway contact wire, both experimental and computational approaches have been developed and are described in this Chapter. The influence of a range of parameters have been investigated in both experimental and computational cases. These are:

- wind velocity,
- the angle of attack of the flow perpendicular to the contact wire, and
- the wear of the contact wire.

In Section 3.1.1, the experimental arrangement using the Large Scale Sheffield Wind Tunnel is described, along with the experimentally determined aerodynamic drag forces in Section 3.1.2, the simulation environment in ANSYS FLUENT is described along with the results generated. Both simulation and experimental techniques have been adopted in this Chapter due to the need to validate the numerical predictions of the aerodynamic loads on a railway contact wire and due to safety limitations placed on operation of the wind tunnel. Wind speeds in the wind tunnel are limited to 10 m/s, whilst wind speeds during train operation can gust above 35 m/s [297]. For this reason, simulation techniques to predict the aerodynamic forces on a contact wire are required to assess the aerodynamic effects on the catenary pantograph interaction, as discussed in Chapter 7.

5.2 Experimental results

For each of the test cases, the aerodynamic loads were measured for 5 s with a frequency of 10 kHz, giving 50,000 data points for each case. From these data points, the mean drag and lift forces were extracted for each case given in Table 5.1. The plate between the contact wire and load cell was accounted for in calculation of the aerodynamic forces for a cylinder using the drag and lift equations,

$$F_{\text{Drag}} = \frac{1}{2} C_d \rho U^2 A, \tag{5.1}$$

$$F_{\text{Lift}} = \frac{1}{2} C_l \rho U^2 D, \tag{5.2}$$

respectively.

Table 5.1 Flow conditions used in the experimental cases. For each velocity in column 1, each of the angles and wear amounts in columns 2 and 3 respectively, were considered. Therefore, the total number of experimental cases was 168.

Air speed (m/s)	Angle of attack (°)	Wire wear (mm)
3.99	-30	0
4.93	-20	2
6.01	-10	4
7.02	0	6
8.15	10	
9.11	20	
	30	

The angles of attack given in Table 5.1 were chosen to consider a range of incident wind directions as well as potential shifting in the contact wire rest position. For example, shifting of supports over the lifetime of the equipment shifts the position of the contact wire at a registration arm causing twisting of the contact wire relative to the track level. Angles of attack up to $\pm 40^\circ$ and $\pm 90^\circ$ have been considered in [176] and [298] respectively.

The measured drag forces are shown in Figure 5.3. The actual aerodynamic drag, D_{actual}, that is the force parallel to the fluid flow, is calculated from the measured flow using,

$$\begin{pmatrix} D_{\text{actual}} \\ L_{\text{actual}} \end{pmatrix} = \begin{pmatrix} \cos\theta & \sin\theta \\ -\sin\theta & \cos\theta \end{pmatrix} \begin{pmatrix} D_{\text{meas}} \\ L_{\text{meas}} \end{pmatrix}, \tag{5.3}$$

where D_{meas} and L_{meas} are the measured drag and lift forces respectively. This gives the actual drag force as

$$D_{\text{actual}} = D_{\text{meas}} \cos\theta + L_{\text{meas}} \sin\theta,$$

for the angle of attack θ. The orientation of the contact wire due to the angle of attack θ is shown in Figure 5.2. Since the angle is altered by rotation of the pivot at the base of the sting, this has the effect of rotating the axes in which the load cell measured the aerodynamic loads. Thus, using the inverse rotation matrix given in Equation 5.3 gives the actual drag force parallel to the direction of the flow and equivalently the lift force orthogonal to the flow.

It can be seen from Figure 5.3a, that negative angles of attack had the effect to reduce the aerodynamic drag compared with a contact wire with zero angle of attack. The clear exception was when the angle of the attack was -30° since the measured load approximately

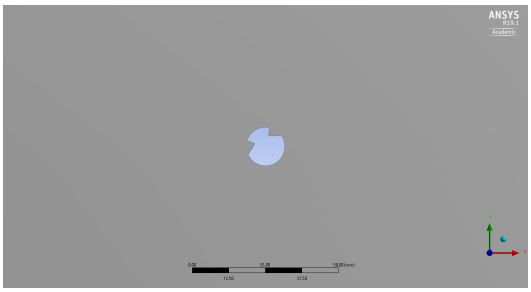

(a) Contact wire orientation when a positive angle of attack θ is applied.

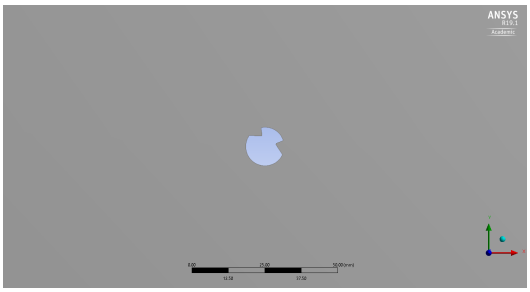

(b) Contact wire orientation when a negative angle of attack $-\theta$ is applied.

Fig. 5.2 Contact wire orientations when angle of attack is applied.

doubled as the wind speed was increased from 7 m/s to 9 m/s. This is in comparison to when $\theta = 0$ and the drag had only small variation as the wind speed increased. This is likely due to the orientation of the contact wire giving the largest surface area facing the incoming flow. When $\theta = 30°$, the aerodynamic drag also increased compared to when $\theta = 0$, likely due to the grooves pointing into the incoming flow and eddies building up within the groove generating an increased drag. Small angles of attack reduced the aerodynamic load compared to when $\theta = 0$, as can be seen in Figure 5.3a, significantly so when $\theta = -10°$ as the measured drag force was 0.5 and 1 N lower than the $\theta = 0$ case.

When the contact wire wear was 2mm the large negative angle of attack $\theta = -30°$ has a smaller effect on the aerodynamic drag, causing only a 0.9 N increase, compared with the 1.2 N increase when the contact wire was unworn. The most noticeable change is the increase in the aerodynamic drag when $\theta = 10°$. When the wear was 2 mm, a $10°$ angle of attack caused the largest measured drag force of 3.3 N compared with only 1.2 N when no angle of attack was imposed.

For more severe wear, such as in Figures 5.3c and 5.3d, the aerodynamic drag is reduced in magnitude, highlighted by the maximum measured drag force being 1.9 N and 1 N when the wire was 4 and 6 mm respectively, compared with the maximum of 3.8 N when the contact wire was unworn. Compared with the maximum aerodynamic drag measured for zero wear which occurs when the angle of attack was $-30°$, the maximum aerodynamic drag for a contact wire with 4 mm and a $-30°$ angle of attack was only 0.97 N, a reduction of 75%. By increasing the wear on the contact wire, the angle of attack causing the largest measured drag has also changed to $\theta = 30°$. In this orientation, the contact wire groove is positioned into the flow and the flat surface due to the wear is angled away from the flow. The groove allows for eddies to build up generating a larger aerodynamic load compared with the contact wire in the opposite orientation when $\theta = -30°$. Despite the large surface area due to the

wear flat, the fluid is allowed to pass along the surface freely compared with the grooved side, thus while increasing the drag compared with $\theta = 0$, this increase is smaller than when $\theta = 30°$. For a wire wear of 6 mm, a 30° angle of attack also gives the largest increase in the aerodynamic drag compared to $\theta = 0$ as shown in Figure 5.3d. For lower angles of attack, the variation between the aerodynamic drag compared with $\theta = 0$, is small, likely due to the large reduction in the cross-sectional area of the contact wire compared with an unworn wire.

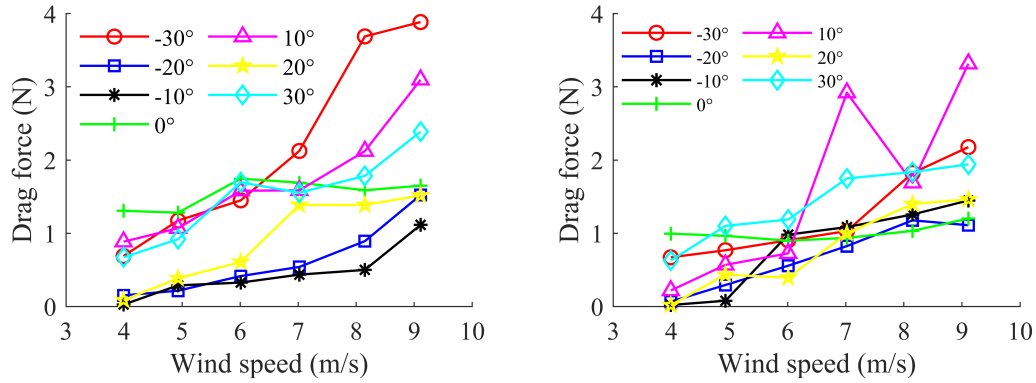

(a) Measured aerodynamic drag on a contact wire with 0 mm wear.

(b) Measured aerodynamic drag on a contact wire with 2 mm wear.

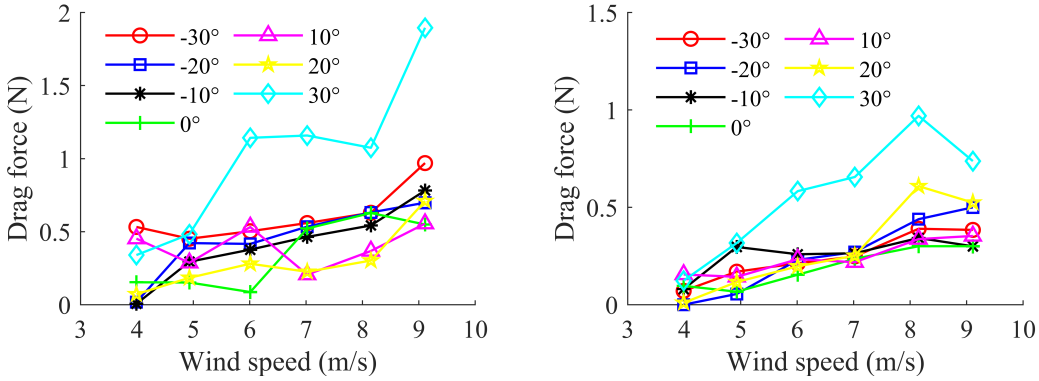

(c) Measured aerodynamic drag on a contact wire with 4 mm wear.

(d) Measured aerodynamic drag on a contact wire with 6 mm wear.

Fig. 5.3 Measured aerodynamic drag due to an incident flow on a contact wire. The legend indicates the amount of angle of attack used in each test case.

Figure 5.4 shows the measured aerodynamic drag due to wind speed and wear state of the contact wire, where the colour of the contour denotes the magnitude of the drag force. The contour plots indicate that the high angle of attack acts to increase the aerodynamic drag on the contact wire by increasing the cross–sectional area presented to the flow. The increased aerodynamic drag would have a corresponding increase in the contact wire blow off. At high wind speeds, the increased blow off would increase the likelihood of a dewirement event.

Since the angle of the incident wind on a contact wire cannot be controlled, this indicates that ensuring that the correct contact wire position is maintained, for example by regular inspection of lineside supports to ensure the correct contact wire geometry to prevent twisting of the contact wire which would cause the contact wire to rotate relative to the track, is vital to reduce the likelihood of dewirement.

The measured drag force was obtained using a sample of contact wire 720 mm long. If the air flow along a typical 60 m overhead line span was uniform, i.e. no significant changes in the air speed along the span length, the measured drag force can be extended to determine the aerodynamic drag on a contact wire span length. The drag values for a single span of railway contact wire are given in Table 5.2. In the wear cases, it is assumed the wear is constant along the entire span length. In reality this is unlikely since variations in the contact force between the contact wire and pantograph carbons will give uneven amounts of wear across the entire span.

Table 5.2 Spanwise aerodynamic drag calculated using the measured drag using a 720 mm contact wire sample. All entries given in N.

Air speed (m/s)	0 mm	2 mm	4 mm	6 mm
3.99	109	82.9	12.8	8.0
4.93	107	80.5	12.7	5.6
6.01	146	74.9	7.2	12.8
7.02	141	78.1	43.5	19.6
8.15	132	86.1	52.3	25.0
9.11	138	100	45.8	25.0

From Table 5.2, it can be seen that as the wind speed increases, the drag force becomes comparable to the mean contact force between the pantograph carbons and contact wire. The growing drag force will also contribute to excessive blow–off increasing the risk of dewirements. The results in Table 5.2 represent the condition of a uniform steady wind acting on a railway contact wire rather than the turbulent conditions that would be created during train passage or discrete ground features that would change the wind direction.

The frequency of the variation in the air pressure around the contact wire can be determined by transforming the measured lift force into the frequency domain using the Fourier Transform. The frequency variation for the cases when the wind speed was 3.99 m/s and 9.11 m/s are given in Figures 5.5a and 5.5b respectively. It can be seen that the measured aerodynamic lift is influenced by a significant amount of noise due to fluctuations in the air in the wind tunnel, evidenced by the large non-commensurate band of frequencies. Significant

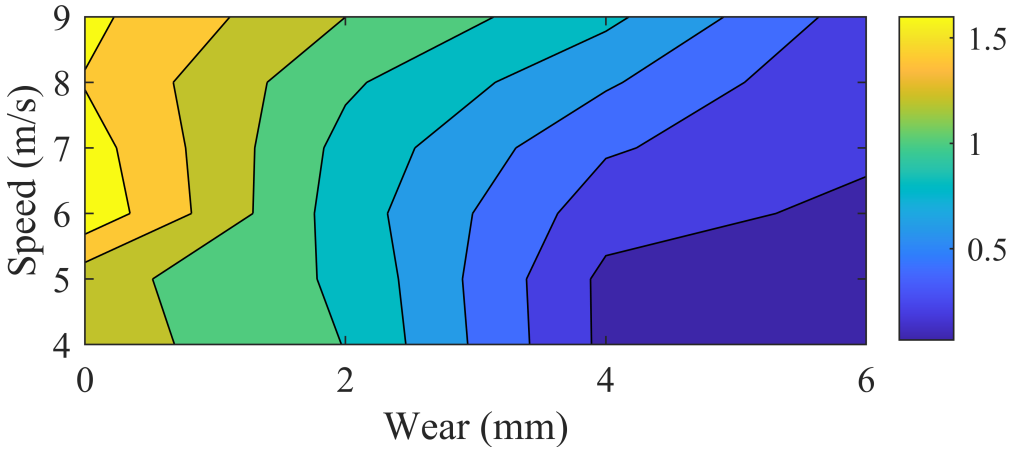

(a) Angle of attack $\theta = 0°$.

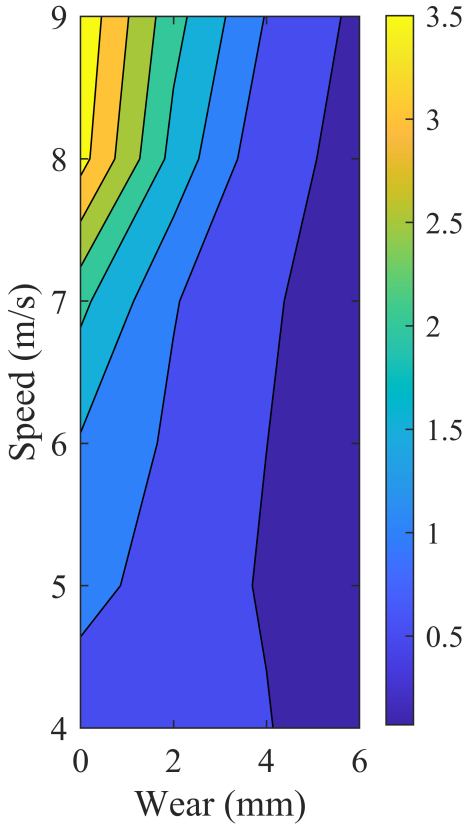

(b) Angle of attack $\theta = -30°$.

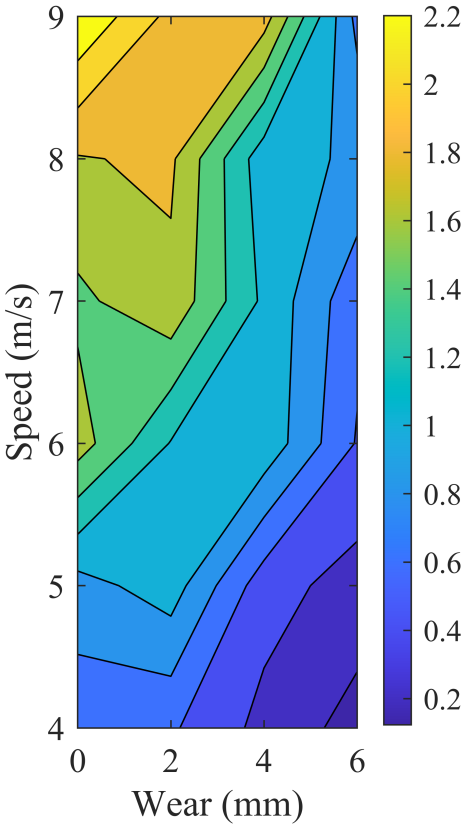

(c) Angle of attack $\theta = +30°$.

Fig. 5.4 Contour plots of measured aerodynamic drag due to wind speed and contact wire wear for angles of attack $\theta = 0°$ and $\theta = \pm 30°$. Legend indicates the magnitude of the mean measured drag.

frequency components can be identified however. For the case when the air speed was 3.99 m/s, a peak is identified at approximately 20 Hz indicating the dominant frequency in the oscillation of the aerodynamic lift. Further harmonics at the frequency can be identified at 37.8 Hz, 60 Hz, and so on. Small variations in the harmonic frequencies are likely due to noise present in the measured lift force.

When the wind speed was increased to 9.11 m/s, the first dominant frequency after the low frequency peak thought to be due to the rotation of the fan, is approximately 46 Hz. Since the wind speed has slightly more than doubled, it follows that the frequency of the lift oscillations has approximately doubled from 20 to 46 Hz. As with the previous case, further harmonics of the dominant frequency can be identified.

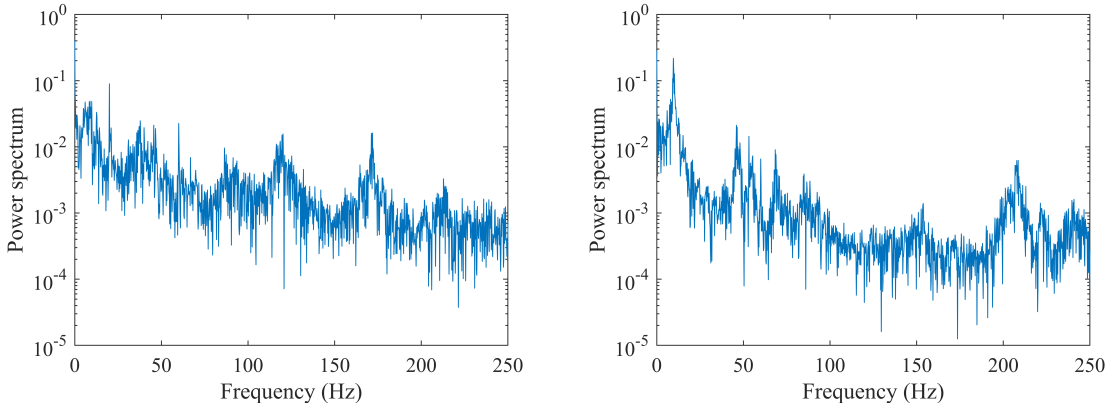

(a) Fourier Transform of the variation in the aerodynamic lift when the wind speed was 3.99 m/s.

(b) Fourier Transform of the variation in the aerodynamic lift when the wind speed was 9.11 m/s.

Fig. 5.5 Power spectra of the variation in the aerodynamic lift force for a contact wire with zero wear and zero angle of attack.

To determine the effect of the angle of attack on the oscillation of the lift force, Figure 5.6 shows the power spectra for a contact wire with 2 mm wear, when the wind speed was 6.01 m/s and the angle of attack was $\pm 10^{\circ}$. As in Figure 5.5, a low frequency peak is observed corresponding to the rotation of the fan and both cases demonstrate a frequency peak at approximately 48 Hz. Whilst Figure 5.6a shows a frequency peak at 33 Hz, since both cases have a wind speed of 6.01 m/s, it is likely that the frequency response to the wind speed is given by the 48 Hz frequency component.

The power spectra indicate that at high wind speed, the lateral deflections of the contact wire under aerodynamic load pose the largest risk to the safe operation of electric trains. The increased aerodynamic drag due to the increased wind speed will cause larger lateral deflections increasing the risk of dewirements. At low wind speeds however, the aerodynamic

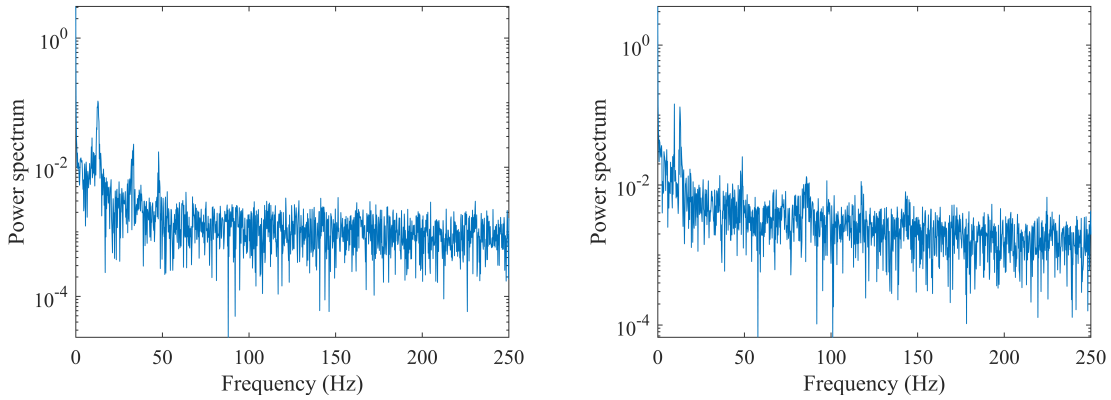

(a) Aerodynamic lift power spectrum when the angle of attack was $-10°$.

(b) Aerodynamic lift power spectrum when the angle of attack was $10°$.

Fig. 5.6 Power spectra of the variation in the aerodynamic lift force for a contact wire with zero wear and wind speed of 6.01 m/s.

lift force oscillates with low frequency. At low frequencies the oscillation amplitude may cause the contact wire to uplift away from the pantograph causing arcing events due to contact loss. This would degrade the current collection quality during train operation and shorten the lifespan of the equipment due to melting of the contact interface. To mitigate the effects of higher wind speeds, adoption of increased line tension would restrict the lateral deflections of the contact wire under high speed aerodynamic loading, and reduce the oscillation amplitude at low speeds, thereby reducing the chance of arcing.

5.3 Simulation results

The simulation output for each of the cases given in Table 3.3 is given in this section. The variation in the drag force on the contact wire due to the air flow is given in Figure 5.8. In the case of a zero angle of attack in Figure 5.7, the drag force grows as the wind speed increases. The largest drag forces are predicted when the contact wire is intact and there is no vertical wear as to be expected since the no wear case presents the largest cross–sectional area to the flow. In all wear cases, the drag force was found to be well fit using a polynomial fit. For example, in the case of zero wear, given by the red line in Figure 5.7, the drag force, $F_{\text{Drag}}(s)$, is predicted by

$$F_{\text{Drag}}(s) = 0.0067s^2 + 0.0547s, \tag{5.4}$$

where s is the wind speed. Equation 5.4 grows as expected since from the drag equation,

$$F_{\text{Drag}} \propto s^2. \tag{5.5}$$

From Figure 5.7 it can be seen that for 0 mm and 2 mm, the fitted curves grow more quickly compared with the curves for the cases of 4 mm and 6 mm wear. It can be seen that as the wind speed increases, the larger aerodynamic forces would induce a larger displacement in the contact wire from the track centre line. However, due to the reduced lateral inertia when a contact wire is severely worn, the larger forces predicted for new or almost new contact wires would not necessarily induce larger displacements in the contact wire lateral position. This will be explored in Chapter 7.

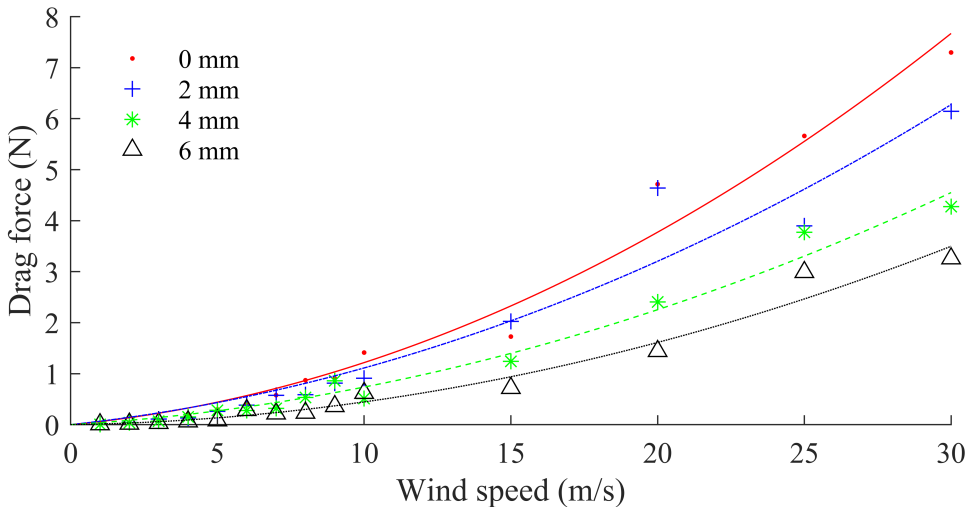

Fig. 5.7 Angle of attack 0°.

Fig. 5.8 Drag force due to an incident flow on a contact wire. Legend indicates the amount of vertical wear applied to contact wear profile. Simulation results are represented by markers in each figure and the lines with the corresponding colour show the polynomial fit to the simulation output.

The fitted curves shown in Figure 5.7 indicate the larger variation in the aerodynamic drag for increasing wind speeds. When the wire was intact with no wear, the largest deviation from the fitted curve was 1.9 N, compared with 0.5 N when the wire wear was 6 mm. This suggests that the increased boundary size when the contact wire cross–section is intact induces large variations in the flow, and in the case of a contact wire, this variation is greatest when the wind speed was 25 m/s. This increased variation at 25 m/s suggests that the contact wire would possibly resonate at this wind speed.

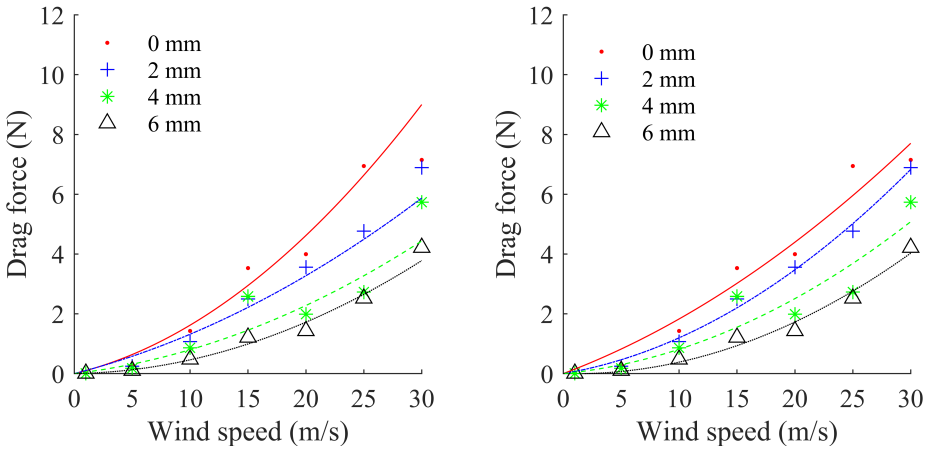

(a) Angle of attack $-30°$.

(b) Angle of attack $-20°$.

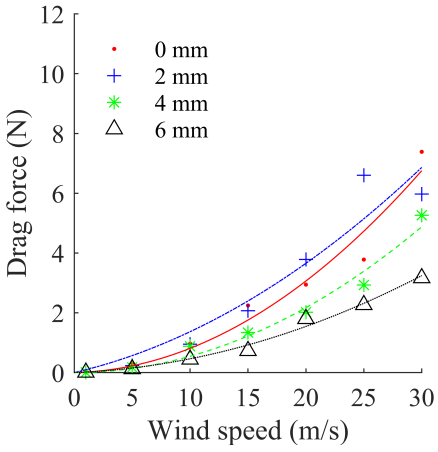

(c) Angle of attack $-10°$.

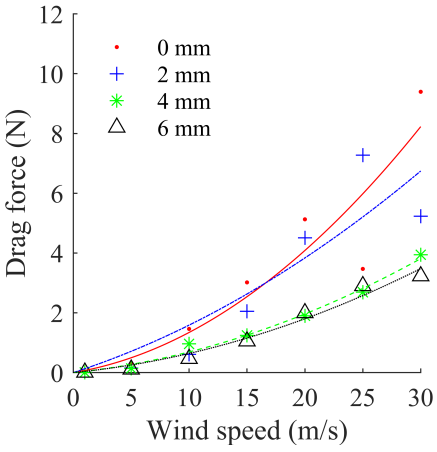

(d) Angle of attack $10°$.

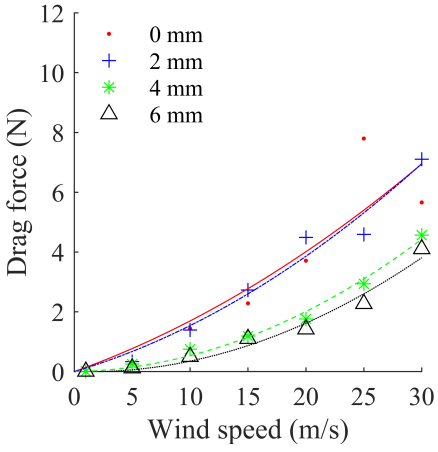

(e) Angle of attack $20°$.

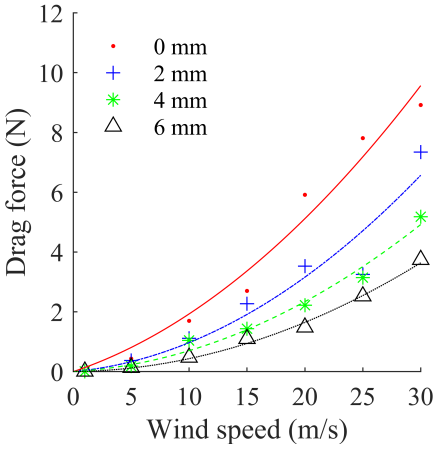

(f) Angle of attack $30°$.

Fig. 5.9 Drag force due to an incident flow on a contact wire at angles of attack between $\pm 30°$. Legend indicates the amount of vertical wear applied to contact wear profile. Simulation results are represented by markers in the figure and the lines with the corresponding colour show the polynomial fit to the simulation output.

The influence of the angle of attack on the aerodynamic drag is shown in Figure 5.9. The orientation of the contact wire due to positive or negative angles is given in Figure 5.2. For negative angles of attack, the contact wire grooves are oriented away from the flow and the air can more easily flow around the smooth semi–spherical boundary along the bottom of the contact wire compared with positive angles where, the grooves are oriented into the flow.

When the angle of attack was 10°, the maximum aerodynamic drag increased from 6 N when the angle was 0° to 10 N. This is likely due to the wire orientation causing a larger pressure on the contact wire in the contact wire grooves. For an angle of -10°, the maximum aerodynamic drag increased also increased, but only to 8 N. When the angle of attack was $\pm 30^\circ$, the maximum aerodynamic drag was 9 N in both cases. In the case of a positive angle, the increased drag was likely due to a greater pressure buildup due to an eddy forming in the contact wire grooves, whereas for a negative angle, the orientation of the boundary allows the fluid to move more easily around the boundary, however the larger surface area in the path of the fluid yields an increased aerodynamic force. The largest predicted drag force occurred for a contact wire with no wear

In a similar way to the case of a zero angle of attack, increasing the wear on the contact wire reduced the aerodynamic drag. For severe wear (4 mm and 6 mm), the variation in the aerodynamic drag was small compared to the variation for 0 and 2 mm wear. When the angle of attack was 10°, the largest variation in the drag between the cases of 4 mm and 6 mm wear was 0.7 N. This increased to 2 N for an angle of attack of -10° and wind speed of 30 $\mathrm{m/s}$.

The aerodynamic lift due to the airflow is shown in Figure 5.11 and Figure 5.12 and each of the curves show the polynomial fit for each of the wear cases. For the 6 mm wear case, the fitted curve has equation

$$F_{\mathrm{Lift}}(s) = -0.139s^2 + 0.0757s, \tag{5.6}$$

which as with the fitted curve for the drag force, is as expected since like the drag equation, from the lift equation $F_{\mathrm{Lift}} \propto s^2$.

It can be seen that as the wind speed increases, the lift force on the contact wire increases in magnitude. For a contact wire with no wear, the contact wire profile is approximately circular, and so experiences a near–symmetric change in the lift force direction compared with the wear cases. This “switching” of the direction of the aerodynamic lift force leads to the large variation in the fitted curves for the aerodynamic lift in Figure 5.12. As the contact wire is worn, there is a trend for the lift force to become negative, most clearly shown in the 4 and 6 mm wear cases. For a contact wire with 2 mm wear, the lift force drops faster than

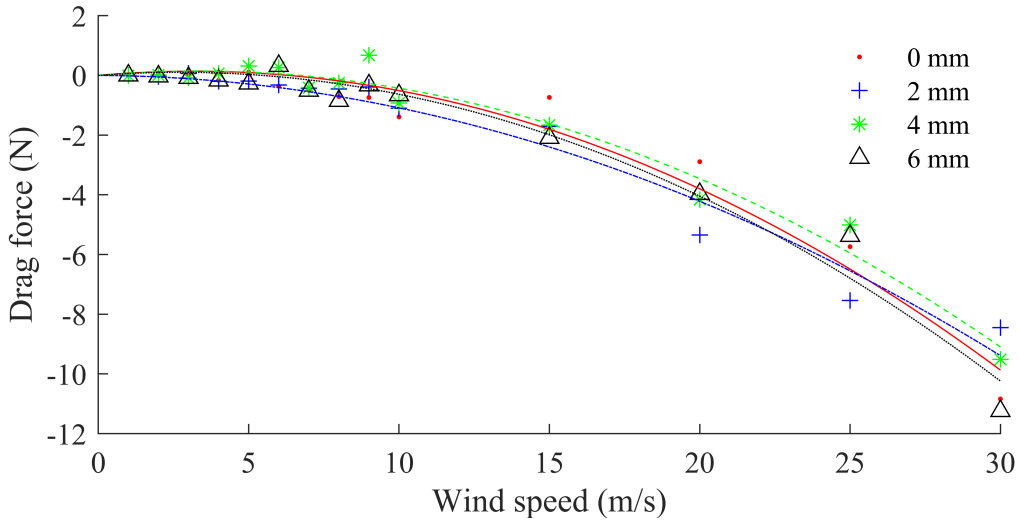

Fig. 5.10 Angle of attack 0°.

Fig. 5.11 Lift force due to an incident flow on a contact wire. Legend indicates the amount of vertical wear applied to contact wear profile. Simulation results are represented by markers in each figure and the lines with the corresponding colour show the polynomial fit to the simulation output.

the lift in the other wear cases, however for a wind speed of 30 m/s, the lift force is smaller in magnitude compared with the other wear cases. From Figure 5.11, for wind speeds less than 10 m/s, the lift force variation due to wear is small, but as the wind speed increases, the wear has a larger effect on the lift of the contact wire. For a wear of 6 mm, the lift force grows more rapidly as the wind speed increases, compared to the 2 mm and 4 mm cases.

The drag and lift coefficients for a contact wire in an incident flow for each of the angles of attack and wear cases given in Table 3.3 are given in Figure 5.13 when the wind speed was 10 m/s. An accepted drag coefficient for a contact wire is given in BS EN 50119 [26] as 1.0 and in [299], the coefficient is given as 0.8. However, the modelling presented here predicts the drag coefficient for a null angle of attack is approximately 1.5 and in [176], the drag coefficient is calculated as approximately 1.4. Both of these results indicate that the expected aerodynamic loads will be underpredicted when calculating the wind load on conductors thus underpredicting the size of the contact wire blow off in windy conditions. This raises the potential for dewirement events that would otherwise be unexpected as the calculated drag forces on the contact wire would be too low.

Due to the oscillations in the pressure caused by the contact wire in the airflow, vortices are shed downstream of the contact wire, generating the classic Von Kármán vortex street.

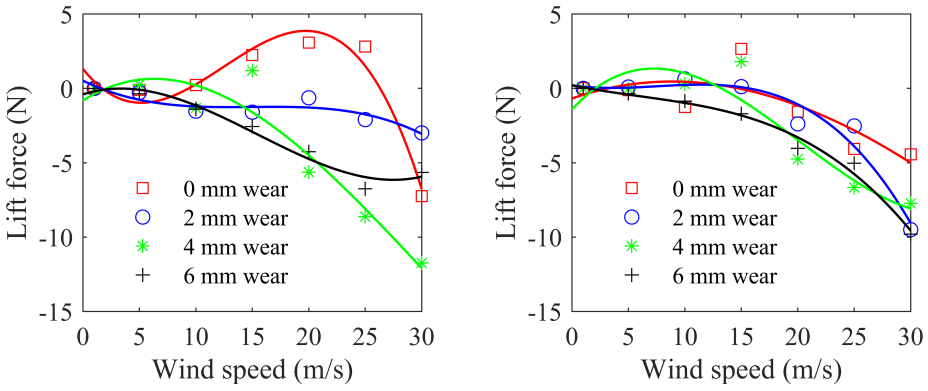

(a) Angle of attack $-30°$.

(b) Angle of attack $-20°$.

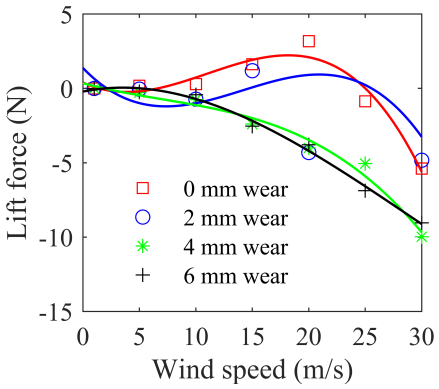

(c) Angle of attack $-10°$.

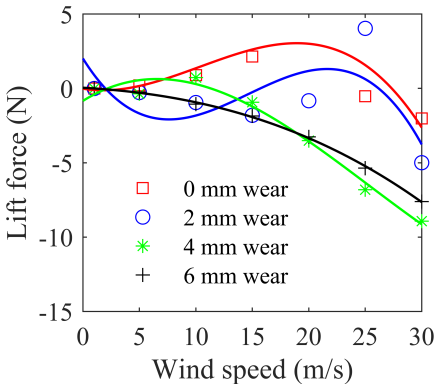

(d) Angle of attack $10°$.

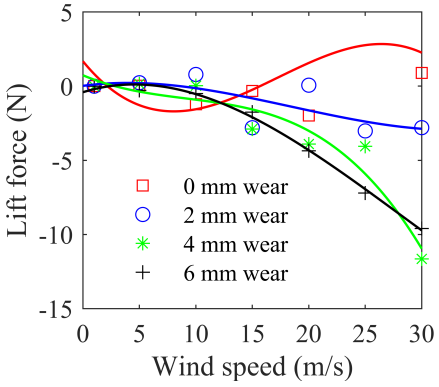

(e) Angle of attack $20°$.

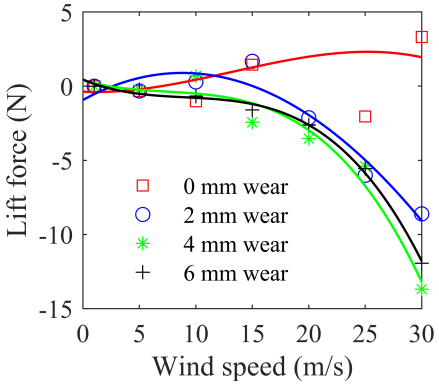

(f) Angle of attack $30°$.

Fig. 5.12 Lift force due to an incident flow on a contact wire. Legend indicates the amount of vertical wear applied to contact wear profile. Simulation results are represented by markers in each figure and the lines with the corresponding colour show the polynomial fit to the simulation output.

The vortex street when the wind speed was 1 m/s and no wear or angle of attack is imposed, can be seen downstream of the contact wire in Figure 5.15a. The asymmetrical contact

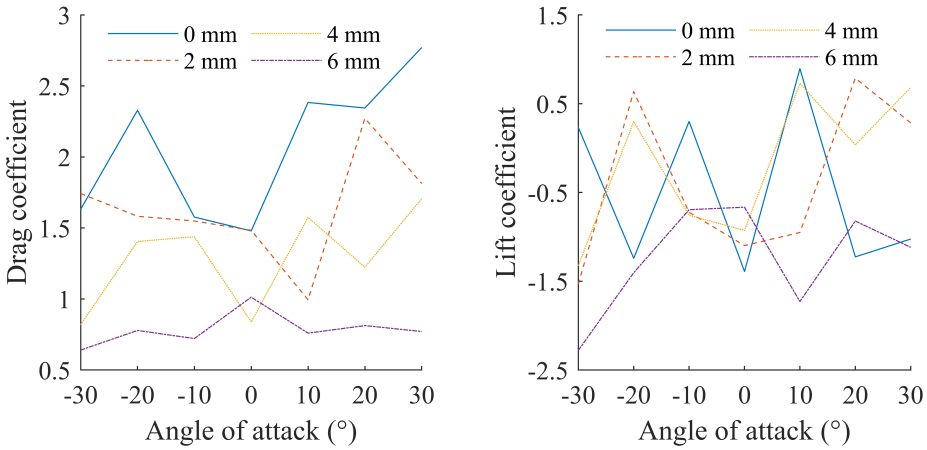

(a) Drag coefficient.

(b) Lift coefficient.

Fig. 5.13 Drag and lift coefficient predictions for each of the considered angles of attack and wear cases given in the legend.

wire boundary causes asymmetrical pressure gradients in the flow resulting in the shedding of the vortices seen in Figure 5.15a. Under aerodynamic load the vortex shedding causes wind–induced vibrations of the contact wire and two types are typically seen with respect to railway overhead lines: buffeting caused by stochastic wind loads and galloping. The onset of galloping is caused by time varying wind loads causing self–excited vibrations of the contact wire with characteristic large amplitudes. The large amplitude vibrations significantly degrade the dynamic performance of the catenary pantograph interaction and severely limit the system's ability to transmit electrical power from the overhead equipment to trains. These large amplitude vibrations cause disruption to the normal operation of electric trains and have the potential to cause large scale damage to the overhead equipment. To assess the likelihood of galloping phenomena, an assessment of the vortex shedding frequencies of the contact wire under aerodynamic load is required, which can be calculated from the time history of the aerodynamic lift, shown in Figure 5.14. The calculated vortex shedding frequencies are then given in Figure 5.16a.

The vortex shedding frequencies for each contact wire wear case is given in Figure 5.16. For a contact wire with 0 mm wear, it is clear that the vortex shedding frequency increases as the fluid velocity is increased. In fact, the vortex shedding frequency for a contact wire with zero wear is well approximated by a logarithmic function $f_v(s) = A\log(s) + B$. As an example, for a zero angle of attack, the vortex frequency can be approximated by the function

$$f_v(s) = 18.53\log(s) + 16.98.$$

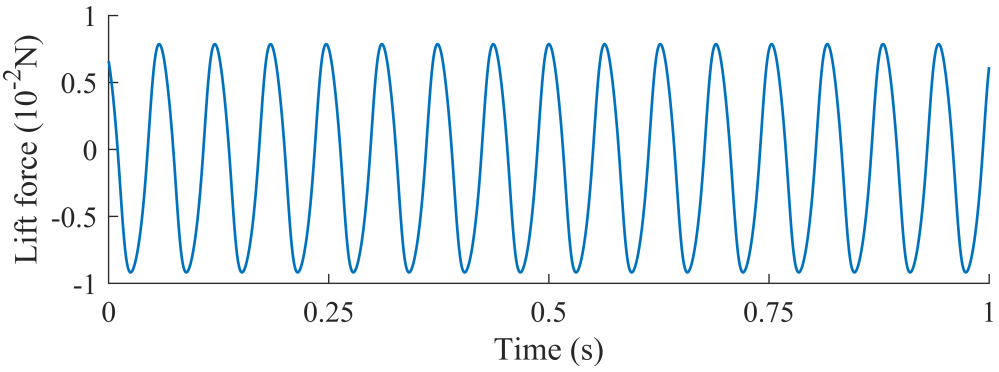

Fig. 5.14 Time varying lift force due to an incident wind load with wind speed 1 m/s and 0° angle of attack on a contact wire with no wear.

From Figure 5.16a, it can be seen that the vortex shedding frequency grows rapidly for wind speeds up to approximately 5 m/s, but then this growth slows as the wind speed increases further. Taking the case of an angle of attack of 30°, the vortex shedding frequency f_v was 14 Hz when the wind speed was 1 m/s and rose to 49 Hz for a wind speed of 5 m/s, compared with an increase in the frequency to 75 Hz when the wind speed was 25 m/s. The increases in the vortex shedding frequency were 250% and 53% respectively, despite the wind speed increase of 400% in both cases.

When the contact wire cross–sectional area is reduced, it can be seen that the vortex shedding frequency increases in magnitude compared with the zero wear case. From Figure 5.16, it can be seen that the maximum frequency increase was relatively small between the zero and 2 mm wear cases as the predicted frequency for zero wear was 88 Hz when the angle of attack was 20°, and for 2 mm wear, the maximum was 107 Hz with a 30° angle of attack. For more severe wear, the increase in the maximum frequency was much larger as the maximum frequencies predicted when the wear was 4 and 6 mm was 262 and 225 Hz respectively. At these higher frequencies, vortices are being shed approximately every 10^{-3} s. Since the timestep used during the simulations was approximately 10^{-5} s, the vortex shedding behaviour was accurately captured.

Figures 5.16c and 5.16d show that as the wind speed increased, at approximately 15 m/s, the vortex shedding frequency increased significantly when the contact wire was severely worn. This behaviour was not predicted for an intact contact wire, as shown in Figure 5.16a. Figure 5.16b suggests that a contact wear of 2 mm is a transition zone for this change in the vortex shedding behaviour, as the predicted frequencies are much less distinctly grouped compared to the 4 and 6 mm wear cases.

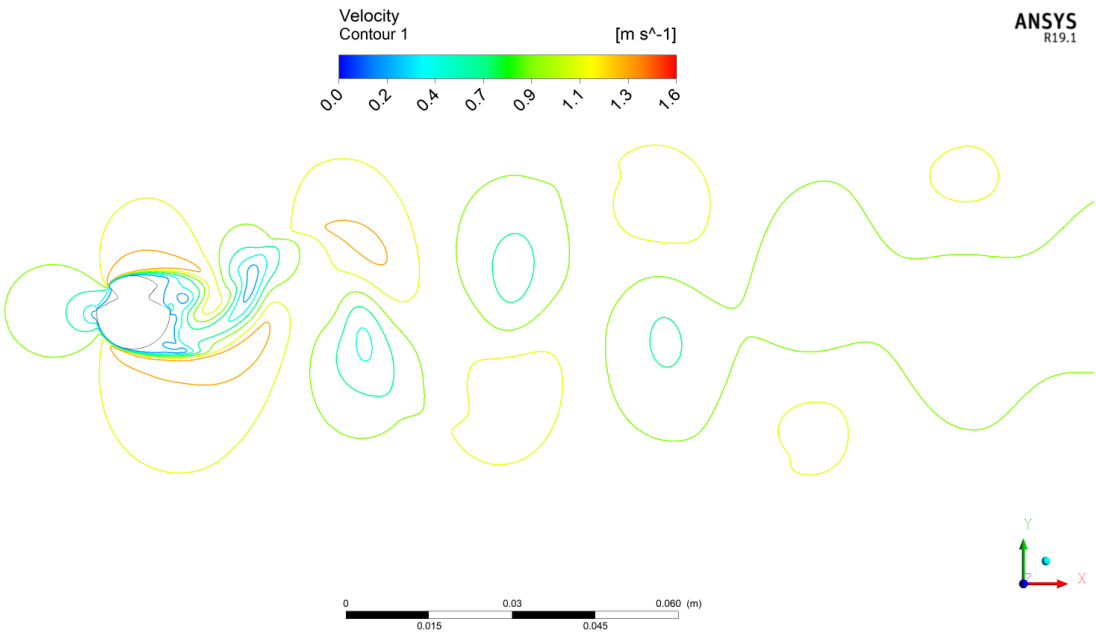

(a) Velocity contour map demonstrating the vortex street developing downstream of the contact wire.

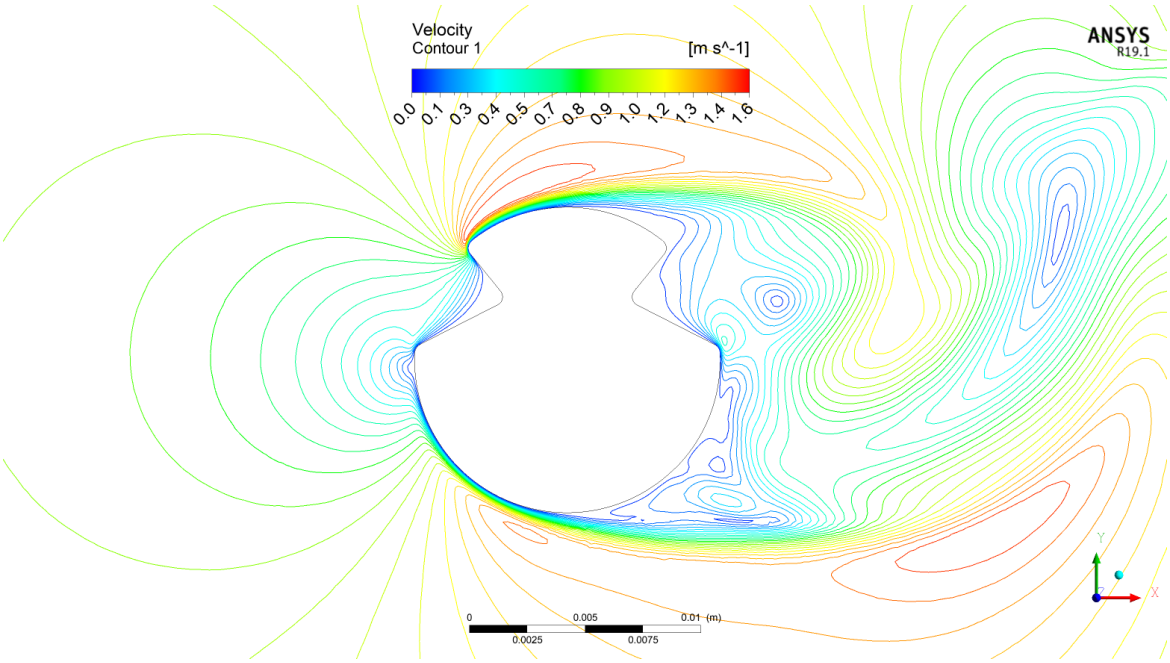

(b) Velocity contour maps in the neighbourhood of the contact wire boundary showing the boundary layer separation.

Fig. 5.15 Velocity contours demonstrating the vortex street and boundary layer separation when a contact wire with zero wear is in a horizontal flow with velocity 1 m/s.

For a given angle of attack θ, from [176], the aerodynamic lift force can be written as

$$F_{\text{Lift}}(s;\theta) = F_{\text{Lift},0} - \frac{1}{2}\rho s A\left(C_D(\theta) + \frac{dC_L(\theta)}{d\theta}\right)u + \mathscr{O}\left(u^2\right) \tag{5.7}$$

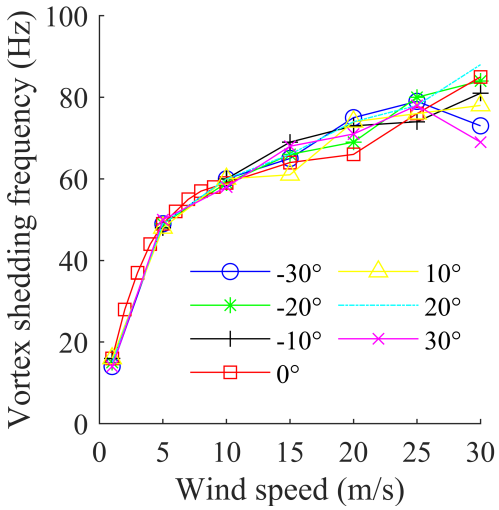

(a) Vortex shedding frequency when the contact wire wear was 0 mm.

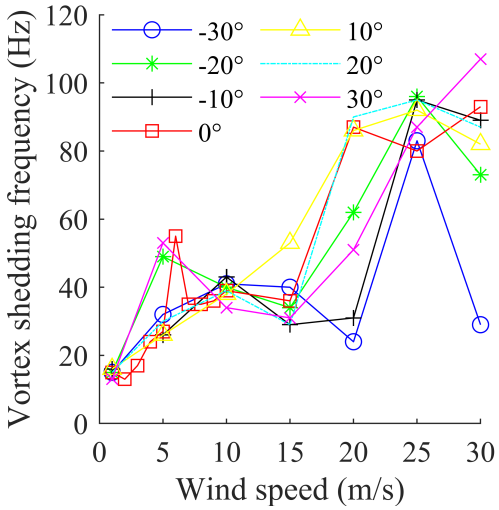

(b) Vortex shedding frequency when the contact wire wear was 2 mm.

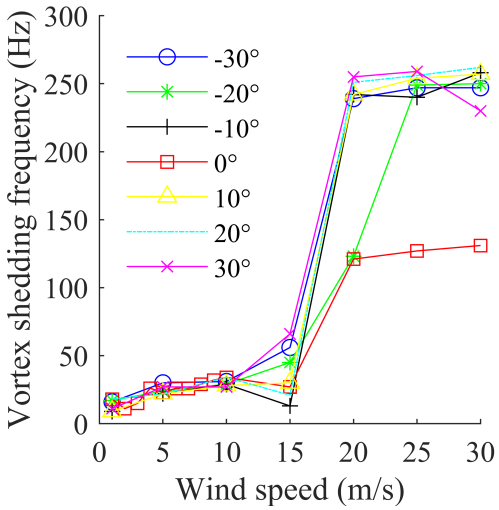

(c) Vortex shedding frequency when the contact wire wear was 4 mm.

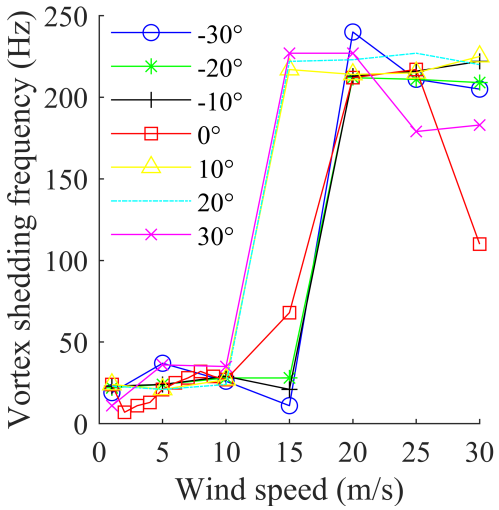

(d) Vortex shedding frequency when the contact wire wear was 6 mm.

Fig. 5.16 The vortex shedding frequencies for a contact wire in an incident flow. The legend indicates the angle of attack of the contact wire in the flow.

where ρ is the fluid density, A is the cross-sectional area of the contact wire, $C_D(\theta)$ and $C_L(\theta)$ are the drag and lift coefficients respectively, which now depend on θ and U_x is the velocity component of the flow perpendicular to the contact wire. Since the vibration of the contact wire is driven by non-constant terms, the aerodynamic damping of the contact wire

C_{fluid} is given by the linear term in Equation 5.7. That is,

$$C_{\text{fluid}} = \frac{1}{2}\rho s A \left(C_D(\theta) + \frac{dC_L(\theta)}{d\theta} \right) u = \frac{1}{2}\rho s A D_h u, \tag{5.8}$$

where

$$D_h = C_D(\theta) + \frac{dC_L(\theta)}{d\theta}, \tag{5.9}$$

is the classic den Hartog coefficient [300]. Typically C_{fluid} is positive and suppresses large vibrations in the contact wire, however changes in the cross-sectional area of the contact wire due to wear or ice loading can lead to negative C_{fluid}. This change in the sign of the aerodynamic damping leads to the onset of large amplitude vibrations known as conductor gallop [301]. For $C_{\text{fluid}} < 0$, it follows that this can only be achieved when $D_h < 0$.

The den Hartog coefficient can be calculated from the drag and lift coefficients predicted during the simulations by way of fitting a polynomial to the output, as in Figure 5.7 and others. Assuming D_{fit} and L_{fit} are fitted polynomials of order N corresponding to C_D and C_L respectively, D_h can be written as,

$$D_h = D_{\text{fit}} + \frac{dL_{\text{fit}}}{dx} = \sum_{n=0}^{N} a_n x^n + \sum_{n=0}^{N} \frac{d}{dx} b_n x^n = \sum_{n=0}^{N} \left(a_n x^n + n b_n x^{n-1} \right). \tag{5.10}$$

In general, the choice of N can lead to differing results in calculation of D_h [302], however the choice of N can be reduced. Since seven data points are provided for both the drag and lift coefficients and from the drag and lift equations, the growth in the aerodynamic force is nonlinear, the polynomials satisfying Equation 5.10 have order $1 < N < 8$. Supposing the lift and drag forces are well fitted by the quadratic polynomials given in Equation 5.4 and Equation 5.6, the polynomials used for the calculation of the den Hartog coefficient can also be taken to be quadratic. Thus, D_h takes the form,

$$D_h = a_0 + b_1 + (a_1 + 2b_2)\, x + a_2 x^2, \tag{5.11}$$

where the coefficients in Equation 5.11 are calculated from D_{fit} and L_{fit}. Using the form of D_h given by Equation 5.11, it follows that the galloping condition $D_h < 0$ is satisfied when Equation 5.11 has real and distinct roots. That is, when

$$(a_1 + 2b_2)^2 > 4a_2 (a_0 + b_1). \tag{5.12}$$

Negating the inequality in Equation 5.12 gives the condition for $D_h > 0$ when galloping cannot occur.

As an example, for the case where the contact wire has zero wear and the angle of attack is 30°, the fitted polynomial for D_h is given by

$$D_h = 3.9 \times 10^{-3} x^2 + 4.3 \times 10^{-3} x. \tag{5.13}$$

Since Equation 5.13 has real distinct roots $x_1 = 0$ and $x_2 = -43/39$, it follows that $D_h < 0$ and galloping can occur.

Equation 5.11 gives no indication for what wind speed the galloping will occur, only that for a the given contact wire wear and angle, if it is possible. To calculate the wind speeds that indicate when galloping is possible, the polynomial Equation 5.11 can be constructed as a function of the wind speed, that is $x \in [0, 30]$, for each angle of attack. Then for each discrete wind speed $x_i \in x$, create the function $x_i(\theta)$ so that x_i is a function of the angle of attack. The graph of each discrete $x_i(\theta)$ is shown in Figure 5.17.

Figure 5.17 gives the den Hartog coefficient D_h against the angle of attack for each of the wear and wind speed cases described in Table 3.3 and the region where $D_h < 0$, known as the galloping region has been highlighted in each case. From Figure 5.17a, it can be seen that galloping can occur most often for angles of attack greater than 15°. In this region, the contact wire is positively oriented as in Figure 5.2a and the build up of eddies within the contact wire groove coupled with the increased air speed around the bottom half of the contact wire is likely to be the driver of the onset of galloping behaviour. Table 5.3 gives the maximum predicted wind speeds for galloping to occur, and it can be seen that when the angle of attack was 20°, the den Hartog coefficient indicated that galloping can occur for wind speeds up to 3.12 m/s. This then drops to 1.56 m/s when the angle of attack is further increased to 30°. For wind speeds beyond these, it is likely that the contact wire resonates and the oscillations are high frequency with low amplitude compared to the low frequency, high amplitude oscillations characteristic of galloping. The small amplitude vibrations however, may lead to an increased number of micro–arcing events as the contact wire is uplifted by the oscillating lift force. Whilst the contact separation between the pantograph head and the contact wire will be small, accumulation of a large number of minor separations will occur for a wire oscillating at high frequency. The large number of micro–arcs at the contact interface will cause melting of the contact surface, shortening the lifetime of the equipment. For negative angles of attack when the contact wire cross–section is intact, D_h indicates that galloping is less likely to occur. As in Figure 5.17a, galloping is predicted only when

the angle of attack is -20° for wind speeds up to 1.65 m/s. For this angle of attack, the contact wire is negatively oriented as in Figure 5.2b and the bottom of the contact wire is oriented into the flow. Since Figure 5.17a indicates galloping is less likely to occur with this contact wire orientation, it follows that this positioning of the contact wire is more resilient to perturbations caused by a steady airflow and will be stable for a larger range of wind speeds and angles of attack. In contrast, as the vertical wear approaches 2 mm, it can be seen from Figure 5.17b that the contact wire is unstable for a much larger range of angles of attack. For a contact wire wear of 2 mm, D_h indicates that galloping is most likely to occur for angles of attack $\theta \in (-15^\circ, 25^\circ)$. For positive angles of attack, galloping is possible for wind speeds up to 3.12 m/s and for a wind speed of 4.05 m/s when the angle of attack is 0°.

Table 5.3 Maximum wind speed for galloping to occur using the den Hartog coefficient. Dashes indicate that galloping is not predicted to occur for any wind speed. All entries given in m/s.

Wear (mm)	-30°	-20°	-10°	0°	10°	20°	30°
0	-	1.65	-	1.62	-	3.12	1.56
2	3.24	-	2.19	4.05	3.12	2.16	-
4	-	-	-	0.66	-	-	-
6	7.21	-	3.99	-	3.6	-	-

The wind speeds at which galloping can occur according to Equation 5.12 are asymmetric with respect to the angle of attack. From the contact wire orientations in Figure 5.2, the contact wire is asymmetric about a vertical axis when rotated. This leads to the asymmetric galloping wind speeds given in Table 5.3. Figure 5.17c shows that galloping is unlikely for a contact wire wear with 4 mm wear. In fact from Table 5.3, it can be seen that galloping behaviour is only possible for a wind speed up to 0.66 m/s. For wear of 6 mm, the onset of galloping occurs over a larger range of angles of attack compared with a contact wire with 4 mm wear, and from Table 5.3, galloping can occur for the greatest possible wind speeds. For a -30° angle of attack, D_h indicates that galloping can occur up to 7.21 m/s. As the angle magnitude is reduced, the maximum wind speed decreases, indicating that galloping becomes less likely for shallower angles of attack in the case of severely worn wires.

The predicted wind speeds for the onset of galloping are consistent with vortex shedding frequencies shown in Figure 5.16. For low wind speeds (less than 5 m/s), the vortex shedding frequencies are approximately less than 20 Hz, indicating that lower frequency behaviour such as galloping is possible. For higher wind speeds (greater than 15 m/s), the vortex shedding frequencies are much higher indicating that resonant behaviour is likely. From

the results in Table 5.3, as the contact wire is worn throughout its service life, the range of wind speeds for which galloping is possible increases. The large amplitude vibrations characteristic of galloping will shorten the lifespan of the equipment due to an increase in cyclic loading, hastening the onset of contact wire fatigue. In the case of a heavily worn contact wire, the yield stress of the equipment is reduced due to the reduced cross–sectional area, thus the galloping phenomena has the potential to cause equipment failures due to exceeding the yield point of the contact wire.

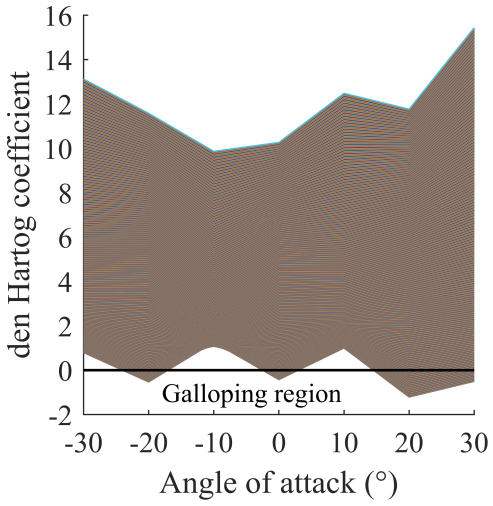

(a) Den Hartog coefficient versus angle of attack for a contact wire with 0 mm wear.

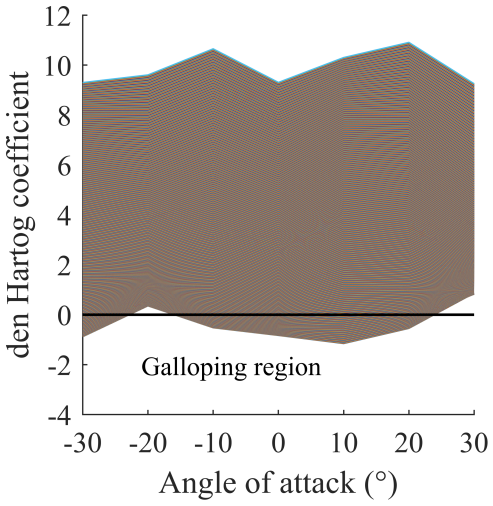

(b) Den Hartog coefficient versus angle of attack for a contact wire with 2 mm wear.

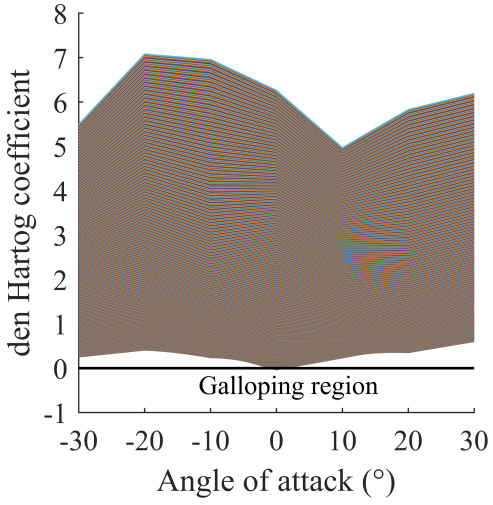

(c) Den Hartog coefficient versus angle of attack for a contact wire with 4 mm wear.

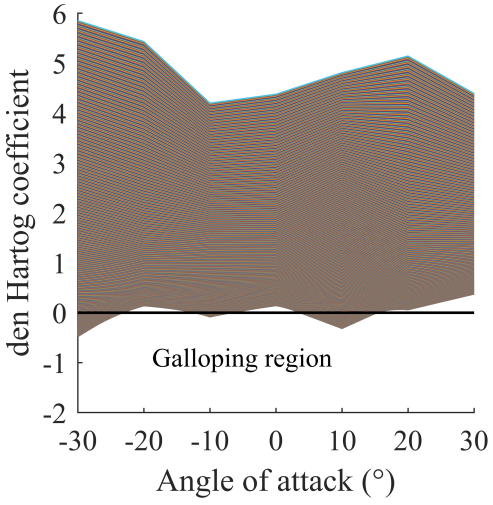

(d) Den Hartog coefficient versus angle of attack for a contact wire with 6 mm wear.

Fig. 5.17 Regions where contact wire galloping may occur using the den Hartog coefficient D_h for 1000 wind speeds between 0 and 30 m/s.

5.4 Comparison between computational and simulated cases

Figure 5.18 gives the comparison between the measured and predicted aerodynamic drag for a contact wire with zero angle of attack. It can be seen that the modelling predictions are in good agreement for the wind speeds considered here. The modelling predictions typically underestimated the drag force on a contact wire, likely due to the idealised nature of the flow compared with the real flow in the wind tunnel. The difference between the measured and simulated drag forces on average are shown in Table 5.4 with largest deviation in the 2 mm wear case.

Table 5.4 Difference between measured and predicted drag values for each of the considered wear cases.

	Wear case (mm)			
	0	2	4	6
Difference (%)	4.1	7.7	1.3	3.7

The differences between the simulated and measured drag forces indicate very good agreement between the two methods showing that the modelling method has been validated giving confidence in the predicted drag forces at wind speeds higher than those permitted in the wind tunnel.

Small deviations between the experimental and simulated cases are likely due to the environmental fluctuations in the wind tunnel, particularly with regards to the wind speed where variation in the wind speed measured at the pitot tube was ± 0.2 m/s. Small variations between the drag values shown in Figure 5.18 may be due to neglecting the effect of vortices that form at the ends of the contact wire sample. In Fluent, these vortices are neglected since the geometry is 2D. Neglecting these vortices requires the vortex drag which occurs when high pressure passes over the end of the contact wire into the low pressure region and dissipates energy from the sample due to fluid viscosity to be neglected. This creates an additional drag that is not captured within a 2D model. The smallness of the variation between the experimental and predicted aerodynamic drag is likely due to the large aspect ratio. Since the length of the contact wire sample was 720 mm long with diameter at most 13.2 mm, this gives an aspect ratio of 55, so the vortex drag, whilst not captured in the 2D model, will only have a small effect on the aerodynamic drag of the contact wire.

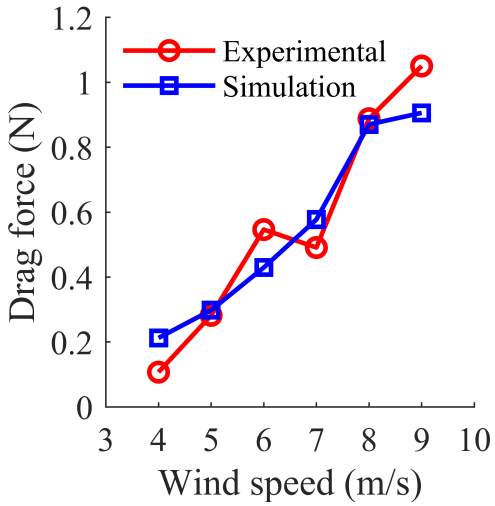

(a) Comparison between experimental and simulation cases with 0 mm wear.

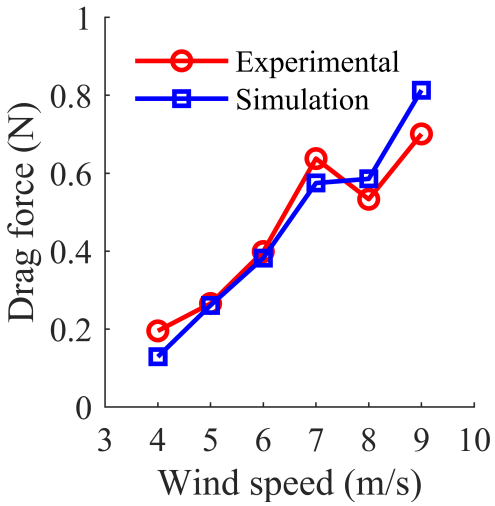

(b) Comparison between experimental and simulation cases with 2 mm wear.

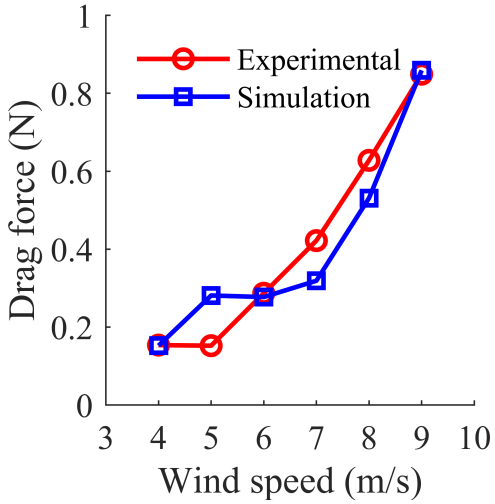

(c) Comparison between experimental and simulation cases with 4 mm wear.

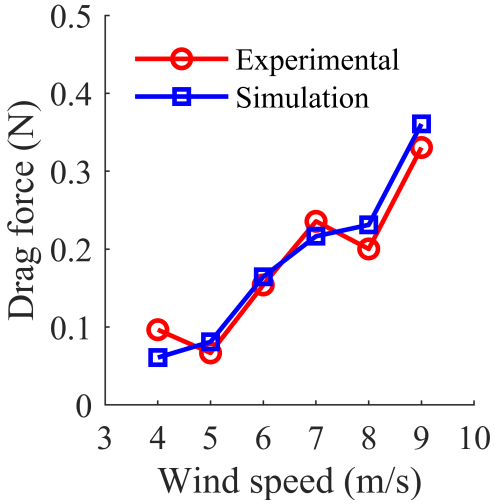

(d) Comparison between experimental and simulation cases with 6 mm wear.

Fig. 5.18 Comparisons between the aerodynamic drag force measured experimentally and those predicted by the simulations for a contact wire with zero angle of attack and the wear cases given.

5.5 Conclusions

Using both experimental and simulation approaches, the aerodynamic loads on a railway contact wire have been determined. With samples of an AC-120 railway contact wire, aerodynamic forces have been measured for a range of test cases using the Sheffield Large Scale Wind Tunnel for a range of wind speeds between 4 and 10 m/s. It was found that the

aerodynamic drag increased as a response to increasing wind speed for each of the four wear cases considered in this study. The test cases identified that the angle of attack can have a significant effect on the aerodynamic drag as the amount of wear is increased. This was most clearly seen when the wear was increased to 4 mm. At this wear rate, the largest aerodynamic drag is due to an angle of attack of 30° compared to -30° when there was no wear applied.

The study was limited to steady sidewinds acting on a railway contact wire in the absence of turbulent effects such as train passage, pressure waves at tunnels or discrete ground features causing changes in the wind direction. Whilst the turbulent effects of train passage have been neglected, the aerodynamic forces on a contact wire in the intervening periods between trains have been considered to determine the wire condition upon the arrival of a train.

From the experimentally derived drag forces, the spanwise drag for a typical span of railway line contact wire has been calculated indicating that as the wind speed increases, the aerodynamic forces are comparable to the contact force between the train and overhead line. Since the forces are comparable it is expected that there will be a significant impact on the current collection quality during train operation. The high frequency behaviour caused by the aerodynamic lift predicted at high wind speeds has the potential to cause micro–arcing between the contact wire and pantograph carbons. Individual micro–arcs are themselves little danger to the catenary pantograph interaction, however at high wind speeds, the high frequency oscillating contact wire will cause a rapid accumulation of micro-arcing events. The sum of each event will deteriorate the contact interface increasing the wear rate during train operation. In contrast, the low frequency phenomena of galloping can lead to damage of the overhead contact system over short timescales due to the large amplitude oscillations of the contact wire.

To overcome the practical limitations of the wind tunnel, a 2D representation of a contact wire in a flow was created in a commercial software to investigate a larger range of air speeds, up to 30 $\mathrm{m/s}$. It was found that the aerodynamic drag decreased with contact wire wear as expected and also that positive angles of attack typically increased the predicted drag, likely due to the orientation of the contact wire placing the contact wire grooves rather than the smooth semi–circular base into the flow.

Aerodynamic lift predicted by the simulations was found to increase in magnitude with increasing wear. For the severe wear cases of 4 and 6 mm, there was small variation between each of the predicted aerodynamic lifts and the magnitude typically grew quadratically. However for the zero and 2 mm wear cases, the lift variation was approximately cubic. As the angle of attack was varied, when the wind speed was approximately 20 $\mathrm{m/s}$, the growth of the lift force changed sign, indicating that flow separation occurs.

The simulations also identified the downstream behaviour due to the flow around the contact wire. Beyond the contact wire, a classic von Kármán vortex street develops due to shedding of vortices from the edges of the contact wire. The frequency at which these vortices were shed was determined using the oscillations in the lift coefficient and it was found that wear is a significant driver for changes in the vortex shedding frequency. For an intact contact wire, the angle of attack had little effect on the shedding frequency and the dominant driver was the wind speed. As the wear was increased however, the vortex shedding transitioned into two clear defined groups. Below wind speeds of 15 $\mathrm{m/s}$, the shedding frequency was less than 50 Hz and for speeds greater than 15 $\mathrm{m/s}$, the frequency significantly increased to approximately 250 Hz. This was most clear for wear greater than 2 mm, with the 2 mm indicating a transition stage. Whilst the amplitude of the oscillations is small for such high frequency, as discussed before, micro–arcing between the contact surfaces would degrade the contact wire surface.

From the drag and lift coefficients generated during the simulation process, calculation of the classic den Hartog coefficient was performed. With this, the onset of galloping of a railway contact wire was established. From the den Hartog coefficient, galloping was indicated to occur most often for positive angles of attack, particularly for mildly worn contact wire. The wind speeds for which it is possible for the contact wire to gallop were also determined. For increasingly worn contact wire, the likelihood of galloping was increased due to a larger range of angles of attack and wind speeds for which it is possible. For a contact wire with 2 mm wear, conductor gallop is possible for almost all angles of attack between -15° and 25° and for wind speeds up to 4 $\mathrm{m/s}$. The calculation of the wind speeds for which galloping is possible was consistent with the change in the vortex shedding frequencies as the wind speed increased. Since conductor gallop was indicated to occur for low wind speeds, this corresponded to low shedding frequencies which were found to occur for speeds less than 15 $\mathrm{m/s}$.

Comparison between the measured and predicted aerodynamic forces was made and there was good agreement between the measured and predicted aerodynamic drag forces for the wind speeds considered during the wind tunnel tests. Variation between the results is thought to be due to 3D effects such as vortex drag that is not captured in the 2D model, however the variation is small. Since the variation between the drag forces was small, the experimental tests performed as a validation of the computational cases, suggesting that the modelling assumptions made are valid for the higher wind speeds considered. With the validation of the numerical methodology, the aerodynamic loads on a range of equipment types can be established, allowing for the prediction of blow off when installed on the rail network, or

for the prediction of conductor gallop situations. With wind speeds expected to increase due to climate change, existing equipment may become susceptible to failure due to increases in wind speed outside of current design limits. The methodology presented here provides a method for predicting the behaviours of existing equipment at those higher wind speeds.

The work performed here has demonstrated the aerodynamic loads on a railway contact wire and serve as input for modelling the effect of wind loading on overhead line equipment and the effect on the current collection quality between a pantograph and catenary system. This will be discussed in the Chapter 7.

Chapter 6

Sensitivity of the catenary pantograph interaction

6.1 Introduction

The catenary pantograph interaction is affected by numerous physical parameters which can be separated into those related to the overhead line and those related to the pantograph. Largely, the overhead line parameters ensure a good vertical wire profile to reduce occurrences of contact loss during train operation. The pantograph parameters ensure a good dynamic response to the sliding contact with the contact wire. This Chapter presents the results of the investigation into a range of the physical parameters of the catenary pantograph interaction using a nonlinear finite element model developed using a commercial package, ANSYS. The modelling methodology was described in Sections 3.2.1 – 3.2.4 and the model is then used both to gain insight into the dynamic response to a change in a parameter but also as a generalisation of the model presented in [241]. In Section 6.2, the effect of alteration of the overhead line is considered with all the pantograph parameters fixed. The parameters varied are:

- the contact wire tension,
- the messenger wire tension,
- the absence of a dropper,
- the contact wire mass per unit length,

and then in Section 6.3, the pantograph parameters altered are:

- the pantograph head collector strip mass,
- the pantograph head frame mass,
- the stiffness of the bar connecting the pantograph head and collector strip, and
- the static uplift applied to the pantograph.

Finally, Section 6.4 considers the effect on the contact force as a response to increasing train speed. Mitigation of the effects of an increased train speed are also discussed with respect to the number of droppers in a span and conclusions based on the results are given in Section 6.5.

Throughout this Chapter the overhead line geometry with respect to the longitudinal positions of the droppers and masts are kept constant except where specified. Twelve identical spans were used, and the support masts are located every 60 m. This allowed a working section between 300 m and 420 m with five spans either side to be used allowing for end effects to be discounted. The number of and length of the droppers was maintained from an as fitted span used as part of the overhead line at Network Rail's Melton Rail Innovation and Development Centre (RIDC) [285]. The physical parameters of the overhead line equipment are given in Table 6.1 and the dropper lengths and their positions within each span are given in Table 6.2.

Table 6.1 Overhead line base case parameters based on UK Series 1 overhead line equipment installed at Network Rail's RIDC.

Component	Parameter	Value	Unit
Contact wire	Tension	16.5	kN
	Mass	1.07	kg/m
	CSA	120	mm^2
Messenger wire	Tension	13	kN
	Mass	0.6	kg/m
	CSA	65	mm^2
Dropper clamps	Mass	0.15	kg
Dropper stiffness	Tension	1260	kN/m
	Compression	0	kN/m

Table 6.2 Dropper locations and their lengths used in the sensitivity analysis.

Dropper	1	2	3	4	5
Location from start of span (m)	5.5	17.75	30	42.25	54.5
Length (m)	1.09	0.94	0.845	0.94	1.09

6.2 Influence of overhead line parameters

6.2.1 Contact wire tension

The contact wire tension directly influences the vertical geometry of the overhead line and is crucial to good current collection quality during operation. The wire tension also affects the mechanical wave speed c_s, in the contact wire given by

$$c_s^2 = \frac{T_{con}}{m_{\text{con}}}, \tag{6.1}$$

where T_{con} is the contact wire tension and m_{con} the mass per unit length. The maximum operating speed for a given overhead line is given as 70% of the mechanical wave speed [13, pg. 155] to ensure no contact losses due the pantograph catching up to the mechanical wave, as discussed in Chapter 2.6. Thus, for the train speed considered, 200 km/h, the minimum contact wire tension required is 6.74 kN.

From Figure 6.1, when the contact wire tension was reduced by 25% to 12.4 kN, a greater variation in the contact force in between the first and last droppers is predicted. The minimum contact force predicted just after the droppers at 318 and 378 m is 18% lower when the contact wire tension is reduced when compared with the base case of 16.5 kN. There is a similarly sized increase at the fourth dropper, where a 15% increase in the contact force was predicted. The largest peak at the last dropper only increased by 3 N in comparison. Since the unsupported length between intermediate droppers is 12.25 m compared to 5.5 m between the supports and first and last droppers, the greater sag due to the reduced contact has a detrimental effect on the dynamic performance.

In contrast, increasing the wire tension lead to predicted smaller force peaks at intermediate droppers in comparison to the base case. The peak force at the last dropper was unchanged when the wire tension was increased by 25%, and only saw a small decrease of 2 N when the tension was increased further. Since the force peak was largely unchanged, it suggests that the droppers remained in tension in the absence of the pantograph uplift even for a 50% higher wire tension. Too high a tension would reduce the contact wire sag for the

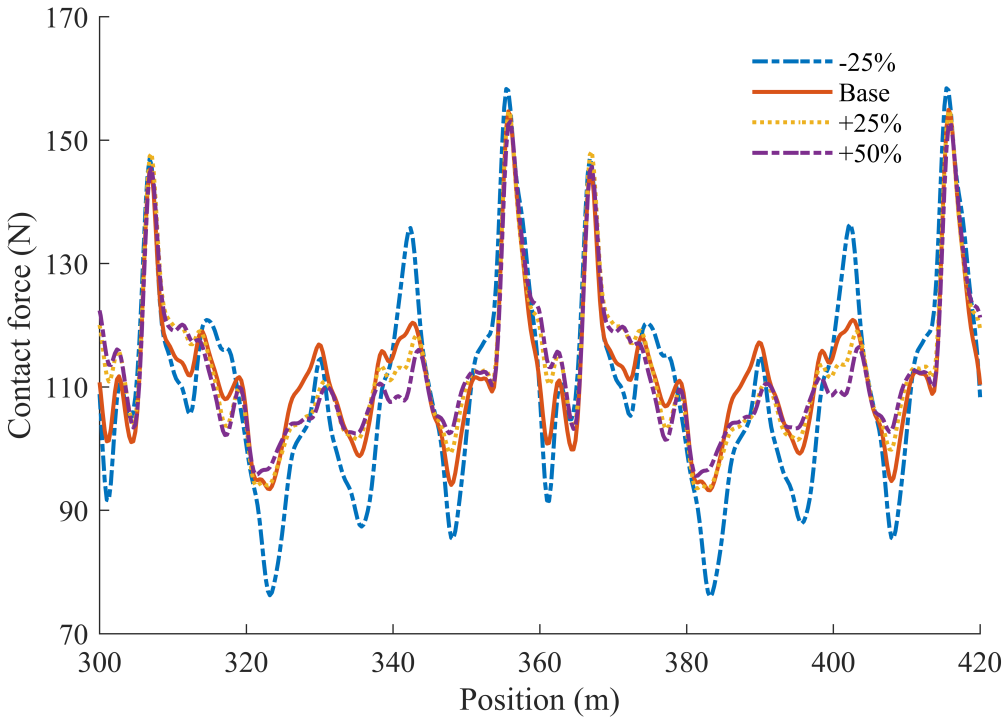

Fig. 6.1 Contact force variation due to different contact wire tensions. Legend indicates the amount the contact wire tension has been varied from the baseline tension of 16.5 kN.

given dropper length leading to dropper buckling giving zero resistance to wire uplift during pantograph passage.

The statistical output for the modelling predictions is presented in Table 6.3 and shows the increased standard deviation of the contact force as a result of the reduced contact wire tension. Whilst the standard variation was within 0.3 N of the base standard deviation when the contact wire tension was increased, in the case of a reduced wire tension, the standard deviation increased by just under 5 N. The significant variation in the contact force at intermediate droppers compared with higher wire tensions is likely responsible for this 43% increase in the standard deviation, despite the mean only changing by 2%. The small change in the mean indicates that the increase in the magnitude of the forces predicted at the intermediate droppers was similar. This is consistent with the changes in the contact force noted above. As the wire tension was increased, the contact force was increasingly positively skewed indicating that the contact force was more consistently below the mean and the peak force at the final dropper was the significant outlier.

As the contact wire tension was increased, the contact wire uplift at the support at 360m decreased. For a wire tension of 12.4 N, the maximum wire uplift at the support was 53

Table 6.3 Contact force statistical output for a level contact wire as the contact wire tension is varied. All results in N.

Tension (kN)	F_m	σ	$F_{D_{\max}}$	$F_{D_{\min}}$	$F_{S_{\max}}$	$F_{S_{\min}}$	Skew	Kurtosis
12.4	110	16.9	158	76.0	161	59.6	0.502	0.217
16.5	112	11.8	155	93.2	147	76.4	1.31	2.42
20.6	113	12.1	155	93.5	149	76.2	1.31	2.11
24.8	112	11.5	153	95.6	147	78.0	1.51	2.38

mm, and this decreased to a maximum wire uplift of 38 mm when the contact wire tension was 24.8 N. The wire uplifts at the support can be seen in Figure 6.2. Changes in the contact wire tension from the base tension of 16.5 kN had little effect on the frequency of the oscillations after the pantograph had passed the support, however a phase shift can be seen. From Equation 2.18, the oscillation frequency of the wire $\omega_m \propto T^{1/2}$, where T is the wire tension. Thus as the wire tension varies, so to does the frequency. The increased frequency as a response to the increased wire tension can be seen from the wire uplift traces in Figure 6.2. Since the amplitude of the wire uplift oscillations was reduced by increasing the contact wire tension this would open up opportunities for reduced clearances under bridges and tunnels when installing overhead line equipment. The increased tension also appears to have little effect on the peak contact forces suggesting that they would not cause significant issues during height transitions where larger forces are predicted due to the pantograph accelerations when changing heights. The increased mechanical wave speed as a response to the increased wire tension would also allow for an increase in the line speed opening up extra line capacity without the need for large scale investment in new lines.

The results show that if the effective wire tension drops, often caused over the lifetime of the equipment as the tensioning equipment becomes less effective, a larger variation in the contact force is predicted which leads to a poorer dynamic performance due to the wire deviating from the vertical profile design due to an increased sag. The same is also true for higher ambient temperatures. Thermal expansion of the contact wire causing an increased contact wire sag leads to a similar contact force variation degrading the catenary pantograph interaction. In contrast, increases the contact wire tension can be implemented to improve the dynamic performance by reducing the peak forces at droppers. This may lead to potential increases in the line speed without the need for a complete redesign of the overhead equipment.

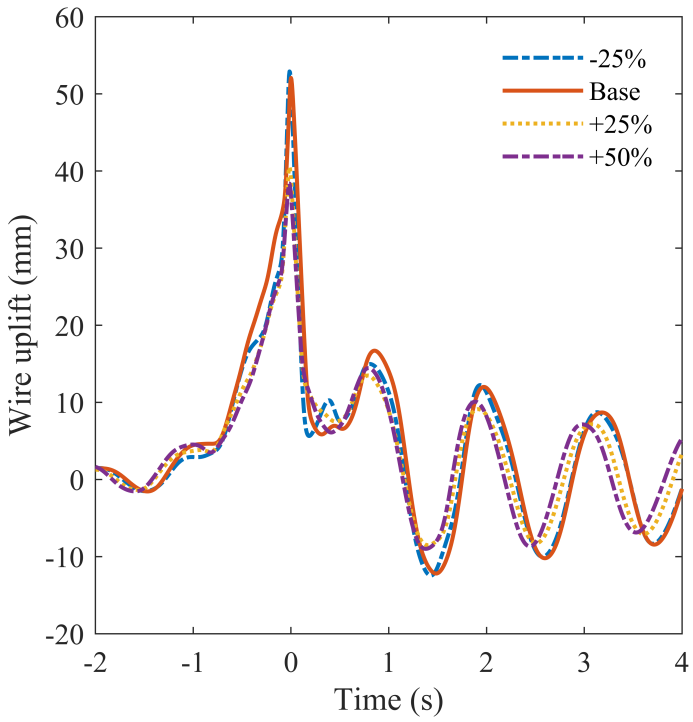

Fig. 6.2 Wire uplift at the support between spans six and seven. Legend indicates the amount the contact wire tension has been varied from the baseline tension of 16.5 kN. Zero time is the moment the pantograph passes the support.

6.2.2 Messenger wire tension

Whilst the contact wire tension largely affects the vertical position of the contact wire and prevents undesired sagging, the messenger wire tension affects the whole vertical geometry of the system due to the droppers coupling the messenger and contact wire geometries. High ambient temperatures or a reduction in the tension effectiveness over the lifetime of the equipment causes extra sagging in the contact wire whilst negative sag occurs if the tension is too high. Naturally, the dropper lengths are chosen to ensure the correct amount of contact wire sag irrespective of the messenger wire tension, however to investigate the influence of the messenger wire tension of the catenary pantograph dynamics, the dropper lengths have been left unchanged throughout.

Figure 6.3 gives the change in the contact force for the catenary pantograph interaction due to the change in the messenger wire tension. It can be seen that reducing the messenger wire tension leads to an increase in the peak forces predicted at the first and last droppers. For wire tensions of 9.8 and 6.5 kN, the peak force increased by 18% and 37% respectively. This likely due to the increased sag in the contact wire due to increased sag in the messenger

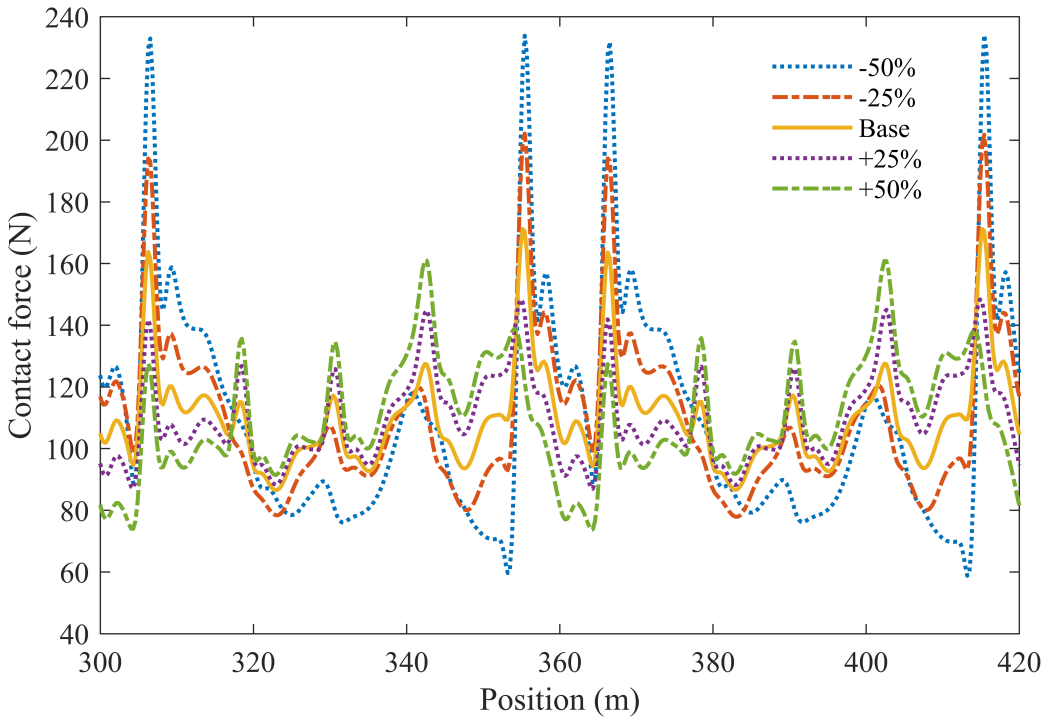

Fig. 6.3 Contact force variation due to different messenger wire tensions. Legend indicates the amount the messenger wire tension has been varied from the baseline tension of 13 kN.

wire as a result of the reduced tension. Since the contact wire height has been reduced, the pantograph head has a larger variation in the operating height when compared with the base case. This larger range of operation requires larger forces to accelerate the pantograph head and change its direction in order to follow the contact wire profile. In contrast, increasing the messenger wire tension has the effect of reducing the sag of the contact wire and leads to reduced peak force. The benefit of increasing the contact wire tension to reduce the peak forces predicted at the first and last dropper appears to be self-limiting for the overhead line geometry used during the simulation however. This is likely due to the increased tension causing an uplift in the contact wire height removing the desired presag. As can be seen in Figure 6.3, increasing the messenger wire tension reduces the peak force at the first and last droppers in a span compared with the base case. However, at other droppers, the local force maxima increased compared to the base case.

Considering the contact force at each time step for the given messenger wire tensions, and plotting the contact force as a function of messenger wire tension rather than time, Figure 6.4 shows that there is a large variation in the contact force at each time step as a function of the wire tension. However, when the messenger wire tension was 16.25 kN, this variation is at a

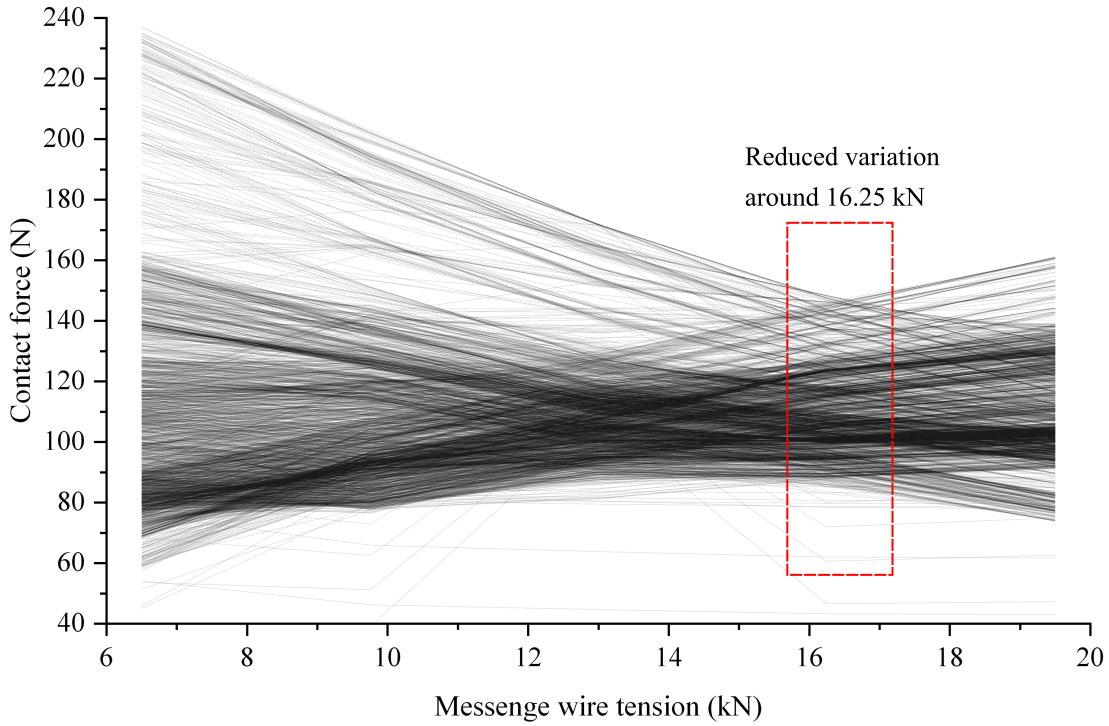

Fig. 6.4 Contact force as a function of the messenger wire tension. The contact force at each time step is plotted for the five messenger wire tensions considered.

minimum suggesting that matching of the contact and messenger wire tensions is beneficial to the catenary pantograph interaction. Since the increased tension is below the breaking load of 35 kN [303], the messenger wire tension could be increased to match that of the contact wire to give a better dynamic performance as indicated by the reduced contact force standard deviation in Table 6.4.

From the statistical output in Table 6.4, the best performing case was when the messenger wire tension was increased by 25% to 16.3 kN, almost to the contact wire tension. The reduced peak forces when compared with the base case would indicate a reduced mechanical wear regime potentially extending the service life of the equipment. The reduced standard deviation also suggests an improved dynamic performance during the catenary pantograph interaction. This is consistent with the decreasing skewness of the contact force.

The effect of the reduced messenger wire tension is most pronounced on the contact wire uplift. The wire uplift at the support at 360 m is given in Figure 6.5, where it can be seen that reducing the messenger wire tension leads to an greater wire uplift. By halving the messenger wire tension, the wire uplift at the support was 60 mm, which was 15 mm greater than in the base case. The reduced tension also lead to a large increase in the amplitude of the

Table 6.4 Contact force statistical output for a level contact wire as the messenger wire tension is varied. All results apart from skewness and kurtosis in N.

Tension (kN)	F_m	σ	$F_{D_{\max}}$	$F_{D_{\min}}$	$F_{S_{\max}}$	$F_{S_{\min}}$	Skew	Kurtosis
6.5	110	36.2	234	58.8	219	1.55	1.32	1.75
9.8	110	25.5	202	77.9	187	33.7	1.42	2.25
13	110	15.9	171	86.5	158	62.5	1.58	3.30
16.3	110	14.2	148	87.0	153	67.4	0.675	-0.182
19.5	110	18.4	161	73.8	165	54.9	0.371	-0.232

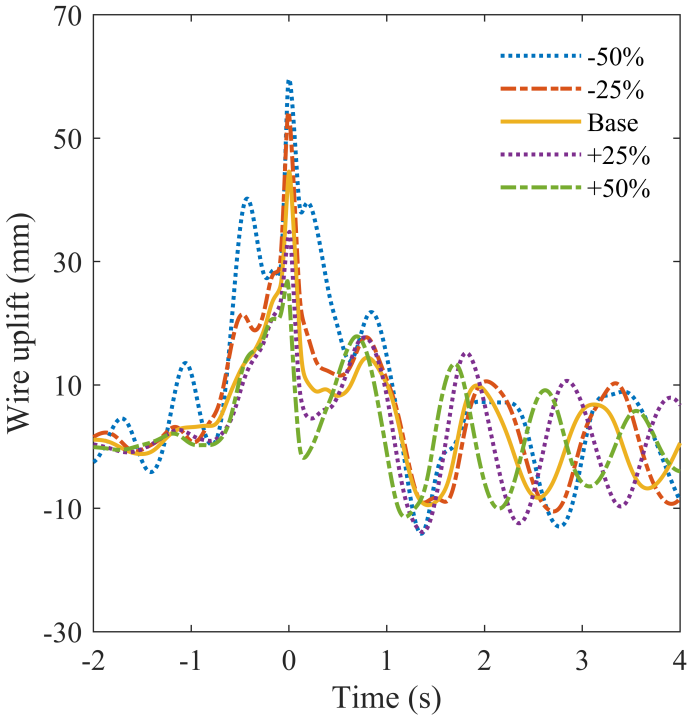

Fig. 6.5 Wire uplift at the support between spans six and seven. Legend indicates the amount the messenger wire tension has been varied from the baseline tension of 13 kN.

oscillations in the wire caused by the mechanical wave before the passage of the pantograph. This greater variation in the oscillations in the contact wire would see a reduced quality in the contact between the contact wire and the pantograph collector strips. The increased cyclic loading of the contact wire due to sustained oscillations would also see a reduction in service life due to an earlier onset of wire fatigue. Increasing the tension in the messenger wire reduced the wire uplift at the support. A 25% increase in the wire tension lead to a 10 mm reduction in the wire uplift and a further increase in the wire tension reduced the wire

uplift even further to 29 mm. The effect on the contact wire oscillation after the pantograph passed was greater when the messenger wire tension was changed compared with the change in the contact wire tension as can be seen in Figure 6.2 and Figure 6.5 where a change in the messenger wire tension allowed for greater amplitude oscillations in the contact wire before the pantograph reached the support in contrast to a change in the contact wire tension where the oscillation amplitude remained small compared with the wire uplift. The larger amplitude oscillations could lead to a shortening of the service life due to an earlier onset of fatigue if the equipment damping was maintained. Increasing the effective damping of the messenger wire using dampers installed at the supports would reduce the transient period after train passage, reducing the number of load cycles thus maintaining the service life while also promoting a better dynamic performance. The variation in the messenger wire tension also lead to a phase shift in the wire oscillations, however the phase shift was greater than that seen as the contact wire tension varied. The larger phase shift is likely due to the factor ρA in Equation 2.18. Since ρA is smaller for a messenger wire compared with a contact wire, it follows that $(\rho A)^{-1/2}$ is larger, thus leads to an increase variation in the wire oscillation frequency compared with the contact wire variation.

6.2.3 Dynamic response to a missing dropper

The droppers are used suspend the contact wire from the messenger wire at the correct height to ensure good dynamic performance during operation. Over the lifetime of the equipment the droppers can become ineffective due to a shift in the equipment due to settlement of the embankment causing movement of the supports or due to damage. Shifting of the equipment can lead to buckling of the droppers whilst damage to the droppers can be minor if the damage occurs away from the contact interface or catastrophic if the dropper hangs down in the path of the pantograph. Removal of the droppers, say due to breakage, is likely to have a detrimental effect on the dynamic performance of the overhead line due to the improper vertical geometry of the contact wire. Thus it is prudent to study the effect a missing dropper has on the catenary pantograph interaction: that effect is presented here and Figure 6.6 shows the overhead line geometry used.

The contact force variation due to the removal of a dropper is shown in Figure 6.7. It can be seen that in the spans before and after the span containing the missing dropper, the contact force is unchanged indicating that the effect of an absent dropper is restricted only to the span without the dropper. In the span where the dropper is missing, the contact wire sags below the normal height as the unsupported length is 24.5 m compared with the usual

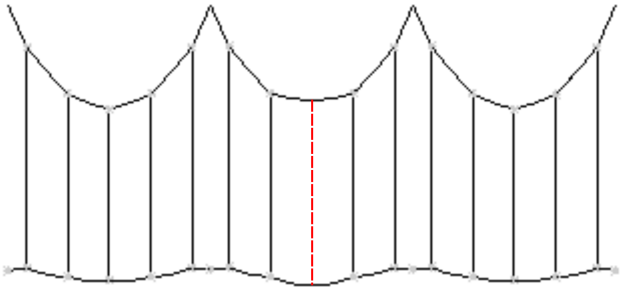

Fig. 6.6 Working section of the overhead line geometry used to represent an overhead line with a missing dropper. The location of the missing dropper at midspan is highlighted by the dashed red line.

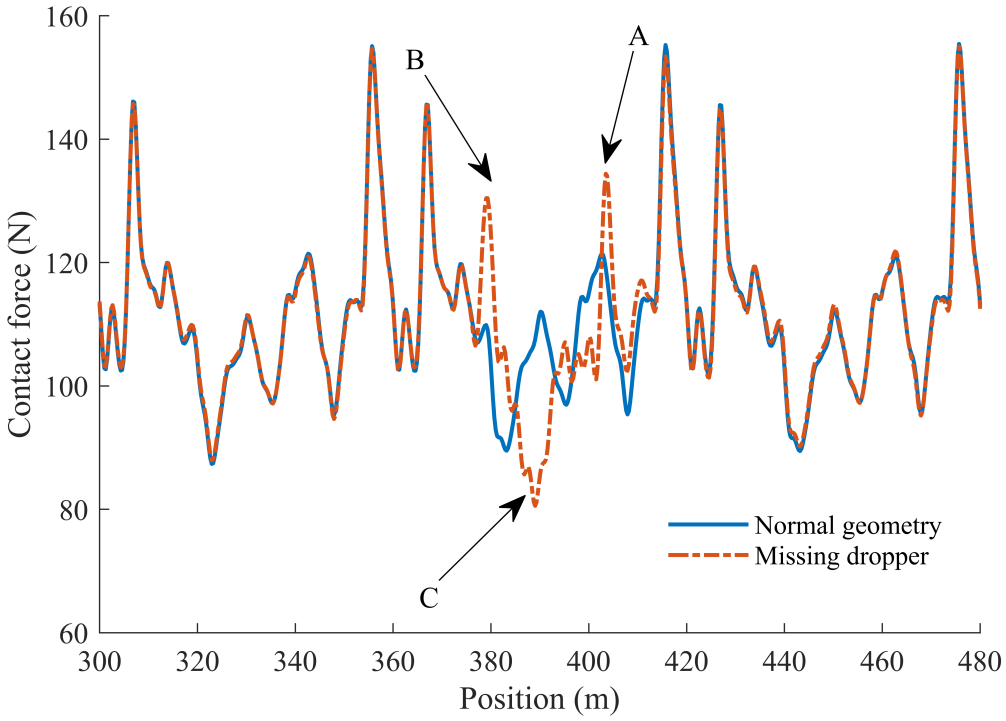

Fig. 6.7 Contact force variation due to a missing dropper. Legend indicates the base case with all droppers present and the case when a dropper had been removed. Locations referred to in the text are labelled A, B and C.

12.25 m. Due to the extra sag in the contact wire at location C in Figure 6.7, an acceleration of the pantograph is required to ensure it follows the new vertical geometry. The required peak forces to accelerate the pantograph are predicted at the droppers at locations A and B. The force peak at location B is 130 N compared with 120 N and the force peak at location A is 135 N compared with 121 N when the dropper is in place. The lack of a dropper at location

C results in a reduced contact force when compared with the normal geometry. Whereas a peak force of 114 N would be predicted at the dropper at location C, the absence of a dropper causes a predicted force of 81 N, a reduction of 29%.

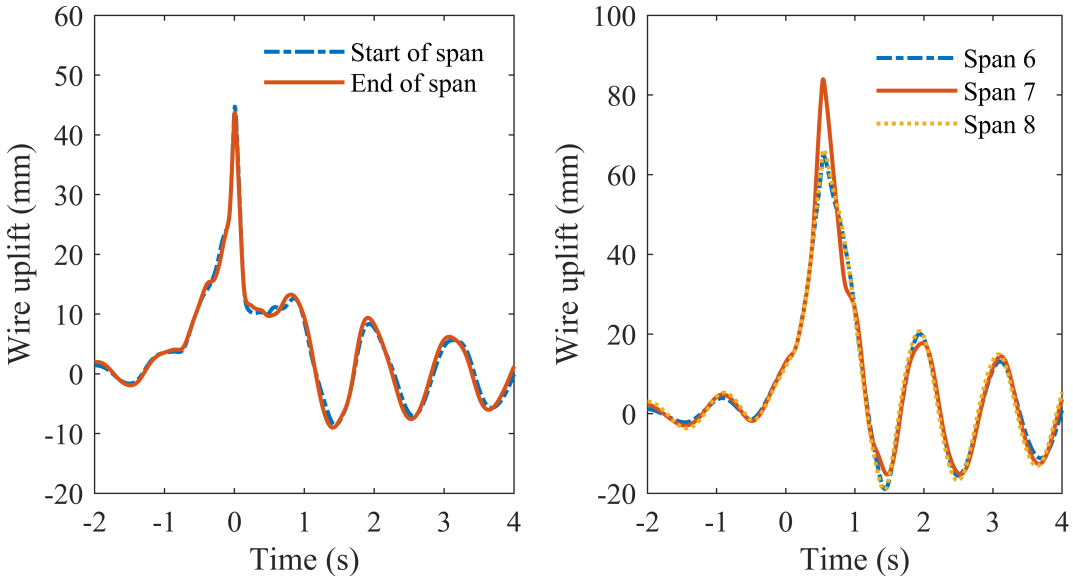

Fig. 6.8 Contact wire uplift at (a) the supports at either end of the span with the missing dropper, and (b) midspan. Span 7 is the span with the missing dropper and spans 6 and 8 are the preceding and subsequent spans respectively. Zero time corresponds to the time when the pantograph passed the location the wire uplift was measured.

The contact wire uplift is given in Figure 6.8. In Figure 6.8a the wire uplifts at the supports at either end of the span with the missing dropper are given. At the support at the start of the span, the wire uplift was 45 mm whilst at the support at the end of the span, the wire uplift was 44 mm. Since the change in the contact wire uplift between the supports was 1 mm, it suggests that the wire uplift away from the missing dropper was unaffected. By comparison, the contact wire uplift at midspan, given in Figure 6.8b, shows the greater available wire height increase due to the larger amount of wire sag in the unsupported wire length. At midspan in span 6, the maximum uplift was 65 mm and in span 8, the uplift at midspan was 66 mm, however at midspan in span 7 where the dropper was removed, the uplift was 84 mm. Since the wire mass and tension was unchanged, the wire oscillation frequency after the pantograph had passed was unchanged. The dynamic contact force shown in Figure 6.7 indicates that the effect is localised to the neighbourhood of the dropper and does not have a significant effect. If the dropper was damaged and hung down in the path

of the pantograph however, the damage would be catastrophic and cause severe damage to both the pantograph and the overhead line equipment. The contact force predictions shown in Figure 6.7 indicate that monitoring of the state of the equipment by achieved by detecting the localised force increases in the droppers either side of the missing dropper. Adopting condition monitoring equipment on passenger trains would allow for the detection of abnormal contact forces or wire uplifts in the neighbourhood of the ineffective dropper (either missing or buckled so providing no support to the contact wire). Detecting the changes in the contact force over longer time scales allows for assessment of the equipment condition outside of scheduled inspection visits or when the equipment fails.

6.2.4 Contact wire mass

Environmental factors typically lead to temporary variations in the contact wire mass during its lifetime. Buildup of ice temporarily increases the total mass supported by the droppers and messenger wire, whilst sliding contact between the contact wire and pantograph induces mechanical wear on the system leading to permanent removal of material, reducing the total supported mass. In both these cases, variations in the total supported mass leads to variations in the vertical geometry of the overhead line affecting the dynamic performance of the total system.

During the lifetime of the equipment, variations in the supported contact mass may be localised to certain parts of the contact wire e.g. localised wear at supports due to increased vertical stiffness compared with the overall system, however for simplicity in the modelling process, it is assumed in this section that the changes in the contact wire mass are global.

The dynamic force response to a change in the contact wire mass per unit length is given in Figure 6.9 respectively. Increasing the contact wire mass from a baseline of 1.07 $\mathrm{kg/m}$ lead to a large increase in the predicted peak forces at the first and last droppers in the considered spans. Increasing the contact wire mass by 25% and 50%, increased the peak force by 20% and 40% respectively. Due to these increased forces, the contact wire would see increased mechanical wear according to the Archard wear equation [304]. Increasing the contact wire mass lead to a predicted increase in the dynamic contact force and reducing the contact wire mass was predicted to lead to an improved dynamic performance due to the lower peak predicted forces as well as the reduced standard deviation compared with the base case of 1.07 $\mathrm{kg/m}$. The increased dynamic force due to the increased contact wire mass would be mitigated if the mechanical wear remained mild. The increased mass would serve to maintain the service life since the shortening of the equipment lifetime due to the increased

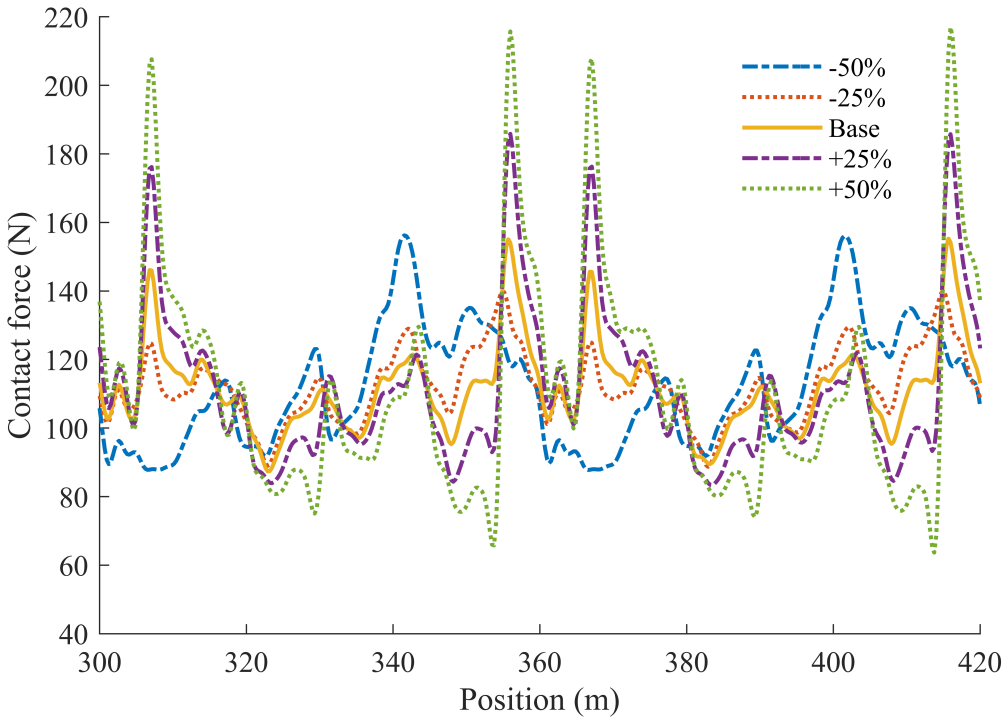

Fig. 6.9 Contact force variation due to different mass per unit length. Legend indicates the amount the contact wire mass per unit length has been varied from the baseline mass per unit length of 1.07 kg/m.

forces would be offset by the increased mass available to wear before the equipment required replacement or failed.

By reducing the contact wire mass to 0.8 kg/m the peak contact force was reduced by 9.7% whilst the mean contact force was unchanged, however reducing the contact wire mass further led to peak force similar to the base case (156 vs. 155 N). A 50% reduction in the contact wire mass also led to predicted increased forces at the third and fourth droppers compared with the other contact wire masses considered. When the contact wire mass was 0.54 kg/m, this increased force was 29% at the fourth dropper when compared with the base case force peak of 121 N. A 50% smaller contact wire mass also led to a reduced contact force around support locations, likely due to the reduced contact wire inertia despite the increase in the vertical stiffness present at supports. A small reduction in the contact wire mass would have an improved dynamic performance as shown in the results here, and would represent a cost saving to infrastructure owners due to the reduced material costs both during the initial capital investment and over the lifetime of the equipment during maintenance. The lower mass would also require a reduced tensioning force to maintain the vertical wire

profile, or the existing wire tension could be maintained to improve the dynamic performance further as shown in Section 6.2.1. The results cannot be extrapolated to further and further reductions of the contact wire mass however, since the size of the contact wire is set by the electrical transmission requirements for train operation. If the mass is reduced too far, Joule heating would cause failures of the contact wire.

Table 6.5 Contact force statistical output for a level contact wire as the mass per unit length is varied. All results in N except skewness and kurtosis.

Mass (kg/m)	F_m	σ	$F_{D_{\max}}$	$F_{D_{\min}}$	$F_{S_{\max}}$	$F_{S_{\min}}$	Skew	Kurtosis
0.54	112	17.4	156	87.8	164	59.8	0.532	-0.478
0.80	112	10.5	140	88.7	143	80.7	0.322	-0.105
1.07	112	12.9	155	87.4	150	73.1	1.08	1.68
1.34	112	21.7	186	83.4	177	46.6	1.42	1.97
1.61	111	31.7	217	63.7	206	16.3	1.30	1.55

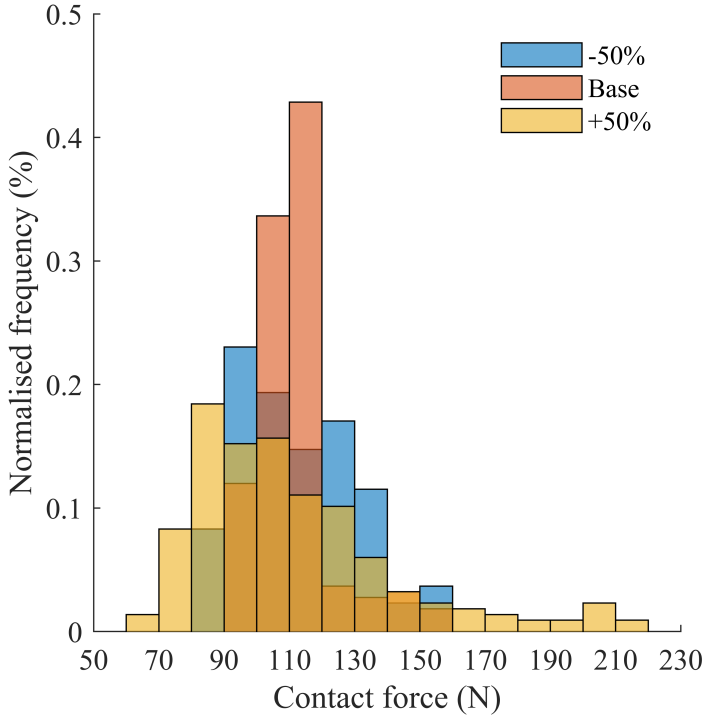

Fig. 6.10 Contact force histogram comparing the distribution of the contact forces of the base case of 1.07 kg/m with the ±50% cases. Legend indicates the change in the contact wire mass per unit length in each case.

Table 6.5 gives the relevant statistical output when varying the contact wire mass per unit length. It can be seen from the statistical output that increasing the contact wire mass would lead to a undesirable overhead line dynamic performance highlighted by the increased standard deviation which was 146% larger for a contact wire mass of 1.605 kg/m compared to a mass of 1.07 kg/m, and large peak force of 217 N. The skewness of the contact force, shown in Figure 6.10 for the base and $\pm$50% cases indicates that the contact force is typically below the mean contact force but the peak forces are significant outliers. This is consistent with the larger kurtosis for increased contact wire mass compared with the reduced cases. This is most clear when the contact wire mass per unit length was increased by 50%. The majority of the contact force is skewed below 110 N, however there is a significant number of occurrences in the region of high contact forces. When the mass per unit length was 0.8 kg/m, the predicted contact force was nearly symmetrical and the kurtosis was -0.105 indicating few outliers. The close to zero kurtosis is due to the lack of sharp peak forces predicted in other cases. The increased contact force standard deviation when the contact wire mass was reduced by 50% can be used as a predictor of significantly worn contact wire requiring replacement. Considering a condition monitoring approach, detection of larger variations in the contact force compared with surrounding regions indicate a significantly worn contact wire. This may indicate the equipment deviating from the design position inducing greater contact forces during train operation leading to an increased in the wear rate.

The contact wire uplift variation due to changes in the contact wire mass is shown in Figure 6.11. The maximum uplift at the support in the base case was 45 mm. For a 25% decrease in the contact wire mass, the wire uplift change was small (0.2 mm) and when the wire mass was decreased further, the wire uplift was reduced to 37.2 mm consistent with the predicted reduction in contact force at supports. As the contact wire mass was increased, there was also a predicted increase in the wire uplift. For a 50% increase in the contact wire mass, the wire uplift at the support was 48.3 mm. Since the increase in the contact force at supports was small as can be seen in Figure 6.9, the only 8% increase in the contact wire uplift is consistent despite the 40% increase in the contact force maxima predicted at the fifth dropper.

It can be seen in Figure 6.11 that when the contact wire mass per unit length was 0.54 kg/m, the amplitude of the oscillations had decayed to a similar magnitude as those prior to the pantograph passage in contrast to the other masses consider. The reduction in the contact wire mass contributes to a reduction in the contact wire kinetic energy due to the passage of the pantograph, and since the wire tension was maintained in each case, the energy

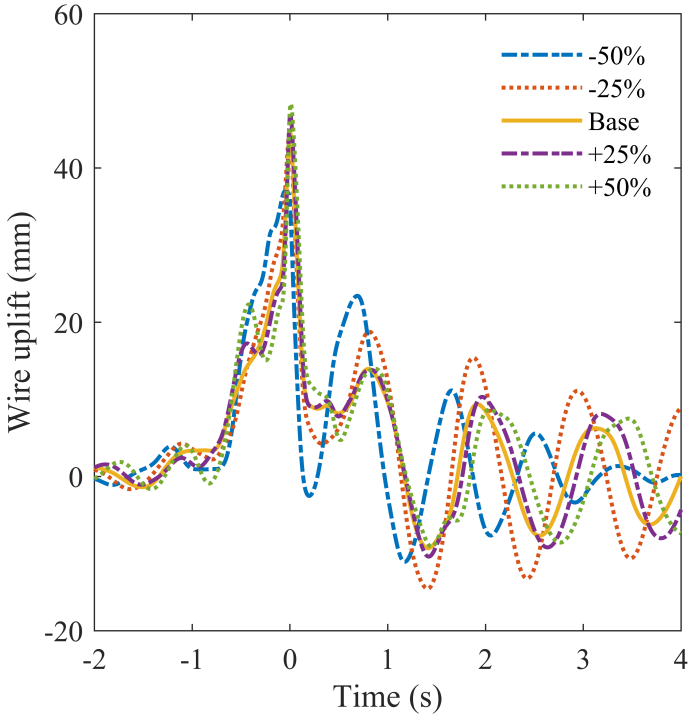

Fig. 6.11 Wire uplift at the support between spans six and seven. Legend indicates the amount the contact wire mass per unit length has been varied from the baseline of 1.07 kg/m. Zero time is the moment the pantograph passes the support.

losses due to friction were maintained thus reducing the time period for the wire oscillations to decay. As discussed earlier, the contact wire mass cannot be reduced indefinitely since the high tension applied to the contact wire to maintain the vertical profile would exceed the yield point of the material, for this and electrical transmission considerations, the results cannot be extrapolated to micron sized wires for example.

6.3 Influence of pantograph parameters

By its very nature, the pantograph catenary interaction is a coupled system with the contact force coupling the dynamics of the overhead line to the dynamics of the pantograph. Thus a study of the effect of the pantograph parameters on the dynamic performance is of value both for the insight into parameter effects and as a generalisation of the model used in this study. As with the key overhead line parameters in the previous section, key parameters of the pantograph are changed here to understand their influence on both the dynamic contact

force between the contact wire and pantograph but also changes in the contact wire uplift. The parameters studied in this section are:

- the pantograph head collector strip mass,
- the pantograph head frame mass,
- the stiffness of the bar connecting the pantograph head and collector strip, and
- the static uplift applied to the pantograph.

The effect of varying the pantograph parameters is determined using the original overhead line geometry described in Section 6.1 with messenger and contact wire tensions of 13 and 16.5 kN respectively.

6.3.1 Pantograph head collector mass

The pantograph collector head is the most important element of the pantograph during the catenary pantograph interaction as maintaining good contact between the collector and the contact wire is key to ensuring good electrical conductivity between the overhead line and the train. Since the collector strips are the only part of the pantograph in contact with the overhead line, optimising the collector mass is important to ensure good dynamic performance, for example, a pantograph head with too great a mass would damage the overhead line at supports and droppers. The pantograph collector strip mass is given as m_3 in Figure 3.18a.

Figure 6.12 shows the contact force trace as the pantograph collector mass is varied. The baseline head mass is 5.3 kg as in [249] and the mass was varied by 25% increments. It can be seen from Figure 6.12, that the largest effect due to a change in the collector head mass is an increase in the peak forces. By increasing the collector head mass by 50%, the peak force increased by 6%. There was a also a 3% reduction in the contact force minimum when the pantograph collector mass was increased by 50%. The increase in contact force at the final dropper is expected due to the increased pantograph inertia. Between the fourth and final dropper, the unsupported length is 12.25 m compared with the unsupported length between the final dropper and the support of 5.5 m. The longer unsupported length leads to a greater contact wire sag in between the droppers and coupled with the sudden increased vertical stiffness at the droppers, a larger force is required to accelerate the pantograph head. This effect is particularly pronounced when the collector head mass is increased. The converse is also true, and predicted by the modelling results. As the collector head mass was decreased by 50%, the predicted peak force at the same location was 8% smaller.

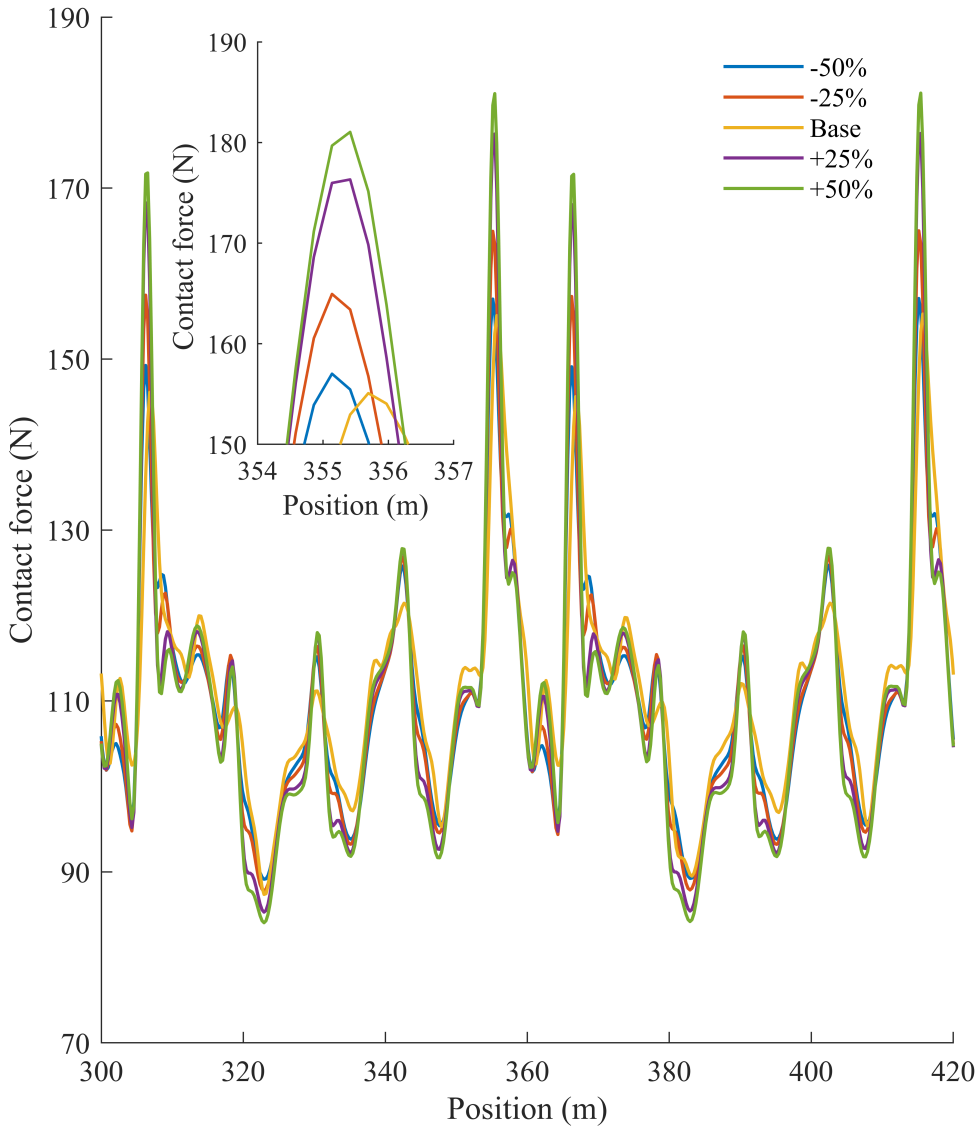

Fig. 6.12 Variation in the contact force due to varying the mass of the pantograph collector head. Legend indicates the change in the mass of the pantograph collector from a base mass of 5.3 kg. The inset figure highlights the discrete contact force maxima.

The statistical output for each of the simulations is given in Table 6.6. Whilst the mean contact force remained unchanged for each of the pantograph masses considered, the growing peak forces contribute to the increase in the contact force standard deviation. The increasing peak forces predicted at the final dropper in the span also indicate the increased force required to accelerate the pantograph to follow the direction of the contact wire. The 6% increase in

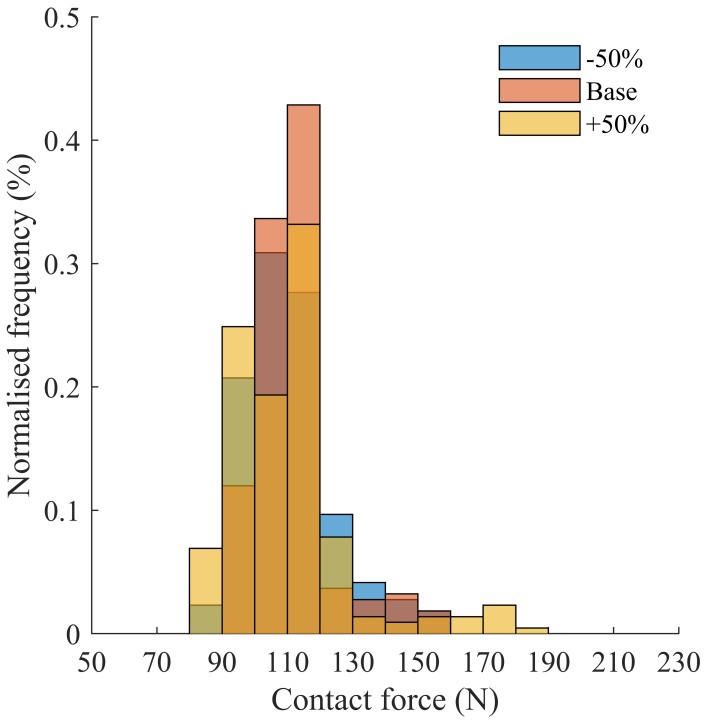

Fig. 6.13 Contact force histogram comparing the distribution of the contact forces during the catenary pantograph interaction for the base pantograph head mass of 5.3 kg and the ±50% cases. Legend indicates the pantograph head mass in each case.

the predicted peak contact force when the collector head mass was doubled results in the increasing kurtosis as the number of outlying force occurrences increased compared with the base case. This can be seen in the distribution of the contact force given in Figure 6.13. The converse is also true since the reduction in the peak force when reducing the collector mass also lead to a reduced kurtosis. The results show that the pantograph head mass should be minimised to achieve good dynamic performance, however this limits the adoption of condition monitoring equipment at the pantograph head. The minimization of the pantograph collector head is also limited by the electrical transmission requirements. The pantograph carbons cannot be reduced to 1 mm cylinders for example, without a significant reduction in the electrical current as Joule heating would melt the equipment. The carbon mass could be reduced with an increase in the transmission voltage above 25 kV, however the electrical clearances would have to be extended to satisfy the air gaps required to prevent arcing occurrences between the live equipment and civil structures (and indeed people at stations for example).

Table 6.6 Contact force statistical output for a level contact wire as the pantograph collector head mass is varied. All results in N.

Mass (kg)	F_m	σ	$F_{D_{\max}}$	$F_{D_{\min}}$	$F_{S_{\max}}$	$F_{S_{\min}}$	Skew	Kurtosis
2.65	110	13.5	157	89.1	151	69.6	1.14	1.48
3.98	110	14.7	165	87.8	154	66.1	1.40	2.54
5.3	110	15.9	171	86.5	158	62.5	1.58	3.30
6.63	110	17.0	176	85.3	164	56.1	1.68	3.73
7.95	110	18.0	181	84.0	165	54.9	1.73	3.91

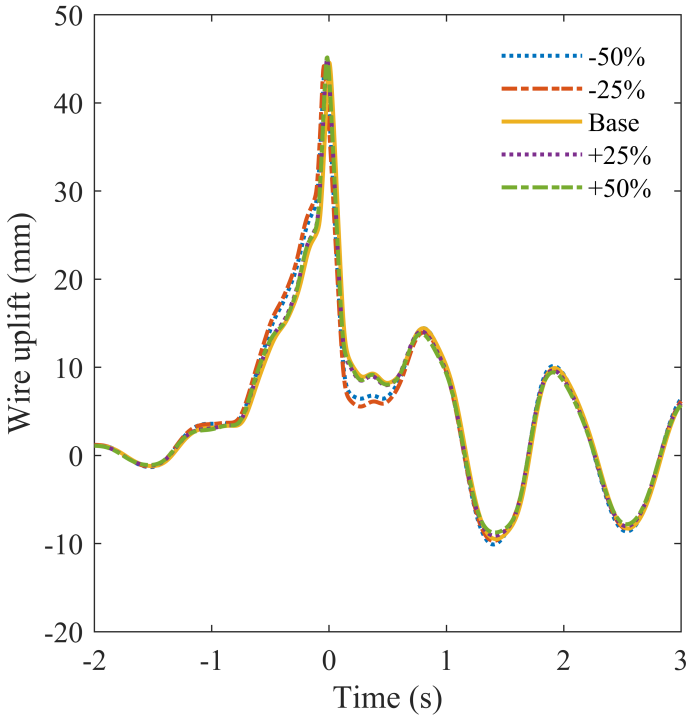

Fig. 6.14 Variation in the wire uplift at the support between spans six and seven due to changes in the mass of the pantograph collector head. Zero time is the moment the pantograph passes the support and the legend indicates the change in the magnitude of the pantograph head collector mass in each case.

The skewness of the contact force, given in Table 6.6, was positive for all of the pantograph collector head masses considered and indicated that the predicted contact force was skewed below the mean with the peak force outliers the dominant drivers of contact force above the mean. The monotonically increasing skew is due to the increasing peak force since the predicted force away from the first and final dropper only showed small variation. The

histogram in Figure 6.13 highlights the skew of the contact force with a significant proportion of the contact force grouped to the left of the mean at 110 N, with only a relatively small (less than 15%) number of force occurrences above the mean.

The wire uplift at the support between spans six and seven at 360 m is shown in Figure 6.14. There was approximately 1 mm variation from the base contact wire uplift of 45 mm in the predicted contact wire uplift at the support as a result of a change in the pantograph collector head mass. The maximum uplift when the pantograph collector head mass was reduced by 50% was 43.8 mm, whilst the maximum uplift when the mass was increased by 50% was 46.5 mm. From Figure 6.14, reducing the pantograph collector mass increased the rate at which the contact wire mass rose during the passing of the pantograph and also allowed the contact wire to drop further immediately after the pantograph had passed. After the initial excitation of the contact wire due to the passing pantograph, the wire oscillated with similar amplitude in all cases: the first uplift minima between 1 and 2 s showed small variation in the amplitude of the oscillations, but no variation was predicted beyond this.

6.3.2 Pantograph collector frame mass

Here, the dynamic response to various pantograph collector frame masses, shown as m_2 in Figure 3.18a, are considered. As in the previous section, the masses being considered were changed in 25% increments with the base case being a collector frame mass of 7.5 kg.

Table 6.7 Contact force statistical output for a level contact wire as the mass of the pantograph collector frame is varied. All results except skew and kurtosis in N.

Mass (kg)	F_m	σ	$F_{D_{\max}}$	$F_{D_{\min}}$	$F_{S_{\max}}$	$F_{S_{\min}}$	Skew	Kurtosis
3.75	110	15.0	169	90.5	155	65.1	1.87	4.44
5.63	110	15.4	170	88.4	156	63.8	1.71	3.82
7.5	110	15.9	171	86.5	158	62.5	1.58	3.30
9.38	110	16.4	172	84.8	159	61.0	1.45	2.82
11.3	110	16.9	173	83.3	161	59.5	1.33	2.41

The statistical output as a result of the variation in the collector head frame mass is given in Table 6.7, where it can be seen that the mean contact force was unchanged. The peak forces were predicted to increase as the head frame mass was increased, however this change was small: the peak force increased by 2.4% despite the head frame mass increasing from 3.75 kg to 11.3 kg, an increase of 200%. In each case, the skewness of the predicted contact force was positive indicating that the contact force was typically less than the mean with only

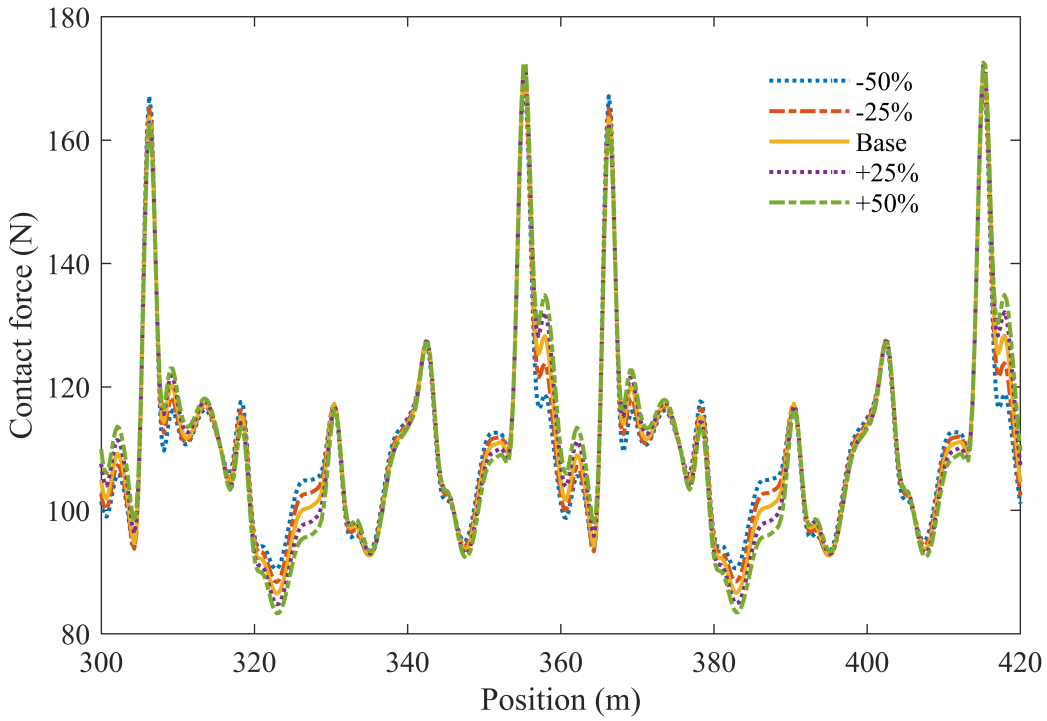

Fig. 6.15 Contact force variation due to different collector frame masses. Legend gives the collector frame mass considered in each case.

the outlying peak contact forces a substantial component of the force distribution above the mean.

Whilst there is little effect on the peak forces due to a change in the collector frame mass, deviations in the contact force trace can be seen at locations away from where peak forces are predicted at the first and last droppers. Figure 6.15 shows these deviations occurring at midspan where the contact wire sags due to the 60 mm presag. At midspan, the increase in the collector frame mass leads to a predicted decrease in the contact force as due to the presag the operating height of the pantograph is almost constant and so only a small acceleration of the pantograph in the vertical direction will occur. The small change in acceleration would result in a decreased contact force for a larger mass, consistent with the force traces in Figure 6.15.

The reduced contact forces observed at midspan with an increased collector frame mass are also consistent with the larger standard deviation. With each 25% increase in the mass of the pantograph collector frame, the standard deviation was predicted to rise by 0.5 N aside from the increase from 3.75 kg to 5.63 kg where the standard deviation rose by 0.4 N.

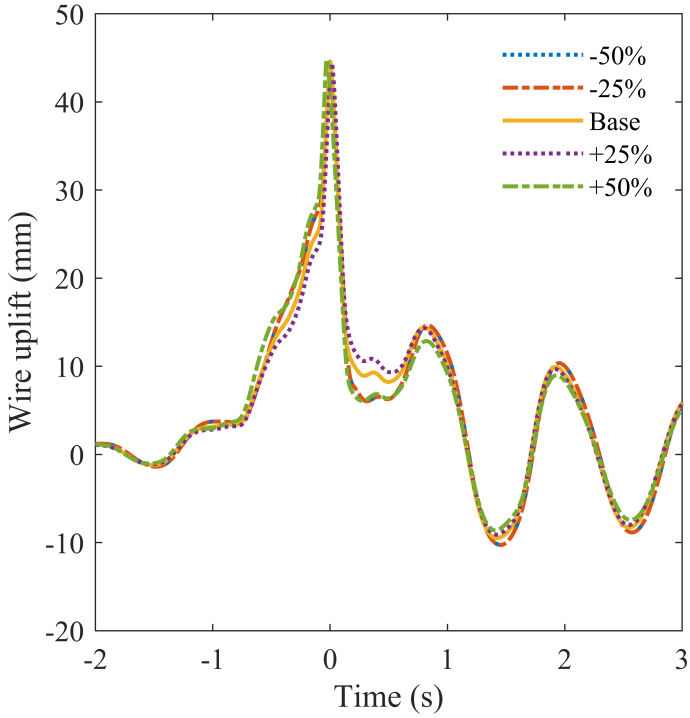

Fig. 6.16 Wire uplift at the support between spans six and seven at 360 m as the stiffness of the pantograph support arm is varied. Zero time is the moment the pantograph passes the support and the legend indicates how much the stiffness has been varied from the base case of 7.5 kN/m.

From Figure 6.16, it can be seen that the mass of the pantograph collector frame has little effect on the wire uplift during operation. The predicted wire uplift was 43.4 mm when the frame mass was 3.75 kg and 44.8 mm when the mass was 11.3 kg. The small 3% change in the wire uplift is consistent with varying only the frame mass since no changes in the nominal wire height were made. Thus, no requirements were made of the frame to provide large changes in the pantograph operating height and so changes in the mass of the frame would have only a small effect on subsequent dynamics. Since the change in the wire uplift was small, the change in the amplitude of the contact wire oscillations were similarly small.

6.3.3 Varying the stiffness of the bar connecting the collector frame and collector strips

Considering the component stiffness between the collector strips and the pantograph, given as k_3 in Figure 3.18a, the statistical output, given in Table 6.8, shows that the stiffness of the connector between the pantograph collector strips and head frame only has a small effect on

the dynamic performance of the catenary pantograph interaction for a nominally level contact wire. The maximum variation in the peak contact force was when the stiffness was reduced by 50% and a 3.2% decrease was predicted. The reduction in contact force is consistent with the reduction in the component stiffness since a reduced force would be required to compress the pantograph by the same amount. The increase in the contact force when the stiffness was increased was similarly small. Increases in the component stiffness 25% and 50% led to peak force rises of 0.6% and 1.3% respectively. The almost unchanged skewness of the contact force is indicative of the smallness of the change in the predicted peak forces as there are no increase in the frequency the contact force rising above the mean contact force of 112 N.

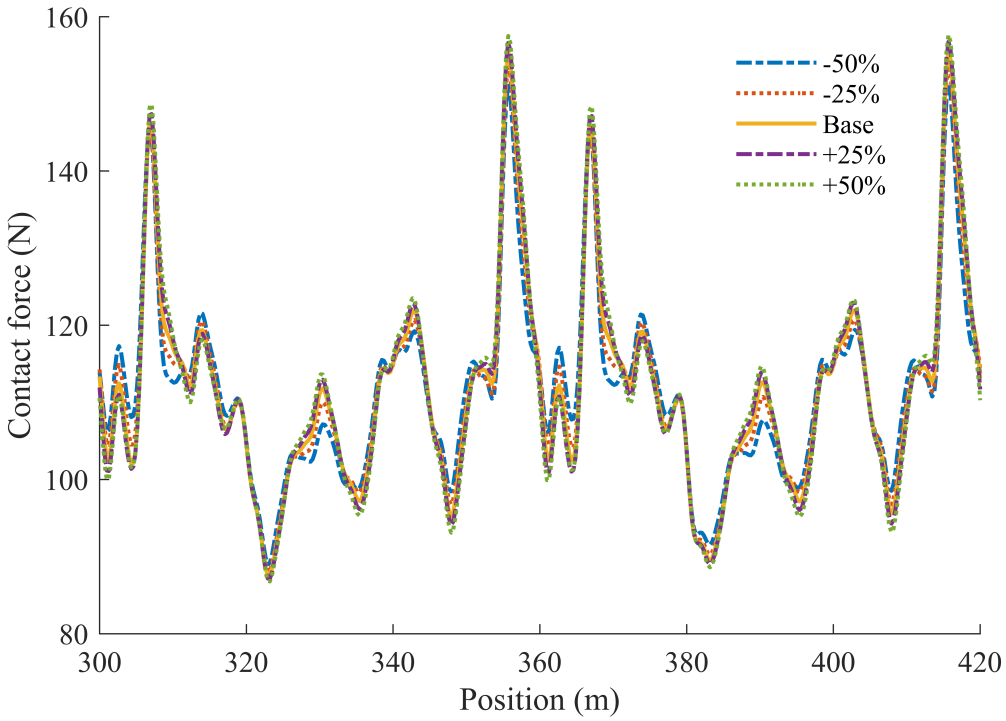

Fig. 6.17 Contact force variation due to varying the stiffness between the pantograph head frame and collector strip. Legend gives the amount the stiffness has changed from the base stiffness of 6.3 kN/m.

The variation in the contact force with respect to position is given in Figure 6.17 for each of the component stiffnesses considered. It can be seen that by reducing the stiffness by 50% to 3.2 kN/m, the force peak that occurs near the third dropper at midspan is reduced by 4.1%, whilst the force just after the supports is increased by 4.4%.

Varying the stiffness of the arm between the collector strip and the collector frame had little effect on the maximum uplift at the supports, as shown in Figure 6.18. The maximum

Table 6.8 Contact force statistical output for a level contact wire as the stiffness between the pantograph head frame and strips is varied. All results except skew and kurtosis in N.

Stiffness (kN/m)	F_m	σ	$F_{D_{\max}}$	$F_{D_{\min}}$	$F_{S_{\max}}$	$F_{S_{\min}}$	Skew	Kurtosis
3.2	112	11.5	151	89.0	146	77.1	1.08	1.91
4.7	112	12.1	154	88.0	148	75.1	1.10	1.88
6.3	112	12.9	156	87.5	150	73.0	1.10	1.73
7.9	112	13.5	157	87.1	152	71.3	1.10	1.59
9.5	112	13.9	158	86.8	153	70.0	1.09	1.50

uplift for the baseline stiffness of 6.3 kN/m was 45.4 mm, whilst a 50% reduction in the stiffness resulted in a predicted wire uplift of 44.2 mm and a 50% increase lead to a wire uplift of 45.9 mm. The small variation in the wire uplift height was as expected since there were no large scale height variations imposed on the contact wire's vertical geometry, thus there were no requirements for the pantograph to be compressed or extended during the modelling. At midspan where the contact wire is allowed to sag by 60 mm, the wire uplift was 65 mm, thus the pantograph head was raised by only 5 mm above the nominal operating height.

6.3.4 Static uplift

The static uplift is the contact force exerted by the pantograph on the overhead line at standstill and is used to ensure good contact between the pantograph collector head and overhead line during operation. Minimum uplift forces vary depending on the pantograph type, but in the UK, the minimum static uplift is 70 N [61] as was used in the majority of this work. Here the results obtained by varying the static uplift are presented. Figure 6.19 gives the contact force response to an increase in the static uplift. It can be seen that characteristic peak forces at dropper locations increase with increasing static uplift and the contact force pattern within a span is maintained. The largest of these peaks are predicted to occur at the first at last droppers in the span where the vertical stiffness is increased due to the proximity to a support.

Table 6.9 gives the statistical output for the catenary pantograph interaction with increasing static uplift. The mean contact force increased in line with the increase in the static upift force, that is for each 10 N increase in the static uplift, a corresponding 10 N increase in the mean contact force was observed. The contact force standard deviation was larger for a 70 N static uplift than for static uplifts of 80 and 90 N. This is likely due to the higher

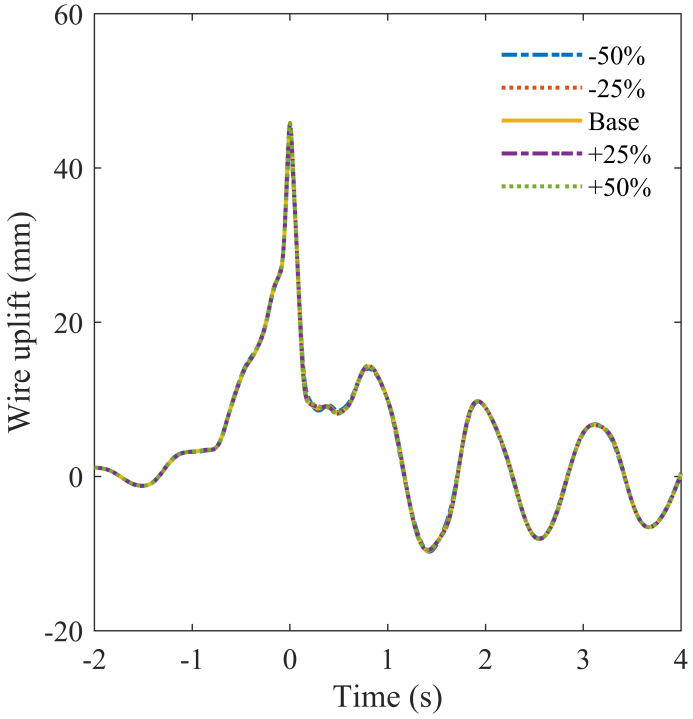

Fig. 6.18 Wire uplift at the support between spans six and seven at 360 m as the stiffness of the collector strips is varied. Zero time is the moment the pantograph passes the support and the legend indicates how much the stiffness has been varied from a base case of 6.3 kN/m.

static uplifts being able to counteract the lower contact forces at midspan where there is a reduced vertical stiffness rather than effects due to the increased peak forces. This can be seen from Table 6.9 as the change in peak forces between 70 and 80 N static uplifts was only 7 N compared with the increase in the minimum force at midspan which was 8.2 N. Whilst the difference between the increases in force maxima and minima is only 17%, since the mean contact force is 10 N lower when using a 70 N static uplift, the consistently lower contact force taken with similar peak forces leads to a greater standard deviation.

The histogram of contact forces given in Figure 6.20 shows the distribution of contact force for each of the considered static uplifts. It can be seen that the contact force distribution when the static uplift was 70 N is dominated by forces in the 100 – 119 N range, consistent with the positive kurtosis of 3.3. From the measure of skewness of 1.58, the contact force was positively skewed so the contact force was largely below the mean contact force of 100 N. As the static uplift was increased, the contact force become less positively skewed indicating that occurrences of forces above the mean become more prevalent as the static uplift increases.

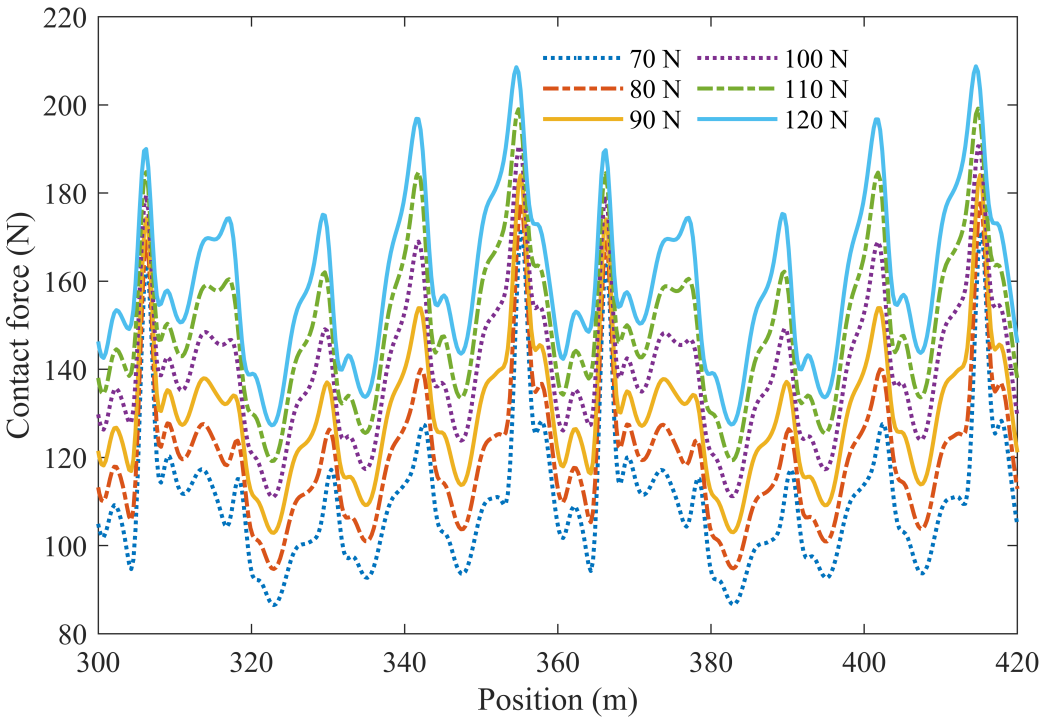

Fig. 6.19 Contact force variation due to increased static uplift force. The baseline case is an uplift of 70 N and this is increased up to 120 N.

From Table 6.9, the kurtosis is decreasing with increasing static uplift, indicating that the predicted contact force has a reduced number of outliers when the uplift is increased. This can be seen in the histogram in Figure 6.20 from the height of the bar showing the distribution of forces below 100 N when a 70 N uplift is used compared with the height of the bar indicating the distribution of forces greater than 200 N when the static uplift was 120 N. Table 6.9 also shows that the kurtosis of the contact force changes sign as the static uplift is increased from 100 N to 110 N which is consistent with the reduced number of contact force outliers predicted when a higher static uplift is used.

Figure 6.22a gives the contact wire uplift at a support between the sixth and seventh spans of the overhead line and Figure 6.22b shows the wire uplift at the support 0.5 s before and after the passing pantograph. The maximum uplift was 45 mm when a static uplift of 70 N was used and this increased to a maximum wire uplift of 60 mm when a static uplift of 120 N was used. This was a 33% increase in the wire uplift compared with a 71% increase in the static uplift force. The increased static uplift force also causes a larger amplitude oscillation in the contact wire once the pantograph has passed. The frequency of the oscillations was unchanged as no changes to the overhead line parameters were made. Figure 6.22a shows

Table 6.9 Contact force statistical output for a level contact wire as the static uplift force is increased. All results except skew and kurtosis in N.

Uplift (N)	F_m	σ	$F_{D_{\max}}$	$F_{D_{\min}}$	$F_{S_{\max}}$	$F_{S_{\min}}$	Skew	Kurtosis
70	110	15.9	171	86.5	158	62.5	1.58	3.30
80	120	15.6	178	94.7	167	73.3	1.27	2.36
90	130	15.7	184	103	177	83	0.95	1.34
100	140	16.2	191	111	189	91.6	0.69	0.51
110	150	17	199	119	201	99	0.54	-0.02
120	160	18	209	127	214	106	0.45	-0.3

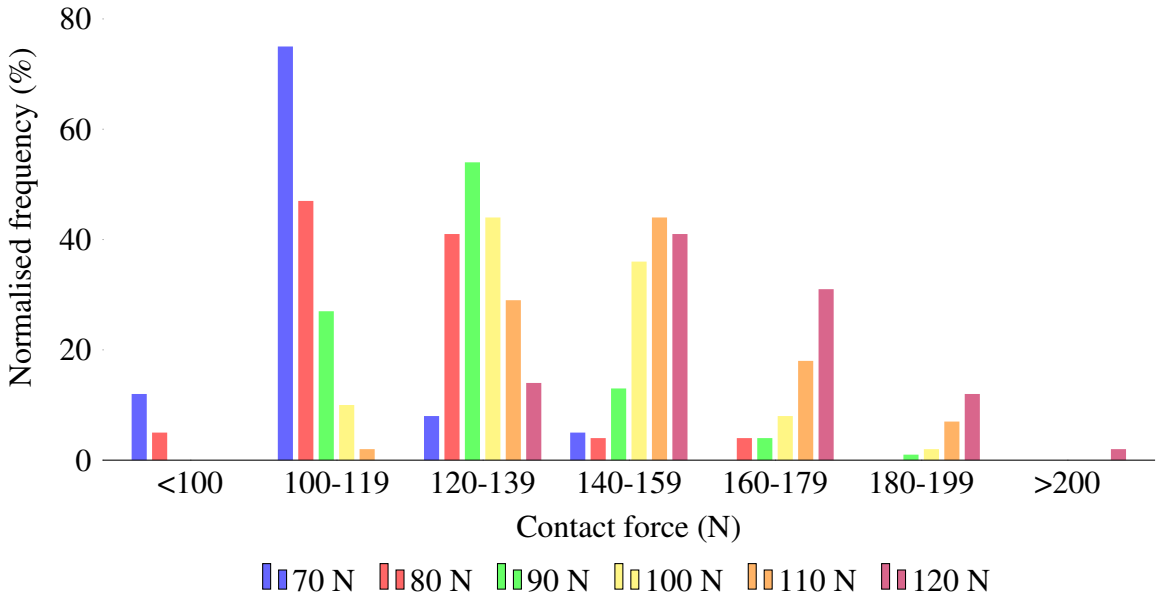

Fig. 6.20 Histogram of contact force for each of the pantograph static uplifts considered. The normalised frequency indicates the percentage of data falling within each bin.

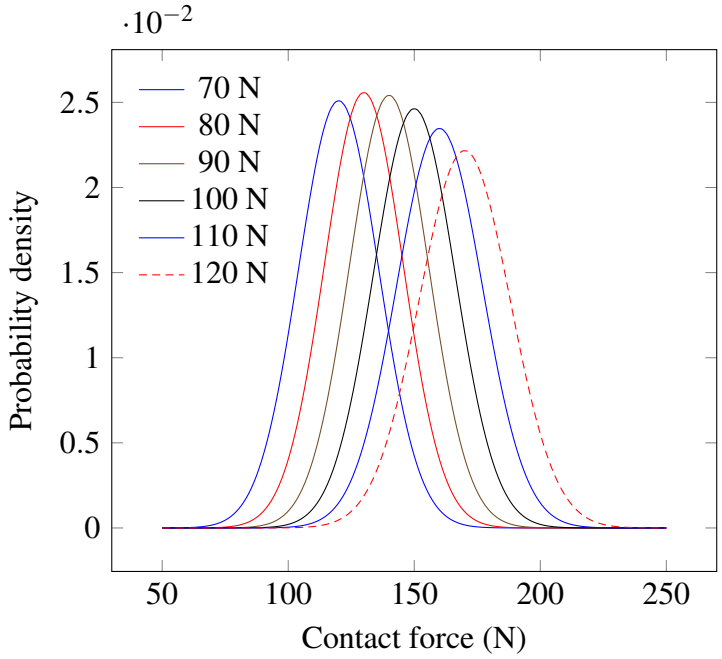

Fig. 6.21 Probability density corresponding to the histogram in Figure 6.20. Legend indicates the static uplift force applied in each case and the curves are derived from the Gaussian $\text{Gauss}(x) = \left(2\pi\sigma^2\right)^{-1/2} \exp\left(-(x-F_m)^2/(2\sigma^2)\right)$, where F_m and σ are given in Table 6.9.

the contact wire is already oscillating before the pantograph reaches the support due to the mechanical wave caused by the contact between the pantograph collector head and contact wire. Figure 6.22b shows that the wire uplift 0.5 s before the pantograph passes the support is between 10 and 15 mm.

The wire uplift at midspan where there is a reduced vertical stiffness was 65 mm for a 70 N static uplift, greater than the presag of 60 mm and the wire uplift increased to 95 mm when the static uplift was 120 N. Given the presag of the contact wire was 60 mm, that is 0.1% of the span length [13, pg. 158], when the pantograph moved along the contact wire with a static uplift of 70 N, the operating height was almost constant as only a 5 mm increase above the nominal contact wire height was predicted whilst a static uplift would see the contact wire rise 35 mm above the nominal wire height.

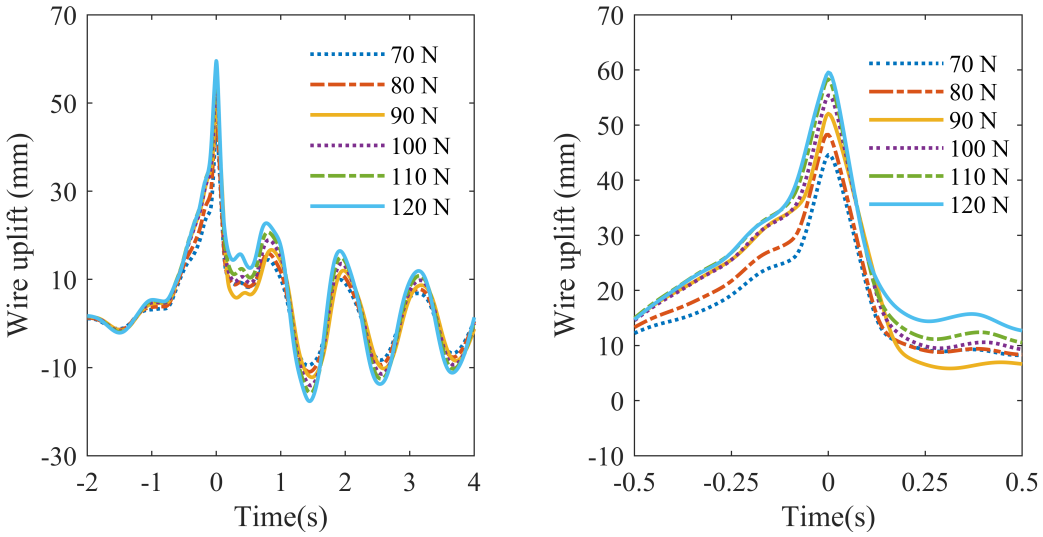

Fig. 6.22 Wire uplift at the support between spans 5 and 6 at 360 m, for each of the static uplifts considered. (a) The uplift and the resulting wire oscillations due to the moving pantograph. (b) The wire uplift 0.5 seconds before and after the pantograph passing highlighting the change in wire uplift due to the static uplift and is a detailed excerpt of (a), i.e., the graph corresponds to the time interval $[-0.5, 0.5]$ in (a). The legend indicates the static uplift being considered in each case and zero time corresponds to the pantograph passing the support.

6.4 Train running speed

The train running speed is a significant contributor to the dynamic performance of the overhead line system. As the train speed increases, the contact force due to the sliding contact between the pantograph collector strip and contact wire is likely to increase. Here, the results of a range of speeds from 40 to 300 km/h are presented using a level overhead line geometry as described in Section 6.1.

The mean contact force growth is shown in Figure 6.23 and it can be seen that the growth of the mean contact force is well approximated by the polynomial curve

$$M(s) = 99 \times 10^{-5} s^2 + 553 \times 10^{-5} s + 69.6. \tag{6.2}$$

The quadratic growth in the mean contact force is consistent with the growth allowed by BS EN 50367 [61], where the mean contact force grows according to the equation

$$M(s) = 97 \times 10^{-5} s^2 + 70. \tag{6.3}$$

Table 6.10 Contact force statistical output with respect to train running speed for a level contact wire. All results in N.

Speed (km/h)	F_m	σ	$F_{D_{\max}}$	$F_{D_{\min}}$	$F_{S_{\max}}$	$F_{S_{\min}}$
40	71.1	2.1	82.6	68.8	77.4	64.8
60	73.6	4.1	96	67.9	85.8	61.5
80	76.4	5.9	107	69.4	94.2	58.6
100	80	7.6	117	69.2	103	57.1
120	85.5	9.2	128	71.3	113	57.9
140	89.7	10.9	139	74.6	122	57
160	95.7	12.4	151	74.3	133	58.5
180	103	14.9	160	82.1	148	58.3
200	110	15.9	171	86.5	158	62.5
220	118	18.7	182	84.7	174	61.9
240	128	21.6	193	90.6	193	63.2
260	138	25.8	212	96.7	215	60.6
280	150	31.5	245	100	245	55.5
300	160	36.8	269	107	270	49.6

At 300 km/h, the highest speed considered, the mean contact force prediction given by Equation 6.2 deviated from Equation 6.3 by only 2.1%. The very good agreement between the design and predicted mean contact force represents a validation of the model predictions beyond the expected validation provided by BS EN 50318 [287].

Figure 6.24 shows the variation of the contact force in a single span along with the corresponding overhead line geometry. The characteristic peak contact forces at dropper locations are observed. At these locations, the additional mass due to the dropper clamps and increased vertical stiffness. At the first and last droppers, the total vertical stiffness is increased due to the relatively short distance (5.5 m) to the registration arms whereas between intermediate droppers, the unsupported length is 12.25 m. The larger unsupported lengths causes a reduction in the vertical stiffness thus the decrease in the contact force as predicted in Figure 6.24. The dropper clamp masses at dropper locations give rise to the observed peak forces, but due to the reduced stiffness, these peaks are smaller than observed elsewhere. Typically the major force peak occurs at or just after the dropper and are well aligned in position irrespective of the speed, as can be seen in Figure 6.24. However at train speeds of 260 km/h and above, the peak force shifts and occurs before the dropper.

Figure 6.24 demonstrates that speed is a significant driver in the variation of the contact force and the statistical output for each of the speeds considered is given in Table 6.10. At

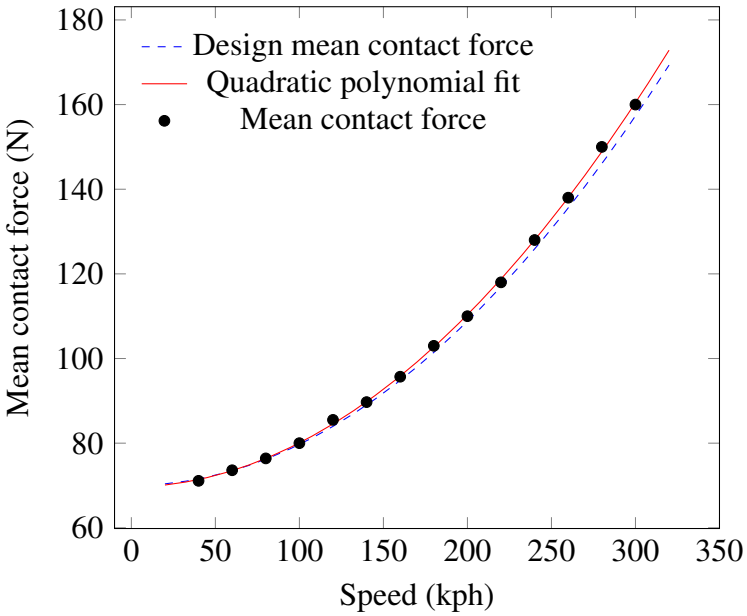

Fig. 6.23 Predicted mean contact force from the finite element model with second order polynomial fit. The design maximum mean contact force according to BS EN 50367 is also given.

low speeds, the static uplift force of 70 N is the major contributor to the contact force as indicated by a mean contact force of 71.1 N when the train speed was 40 km/h. As the speed increases, the contact between the overhead line and the pantograph becomes a greater influence as shown by the increasing mean contact force.

The peak forces observed at the droppers is likely responsible for the increase in the standard deviation of the contact force. When the train speed was 40 km/h, the standard deviation was 2.1 N and between droppers, the predicted contact force was almost constant as can be seen in Figure 6.24. As the speed increased to around 160 km/h and the peak observed at the first dropper rose, the contact force quickly drops towards the static uplift force of 70 N before the second dropper where another peak is observed. At speeds beyond 200 km/h, the lower force just before the second dropper has shifted towards the first dropper and now occurs approximately halfway between the first and second droppers. Since no changes to the wire geometry were made, the changes in the contact force are solely down to the increased speed. The shifting of the spatial locations of the local maxima is likely due to partially reflected waves at the dropper and support clamps. As the train speed increases, the reflected wave meets the pantograph at different locations resulting in the shifting of the local maxima spatial positions.

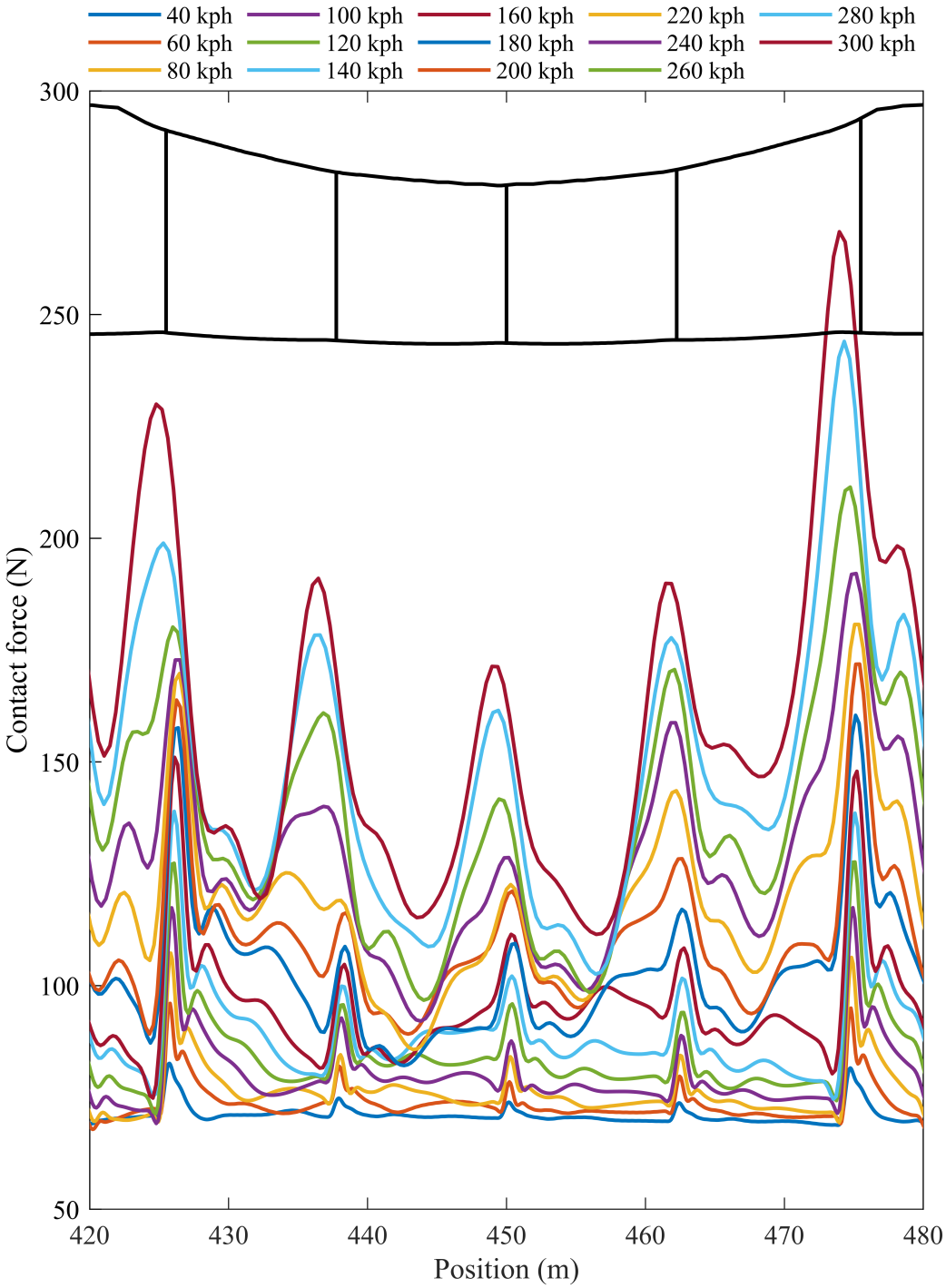

Fig. 6.24 Contact force between the pantograph collector strip and the contact wire in a single span, for train running speeds between 40 and 300 km/h. Legend indicates which train speed is considered and the corresponding overhead line geometry is given. The pantograph moves from left to right.

The largest peak in the contact force at the last dropper can be reduced by increasing the number of droppers in a span, the locations and lengths of which are given in Table 6.11. Figure 6.25 shows the comparison in the contact force when the number of droppers in the span is increased from five to nine and the train speed was maintained at 300 km/h.

Table 6.11 Dropper locations and their lengths used in a span with nine droppers.

Dropper	1	2	3	4	5	6	7	8	9
Location from start of span (m)	5	10.5	17	23.5	30	36.5	43	49.5	55
Length (m)	0.986	0.805	0.648	0.554	0.523	0.554	0.648	0.805	0.986

As in Figure 6.24 the dropper passing frequency is clear in the contact force oscillation, however the peak force predicted at the first dropper is replaced by a force minimum whilst the peak at the last dropper is reduced. It can be seen from Figure 6.25 that the increased number of dropper gives a more consistent contact force oscillation at midspan and the deviations from this oscillation at the ends of the spans are due to the supports rather than any significant increases in the unsupported contact wire lengths (the unsupported lengths when using nine droppers are 5.5 and 5 m, compared with 5.5 and 12.25 m when using five droppers).

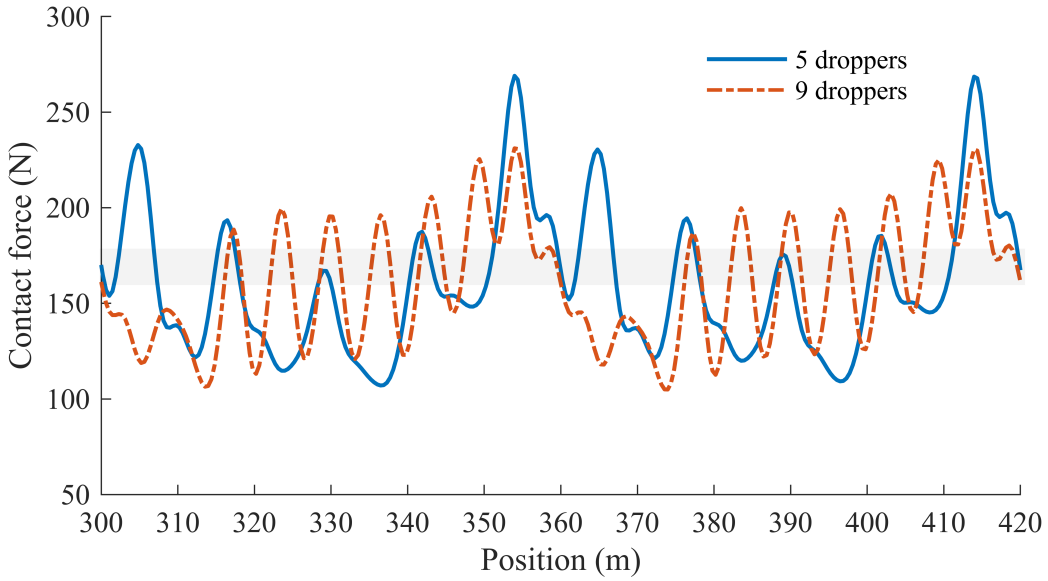

Fig. 6.25 Contact force for overhead line geometries with five and nine droppers. The 160 – 179 N band of contact force referred to in the text is highlighted by the grey band.

From Table 6.12, the mean contact force was unchanged at 160 N when increasing the number of droppers in the span and the contact force standard deviation was reduced by 14%. The reduction in the peak force at the final dropper was also 14% and was the major contributor to the reduction in the standard deviation when compared to the 2% decrease in the contact force minimum.

Table 6.12 Statistical output comparison for overhead line geometries with five and nine droppers and a maintained train speed of 300 km/h.

No. of droppers	F_m	σ	$F_{D_{\max}}$	$F_{D_{\min}}$	$F_{S_{\max}}$	$F_{S_{\min}}$
Five	160	36.9	269	107	271	49.7
Nine	160	31.6	231	105	255	65.5

By reducing the unsupported length in a span of overhead line, from Figure 6.25 and Table 6.12, it can be seen that there is little change in the mean behaviour of the catenary pantograph interaction as indicated by the unchanged mean contact force. This is due to the smaller but more regular peak forces observed in a span of nine droppers compared to the larger variation in contact force when using five droppers. By using five droppers, the peak force is 16% larger and the contact force towards midspan is consistently lower than when using nine droppers. The larger contact force variation indicated by the 17% larger standard deviation is likely due to the greater flexibility in the contact wire due to larger unsupported lengths when using five droppers compared to using nine. Using only five droppers would lead to greater discrete mechanical wear at the force peaks however larger sustained mechanical wear would be predicted by the Archard wear law, throughout the span when using nine droppers as indicated by the sustained higher force trace in Figure 6.25. The peak forces predicted towards the end of each span when using nine droppers are due to the pantograph moving towards the region of increased vertical stiffness at the supports. Since the extra droppers smooths out the transition between the low and high stiffness regions, the peaks are smaller than those when only using five droppers. The decreasing contact force after moving past a support in the nine dropper case is a result of the pantograph moving away from the higher stiffness region.

The histogram of contact force in Figure 6.26 shows the number of occurrences of the contact force for both the five and nine dropper cases. For both five and nine dropper cases, the number of contact force occurrences were positively skewed with skewness of 0.9 and 0.3 respectively. The larger positive skew of the five dropper case is consistent with the nine dropper cases predicting over 20% of the contact force in the 180 - 199 N range despite the mean contact force only being 160 N. Predicted forces greater than 260 N lead to a positive

kurtosis of 0.4 in the case of five droppers used compared with a negative kurtosis of -0.9 in the case of nine droppers used. This indicates that a smaller number of droppers results in more extreme contact forces. This is consistent with the force trace in Figure 6.25 where the peak forces are higher in the five dropper case. The histogram also shows a drop in the contact force in the 160 – 179 N range when nine droppers are used. This corresponds to the forces either side of the local maxima at droppers in the middle of the spans. As a proportion of the entire contact force trace, this band, shown by the grey bar in Figure 6.25, corresponds to only a small number of force occurrences thus gives a smaller peak in the histogram.

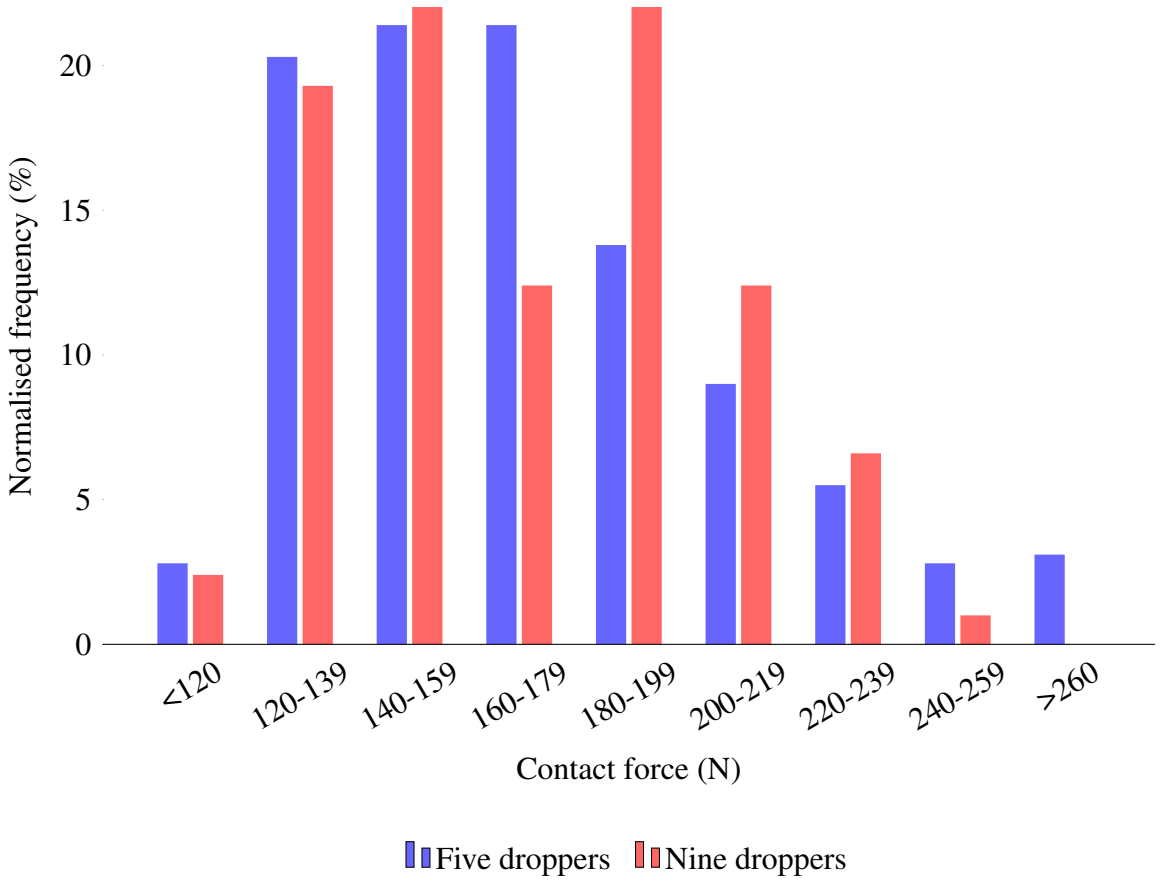

Fig. 6.26 Histogram of contact force for the cases of five and nine droppers in a span. The normalised frequency indicates the percentage of data falling within each bin.

From the results, increasing the number of droppers reduces the variation in the contact force by smoothing out the vertical stiffness variations along a span. The extra droppers however, increase the vertical stiffness at midspan, thus the contact force is higher away from supports compared with the five dropper case. A combination of the two different dropper arrangements could therefore possibly reduce the contact force variation. By installing more

droppers towards the ends of the span, i.e. keep the spatial separation between droppers small, the larger stiffness variations due to the supports would be smoothed out, reducing the contact force around supports compared with the five dropper case, whilst having a larger dropper separation towards midspan would reduce the vertical stiffness leading to fewer local contact force maxima.

6.5 Conclusions

In this Chapter, the influence of changes in both the characteristics of the overhead line equipment and the pantograph on the dynamic performance of the catenary pantograph interaction has been investigated.

With respect to the overhead line equipment:

- Increasing the contact wire tension lead to an improved dynamic performance as indicated by the reduced contact force standard deviation. The increased tension also reduced the amplitude of the oscillations of the contact wire post pantograph passage indicating that the onset of fatigue could be extended due to the reduced contact wire stress during each load cycle. The reduction in the contact wire uplift would also allow for the reduction of electrical clearances when installing overhead line equipment under low clearance structures such as bridges without an increase in the risk of arcing events between the overhead line and civil structures. This would have the potential to reduce the capital investment requirements when installing electrification on existing lines where the clearances to structures are small. The increased wire tension also increases the mechanical wave speed in the wire allowing for a potential increase in the line speed so long as the contact force maxima were acceptable.

- Increases in the messenger wire tension also reduced the contact wire uplift at the supports, however the oscillations after the pantograph passed had a larger amplitude and decayed more slowly compared with the base. The increased number of load cycles with a larger amplitude would lead to an earlier onset of fatigue shortening the lifetime of the equipment. The amplitude of the oscillations could be mitigated with the addition of control elements at supports to increase the effective damping of the system. By reducing the period in which the system oscillates, the reduced number of load cycles would maintain the service life despite the increased amplitude. The increased messenger wire tension would also cause an uplift in the contact wire height under static conditions, removing the desired presag of the contact wire if the contact

wire tension was left unchanged. Matching the contact and messenger wire tensions however, was predicted to improve the catenary pantograph interaction, reducing the variation in the contact force as indicated by the standard deviation.

- The dynamic response to a missing dropper was also studied in this Chapter. The removal of a dropper from the overhead line was predicted to have a small localised effect on the dynamic contact force. At the location of the preceding dropper, an 8% increase in the contact force was predicted, coupled with a 12% increase in the contact force at the successive dropper. The results show that the effect on the contact force due to the removal of a dropper (or if the dropper buckles due to shifting equipment) is minimal however, it is noted that if the dropper was damaged and hung down in the path of the pantograph, the damage would be catastrophic. By predicting the dynamic response to non–functioning dropper, the results have highlighted that the contact force trace can be used to monitor the state of the overhead line. If the equipment shifts and the dropper buckles, the increased forces in the droppers either side serve as an indicator that the equipment has deviated from the design arrangement and requires maintenance. Taking this approach would represent a cost saving compared with manual inspections which would be unlikely to observe the problem directly without impractically regular inspections.

- A small reduction in the contact wire mass per unit length was predicted to improve the dynamic performance. By reducing the contact wire mass whilst also satisfying practical considerations such as electrical transmission requirements, alongside the improved dynamic performance as a result of the reduced contact wire inertia, material costs during the lifetime of the equipment would be reduced as well as a reduced need for high tensioning forces due to lower contact wire sag. The modelling also indicates a potential predictor of poor dynamic performance as part of ongoing assessment of installed equipment. For the most reduced contact wire mass, the dynamic performance was predicted to degrade as indicated by the large contact force variation, thus over the lifetime of the equipment, detection of a greater force variation sooner than expected in the contact wire lifetime would indicate excessive wear of the contact wire. The large variation indicating excessive wear would provide an indicator of potential deviations in the overhead line geometry before the deviations were great enough to cause equipment failure.

As well as variation in the overhead line arrangement, the effects of varying the pantograph parameters have been considered:

- The results show that minimising the pantograph head mass leads to the best dynamic performance as lower forces between the contact wire and the pantograph are required to accelerate the pantograph as the wire height changes due to sag in between the droppers. The smaller pantograph head mass also leads to a reduced contact force at locations of increased vertical stiffness such as at supports. By desiring to reduce the pantograph head mass, this limits the use of active pantograph control with respect to the pantograph head. Any additional mass due to control features would act to degrade the catenary pantograph interaction for an unchanged overhead line system. Optimisation of both the pantograph head mass and the vertical stiffness of the overhead line would lead to an improved dynamic performance however.

- The static uplift of the pantograph was increased from 70 to 120 N. With the linear increase in the static uplift force, a corresponding linear increase in the mean contact force was predicted. The frequency distribution indicated that the larger static uplift force would cause the occurrence of higher peak forces, leading to an increased mechanical wear regime. Due to the higher contact forces, the wire uplift at the supports was also found to increase. Under low clearance structures the increased uplift could lead to excessive uplift, exceeding the electrical clearances and causing arcing events. At height transitions where the contact force is predicted to increase, these uplifts would be even greater, requiring larger clearances. Active pantograph control would provide a method reduce the wire uplift at the supports in these situations, reducing the static uplift as the pantograph collector head experiences large scale height variations, thereby reducing the peak contact forces.

Finally the effect of train speed on the dynamic contact force was investigated. The mean contact force as function of the train speed was found to be in good agreement with the required design mean contact force according to BS EN 50367 [61], indicating that the modelling predictions are an accurate representation of the catenary pantograph interaction. The largest variation between the fitted mean contact force and the design mean was only 2.1% representing very good agreement even above the pantograph design speeds. This indicates that current pantograph designs could be adopted on higher speed lines that they currently operate without significant impact on the current collection quality. To mitigate the increased contact forces characteristic of the higher train speeds, droppers were added to the overhead line geometry so that each span contained nine droppers. When using nine droppers, the contact force variation was reduced indicating better dynamic performance, however midspan contact forces were predicted to be higher than the five dropper case. Since

the vertical stiffness is greatest at supports, the increased number of droppers smoothed out the transition between vertical stiffnesses, so it is proposed that dropper positioning can be altered to concentrate more droppers towards the ends of a span, mediating the varying contact force due to the increased vertical stiffness, whilst the dropper spacing at midspan is greater where the contact force is predicted to be lower. This would have the benefit of reducing the contact force variation compared to the five dropper case but also reducing the bulk contact force at midspan compared to the nine dropper case, potentially extending the equipment lifetime through a reduction in mechanical wear.

Overall, in this Chapter, the results of varying the parameters involved in the catenary pantograph interaction have been presented, both to better understand the effect each parameter has on the dynamic performance but also as a generalisation of an existing model. Throughout, no considerations have been given to environmental effects on the catenary pantograph interaction, such as wind loading. In the next Chapter, this will be considered.

Chapter 7

Effect of wind loading on an overhead line system

The long slender cables of an overhead line system are susceptible to aerodynamic loading, with lateral crosswinds contributing to excessive contact wire blow–off, increasing the risk of lateral dewirements, and large amplitude oscillations caused by steady wind causing damage to structures and the pantograph during train operation.

Parts of the UK rail network such as the West and East Coast Mainlines were electrified in the 1960s and 1980s respectively, using slender, lightweight supports, such as the ones shown in Figure 2.7. The lightweight structures deflect under aerodynamic load altering the lateral position of the contact wire, with large deflections contributing to dewirement events. These structures have been superseded by larger lineside supports such as those used in the electrification of the Great Western Mainline [305]. The larger, heavier structures provide greater resistance against aerodynamic loading compared with older structures, reducing the bulk deflections under high winds.

The average wind speeds in eastern regions of UK are typically 4 – 5 $\mathrm{m/s}$ [306], with maximum wind speeds of 74 and 79 $\mathrm{m/s}$ for the 10 and 100–year return periods [297]. As temperatures increase due to climate change, the average 100–year return speeds are expected to increase between 3 and 5% [307], indicating an increase in wind speed of up to 5 $\mathrm{m/s}$. The existing lightweight structures on the East and West Coast Mainlines will experience greater bulk deflections as wind speeds increase, thus the risk of excessive lateral blow–off increases. In [308], the West Coast Mainline was identified as being particularly prone to excessive blow–off due to a large number of exposed locations and higher wind speeds. Excessive blow–off also occurred due to canted track as the deflections due to sidewinds and track cant are additive contributing to an increased risk of dewirement.

In Chapter 5, the aerodynamic drag and lift forces on a railway contact wire were determined with both experimental and computational techniques. In this Chapter, the effect of these aerodynamic forces on the overhead line equipment and the dynamic response during the catenary pantograph interaction will be studied. The first half of this Chapter considers the deflection of the overhead line equipment subject to aerodynamic force in the absence of a moving pantograph, and the second half introduces the pantograph to determine the effect of aerodynamic forces on the dynamic contact force. To determine the effect of sudden wind loading versus sustained wind loading, this Chapter considers geometries representing:

- Exposed overhead line equipment, such as the Durham viaduct, with gust speeds up to 40 m/s and the East Coast Mainline in Cambridgeshire, where gust speeds of 45 m/s at Wittering weather station were measured [309].
- Overhead line equipment installed under a bridge.
- Equipment installed through a tunnel, transitioning to an exposed area (e.g. Landwasser viaduct, Switzerland).

Limitations of the current study restrict this investigation to large scale deflections of the contact wire under sidewinds in the absence of deflections of the train body or the effects of turbulent air flow during train passage. The aim is study the effect on the dynamic contact force and contact wire uplift as a pantograph meets an overhead line arrangement already under the influence of an aerodynamic load. The dynamic response of the catenary pantograph interaction presented in this Chapter has not been validated, and is presented as an exploratory study in the dynamics of the catenary pantograph interaction under the influence of an incident wind load. It is known that at locations of sudden wind loading on the overhead line system (e.g. at the exit of tunnels), oscillations of the contact wire can differ significantly in windy conditions compared to the behaviour in still air, however little research into the effects during train passage has been performed. It is the purpose of this investigation then, to begin to quantify the potential effects wind loading has beyond anecdotal evidence, and also to demonstrate that there is an effect due to wind loading. To assess the accuracy of the modelling predictions od any resultant overhead line dynamics due to aerodynamic effects, proposals to validate the work are given in Chapter 9.2.

7.1 Static contact wire deflections due to wind loading

In this Section, the deflection of a contact wire under uniform aerodynamic drag will be considered. In Chapter 5, it was proposed that the contact wire wear would allow for greater

deflections under smaller aerodynamic loads due to the reduced contact wire inertia. The greater contact wire blow–off as the wear increases over the lifetime of the equipment would increase the likelihood of a dewirement event despite the reduced aerodynamic forces on the contact wire. Thus to determine the effect contact wire wear has on the lateral deflections, a finite element model representation of the overhead line subject to uniform aerodynamic loads was adopted.

Assuming the contact wire under static deflection due to aerodynamic drag is approximately a parabola, the lateral deflection $w_{\text{lat}}(x)$, can be calculated using,

$$w_{\text{lat}}(x) = \frac{F_{\text{Drag}}}{2T_{\text{con}}}\left[\left(\frac{L_s}{2}\right)^2 - \left(x - \frac{L_s}{2}\right)^2\right], \tag{7.1}$$

where F_{Drag} is the aerodynamic drag force on the contact wire and x is the spatial coordinate along the parabola, L_s is the span length and T_{con} is the tensile load. The maximum deflection at midspan is given by

$$w_{\text{lat}}\left(\frac{L_s}{2}\right) = \frac{F_{\text{drag}}}{2T_{\text{con}}}\left(\frac{L_s}{2}\right)^2 = \frac{F_{\text{Drag}}L_s^2}{8T_{\text{con}}}. \tag{7.2}$$

The lateral deflection of the contact wire under uniform aerodynamic load given by Equation 7.1 takes the same form as the vertical deflection under uniform gravitational load given in Equation 2.25. The true deflection of the contact wire is therefore the vector sum of these two quantities.

Table 7.1 gives the comparison between the calculated deflections using Equation 7.2 and the predictions using the finite element model described in Chapter 6. The aerodynamic drag was assumed to act uniformly across the span length and thus could be represented by a point force at midspan. Table 7.1 shows that whilst Equation 7.2 gives an approximation of the contact wire blow–off, it overestimates the amount of lateral deflection of the contact wire as the effects of the droppers and messenger wire are neglected. This can be seen from the model predictions for a single wire where the droppers and messenger wire have been neglected.

The aerodynamic loads used in Table 7.1 are arbitrarily chosen to compare Equation 7.2 and the finite element predictions. Figure 7.1 gives the lateral and vertical contact wire deflections using the calculated static drag and lift forces described in Chapter 5.

As the contact wire wear is increased giving a reduced cross–sectional area, the reduction in lateral inertia due to the removal of effective contact wire mass, reduces the contact wire resistance to deflections due to aerodynamic drag. This can be seen in Figure 7.1a, although it

Table 7.1 Comparison between calculated deflections due to aerodynamic drag and the finite element predictions for a single wire and the whole overhead line. All deflections given in m.

Drag force (N/m)	Equation 7.2	FE Predicted (single wire)	FE Predicted (OLE)
1	0.027	0.023	0.018
5	0.136	0.124	0.090
10	0.273	0.295	0.181
15	0.409	0.407	0.271
20	0.545	0.589	0.361

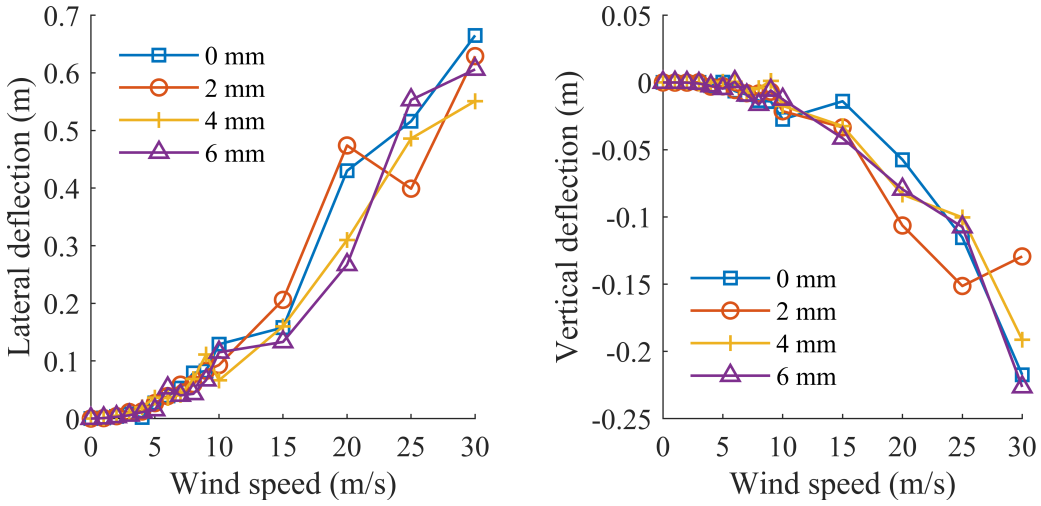

(a) Lateral deflection of a contact wire due to aerodynamic drag. Positive deflection indicates the contact wire deflects in the direction of the aerodynamic load.

(b) Vertical deflection of a contact wire due to aerodynamic lift. Negative deflection indicates the contact wire sag increased due to the aerodynamic lift force.

Fig. 7.1 Static deflections of a steady state railway contact wire due to aerodynamic drag and lift forces. The contact wire deflection is measured at the midspan where the deflection is greatest. The legend indicates the contact wire wear case under consideration.

is not a strong trend. Despite the larger drag forces predicted for a contact wire with no wear, the resultant deflection is similar for each case as the contact wire wear was increased. The lateral deflections shown in Figure 7.1a are an overestimate of the total lateral deflection due to the aerodynamic drag, as only the contact wire was considered. In an installed overhead line system, the messenger wire, connected to the contact wire by the droppers, restricts the lateral displacement.

The static deflections presented here, do not include any dynamic effects due to pantograph passage or oscillations in the aerodynamic forces, which were presented in Chapter 5. The next section introduces the dynamic response during the catenary pantograph interaction.

7.2 Effect of dynamic wind loading on the catenary pantograph interaction

Having considered the contact wire deflections under uniform static load, the model was extended to consider the effect of time varying aerodynamic loads. The static cases presented in the previous Section are a special case of this more general treatment. The examples considered here are comparable to a steady wind load acting on an exposed length of an overhead line, for example the East Coast Mainline or the Fen line in the UK.

7.2.1 Dynamic lift force and the catenary pantograph interaction

Figure 7.2 shows the contact force between the overhead line system and the pantograph head when a time varying aerodynamic lift force

$$F(t) = \mu_{\text{aero}}\left(1 + \sin(2\pi f t)\right), \tag{7.3}$$

is applied to the spans between 540 and 660 m when the contact wire is intact (i.e. no wear). It can be seen that for wind speeds up to 20 m/s, the contact force variation between different aerodynamic load cases is small as evidenced by the small change in the mean contact force (less then 3 N). As the wind speed increases beyond 20 m/s, the peak contact force rises rapidly, increasing from 162 to 186 N as the wind speed increased from 10 to 20 m/s. As in the case when no wind load is applied (as in Chapter 6), the peak forces occur at the first and last droppers in the spans where the vertical stiffness increases due to the proximity to the contact wire supports. The increases in the peak force indicates that the mechanical wear at discrete locations would increase at the contact surface shortening the lifetime of the equipment. To ensure the safe operation of the equipment, more regular inspections and wire replacements would be required due to the increased wear regime caused by the aerodynamic loading, increasing the life cycle costs of the equipment.

For wind speeds above 20 m/s, the discrete maximum force at the two droppers either side of the support at 600 m increases significantly. At the maximum considered wind speed of 30 m/s, the maximum contact force was predicted to be 270 N, compared with 160 N

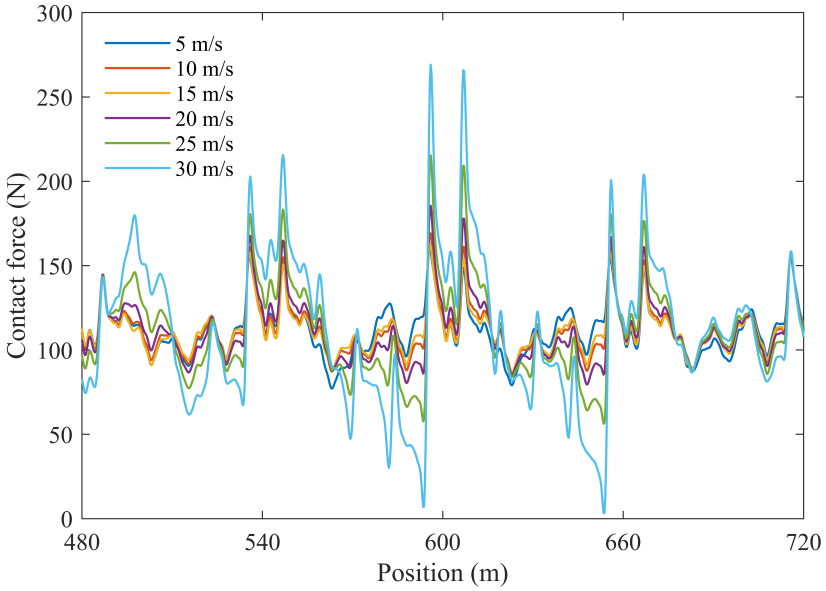

Fig. 7.2 Contact force variation due to a time varying aerodynamic lift force on an intact (i.e. zero wear) contact wire. The legend indicates the wind speed considered in each case.

for a wind speed of 5 m/s. The large increase in the maximum contact force is likely due to larger amplitude oscillations in the contact wire due to the sinusoidal lift force that is not present for the case of a contact wire in still air. These wind induced oscillations act similarly to those experienced by trailing pantographs during multiple pantograph operation and as such act to increase the contact force on the pantograph. The vertical wire oscillations caused by the aerodynamic load also increase the risk of arcing events due to the wind load lifting the contact wire above the pantograph head. Since the ascent of the pantograph is limited, at higher wind speeds, the uplift may exceed the rate of ascent of the pantograph causing contact loss. It can also be seen from Figure 7.2, that significantly lower contact force minima are predicted when the wind speed was 30 m/s. It is likely that at the contact force minima locations, the contact wire is rising due to the wind induced oscillations and due to the fixed rate of ascent of the pantograph, a smaller contact force is predicted. The locations of low contact force are also between droppers where the contact wire is most flexible and therefore most susceptible to variation in the contact wire height due to vertical oscillations caused by wind loading.

Table 7.2 gives the statistical output for the contact force variation when the contact wire was intact with zero wear. It can be seen that variation in the mean contact force is small suggesting that oscillating lift forces act to increase or decrease the contact force almost evenly, as evidenced by the large increases to the peak forces and decreases to the minimum

forces respectively, shown in Figure 7.2. The large changes in these contact force extrema are reflected in the variation in the contact force standard deviation. When the wind speed was 5 m/s, the contact force standard deviation was comparable to that of a contact wire in still air, however this increases by approximately 200% for the maximum wind speed case. The significant low force of 3.3 N given in Table 7.2 indicates that contact loss may occur as the wind speed is increases beyond 30 m/s. This would likely result in increased arc discharge occurrences shortening the lifetime of the overhead line. Fatigue failures of the contact wire would also occur more quickly as the lift induced oscillations increase the number of load cycles the contact wire will undergo compared with lower wind speeds shortening the overall lifespan of the equipment.

Table 7.2 also gives the kurtosis of the contact force data. The kurtosis indicates that for wind speeds below 20 m/s, the force extrema are less likely to occur and the contact force is more likely around the mean force, however for higher wind speeds, the kurtosis is reduced indicating that the extreme contact forces occur more often as can be seen in the histograms given in Figure 7.6. The standard variation given in Table 7.2 as a response to the aerodynamic loading is larger than the standard deviation of the contact force in the previous catenary pantograph simulations and so causes negative statistical minima. It is noted that a negative contact force between the pantograph and the contact wire is not physical, the results have not been truncated to zero to highlight the large variation in the contact force.

Table 7.2 Statistical output for a overhead line system with no wear subject to wind loading. All results except skew and kurtosis in N.

Wind speed (m/s)	F_m	σ	$F_{D_{\max}}$	$F_{D_{\min}}$	$F_{S_{\max}}$	$F_{S_{\min}}$	Skew	Kurtosis
5	112	15.0	160	77.4	157	66.5	0.623	0.705
10	112	14.9	169	86.4	157	66.9	1.23	1.84
15	114	13.8	162	86.9	155	70.4	1.21	1.88
20	115	18.6	186	79.5	171	56.1	1.10	1.46
25	116	27.0	215	56.3	197	30.6	0.749	0.850
30	119	43.9	270	3.3	251	-19.9	0.387	0.493

The statistical output when the contact wire vertical profile was reduced by 2 mm is given in Table 7.3. It can be see that the reduced effective mass of the contact wire has decreased the mean contact force compared with an intact contact wire even for low wind speeds. As in the previous case, the increased aerodynamic load due to the increasing wind

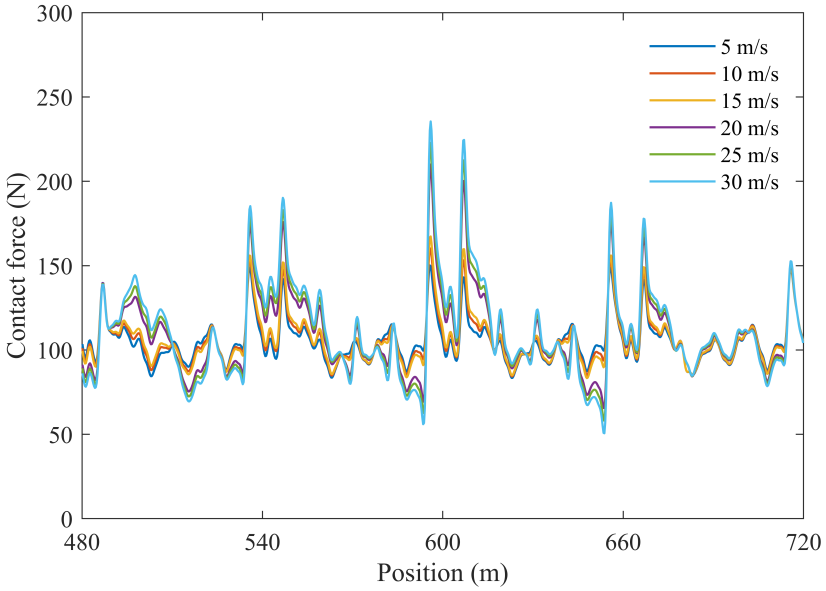

Fig. 7.3 Contact force variation due to a time varying aerodynamic lift force using a contact wire with 2 mm vertical wear.

speed increases the mean contact force, although this increase in the mean contact force is small (6%) compared with the increase in the wind speed (500%).

Table 7.3 Statistical output for a overhead line system with a contact wire with 2 mm vertical wear subject to wind loading. All results except skew and kurtosis in N.

Wind speed (m/s)	F_m	σ	$F_{D_{\max}}$	$F_{D_{\min}}$	$F_{S_{\max}}$	$F_{S_{\min}}$	Skew	Kurtosis
5	105	12.6	150	83.4	143	67.0	1.32	2.18
10	106	13.9	160	84.4	147	64.0	1.42	2.38
15	106	14.9	167	83.3	151	61.4	1.44	2.46
20	109	23.0	210	65.6	178	40.3	1.22	2.17
25	110	25.7	223	58.2	187	33.0	1.14	2.03
30	111	28.6	235	50.6	197	25.5	1.07	1.91

Figure 7.2 gives the contact force trace as the aerodynamic lift force applied to the overhead line is varied. In the first span (480 to 540 m), where no aerodynamic lift was applied, it can be seen that the wind load in the subsequent spans acts to increase the contact force. This is due to the larger amplitude vertical oscillations in the contact wire due to the applied aerodynamic lift, compared to the still case where only the oscillations due to the mechanical wave caused by the pantograph are present. It can also be seen in the first span

that the contact force is split between two bands. When the wind speed was between 5 and 15 m/s, it can be seen that there was small increase in the dynamic contact force, however as the wind speed was increased, the contact force jumped and formed a new band consisting of the contact forces when the wind speed was between 20 and 30 m/s. Moving into the second span between 540 and 600 m, where the aerodynamic lift is applied to the contact wire, it is clear that a much greater variation in the contact force is present. The peak predicted at the first dropper increases significantly compared with the previous span, where the magnitude of the peak when the wind speed was 5 m/s is comparable to the peak at the same location in the previous span when the wind speed was 30 m/s.

The largest peak forces shown in Figure 7.3 are predicted to occur at the droppers either side of the support at 600 m. This location is the centre of the spans where the aerodynamic lift force was applied and so is affected by the contributions of the applied distributed aerodynamic load in both spans. As the wind speed increased, the maximum predicted contact force was 235 N, a 57% increase compared with the peak contact force for a contact wire in a 5 m/s wind. This large increase in the peak force is the driver of the increase in the contact force standard deviation as the contact force minimum decrease was 39% when increasing the wind speed from 5 to 30 m/s. Between the first and last droppers, it can be seen from Figure 7.3, that the contact wire variation between different wind cases is smaller than the variation predicted close to supports. This is likely due to the reduced vertical stiffness found at midspan. The reduced vertical stiffness decreases the contact wire resistance to vertical displacements thus reduces the requirement of the pantograph to undergo accelerations to follow the contact wire position. The lack of accelerations of the pantograph compared with the change in the pantograph directions at supports reduces the force between the pantograph carbons and contact wire.

In the final span between 660 and 720 m, it can be seen that since the aerodynamic lift is no longer applied to the overhead line, the contact force sees little variation irrespective of the magnitude of the applied load in the previous spans. As the pantograph moved along further spans, the contact wire was approximately still relative to applied aerodynamic loads and the contact force returned to similar oscillatory patterns predicted in Chapter 6.

During the lifetime of the equipment, due to the sliding contact between the pantograph and contact wire, the contact wire wear increases. When the contact wire wear is 4 mm, the peak forces increased compared to the 2 mm wear case, likely due the larger amplitude oscillations in contact wire due to the aerodynamic load. The peak forces are again predicted to occur at the droppers closest to supports where the vertical stiffness is increased and can be seen in Figure 7.4. The large peak forces due to the increased amplitude oscillations as a

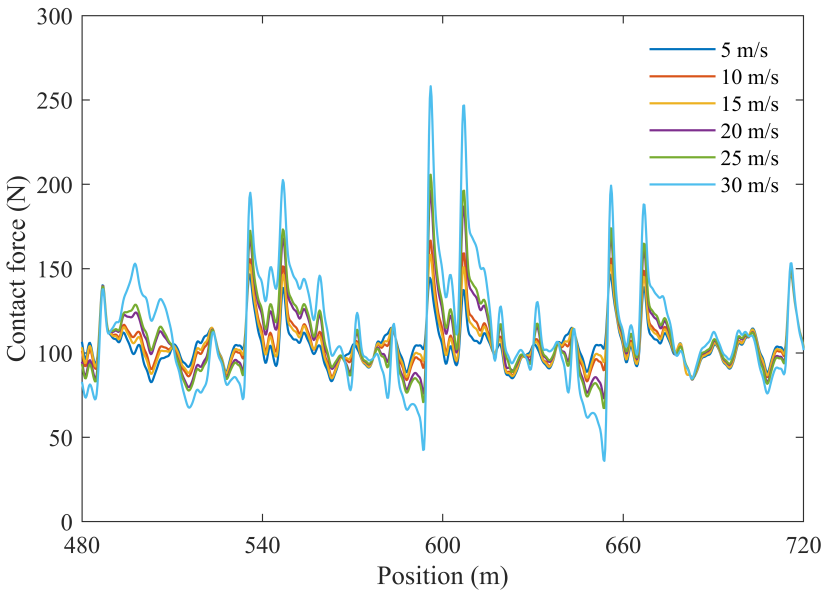

Fig. 7.4 Contact force variation due to a time varying lift force for a contact wire with 4 mm vertical wear.

response to the reduced contact wire mass will increase the wear rate at discrete locations of increased force shortening the lifetime of the equipment. The increased wear rate also hastens the onset of greater amplitude oscillations due to the increased removal of material.

The variation between different wind speed cases is small in Figure 7.4 up to a wind speed of 15 m/s and the variation between the 20 and 25 m/s is also small, with only the 30 m/s case having a larger variation compared with the rest. The trend of decreasing contact force at midspan away from increased vertical stiffness continues even as the wear profile is increased and the contact force minima decrease compared with the 2 mm case. This is likely due to the contact wire lifting from the nominal height due to the oscillations caused by the aerodynamic lift and since the rate of ascent of the pantograph is fixed, the contact force between the pantograph and contact wire is reduced. From Table 7.4, the increased contact force maxima compared with an intact wire, indicates that despite the reduction in inertia from the reduced contact wire mass, the larger amplitude oscillations in the contact wire increase the contact force more than the contact force decrease due to only a reduction in mass.

When the contact wire was most severely worn in the 6 mm wear case, from Figure 7.5, it can be seen that the largest contact force maxima are predicted for this wear case. Compared with the previous cases, the contact force rose to 340 N at the dropper preceding the support at 600 m. This large, approximately 300 N, contact force increase, as can be seen in

Table 7.4 Statistical output for a overhead line system with a contact wire with 4 mm vertical wear subject to wind loading. All results except skew and kurtosis in N.

Wind speed (m/s)	F_m	σ	$F_{D_{\max}}$	$F_{D_{\min}}$	$F_{S_{\max}}$	$F_{S_{\min}}$	Skew	Kurtosis
5	104	12.0	148	82.7	140	68.3	1.25	2.10
10	105	13.5	158	85.0	146	64.9	1.43	2.42
15	106	14.7	167	83.2	150	61.7	1.46	2.52
20	108	19.9	196	73.2	168	48.2	1.34	2.42
25	109	21.9	206	67.4	175	43.0	1.27	2.32
30	113	33.5	258	36.0	213	12.4	0.996	2.88

Figure 7.5 would have a detrimental effect on the lifespan on the contact wire at this location. Considering the Archard law, the 100% increase in the contact force compared with the 5 m/s case, would indicate a doubling of the contact wire wear if the wear regime remained mild. For a severely worn contact wire, the lifetime would be substantially shortened and likely fail. The large change in contact force magnitude indicates that contact wire is being displaced downwards due to the aerodynamic load occurring when the wind speed is 30 m/s and pushes onto the pantograph head. Due to the static uplift, the pantograph rate of descent is fixed and so a large dynamic force is required to accelerate the pantograph head to follow the new contact wire height.

Table 7.5 Statistical output for a overhead line system with a contact wire with 6 mm vertical wear subject to wind loading. All results except skew and kurtosis in N.

Wind speed (m/s)	F_m	σ	$F_{D_{\max}}$	$F_{D_{\min}}$	$F_{S_{\max}}$	$F_{S_{\min}}$	Skew	Kurtosis
5	105	15.9	170	83.7	152	56.9	1.84	4.14
10	105	16.5	176	83.0	155	55.6	1.87	4.28
15	106	19.4	202	77.5	165	48.4	1.85	4.50
20	108	23.9	217	66.4	180	36.5	1.48	3.37
25	110	27.7	260	53.2	193	26.6	1.61	4.41
30	115	41.8	340	19.7	241	-10.6	1.48	4.48

The contact force histogram for each of the wear cases considered for wind speeds of 5 and 30 m/s are given in Figures 7.6a and 7.6b respectively. For the low wind speed in case in Figure 7.6a, it can be seen that the contact force variation is small, in contrast to the high wind speed case shown in Figure 7.6b. From the histograms given in Figure 7.6, as with the

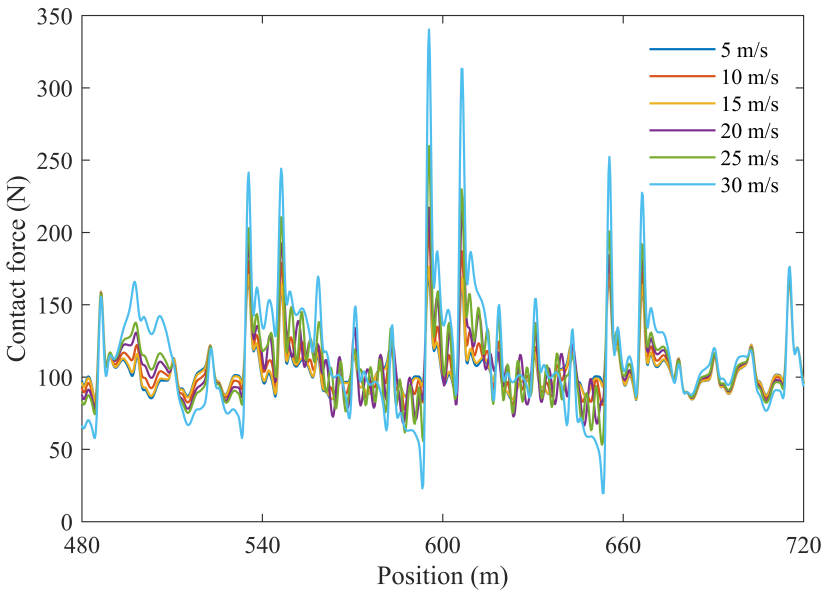

Fig. 7.5 Contact force variation due to a time varying lift force for a contact wire with 6 mm vertical wear.

case of an intact contact wire, the aerodynamic load acts to increase the spread of the contact force resulting into a greater number of extreme force occurrences.

The histograms highlight the increased contact force variation as the wear of the contact wire increases. As the contact wire cross–sectional area is reduced due to the sliding contact with the pantograph, the aerodynamic lift force causes a larger oscillation in the contact wire leading to the large peak forces predicted, particularly in the case when the wind speed was 30 $\mathrm{m/s}$. The contact force predictions indicate that the wear state of the contact wire should be closely monitored over the lifetime of the equipment as in addition to changes in the contact wire profile due to the reduced sag as the wear increases, the degradation of the contact between the contact wire and pantograph under aerodynamic loading is clear and that unwanted dynamic effect such as large peak forces and large contact force variations are prevalent as the wear increases.

The contact wire uplift at the support at 600 m for each of the wear cases is given in Figure 7.7. It can be seen that as the wind speed is increased, larger amplitude oscillations due to the wind loading overtake those due to the mechanical wave caused by the moving pantograph. In Figure 7.7, zero uplift is taken to be the contact wire height in the static state after tensioning and gravitational loads have been applied, thus for sufficient wind speeds, the contact wire height decreases due to the aerodynamic load and the uplift due to the pantograph is insufficient to return the contact wire to its original height. In contrast to

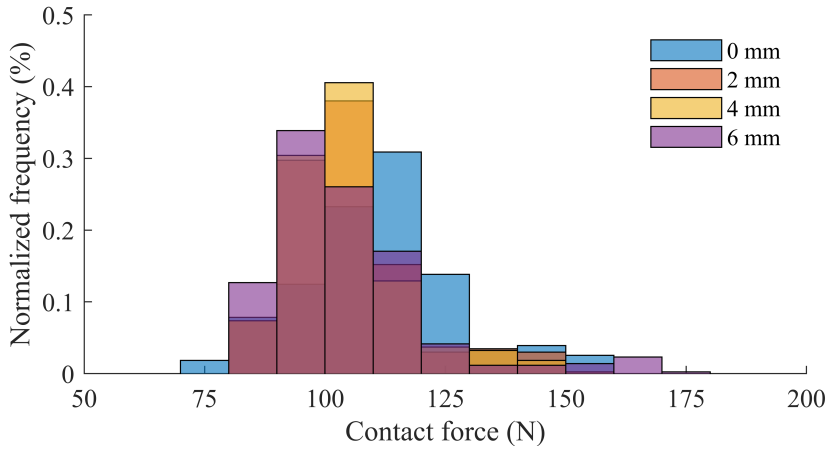

(a) Histogram of contact force when the wind speed was 5 m/s.

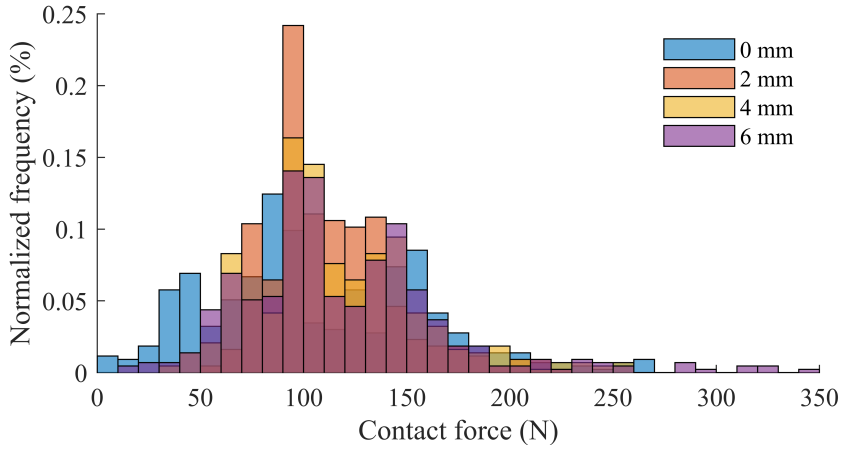

(b) Histogram of contact force when the wind speed was 30 m/s.

Fig. 7.6 Contact force histograms for the catenary pantograph interaction for each contact wire wear profile considered under aerodynamic load.

the typical wire uplifts described in Chapter 6, the addition of aerodynamic load causes a larger amplitude oscillation before the pantograph passes the support, and then the passage of the pantograph damps out the wind induced oscillations and causes the wire to oscillate with small amplitude. This can be seen in Figure 7.7a for the case of a 5 m/s where the amplitude of the uplift is small for negative time and then oscillates for positive time after the pantograph has passed, however for the larger magnitude wind speeds, increased oscillation amplitudes are predicted for negative time which are damped out and replaced by small amplitude variations after the pantograph has passed the support.

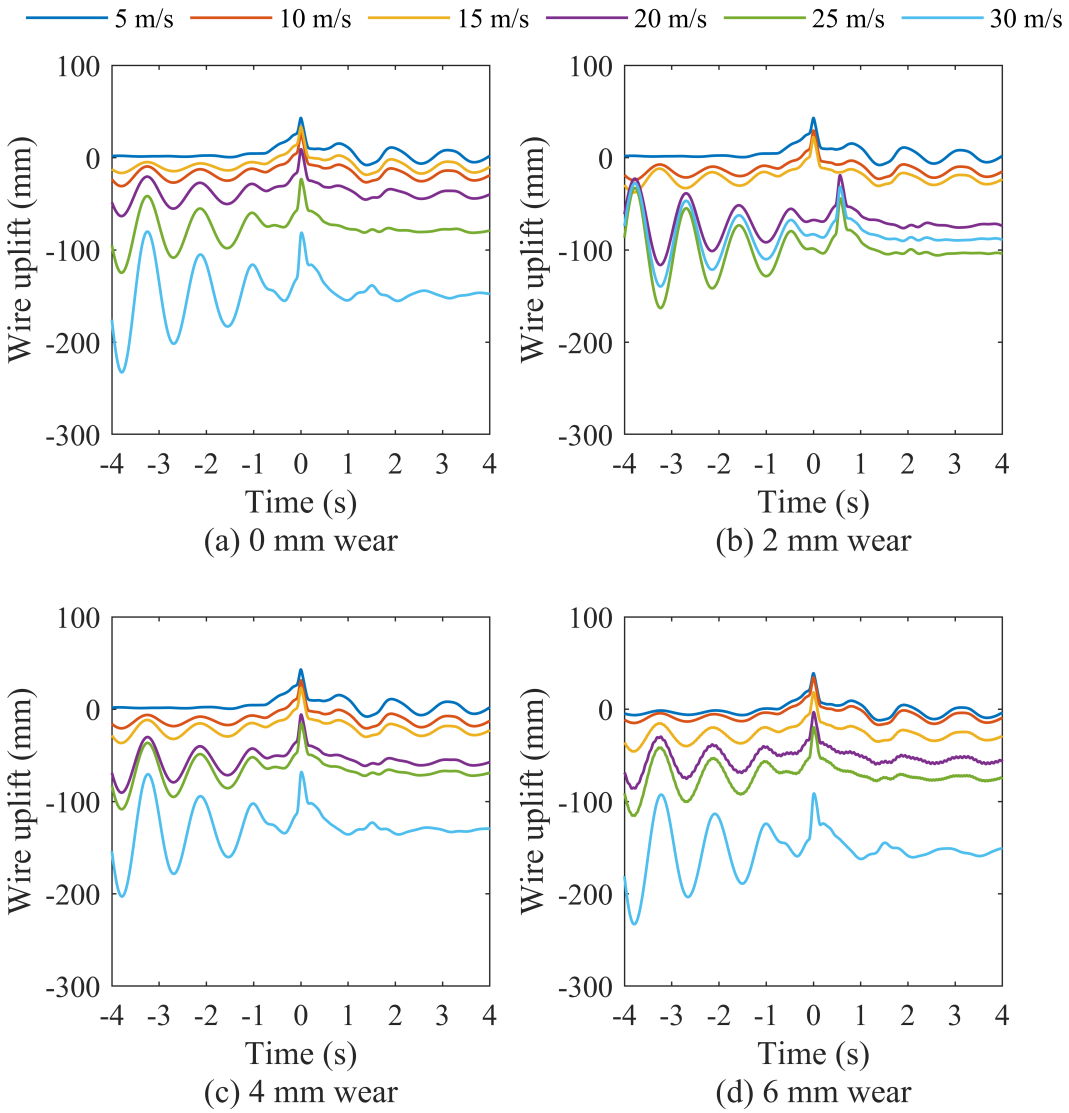

Fig. 7.7 Contact wire uplift at the support between spans 5 and 6. Legend indicates the wind speed corresponding to the aerodynamic lift applied.

7.2.2 Effect of aerodynamic drag on the catenary pantograph interaction

In Section 7.1, only the aerodynamic drag on the contact wire was considered to determine the magnitude of the blow–off due to the aerodynamic load and in Section 7.2.1, the effect of a time varying aerodynamic lift force was applied to the catenary pantograph interaction. Lateral deflections of the contact wire away from the static position act to increase the tension in the contact wire. In this Section, the effect of lateral drag forces increasing the contact

wire on the dynamic contact force of the catenary pantograph interaction will be assessed. To determine the effect of the lateral aerodynamic drag during the catenary pantograph interaction is considered, the deflection of the pantograph mechanism due to aerodynamic load is also required. As with the overhead line, the aerodynamic load and the pantograph are assumed to be orthogonal. No aerodynamic flow not in the plane orthogonal to the pantograph motion was considered to avoid the effects of pantograph lift due to the flow.

Lateral deflections of the train body under lateral wind loading were not considered here as bulk deformation of rail locomotives, such as British Rail Class 91 electric locomotives used on the East Coast Mainline with a mass of 81.5 tonnes, is small for high frequency vibrations caused by aerodynamic loads.

The aerodynamic load on the pantograph was approximated by taking each of the pantograph arms $P_1'P_2'$ and $P_2'P_3'$, as in Figure 7.8, to be a circular cylinder and rectangular plate respectively, with lengths $P_1'P_2' = P_2'P_3' = 1.5$ m and thickness 0.1 m giving a reference area of 0.15 m. The base of the pantograph P_3', at the train body was taken to be fixed with regards to displacement, as lateral deflection due to sidewinds on the train body were not considered, however rotations of the point P_3' were permitted to allow displacement of P_2' and P_3' in the direction parallel to the aerodynamic drag. Since deflections due to the train body were not considered, only high frequency vibrations of the pantograph model were included in assessment of the dynamic performance under wind loading, rather than bulk deformations under which dewirement might occur. This addition of the aerodynamic load extends the work in [298], where no reference to aerodynamic loads of the pantograph was made.

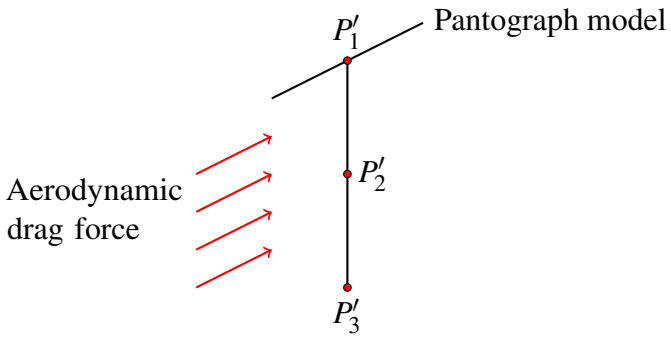

Fig. 7.8 Schematic of pantograph model with locations referred to in the text labelled.

For the wind speeds considered, the maximum Reynolds number was approximately 2×10^5, and the drag coefficient for a rectangular plate for the given Reynolds number is $C_D = 1.2$ [310] and for the circular cylinder $C_D = 1.0$, since a rectangular cross–section has a higher drag coefficient than an equivalent diameter circular cross–section due to the

discontinuities at the corners. Thus, the drag force on the pantograph frame is given by

$$F_{\text{frame}} = F_{DC} + F_{DR} = \frac{1}{2}\rho U^2 A \left(C_{DC} + C_{DR}\right), \tag{7.4}$$

where the subscripts $_{DC}$ and $_{DR}$ denote the drag on the circular and rectangular cross–sections respectively. For the maximum wind speed of 30 m/s,

$$F_{\text{frame}} = 0.5 \times 1.225 \times 0.15 \times 900 \times (1.0 + 1.2) \approx 182 \text{ N}.$$

At the pantograph head, as shown in Figure 7.9, the drag coefficient can be approximated by taking the horns to be a flat plate in an incident flow. This gives a drag coefficient of 1.2. The area is approximately $2 \times 0.3 \times 0.03 = 0.018$ m^2 and so the drag on the pantograph horns for the maximum wind speed of 30 m/s, is

$$F_{\text{head}} = 0.5 \times 1.225 \times 900 \times 0.018 \times 1.2 \approx 12 \text{ N}.$$

This gives a total drag force on the pantograph of 194 N. The drag force is distributed amongst the masses comprising the lumped–mass model, thus the frame load is applied at location P_2' and the head load is applied at location P_3'. In modelling the pantograph response to the aerodynamic load, the pantograph head stiffness is assumed to be constant. However, in practise the stiffness of the pantograph head varies due to the support arms connecting the ends of the pantograph head to the main support arm. This stiffness variation will cause a variation in the contact force as the contact wire moves laterally due to stagger and at supports where the vertical stiffness will be asymmetrical due to alternating push–off and pull–on registration arms. The effects due to the varying stiffness have not been considered here.

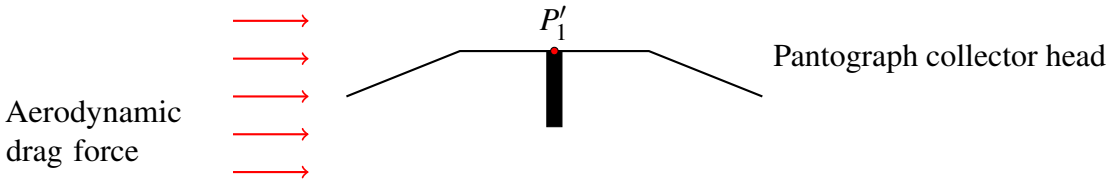

Fig. 7.9 Pantograph collector head indicating the direction of the aerodynamic load relative to the pantograph.

The contact force variation due to the applied aerodynamic load with zero angle of attack is shown in Figure 7.10. Figure 7.10 shows that applying an aerodynamic drag on the contact wire has little effect on the contact force variation and that the reduction in the effective

contact wire mass, caused by the increased wear, is the dominant driver of the variation in the contact force. The force trace in Figure 7.10 indicates two distinct contact force regimes: the predicted contact force for no wear and 2 mm wear, and the regime for the cases of 4 and 6 mm wear. In either of the two contact force regimes, the effect of the angle of attack of the aerodynamic drag is minimal.

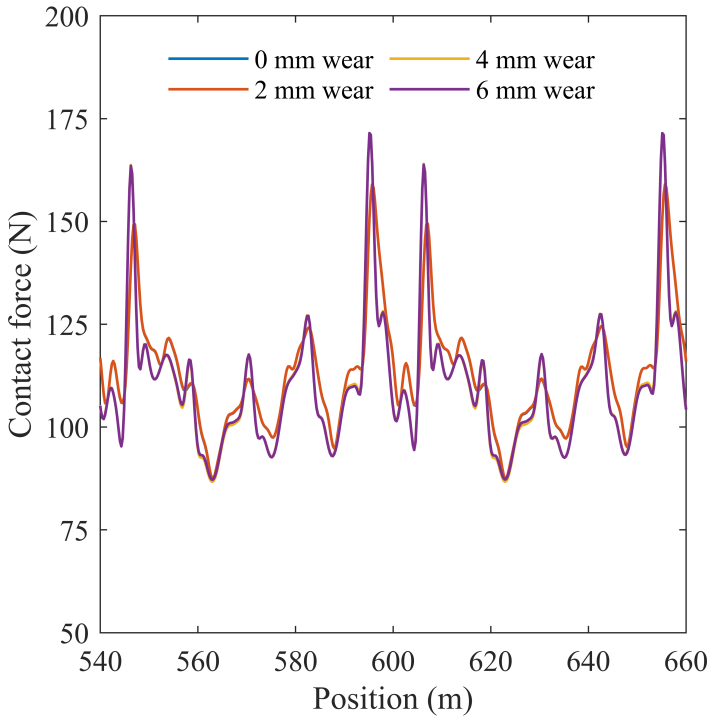

Fig. 7.10 Contact force variation for a contact wire in an lateral flow with wind speed 30 m/s and 0° angle of attack. The dynamic effects of the lift component of the wind are shown in Section 7.2.1.

It is clear from Figure 7.10 that as the contact wire surface wears during operation. the contact force at the droppers either side of the supports increases. At these locations, the contact force is predicted to rise by approximately 8%. No similar reduction in the contact force at discrete minima is predicted however. From the predicted contact force, the aerodynamic drag which acts to increase the contact wire tension by deflecting the contact wire away from the static position, has little effect. This is likely since the deflection of the contact wire in the lateral direction is small relative compared to the span length. For the largest deflections given in Figure 7.1a, the deflection is less than 2% of the span length so any increase in the effective contact wire tension due to the lateral deflection, is likely to be small relative to the 16.5 kN tension applied to the contact wire.

The contact force traces for each of the non–zero angles of attack are given in Figure 7.11. As in the case of a zero angle of attack, the force trace can be split into two regimes: the zero and 2 mm wear cases and the 4 and 6 mm wear cases. At the first and last droppers in the spans, the contact force is increased for the higher wear cases, whilst at midspan, the contact force variation between the two regimes is small. Figure 7.11 indicates that the angle of attack has little effect on the predicted contact force between the contact wire and pantograph.

In the previous sections, the effects of aerodynamic drag and lift have been considered separately to highlight the core effects of each. Using two case studies, a train leaving a tunnel and a train passing under a bridge, both the aerodynamic lift and drag will be incorporated to predict the total dynamic effects of wind loading on an overhead line.

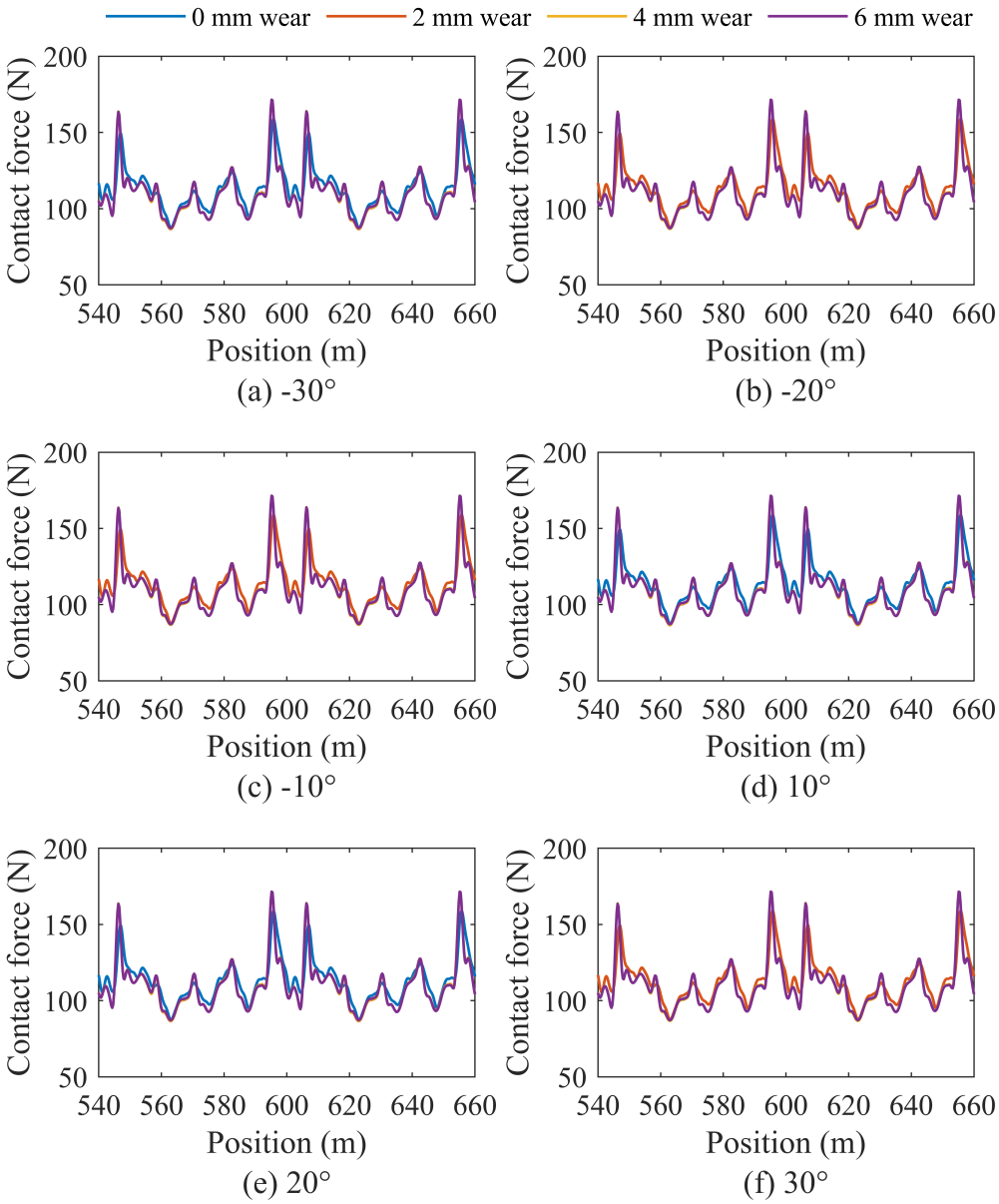

Fig. 7.11 Contact force variation for a contact wire in an incident flow with wind speed 30 m/s and a range of angles of attack. Legend indicates the wear case being considered.

7.3 Case Study I: Sudden aerodynamic loading due to a train leaving a tunnel

In this section, a train leaving a tunnel is considered, such as the arrangement shown in Figure 7.12. In this case, a sudden aerodynamic sidewind can be applied to the pantograph

Fig. 7.12 Overhead line equipment installed on a line passing from a tunnel to an exposed environment on the Landwasser viaduct, Switzerland. Image from [311].

and overhead line. For simplicity, the pressure wave at the front of the train caused by the train passage through the tunnel is not considered, nor was any flow parallel to the track, i.e. all aerodynamic loads were considered perpendicular to the line. To include the effects of the pressure wave being released at the exit of the tunnel, a full fluid–structure interaction between the atmospheric conditions and the overhead line and rolling stock is required. Figure 7.13 gives a schematic of the situation being considered. The tunnel under consideration is taken to be sufficiently long enough that aerodynamic effects due to wind loading at the mouth of the tunnel can be neglected and only the effects of the aerodynamic loading as the train leaves the tunnel are considered.

The results presented here are based on a validated finite element model presented in [139] and seek to push the utility of the model with the addition of aerodynamic sidewinds. No validation of the predicted contact forces presented here has been attempted, however methods of validation are discussed in Chapter 9.2.

Figure 7.14 shows the predicted contact force for a train leaving a tunnel and meeting an already oscillating contact wire due to aerodynamic loading. The aerodynamic load was perpendicular to the overhead line, with a wind speed of 30 m/s and 0° angle of attack. The mouth of the tunnel is situated at 600 m in Figure 7.14. It can be seen that as the

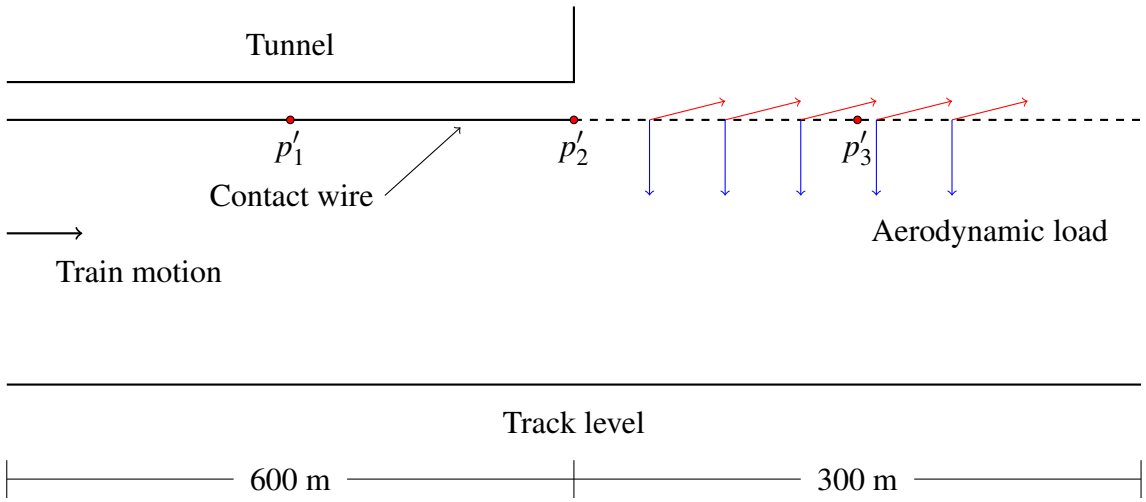

Fig. 7.13 Not to scale. Schematic of the overhead line arrangement with the location of the applied aerodynamic loads highlighted by the dashed line. Supports, droppers and the messenger wire have been omitted for clarity. Locations referred to in the text are labelled.

train leaves the tunnel, there is large increase in the contact force at the droppers either side of the supports, compared with the droppers either side of supports inside the tunnel. The increase in the maximum contact force is given in Table 7.6, where the increase in the discrete maximum was approximately 29%. The contact force trace inside the tunnel is also affected by the oscillating contact wire outside of the tunnel. In the case where no aerodynamic load is applied (as in Chapter 6), the maximum predicted contact force was 115 N, whilst the aerodynamic load outside the tunnel, increases the peak force inside the tunnel to 169 N due to transmission of mechanical waves from outside the tunnel back towards the pantograph. The oscillating aerodynamic load outside of the tunnel also acts to reduce the discrete contact force minima compared with a case of still air. Inside the tunnel, the discrete minima was 47.3 N, a 49% decrease compared with the still air case. This is likely due to the contact wire lifting from the static equilibrium position due to the aerodynamic load, reducing the load between the contact wire and pantograph at these locations, due to the finite static uplift force applied to the pantograph limiting the rate at which the pantograph can rise with the uplifted contact wire.

The mean contact force either inside or outside of the tunnel is unchanged, as given in Table 7.6. This is due to any increases in the contact force maxima at the droppers is also accompanied by an equivalent fall in the contact force at intermediate locations between the first and last dropper. This can be seen in Figure 7.14, where the contact force between the peaks at locations outside of the tunnel (between 600 and 900 m), consistently drops below the equivalent locations inside the tunnel (300 to 600 m). The reduced contact force at

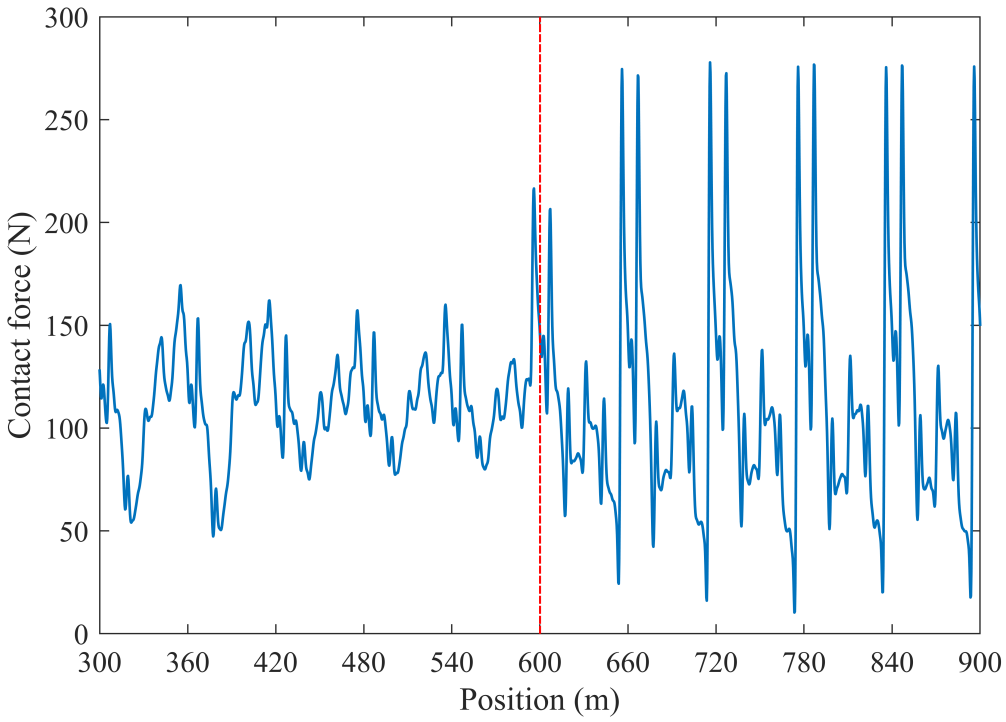

Fig. 7.14 Contact force variation for a pantograph moving along a contact wire inside a tunnel, to outside of a tunnel where aerodynamic loading is applied. The lateral wind speed applied was 30 m/s with a 0° angle of attack. The dashed line indicates the location of the tunnel mouth.

midspan is due to the reduced vertical stiffness away from the supports and at these locations, the contact wire is most susceptible to vertical deflections due to wind loading since there are no supports to restrict the vertical displacements.

The increase in the contact force inside the tunnel in still air indicates that the transmitted effects due to the aerodynamic loading outside the tunnel will degrade the current collection quality by causing undesirable wire oscillations. Large amplitude oscillations due to wind loading may also exceed required electrical clearances in the tunnel during train passage causing arcing events between the tunnel and train. The wire uplift due to the aerodynamic loads can be mitigated with an increased wire tension to restrict the oscillation amplitude, whilst also reducing the necessary clearances in the tunnel for overhead equipment.

The 116% increase contact force standard deviation given in Table 7.6 for the transition from inside to outside the tunnel, indicates that the inclusion of aerodynamic loading significantly degrades the current collection quality by increasing the magnitude of the peak contact forces at locations of increased vertical stiffness, and reducing the contact force

Table 7.6 Statistical output for a overhead line system leaving a tunnel and being subject to an incident wind flow with velocity 30 m/s. Inside corresponds to the statistical averages of the contact force inside the tunnel where no aerodynamic load is applied and outside corresponds to outside the tunnel, where the system is subject to wind loading.

Location	F_m	σ	$F_{D_{\max}}$	$F_{D_{\min}}$	$F_{S_{\max}}$	$F_{S_{\min}}$	Skew	Kurtosis
Inside	110	24.1	169	47.3	182	38.1	-0.230	-0.047
Outside	110	52.0	278	10.3	266	-45.8	1.13	1.30

elsewhere due to lifting of the contact wire. The reduced contact force minima as a response to the aerodynamic lift increase the potential for arcing events at the contact interface, which would lead to a degraded contact surface due to melting and vaporisation of the contact wire and pantograph carbons. This large increase in the standard deviation occurs due to the large magnitude variation between the contact force maxima and minima, which from Figure 7.14 occur at the locations of the last dropper in each of the spans. The approximately 250 N change in the contact force over the short distance (the length between the penultimate and last droppers is 12.25 m) will likely have a detrimental effect on the contact interface, potentially causing surface defects in either the pantograph carbon or contact wire. Defects in either of the contact surfaces increases the likelihood of arc discharge events, further degrading the contact surface and shortening the service life of the equipment. Table 7.6 indicates that the contact force is negatively skewed inside of the tunnel, suggesting that contact forces above the mean are likely. This is in contrast to positively skewed contact force outside of the tunnel. The positive skew is due to the lower predicted force minima and the consistently lower contact forces between the first and last droppers in each of the spans. The small kurtosis for the contact wire inside of the tunnel indicates that fewer extreme force occurrences are predicted compared with the positive kurtosis outside of the tunnel. The histograms given in Figures 7.15a and 7.15b, show the greater spread of contact force for the outside case.

Since the aerodynamic loads and the arrangement of the overhead line spans are periodic, this results in the periodic contact force trace seen in Figure 7.14. At the mouth of the tunnel, located at 600 m, the transition from no aerodynamic loads to aerodynamic loading can be seen by the smaller increase in the contact force, compared with the peaks after this location. At this location, the contact wire in the preceding span oscillates due to transmitted waves from the spans after the transition at 600 m and so the contact wire exhibits smaller oscillations resulting in a smaller increase in the contact force. This transmission of the aerodynamic oscillations back along the contact wire (i.e. to the left in Figure 7.14) is the

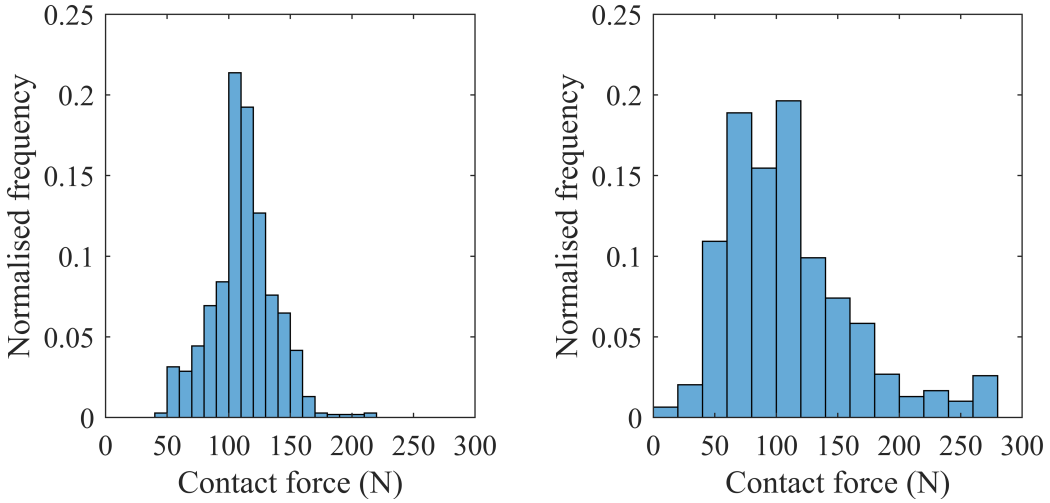

(a) Contact force histogram for the interaction between the pantograph and contact wire inside the tunnel.

(b) Contact force histogram for the interaction between the pantograph and contact wire outside the tunnel.

Fig. 7.15 Contact force histograms for the cases of inside the tunnel where no aerodynamic load is applied, and outside the tunnel where the contact wire oscillates due to wind loading.

source of the increased contact forces predicted inside the tunnel, despite no aerodynamic loading applied to the contact wire.

The contact wire uplifts at locations p_1', p_2', and p_3', highlighted in Figure 7.13, are given in Figure 7.16. Inside the tunnel, the contact wire oscillates due to the wave caused by the aerodynamic load outside of the tunnel, as can be seen in Figure 7.16a. It can also be seen that the mechanical wave caused by the moving pantograph interferes with the wave caused by the aerodynamics, damping the amplitude of the oscillations caused by the sinusoidal aerodynamic load. At zero time when the pantograph passes the point of interest, it can be seen that the uplift due to the pantograph is larger than the uplift due to the aerodynamic induced wave, and once the pantograph has passed, the amplitude of the oscillations decays to approximately 25% of the amplitude prior to the passage of the pantograph. Since location p_1' is inside the tunnel, the amplitude of the contact wire vertical deflection due to aerodynamic loading was smaller than the uplift caused by the pantograph. However, at locations p_2' and p_3', the vertical deflection of the contact wire due to the aerodynamic oscillations is sufficient to reduce the contact wire so that the contact wire uplift due to the pantograph is insufficient to return the contact wire to the static equilibrium height, as shown in Figures 7.16b and 7.16c. At location p_2', the contact wire is oscillating with a smaller amplitude before the arrival of the pantograph, compared with location p_1', since as the pantograph approaches the

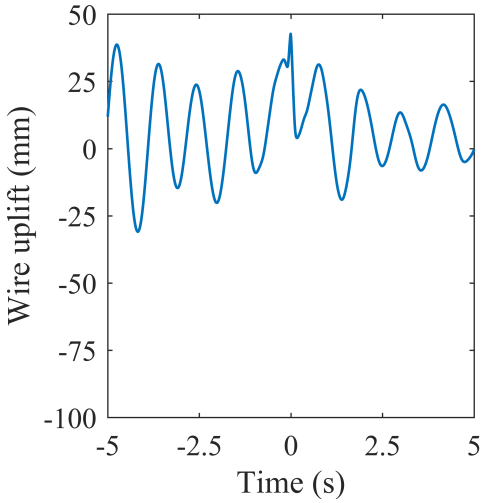

(a) Contact wire uplift inside the tunnel at location p_1'.

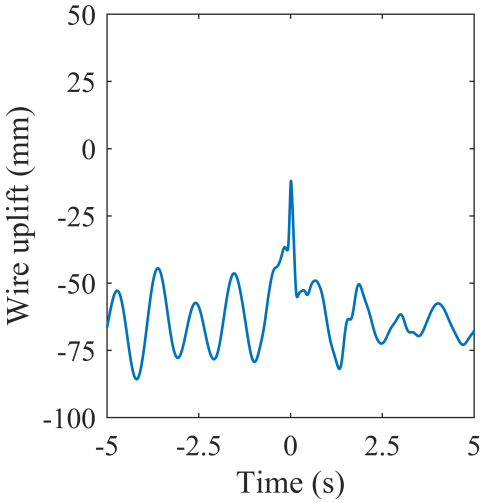

(b) Contact wire uplift at the mouth of the tunnel at location p_2'.

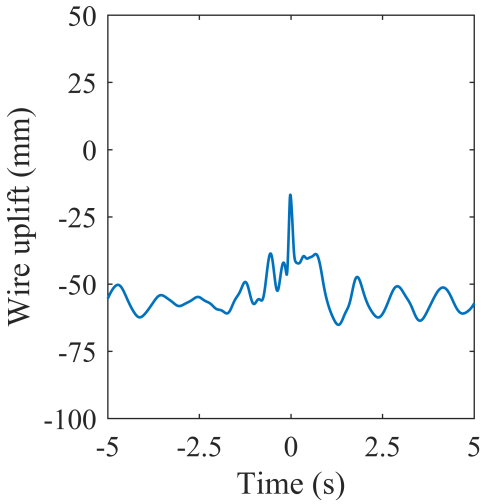

(c) Contact wire uplift outside of the tunnel at location p_3'.

Fig. 7.16 Contact wire uplift due to the aerodynamic load and the passage of the train pantograph, at locations p_1', p_2' and p_3' as shown in Figure 7.13. Zero time indicates the time the pantograph passed the location of interest.

location, the uplift due to the pantograph becomes dominant rather than the effects of the aerodynamic loading.

The large peak forces predicted due to aerodynamic loads on exposed parts of an overhead line can be mitigated by reducing the amplitude of the wire oscillations. Shortening the span length in areas susceptible to high winds reduces the total wire length, restricting the

amplitude of the oscillations. However, this is offset by the increased capital investment required during installation of overhead line equipment for the greater number of supports required. Shortening of the span length, however also reduces the magnitude of contact wire blow–off in exposed locations such as the one shown in Figure 7.12. Since excessive blow–off can lead to catastrophic dewirement events, the greater capital investment is mediated by any reduction in overhead line and rolling stock repairs caused by dewirements.

In each case, the wire uplift due to the pantograph was comparable, as the pantograph passage is the dominant behaviour compared with the aerodynamic loading. Since the cyclic load due to the oscillating aerodynamic load is small amplitude but high frequency, a large number of load cycles will accumulate more rapidly compared with a static wire. In the case of a wind speed of 30 $\mathrm{m/s}$, the load frequency was 85 Hz compared with approximately 1 Hz natural frequency of the overhead line, thus the accumulation of load cycles will have a corresponding increase due to the aerodynamic load frequency.

7.4 Case Study II: Passage of a train under a bridge providing protection against aerodynamic loading

The previous case study concerned the effect of a contact wire with a large proportion not under the dynamic effects of wind loading. In this case study, the effects of only a small section of overhead line is unloaded and the rest of the contact wire length is under aerodynamic loading. The contact wire arrangement with the locations of the aerodynamic loading is given in Figure 7.17 and no wire height changes besides presag were used, so that only the effect of aerodynamic loading was considered in this case study. This arrangement represents a contact wire passing under a bridge, thus the bridge supports protect the overhead line system from dynamic effects due to a lateral wind load. The bridge section is 20 m long in an otherwise typical 60 m span. As such, the length of the overhead line corresponding to the bridge section does not have an aerodynamic load applied. Changes in the air pressure around the overhead line and pantograph due to passing under the bridge or turbulent effects at discontinuities along the bridge deck and supports are not considered here, and it assumed that the bridge is sufficiently high enough that the required clearances to ensure no reduction in the contact wire height are necessary. The effect of large scale changes in the overhead line height will be considered in Chapter 8.

Figure 7.18 gives the contact force trace for the catenary pantograph interaction considered here. In contrast to the previous simulation cases in this Chapter, the aerodynamic

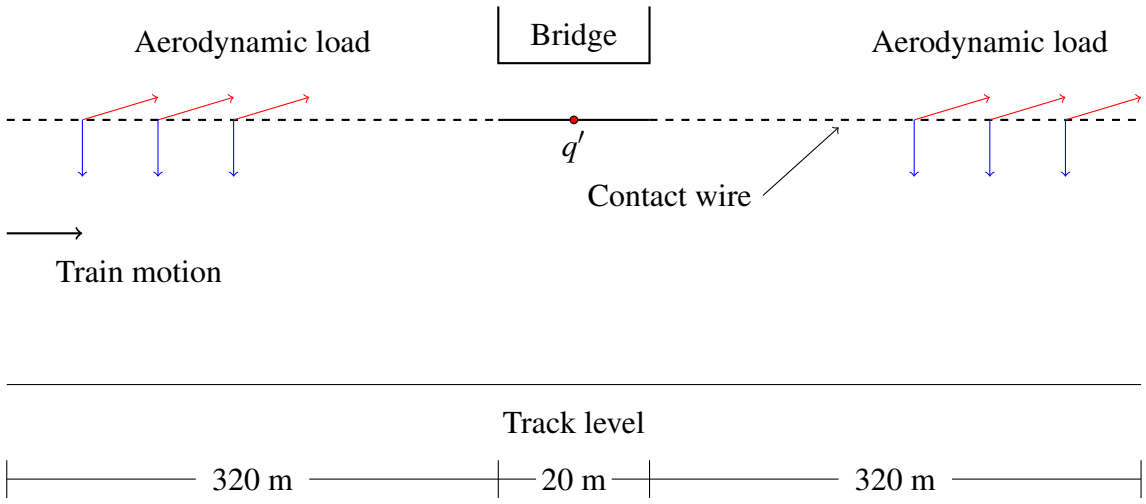

Fig. 7.17 Not to scale. Schematic of the overhead line arrangement with the location of the applied aerodynamic loads highlighted by the dashed line. Supports, droppers and the messenger wire have been omitted for clarity. Locations referred to in the text are labelled.

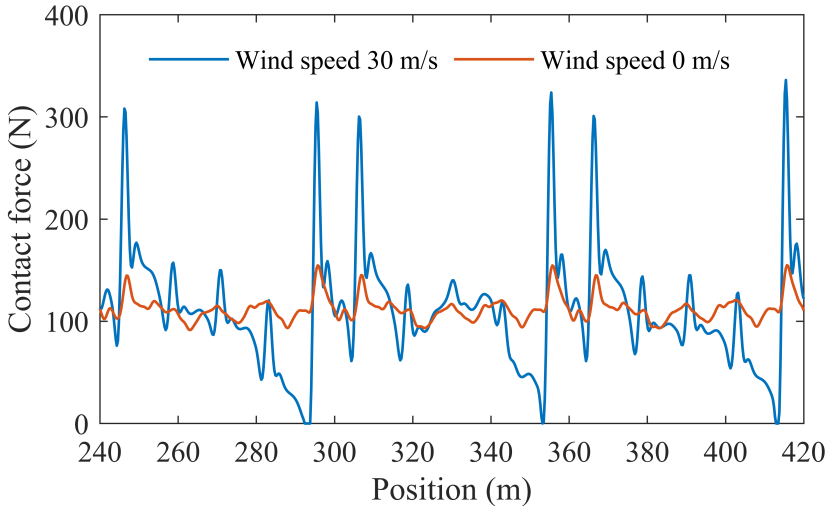

Fig. 7.18 Contact force variation for a contact wire passing under a bridge located from 320 to 340 m. Spans referred to in the text are: Span 1 between 240 and 300 m, Span 2 between 300 and 360 m and Span 3 between 360 and 420 m.

loading has caused contact losses between the overhead line and the pantograph. The contact losses occur periodically at locations just before supports and are likely to be periodic due to the periodic aerodynamic loading. With an aperiodic loading, the spatial location of any potential contact loss events would have changed. The predicted contact losses would lead to an increase in arcing of the contact wire shortening the service life of the equipment due to melting and vaporisation of the contact wire surface. The large discrete contact force

maxima occurring after contact between the pantograph and the contact wire has reoccurred would also shorten the life further due to damage caused by the impact of the sliding contact reoccurring. The peak force in the span containing the 20 m length of overhead line not subject to aerodynamic loading is reduced compared with the spans either side of the bridge, as can be seen in Table 7.7, indicating that the aerodynamic loading is detrimental to the current collection quality. This is further evidenced by the reduced contact force standard deviation. Whilst the standard deviation in the span containing the bridge section is reduced compared to the spans either side, the standard deviation is still larger than for a system not subject to aerodynamic loading. By comparison, the standard deviation in the central span is 121% larger than the standard deviation of the contact force inside the tunnel in the previous case study, where 50% of the overhead line was not subject to the aerodynamic load.

Table 7.7 Statistical output for a overhead line system passing under a bridge and being subject to an incident wind flow with velocity 30 m/s. Statistical output corresponds to the spans before and after the bridge and the span under the bridge where no wind load is applied on the contact wire corresponding to the 20 m length under the bridge.

Location	F_m	σ	$F_{D_{\max}}$	$F_{D_{\min}}$	$F_{S_{\max}}$	$F_{S_{\min}}$	Skew	Kurtosis
Span 1	111	59.1	314	0	288	-66.4	0.849	2.03
Span 2	114	53.2	324	0	274	-45.0	1.33	3.63
Span 3	109	57.0	336	0	280	-62.1	1.45	3.41

As in all cases, the peak contact forces occur at the first and last droppers in the spans consistent with the increased vertical stiffness due to the dropper proximity to the supports (the distance from a support to the nearest dropper is 5.5 m), however the addition of the aerodynamic load acts to increase the peak forces. Compared with the case of no wind loading, the peak contact force here is 117% larger in Span 3. The mean contact force is largest in Span 2 due to the maintained larger contact force throughout the section with no aerodynamic load imposed, compared with the consistently trend of decreasing contact force apart from at droppers in either of the other two spans.

The distribution of the contact force in each of the three spans considered is given in Figure 7.19. In all three spans, the contact force is positively skewed due to the contact loss occurrences in each span, however Span 1 is predicted to have fewer extreme contact force events as indicated by the smaller positive kurtosis compared with Spans 2 and 3. This is likely due to Span 1 preceding any spans where the behaviour is aperiodic. Up to Span 1, the aerodynamic load is consistent across each span and thus there are no extra dynamic effects. In contrast, the 20 m section of Span 2 with no aerodynamic loading breaks the

periodic behaviour. After the bridge section at 340 m, the contact force drops due to the oscillating contact wire, compared to a small peak in the contact force at the same location in the previous span. This decrease in the contact force is indicated by the increased kurtosis. In Span 3, which can be thought of as a transition span back to periodic behaviour, the dynamic effects of the pantograph passing the bridge section are transmitted into this span causing the increased peak force. Since the small peak at the penultimate dropper that is predicted in Span 1 reoccurs in Span 3, this causes a small decrease in the kurtosis when comparing Spans 2 and 3.

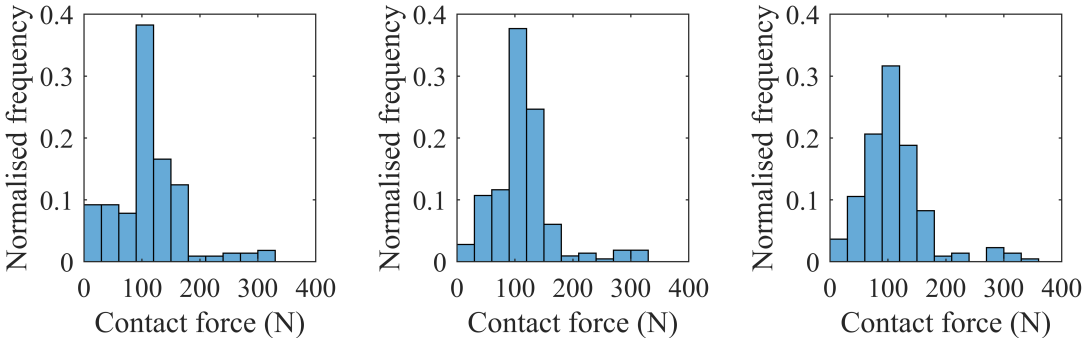

(a) Contact force distribution for Span 1.

(b) Contact force distribution for Span 2.

(c) Contact force distribution for Span 3.

Fig. 7.19 Distribution of the contact force for each of the spans considered.

From the force trace in Figure 7.18, and the force distributions in Figure 7.19, it can be seen that when the bridge length is much shorter than the span length, the protection provided by the bridge supports to lateral crosswinds is minimal, and the dynamic behaviour is dominated by the effects of the aerodynamic loads on the exposed equipment.

The contact wire uplift directly underneath the centre of the bridge is given in Figure 7.20, shown as location q' in Figure 7.17. It can be seen that the contact wire oscillates with an amplitude of approximately 130 mm, which decays as the pantograph moves towards location q'. At q', the wire uplift due to the pantograph is larger than the amplitude of the oscillations caused by the sinusoidal wind load, however is insufficient to lift the contact wire to the static equilibrium position (taken to be zero in Figure 7.20). After the pantograph has passed location q', the amplitude of the contact wire continues to decay. It can be seen that in contrast to the previous case study, where the dynamic contact wire uplift after the passage of the pantograph was dominated by the pantograph passage, in this case, the dynamic uplift at location q' is driven largely by the aerodynamic loading and the pantograph acts only to increase the uplift at the zero time in Figure 7.20.

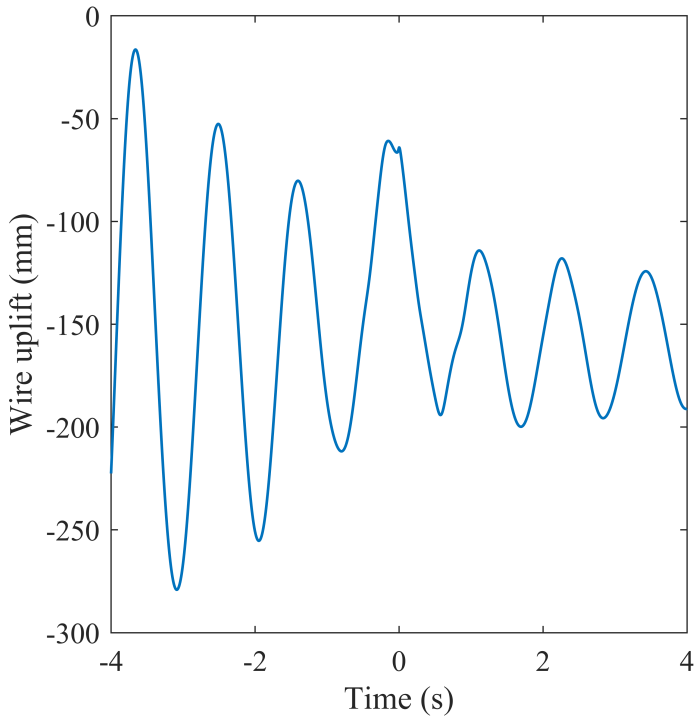

Fig. 7.20 Contact wire uplift at midspan of the span underneath the bridge, shown as location q' in Figure 7.17.

As in the previous case study, it has been indicated that the oscillating contact wire increases the contact force maxima during the catenary pantograph interaction. These large peak forces would lead to an increase in the mechanical wear according to Archard's law, in addition to an increase in arcing effects between the contact surfaces due to the periodic contact losses. An increase in the wire tension would act to reduce the contact wire oscillation amplitude, however may lead to an increase in the contact force (as discussed in Chapter 6), although this force increase due to an increased line tension is smaller than the increase due to the aerodynamic lift force. Increases in the line tension also reduces the risk of galloping phenomena under steady winds [176]. Under bridges where clearances are limited the increase in the line tension can be accompanied with shorter span lengths to reduce the available contact wire length, thereby reducing the contact wire uplift due to the aerodynamic uplift.

Whilst in the case presented here, the aerodynamic lift force increased the sag of the contact wire, as indicated by the negative wire uplift prior to the pantograph passage, the static electrical clearances are still required to be satisfied. The larger predicted peak forces due to the aerodynamic load will cause the wear of the contact wire to increase more rapidly

compared with an unloaded case, removing material from the contact wire and therefore reducing the sag. As shown in Section 7.2.1, the aerodynamic effects worsen as the wear increases, potentially leading to greater wire uplifts that would exceed electrical clearances. Thus reinforcing the equipment with the addition of bridge arms or shorter span lengths at bridge locations would restrict the available contact wire uplift in windy conditions, reducing arcing events between the overhead equipment and structures during windy conditions.

7.5 Conclusions

In this Chapter, a "first look" into the effects of aerodynamic loading on the catenary pantograph interaction has been presented. Whilst the mean wind speeds in the UK are approximately one sixth of the maximum wind speeds considered here, the gusting speeds described at the beginning of this Chapter indicate that investigating the resilience of the system under high wind speeds is important. It was found that aerodynamic loading at high wind speeds leads to a significant degradation of the current collection quality even when considering only level wires. Using aerodynamic loads calculated using both computational and experimental approaches, the contact wire blow–off for a range of wear cases has been predicted and two case studies have been used to investigate the effects of sudden application and removal of aerodynamic loading.

The static deflection calculations predicted that for lateral side loads caused by crosswinds up to 30 m/s, the lateral deflection was approximately 0.7 m, larger than the working section of the pantograph head, indicating that dewirement becomes likely at high wind speeds. The calculated lateral deflections presented here are noted to be an overestimate since the effects of the messenger wire restricting the displacement of the contact wire were neglected. In the static case, the wear of the contact wire was found to have little effect on the total deflection of the contact wire at midspan. Despite the reduced area causing a reduced aerodynamic force, the reduced lateral inertia provided less resistance to the deflection giving similar contact wire blow–off for the wear cases considered. Considering a standalone contact wire, the predicted deflections using a finite element method were found to be in good agreement with the analytical calculation. At low lateral force (1 N/m), the difference between the analytical and finite element predictions were approximately 4 mm, and at the high lateral force (20 N/m), the difference was approximately 8%.

By introducing lateral and vertical forces representing the drag and lift forces respectively, to a finite element model of the catenary pantograph interaction, the dynamic effects of an aerodynamically loaded system have been studied. It was found that increasing aerodynamic

lift forces due to increased wind speed degraded the dynamic performance of the overhead line due to large increases in the contact force variation and discrete maxima. The oscillations in the contact wire caused by the sinusoidal lift force acted to increase the discrete contact force maxima to approximately 270 N, a 74% increase compared with an unloaded overhead line. This increase in the peak contact force would lead to a shortening of the contact wire service life due to an increased wear regime. Assuming the Archard wear law holds, the increased dynamic load between the contact wire and the pantograph would increase the material wear rate by a commensurate amount, e.g. even for a wind speed of 10 m/s, the increase in the peak force was approximately 10% thus increasing the wear rate by 10% assuming wear remained mild. Due to the aerodynamic lift force, the overhead line would rapidly accumulate a high number of load cycles compared with an unloaded case that would oscillate at the natural frequency. These small amplitude, high frequency oscillations are predicted to have an effect on the service life of the equipment, however further work is required to assess the effects of these oscillations.

In contrast to the static case, and considering the wear state of the contact wire, a noticeable effect on the dynamic contact force was predicted when aerodynamic lift was applied. Including the wear state of the contact wire in addition to aerodynamic loads, this work extends previous analyses in the literature such as [176] where no contact wire irregularity was considered. The reduced mass allowed for greater amplitude oscillations in the contact wire due to the aerodynamic load which caused an increase in the contact force maxima. Comparing the 0 and 6 mm wear cases, the discrete maxima increased by 26%. Since the wear of the contact wire was high, coupled with the larger contact force, it is predicted that the contact wire would be significantly at risk of failing in this scenario. Increasing the wear of the contact wire also increased the likelihood of contact loss between the overhead line and the pantograph. For the most worn case, the minimum contact force was predicted to be less than 20 N. Since the maximum serviceable wind speed for a UK overhead line is 37 m/s, it is possible that the increased wind speed would lead to contact loss events, leading to arcing between the contact surfaces. The arcing events would also lead to a shortening of the service life of the equipment.

Implementing aerodynamic drag on both the contact wire and the pantograph indicated that there is little effect on the contact force during train operation due to an increase in the drag force. This was predicted to be due to any increase in the contact wire tension due to lateral displacements being small relative to the 16.5 kN tension already applied to the system. It was also found in the drag cases, that decreases in the contact wire mass due to

wear were a more significant factor in variations in the predicted contact force compared with applied aerodynamic drag.

Since a real life installation cannot consider aerodynamic drag and lift as discrete effects, two case studies were considered where both the drag and lift forces were applied. In the first case study, a train leaving a tunnel was considered. Due to the aerodynamic load on the exposed section of the overhead line outside the tunnel, dynamic effects due to the wire oscillation were transmitted back along the wire inside the tunnel increasing the contact force maxima, despite the contact wire being considered to be in still air. The larger peak forces were found to increase the amplitude of the wire oscillations after pantograph passage inside the tunnel. The increase in amplitude acts to increase the stress in the contact wire during each load cycle, shortening the lifetime of the equipment by hastening the onset of fatigue failures. These effects could be reduced with the adoption of shorter span lengths inside the tunnel to restrain the wire uplift, thereby reducing the amplitude of the oscillations, whilst also ensuring electrical clearances between the contact wire and the tunnel are met. Whilst the wire uplift at a support inside the tunnel at the moment the pantograph passed was predicted to be comparable to the uplift of an unloaded wire, with expecting wind speed increases due to increasing global temperatures, the uplift would likely increase with the wind speed, thus requiring greater electrical clearances to prevent arcing if the existing distances between supports was maintained.

In the second case study, the effects of wind loading on an overhead line passing under a bridge were considered. Since the length of the bridge was much shorter than the span length, the absence of wind loading under the bridge had little effect on the dynamic contact force. Compared with the unloaded case, the peak forces at droppers were significantly higher due to the long cables oscillating. This indicates that in locations susceptible to high winds, shorter span lengths should be adopted to reduce the amplitude of the oscillations, therefore reducing the discrete contact force maxima.

In this Chapter only level wires have been considered to demonstrate the core effects of the aerodynamic load. In the next Chapter, the effects of introducing a contact wire gradient on the catenary pantograph interaction will be explored.

Chapter 8

Effect of wire gradient on the dynamic performance of the catenary pantograph system

8.1 Introduction

In this Chapter, the influence on the dynamic contact force during the catenary pantograph interaction of different gradients in the contact wire and the length of droppers between the contact and messenger wires of a railway overhead line are investigated. Imposing large scale variations in the height of the contact wire leads to a corresponding height variation in the train mounted pantograph head and to achieve the changes in direction due to the height variation, the pantograph head must be accelerated. These accelerations are accompanied by a corresponding force. In this Chapter, the contact force during those height transitions and in particular the force peaks are predicted for a range of different overhead line geometries corresponding to geometries relevant to retro–fitting electrification to pre–existing UK rail infrastructure.

To simulate the catenary pantograph interaction, a nonlinear finite element model has been generated in commercial finite element software ANSYS and the modelling methodology has been described in Chapter 3, Section 3.2.1. Using the described methodology, the required geometries in order to perform the simulations are described in Section 3.4.1.

Validation of the modelling process is described in Section 4.2.2, and is performed using test track data provided from Network Rail's Melton Rail Innovation and Development Centre. Following validation, the model is used to investigate a range of overhead line wire

gradients using an idealised overhead line geometry where the dropper lengths are maintained in each span in Section 8.2.1, and to analyse the output from each of the simulations the windowing technique introduced in Section 3.4 is used alongside the usual statistical analysis.

Whilst the influence of a range of gradients is highlighted strongly using an idealised overhead line geometry in Section 8.2.1, two realistic geometries are also described and modelled in Section 8.2.3. In these two geometries, the dropper lengths are allowed to vary, better representing a real overhead line installation making best use of available space under low clearance structures. Once again the windowing technique is applied to the outputs from these simulations. Finally in Section 8.2.5, the consequences of the effects of sharp wire gradients in an overhead line are discussed and mitigation methods for these consequences are proposed.

8.2 Results and discussions

In this section, the results of the study into the effect of gradients on the dynamic performance of the catenary pantograph interaction are presented. To study the influence of contact wire gradients in the performance, models 2, 3 and 4 described in Section 3.4.1 are used to represent different options available when reducing the contact wire height. Since the analyses include the effects of both falling and rising wire heights, analysis was performed using two techniques:

1. Performing the statistical analysis across the entire length of the wire run, and
2. Using a moving window analysis to focus on discrete behaviours across individual sections of the overhead line.

By introducing the moving window, discrete variations in the contact force masked by averaging across the length of the working section can be detected. Regions that were of particular interest included the transition regions between spans of differing contact wire gradient.

8.2.1 Overall behaviour predicted by model 2

The predicted contact force between the overhead line and the pantograph is shown in Table 8.1. Each column details the statistical output for each of the wire gradients between 1:500 and 1:100. From Table 8.1, it can be seen that increasing the gradient beyond the current maximum allowed of 1:500 has very little effect on the overall dynamic behaviour.

The mean remains unchanged for all of the chosen gradients apart from when the gradient is 1:100 and the variation in the mean force is less than 1%. Larger variation can be seen in the standard deviation of the contact force with the largest standard deviation occurring when the wire gradient is 1:100 and is 36% larger than the standard deviation for a level contact wire, and approximately 28% larger than when the gradient is 1:500.

Peak contact force increased with increasing gradient with the peak force occurring at the transition from a level to a negatively graded contact wire, shown as location 1 in the contact wire schematic in Figure 3.22. Here, the required acceleration to change the direction of the pantograph head increases as the wire gradient increases correlating to the increasing contact force. It is observed that a 400% increase in the contact wire gradient from 1:500 to 1:100 resulted in only a 14.3% increase in the peak contact force and a 150% increase to a wire gradient of 1:200 from 1:500 resulted in a peak force increase of 5.6%.

Further peaks in the contact force are predicted when the contact wire changes from a rising gradient to the transition gradient at location 3 and then from transition to level at location 4 and once again the pantograph is required to change direction to follow the contact wire. This requires a further acceleration of the pantograph resulting in the peak contact force. The peak forces predicted at location 4 are lower than those predicted at location 2 as the level contact wire allows a small continued rise in the pantograph after the transition span when compared with the pantograph moving from a level span to a transition span where the rise in the contact wire is restricted due to the lower support at the end of the span.

Table 8.1 Results for model 2 for each gradient. Mean and standard deviation are taken over the working section described earlier. The data includes variation in the contact force due to both decreasing and increasing wire heights. All results are given in N.

Wire gradient	Level	1:500	1:400	1:300	1:200	1:100
F_m	112	112	112	112	112	111
σ	11.5	12.9	13.0	13.6	14.7	18.0
$F_{D_{\max}}$	154	161	162	164	170	184
$F_{D_{\min}}$	90.2	86.4	85.5	83.6	80.1	75.4
$F_{S_{\max}}$	146	151	151	152	156	165
$F_{S_{\min}}$	77.4	72.9	72.6	70.9	67.5	57.3

The minimum contact for each gradient shows a similar decreasing trend with increasing gradient. The decreasing contact force trend typically occurs between locations 2 and 5 in Figure 3.22 when the pantograph is moving downwards towards the centre of the working section and then as it rises again at location 5. As the gradient increases, the finite static and aerodynamic uplift forces available, limit the rate at which the pantograph can rise, thus the

contact force between the pantograph and overhead line is reduced when compared with accelerating the pantograph downwards. As the wire gradient is increased from 1:500, the minimum contact force decreases by 12.3% when the wire gradient is 1:100. When the gradient is 1:200 this reduction in the contact force minima is only 7.3%. The sustained decreasing contact force is apparent in the force trace when the gradient is 1:100 as shown in Figure 8.1, and the decreasing contact force throughout the decreasing wire height is consistent throughout all the gradients studied as shown in Figure A.5 and Figures A.2, A.3 and A.4 included in Appendix A.2.

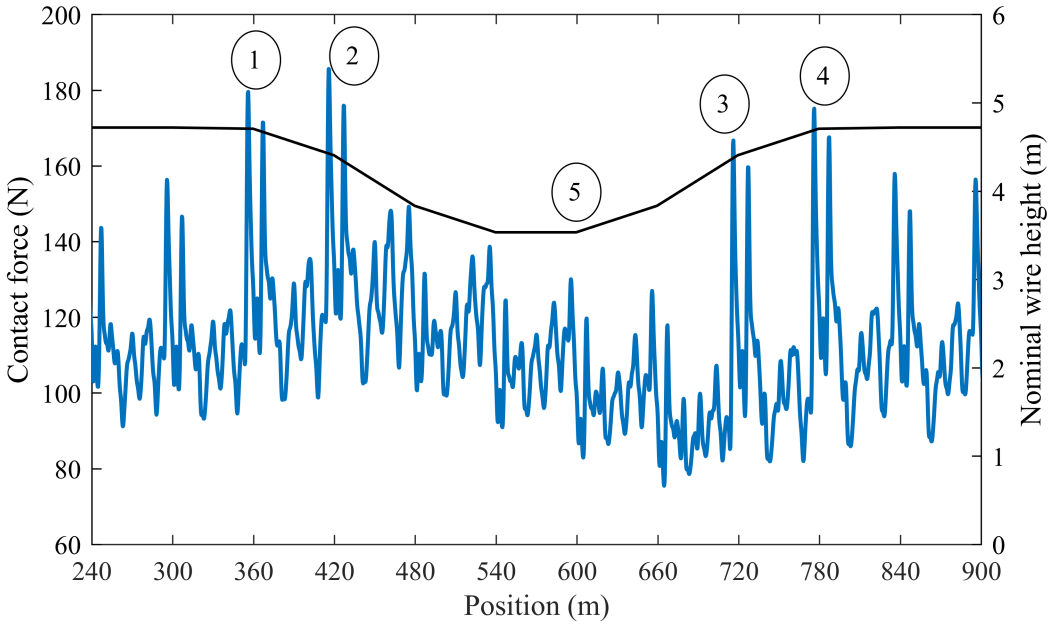

Fig. 8.1 Contact force trace when the contact wire gradient was 1:100. The nominal contact wire height, between 3.5 m and 4.7 m, is given and mast locations are given on the horizontal axis. Key locations referred to in the text are numbered 1-5.

To counteract the reduced contact force, an increased static uplift force while the wire height increases can be applied, however with a conventional passive pantograph this would also apply sustained higher contact forces across the rest of the overhead line shortening the overall system life. Active pantographs with variable uplift forces would provide a means of achieving a contact force with a lower variation.

The histogram of contact force for each of the wire gradients is shown in Figure 8.2. From the histogram it can be seen that with increasing gradient, there is a proportional

increase in the contact forces at the extremes of the distribution, evidenced by the 55% increase in the excess of kurtosis when increasing the wire gradient from 1:500 to 1:100. The increased kurtosis indicates that the distribution has heavier tails indicating the presence of an increased number of extreme contact forces, the clearest example being the occurrence of contact force in the range 80 – 90 N when the wire gradient was 1:100. This large increase in the frequency of low forces occurring when the wire gradient is steeper, likely occurs between locations 2 and 5 in Figure 8.1 when the contact wire is height is increasing. In fact, when the wire gradient was 1:100, there were 7% more instances of contact force below 100 N when compared to a wire gradient of 1:500. By comparison, there were 1.5% more instances of the contact force being over 160 N for a 1:100 wire gradient. In all cases, no contact loss was predicted, thus any mechanical wear increase would be due to the increased sliding contact load.

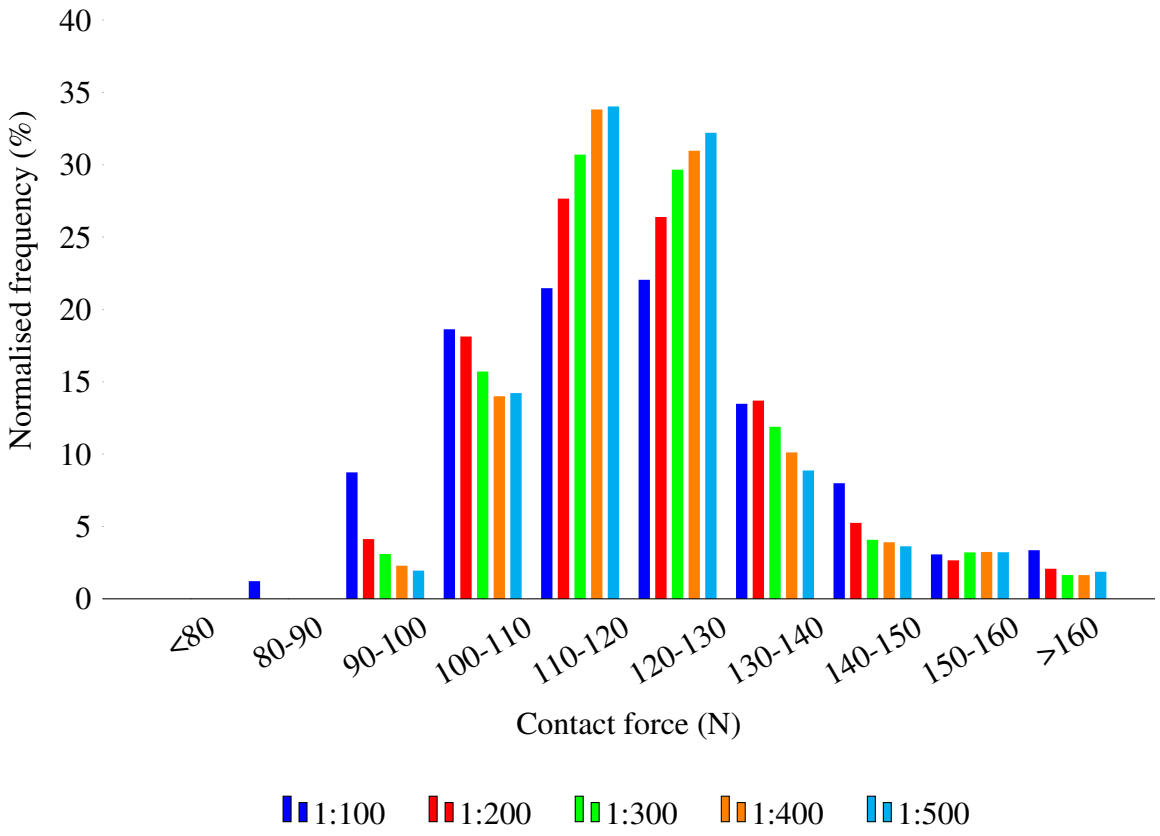

Fig. 8.2 Histogram of contact force for each of the wire gradients. Relative frequency gives the percentage of data falling into each bin accounting for the greater number of datum points for the larger working sections for shallower gradients.

High frequency and band frequency analysis

The data given in Table 8.1 was calculated after the contact force had been passed through the 20 Hz low-pass filter. To investigate the higher frequency response, the raw data was passed through filters that attenuated data over 80 Hz. Figure 8.3 gives the variation in the contact force standard deviation as the filtering frequency is increased. It can be see that as the filtering frequency is increased, the variation in the contact force increased as the peak forces occurring at higher frequencies are captured. The contact force standard deviation maximum occurred when filtering at 40 Hz where the standard deviation was approximately 6% higher in each case.

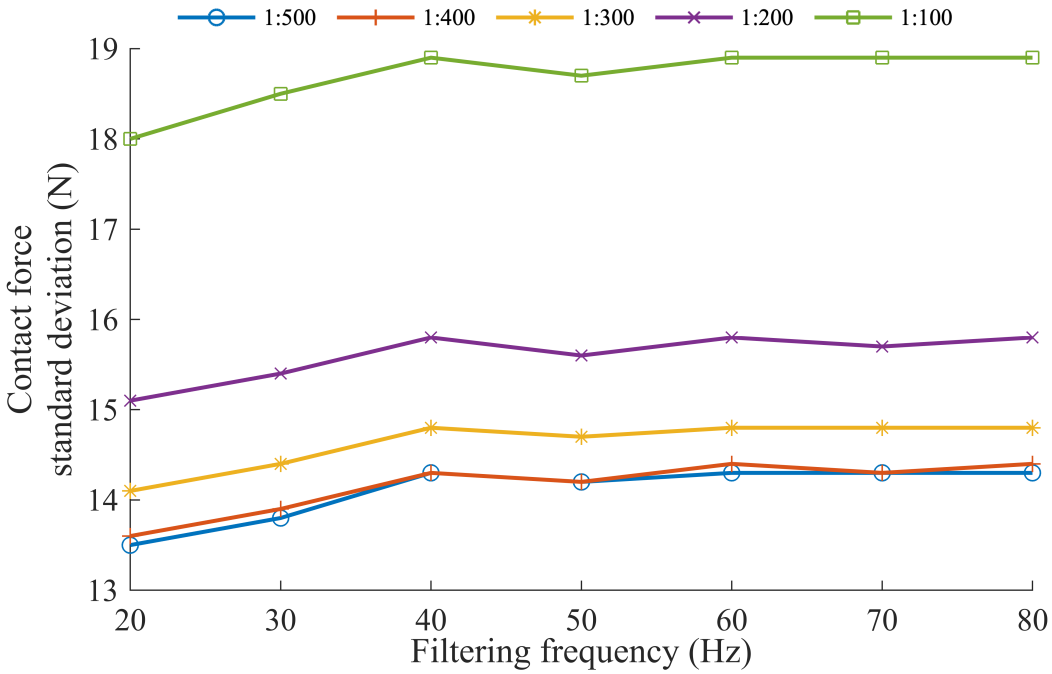

Fig. 8.3 Variation in the contact force standard deviation when filtering at a range of frequencies. The legend indicates which contact wire gradient is considered.

Variation in the contact force standard deviation is consistent with the variation in the contact force maxima and minima shown in Figures 8.4a and 8.4b respectively. As the filtering frequency was increased from 20 Hz to 50 Hz, the predicted peak force increased from 186 N to 199 N when the wire gradient was 1:100 and rose from 163 N to 175 N when the gradient was 1:500. The largest increase in contact force magnitude was 25 N, when a filtering frequency of 50 Hz was used, representing a 12.6% increase, however this was lower than the 14.1% increase when a 20 Hz filter was used.

From Figure 8.3, the standard deviation of the contact force showed small change at each of the seven filtering frequencies suggesting that increasing the contact wire gradient from 1:500 to 1:400 was of little consequence of the contact force. Change in the peak contact force due to change in gradient was similarly small as can be seen in Figure 8.4a. Only the minimum contact force showed a clear change due to the change in gradient. Figure 8.3 also showed that increasing the gradient resulted in subsequent larger variation even with the constant increase in the wire gradient: the increase in the standard deviation from a gradient of 1:400 to 1:300 was 4%, whilst from 1:200 to 1:300 was 7% and from 1:200 to 1:100 was 19%. The trend of larger variation with subsequent increases in the statistical output are clear in Figures 8.4a to 8.4d.

The minimum contact force magnitude decreased as higher frequency filters were used. As the filtering frequency increased, the minimum contact force typically reduced by around 5 N compared to the larger increases in the peak forces. Since the mean contact force was left unaltered by variation in the filtering frequency, any change in the statistical maxima and minima, shown in Figures 8.4c and 8.4d respectively, was driven solely by changes in the standard deviation as the filtering frequency was changed.

From Figures 8.3 and 8.4, whilst there was some variation as a result of increasing the filtering frequency due to including a larger proportion of the data, largely the variation was minimal. With respect to each of the gradients considered, increasing the filtering frequency did not affect the "ranking" of the each of the gradients i.e. for all filtering frequencies, a gradient of 1:100 gave the largest standard deviation, highest discrete maxima, etc.

As well as considering the high frequency behaviour, the data was processed using a low-pass filter with a cut-off frequency of 5 Hz and a band-pass filter with cut-offs at 5 Hz and 20 Hz. The statistical output for each of these filtering processes is shown in Figure 8.5. It can be seen that low frequency behaviour in the 0-5 Hz range (such as at the dropper passing frequency of 4.89 Hz) is the dominant component of the contact force. This is highlighted in the peak contact force where the component of force in the 0-5 Hz range is around 20 N higher than the component in the 5-20 Hz range.

Contact wire uplift at supports

Wire uplifts at the wire supports is influenced by the contact force due to the sliding contact. Figure 8.6 shows the variation in the uplift at four supports in the cases of a wire gradient of 1:100 and 1:500. In each case, the uplift due to the passing pantograph is approximately 40 mm. The largest variation in wire uplift, shown in Figure 8.6a occurred at the support at the beginning of the first transition span where the uplift when the gradient was 1:100 was

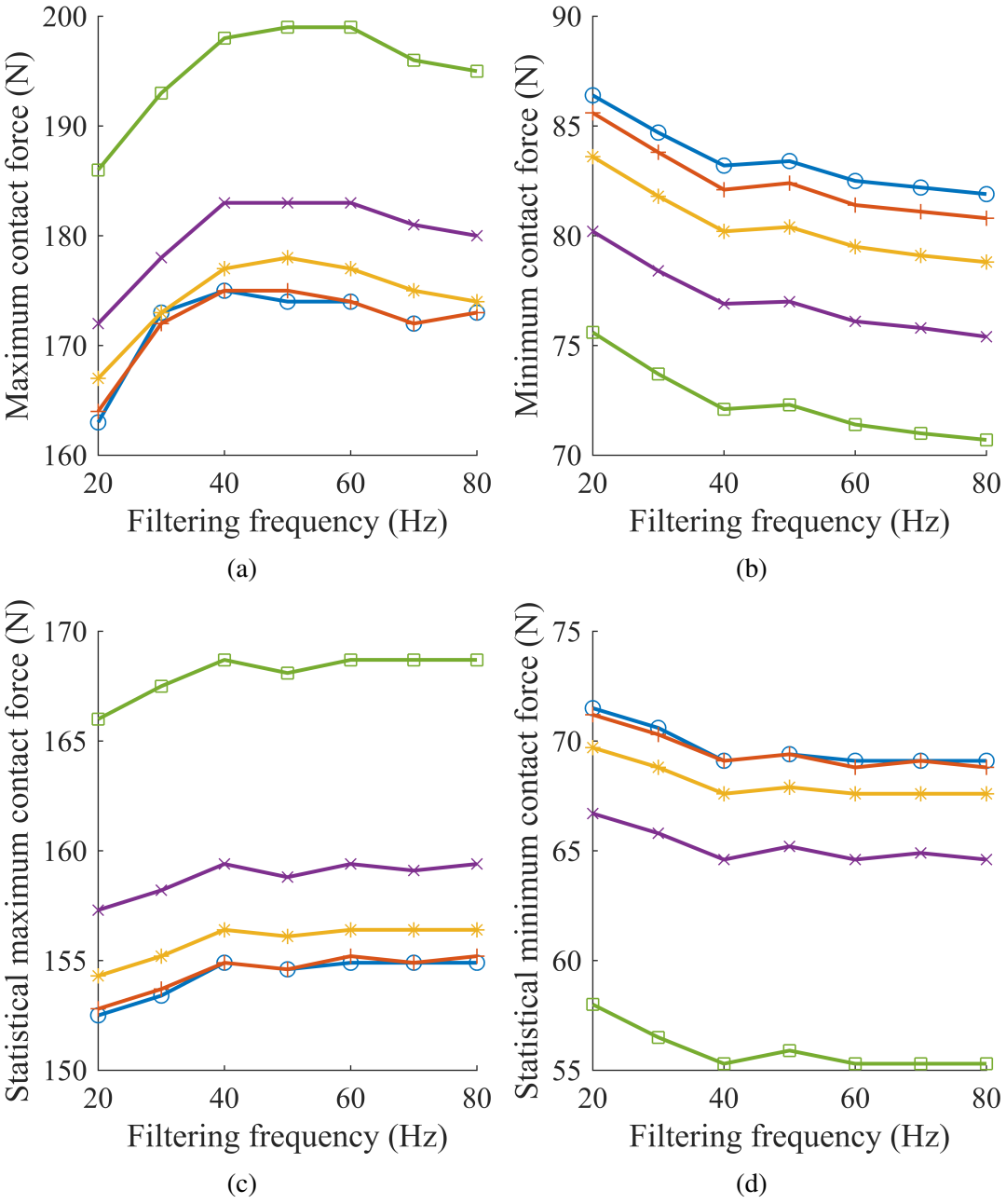

Fig. 8.4 Statistical output after filtering the modelling output between 20 Hz and 80 Hz.

12% higher than at the same location when the wire gradient was 1:500. This is consistent with the 14% increased contact force observed in this span. The larger contact forces also increased the amplitude of the oscillations in the contact wire after the pantograph had passed the support.

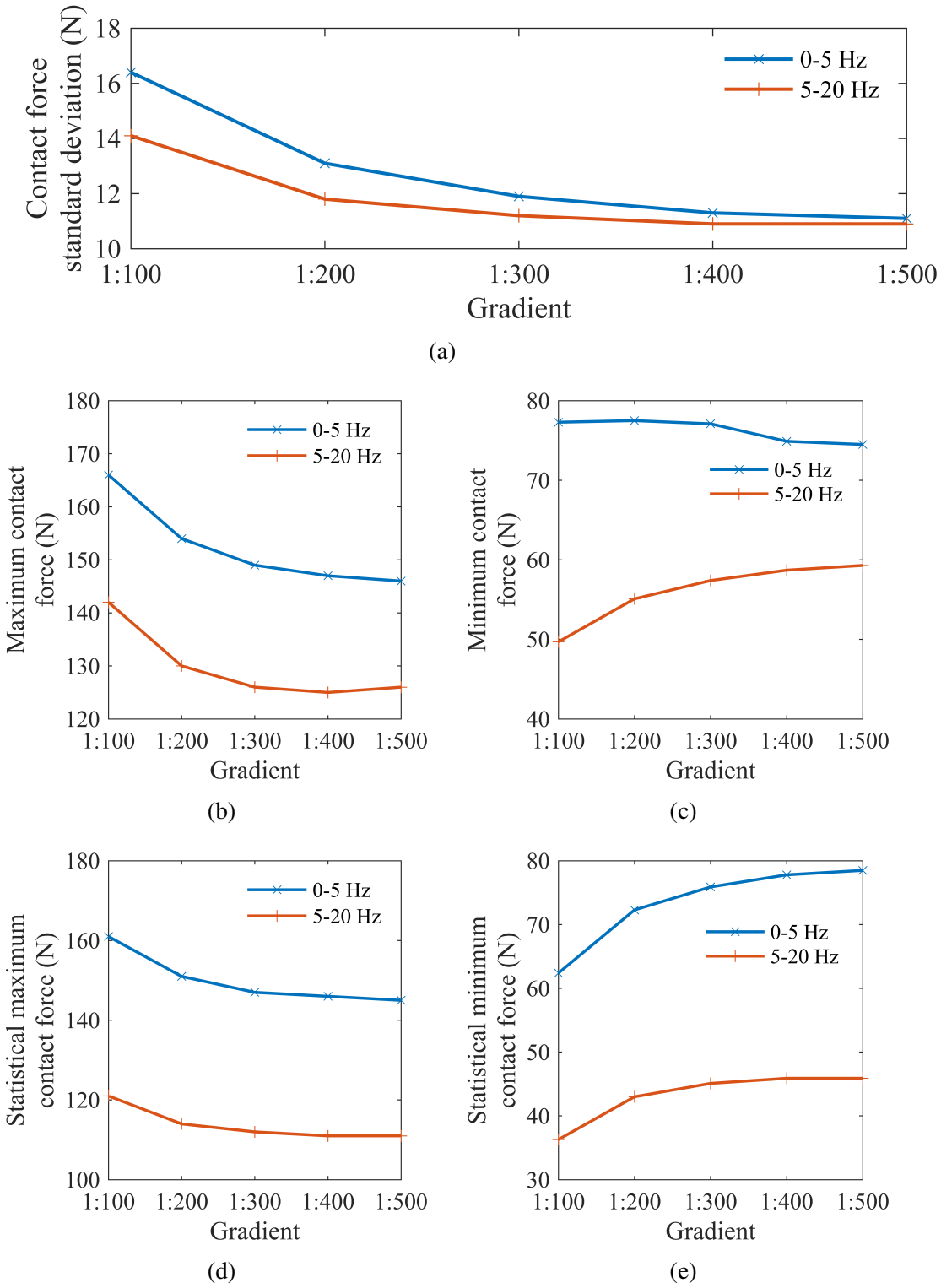

Fig. 8.5 Statistical output for frequencies below 20 Hz. A low-pass filter of 5 Hz and band pass filter of 5-20 Hz was applied in each case. The legend indicates which filter is used.

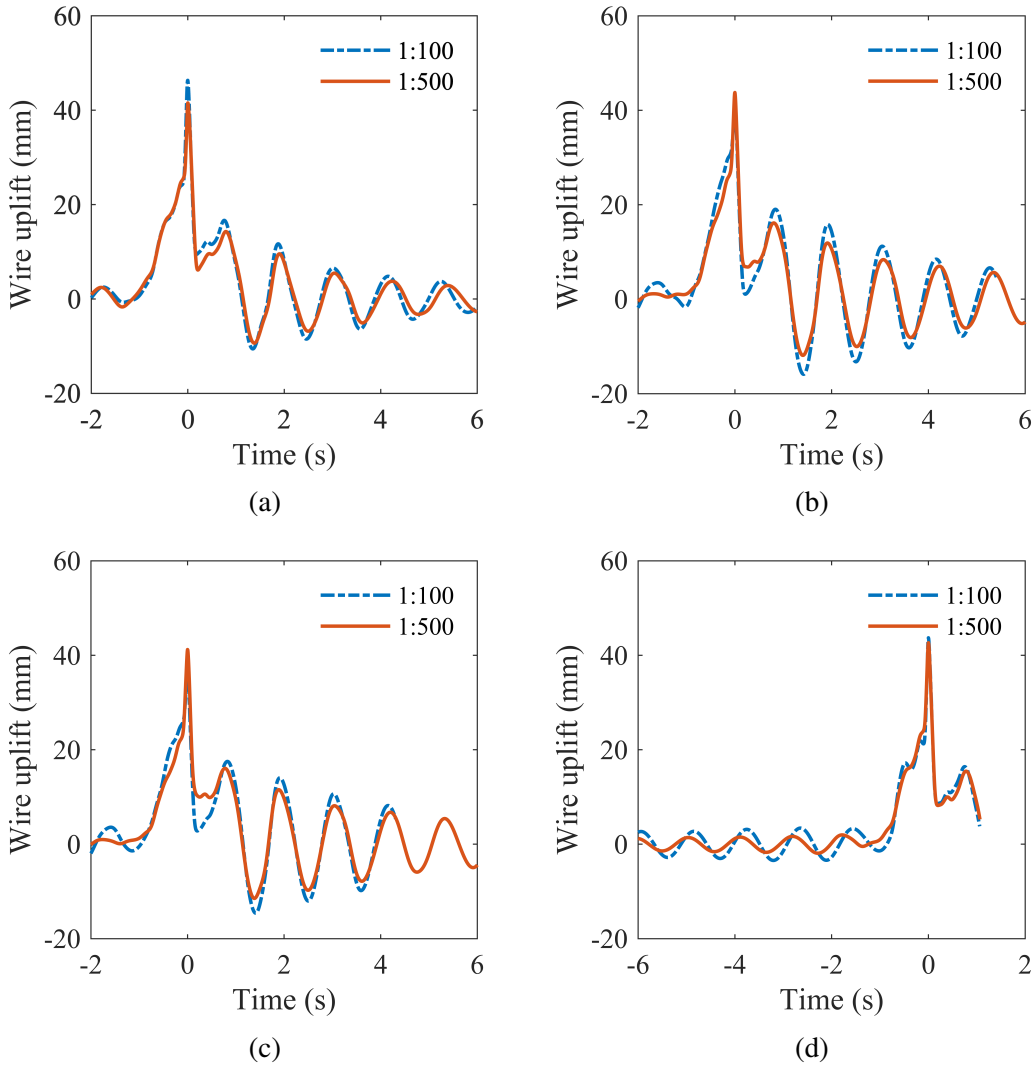

Fig. 8.6 Wire uplift at (a) the beginning of the first transition span, (b) the end of the second, (c) the beginning of the third and (d) the end of the fourth. Legend indicates the gradient being considered in each case and zero time corresponds to the pantograph passing the support.

Thus far only the overall behaviour of the dynamic interaction has been considered with the statistical analysis covering the entire working section. For a wire gradient of 1:500, this represented a working section of 1800 m, and thus discrete features may be hidden when taking averages across this length. By using the entire working section, this also includes contributions from both the rising and falling wire gradients. To be able to investigate the discrete behaviours, a windowing technique is introduced.

8.2.2 Discrete behaviours predicted by model 2 using a window filter post–process

The windowing method, introduced in Section 3.4.1, was performed to generate the mean contact force throughout each of the working sections. The results are shown in Figure 8.7. Due to the different lengths of the working sections, the horizontal lengths required for each gradient were scaled to correspond to a unit length as follows:

- Section 0 - 1 corresponds to the first ungraded span and the first transition span,
- Section 1 - 2 corresponds to the primary falling gradient spans,
- Section 2 - 3 corresponds to the second transition span, the central level span and the third transition span,
- Section 3 - 4 corresponds to the primary rising gradient spans, and
- Section 4 - 5 corresponds to the final transition and level spans.

From Figure 8.7 it can be seen that as the pantograph moves from the level span into the transition span, the contact force rises, with the sharpness of the rise increasing with the increasing gradient. Once the pantograph has moved on from the initial change in gradient, the contact force falls back towards the overall mean calculated in Section 8.2.1. When the gradient is shallow and there are a significant number of spans with the primary gradient, the mean contact force shows the oscillatory pattern typically associated with level contact wire and identical spans. As the gradient section shortens, this pattern is lost. When the gradient is 1:100, there is only a single primary gradient span and no opportunity for the oscillatory pattern to become established.

Towards the end of the primary gradient section, all cases see the mean contact force fall to the overall mean and then continue to fall as the pantograph reaches the central level span. Here the static uplift counteracts the descending pantograph to keep it in contact with the contact wire giving a lower resultant contact force. This force drops again as the contact wire begins to rise and the static uplift is required to force the pantograph to continue following the wire.

During the primary rising gradient spans, when the gradient is shallow, the oscillating pattern is once again re-established, but is lost for the steeper gradients, consistent with the behaviour from the primary falling gradient spans. Only here, the contact force is low compared with the standard mean. Once the pantograph moves towards the end of the

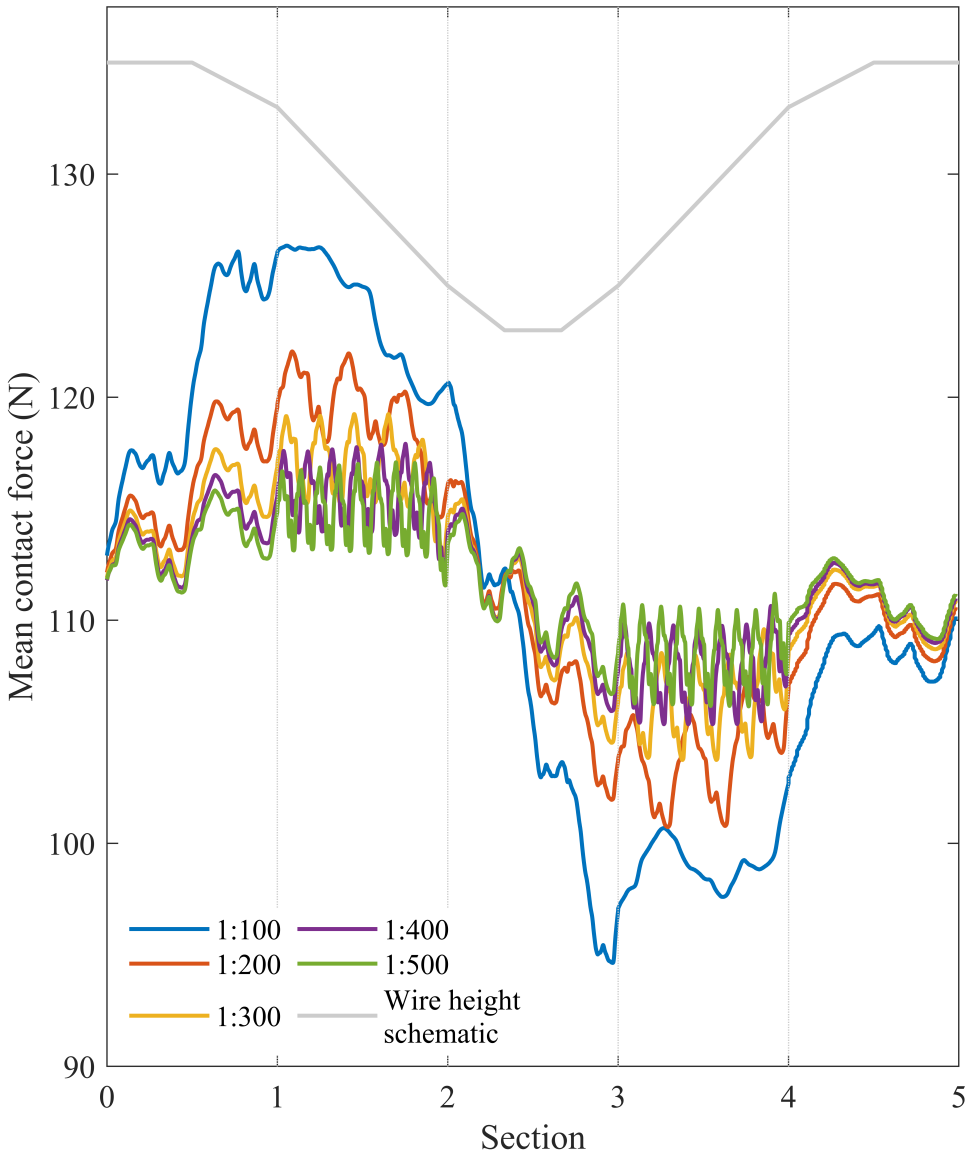

Fig. 8.7 Moving average of the contact force using model 2 for each gradient investigated. Window used was 60 m long. Legend indicates the gradient used in each case.

working section into the final level span, the contact force returns to the usual mean from Section 8.2.1.

The output summarised in Table 8.2 are the ranges in the mean and standard deviation of the contact force. Increasing the wire gradient from 1:500 to 1:100 increased the range of the mean contact force by approximately 20 N and a larger range in the standard deviation of approximately 7 N was also predicted. Whilst the mean contact force was found to vary greatest when the pantograph moved from the first transition span to the falling contact wire,

Table 8.2 Change in the mean and standard deviation of the contact force with increasing gradient using the windowing method compared with the level wire geometry in the BS EN50318:2002 standard. All values given in N.

Wire gradient	Range of mean contact force	Range of standard deviation
Level	0.437	0.660
1:500	10.9	3.0
1:400	12.6	5.0
1:300	15.5	4.9
1:200	21.3	6.6
1:100	32.2	10.3

shown as location 1 in Figure 3.22, the standard deviation varies more when the pantograph moved from the rising contact wire to a shallower transition span, given by location 3 in Figure 3.22.

8.2.3 Results of models 3 and 4

The results obtained in Section 8.2.1 were obtained with an overhead line where the dropper lengths are maintained throughout a transition under an overbridge. In this section the results of the simulations using models 3 and 4 described in Section 3.4.1 are described.

The statistical analysis of the overall behaviour of the two models is presented in Table 8.3 along with the output from model 2. From the data in Table 8.3, it can be seen that varying the system height has little overall effect on the contact force, the mean contact force was unchanged in all three simulations. Model 4 predicts a smaller standard deviation than the two other models suggesting that the change in pantograph height is influential in the dynamic performance of the system. Changing from a level contact wire to a graded contact wire yielded an approximately 30% increase in the contact force standard deviation, and reducing the dropper lengths as well as the contact wire height resulted in a 9.5% increase in the standard deviation when the wire gradient was maintained at 1:100.

From the output, the dynamic performance appears to be worst for reductions in both wire and system heights. This is not unexpected due to being the least like a conventional overhead line with a level contact wire and identical spans. It is sensible then that the best performing was model 4 with the level contact wire and no requirement for the pantograph to undergo large scale height changes. Model 2 with the dropper lengths maintained performed as expected and fell in between models 3 and 4, however the results tended towards those

Table 8.3 Statistical output for models 2, 3 and 4. The wire gradient is maintained at 1:100 and data is taken over the whole working section and includes contributions from both falling and rising wire heights. All quantities given in N.

Output	Model 2	Model 3	Model 4
F_m	111	111	111
σ	18.0	19.9	13.6
$F_{D_{\max}}$	184	182	163
$F_{D_{\min}}$	75.4	57.2	79.4
$F_{S_{\max}}$	165	171	155
$F_{S_{\min}}$	57.3	51.6	73.6

of model 3 than model 4 suggesting that the gradient changes are a significant factor in the dynamic performance of the overhead line.

The force traces of the two simulations using models 3 and 4 are shown in Figure 8.8, and a force peak predicted by model 3 is observed at location X_1 consistent with the force peak observed at location 1 from model 2. This is due to the pantograph head accelerating due to the falling wire gradient as in model 2. A similar force peak occurs when the pantograph stops rising towards the end of the wire run, shown as location Y_1.

In model 4, no wire gradient changes are imposed on the contact wire, and the reduced system height yields a change in the vertical stiffness of the system due to the shortening of the droppers. This change in vertical stiffness results in a variation in the contact force such as the peak at location B in Figure 8.10. Whilst there is a force peak, it is over 10% lower than corresponding force peaks predicted by models 2 and 3, where wire height changes are implemented. Beside the force peak, the contact force displays a typical oscillation associated with level contact wires, which is lost when the contact wire height is varied.

The falling contact force seen in model 2 is also predicted by model 3, however the reduction in the system height reduces the contact force further than previously seen, reducing it by 24%. This is in contrast with the predicted force peak which is almost unchanged between models 2 and 3 as it occurs in the first transition span, where the dropper lengths are only 1% shorter in model 3, than in model 2, whereas the larger variation between the models in the central span is thought to occur due to the droppers being approximately 50% shorter than in model 2.

The windowing method introduced in the previous section was also applied to models 3 and 4, and the results are shown in Figure 8.10. The geometry schematics for each of the models are shown in Figure 8.9. Reducing the dropper lengths reduces the moving average contact force between locations B and C in Figure 8.10, however a 2.4% larger peak in the

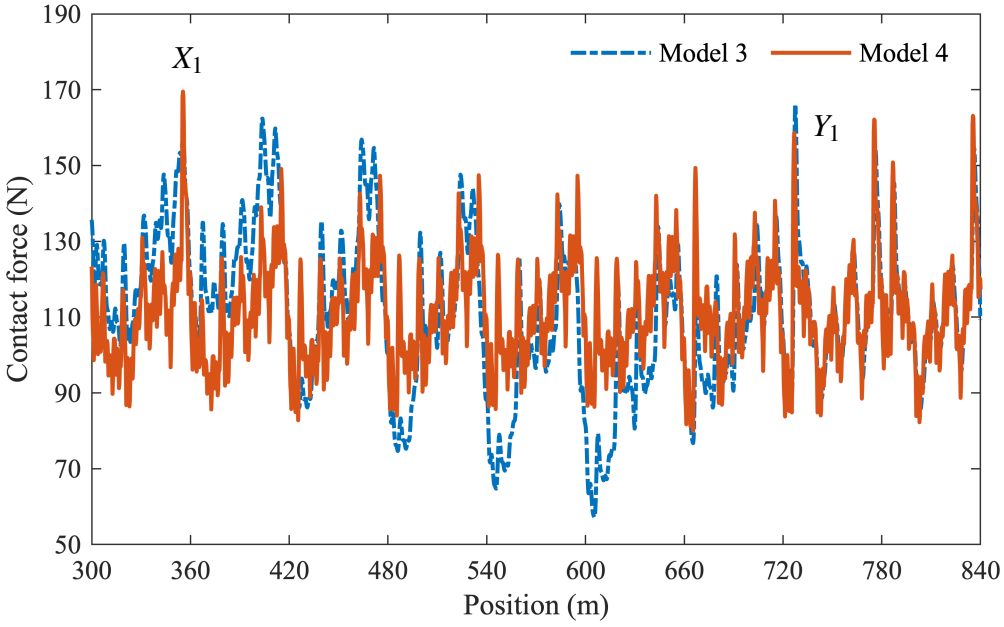

Fig. 8.8 Contact force trace between the pantograph collector strip and contact wire for models 3 and 4.

mean force is predicted by model 3 than model 2 when transitioning from a level to graded contact wire. This is in contrast to a 2.7% predicted decrease when transitioning from the rising contact wire gradient back to a level wire at location D.

Each of the three models where a height change was imposed demonstrate a typical sawtooth pattern of contact force with local maxima being observed at the dropper locations, and the largest variation in the mean contact force is predicted using model 3, where the range is 63 N, whilst the ranges in contact force for models 2 and 4 are 51 N and 20 N respectively. The combination of a varying contact wire height appears to effect a detrimental change in the dynamic performance when compared with maintaining at least one of the wire or system heights. As in model 2, no contact losses were predicted by models 3 and 4.

When no gradient changes were imposed in model 4, it can be seen from Figure 8.10 that the mean contact force shows little variation span-span and a consistent oscillation can be observed with the contact force falling towards the centre of the span and then rising again when the vertical stiffness increases towards the registration. This pattern is also present in the force traces for models 3 and 4, shown in Figure 8.10, however it is clear that the height

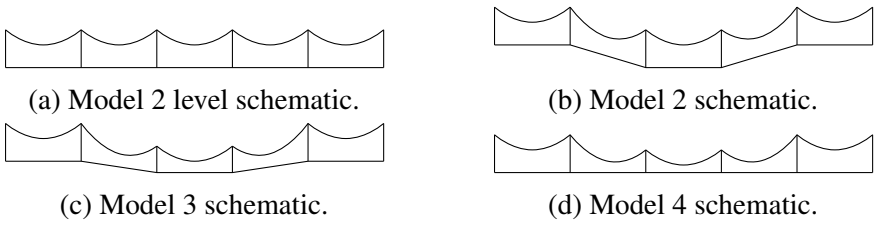

(a) Model 2 level schematic.

(b) Model 2 schematic.

(c) Model 3 schematic.

(d) Model 4 schematic.

Fig. 8.9 Model schematics. Droppers are omitted for clarity.

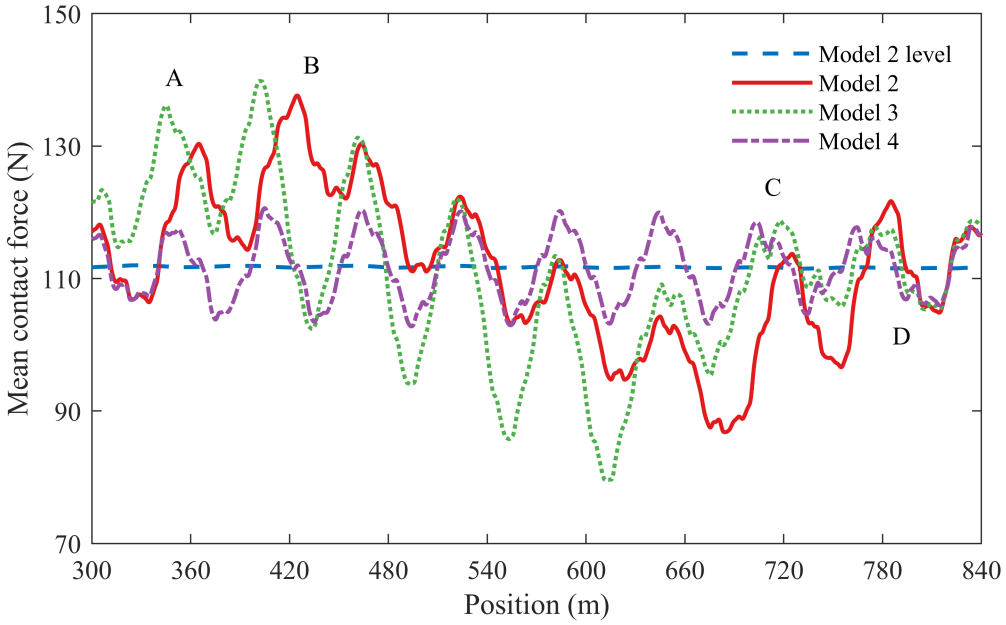

Fig. 8.10 Moving average contact force for models 2, 3 and 4 using a 60 m window. Both level and gradient cases using model 2 are included as indicated by the legend.

variation in the contact wire contributes to a much greater deviation away from the overall mean contact force of 111 N.

As a comparison, model 3 was also used to predict the contact forces when the wire gradient was 1:200. The output from this simulation is presented in Table 8.4 along with the results when the gradient was 1:100. It can be seen that as with the predictions of model 3, the shallower wire gradient of 1:200 yields small improvement in the dynamic performance with a 3% decrease in the contact force standard deviation whilst the mean contact force was unchanged. In each of the four other statistical outputs, all variations between a gradient of 1:00 and 1:200 were below 8%, with the discrete minimum contact force undergoing the

largest variation due to the change in contact wire gradient. This is thought to be a result of the shallower gradient

Table 8.4 Statistical output for model 3 when the contact wire gradients are 1:100 and 1:200. All quantities given in N.

Output	1:100	1:200
F_m	111	111
σ	18.0	17.5
$F_{D_{\max}}$	184	175
$F_{D_{\min}}$	75.4	70.0
$F_{S_{\max}}$	165	164
$F_{S_{\min}}$	57.3	58.9

The force trace and the moving average of the contact force for a wire gradient of 1:200 and a reduced system height is shown in Figure 8.11. It can be seen that the trend of decreasing contact force throughout of the height transition is consistent when compared with the output from each of the other simulations. The sinusoidal pattern of contact force is even more apparent when the gradient is 1:200 as the larger number of spans allow for a consistent variation in the contact force. This is made obvious when the moving average of the contact force is considered, with peaks of contact force occurring in each span. The extension of the number of spans over which the pantograph changes height has reduced the variation in the contact force to a range of 41 N compared with a range of 63 N when the gradient was 1:100.

From the averaged forces shown in Figure 8.10, it can be seen that when there is a limited height clearance, a change in the system height only is predicted to give the best dynamic performance. Large–scale changes in the contact wire height, both with and without system height changes are predicted to have comparable dynamic performance with respect to the largest predicted forces, however both reductions in the system and wire heights leads to larger contact force variation throughout the height transition compared with only wire height changes.

8.2.4 Contact force response to train speed

The previous sections have focused on a train running speed of 200 km/h. To generalise the results presented here, two further train speeds were considered: 130 and 225 km/h. Using model 2 with a wire gradient of 1:200, the statistical output for these running speeds are presented in Table 8.5. The statistical output shows that the train running speed is a dominant

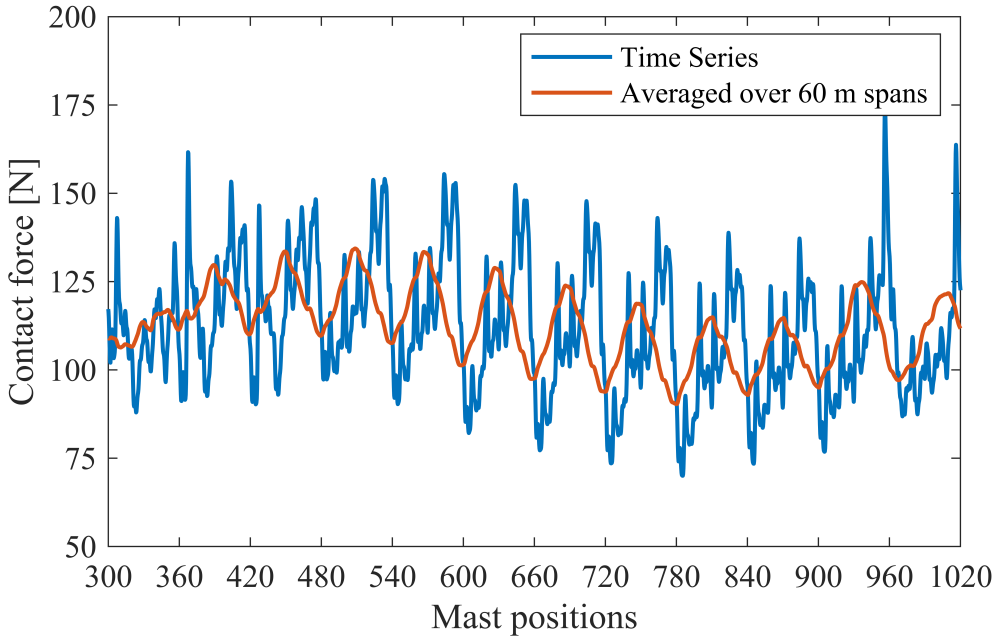

Fig. 8.11 Contact force trace and the moving average of the contact force for a reduced system height and a contact wire gradient of 1:200.

driver of the variation in the contact force with a predicted 26% increase in the mean contact force when the train running speed was increasing by 54% from 130 to 200 km/h. Between 200 and 225 km/h this increase was 9%. Peak contact forces follow a similar increasing trend as the peak force for a train speed of 80 km/h was 141 N and increased to 170 and 187 N for train speeds of 200 and 225 km/h respectively. These increases are larger than the increases observed for a constant running speed of 200 km/h but with an increased gradient of 1:100 suggesting that speed is a more dominant driver of the increased forces when compared with the wire gradient. The rising peak force maxima can be seen in Figure 8.12 for a level wire and a wire with a 1:200 gradient. Compared with a level wire, when the contact wire had a 1:200 gradient, the increase from 200 to 225 km/h lead to a sharper increase in the peak force, indicating that as the train speed increases, the larger peak forces rise more rapidly and that undesirable catenary pantograph interaction occurs for a lower train speed. Thus if a steeper wire gradient was desired, the line speed would have to be limited to ensure acceptable levels of wear as a result of the increased force.

Table 8.5 Results for model 2 with a wire gradient of 1:200. Statistical output considers the entire working section and includes contributions from both rising and falling wire gradients. All results in N.

Speed (km/h)	F_m	σ	$F_{D_{\max}}$	$F_{D_{\min}}$	$F_{S_{\max}}$	$F_{S_{\min}}$
130	89.2	10.3	141	74.5	120	58.3
200	112	14.7	170	80.1	156	67.5
225	122	18.3	187	64.2	177	67.1

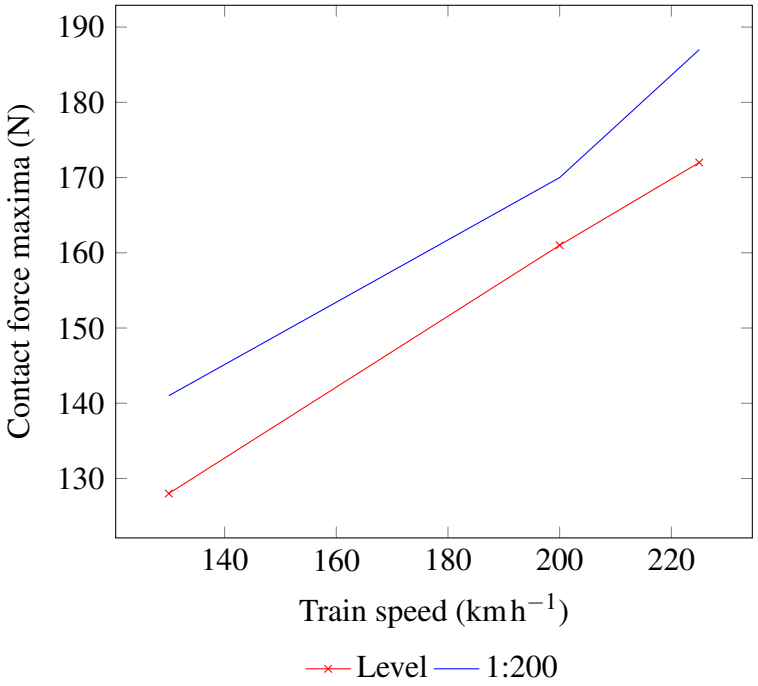

Fig. 8.12 Comparison between the peak contact force for level and graded contact wires.

8.2.5 Consequences and mitigations

Using model 2, contact force is predicted to increase with increasing wire gradient. Comparing wire gradients of 1:500 and 1:100, it can be seen that the peak contact force increased by 14% against a 400% increase in the wire gradient. This 14% increase in the peak force at location 2 in Figure 3.22 would be expected to see an increased wear regime due to the increased contact force. An increase in the wear would lead to a shortening of the overall lifetime of the equipment.

Assuming that the wear regime is governed by Archard's Law, and the system maintained a mild wear regime, a 14% increase in the contact load would suggest a corresponding 14%

increase in the mechanical wear at this location for the worst case gradient. In the case of a 1:200 gradient, this increase in contact force is 5.6% which would suggest only a lifetime shortening of approximately 20 months for a typical 30 year equipment lifetime. Since no contact loss was predicted in any of the simulations, arcing effects are not expected to increase thus none of the associated equipment degradations would increase. If the rise in the contact force at this location was carried through to the entire network, a 14 or even 5% reduction in the overall lifetime may be acceptable against the alternative of bridge reconstruction. The wear regime at the sliding interface is not solely driven by the mechanical wear as discussed in Chapter 2.3 and is a complex combination of mechanical and electrical wear and fatigue. The dynamic effects due to gradients on the electrical wear regime require further investigation to complete the assessment of the effects of steeper contact wire gradients on the catenary pantograph interaction.

Mitigation of the increased wear could be pursued using a variety of options aimed at reducing the impact of the increased wear regime and thus maintaining the overall lifetime of the overhead line equipment. Three such mitigation methods are proposed:

- Installation of a thicker contact wire throughout the height transition.
- Installation of a secondary contact wire, similar to a traditional wire overlap with the aim to allow the contact force to be shared across the two contact wires.
- Installation of a 'contenary' wire, or double contact wire, eliminating the messenger wire and allowing for a thicker contact wire to be installed under structures.

Each of the proposed mitigation methods would represent a cost saving when compared with the reconstruction of overbridge, where capital expenditure during the reconstruction process is typically £5 million [312] compared with approximately £18,000 km^{-1} for the contact wire [313]. The practicalities of sourcing, installing and maintaining a thicker contact wire over installation of a secondary contact wire would dictate which of the proposed methods would be used. For all of the proposed methods, the increase in the effective mass of the contact wire would have an effect on the dynamic behaviour and could have a detrimental effect on the pantograph head during high speed running. Figure 8.13 shows the increase in the contact force due to a 25% increased contact mass when the wire gradient was 1:100. The feasibility of each of these options can be determined through further dynamic modelling. Also an understanding of any alterations to other overhead line parameters, such as wire tension, is required, alongside an evaluation of the proposed mitigation methods costs compared against the current bridge reconstruction methods.

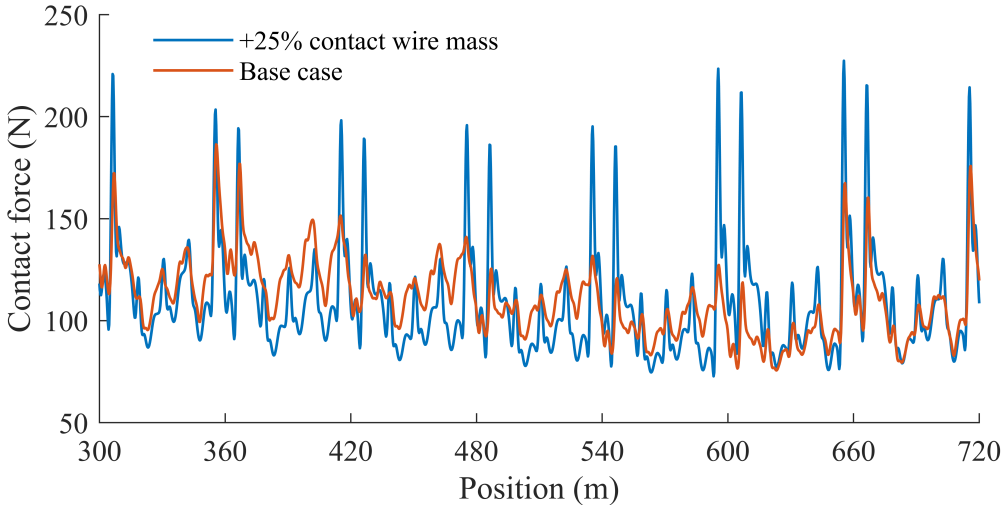

Fig. 8.13 Effect of an increase in the effective contact wire mass when the contact wire gradient is 1:100.

As well as assessing the feasibility of the proposed mitigation methods, further analyses would be required to assess the safety of implementing steep wire gradients on the railway network. Such factors affecting the safe implementation of the steep wire gradients would include:

- A larger range of train running speeds not considered here. Vibrational frequencies due to the sliding contact between the pantograph and overhead line can lock-in with the natural frequencies of the structure resulting in the associated high-force resonances. Here only a single span length and three train running speeds have been considered and whilst no resonances were predicted from the simulations, at different train running speeds, it may become apparent that the span length would need to differ to alter the natural frequency of the overhead line equipment to ensure no vibrational lock-in could occur during normal operation.

- Different pantograph designs. Whilst a typical design of pantograph for high-speed operation was used throughout the simulations, on the UK railway network alone there are a range of pantographs in operation and each would have a unique dynamic performance for the geometries considered here. For safe operation, a range of pantograph types would be investigated along with a range of pantograph parameters, e.g. pantograph head damping during steep wire transitions.

- Multiple pantograph operation. Since trailing pantographs typically undergo degraded dynamic behaviour when compared with the leading pantograph, the effect of the

predicted peak forces on multiple pantograph operation would need to be understood before safe implementation on the network. Whilst no contact loss was predicted during the simulations, contact loss is most frequently associated with trailing pantographs and any contact loss would lead to arcing between the pantograph and the contact wire. Damage due to arcing coupled with the increased peak force, would shorten the equipment lifetime further than the possible 14% reduction if only the peak contact force was the driver behind an increased wear regime. The effect of multiple pantograph operation on level wires is shown in Figure 8.14, however the dynamics during multiple pantograph operation have not been validated nor has the effect of the second pantograph throughout the height transition been considered here.

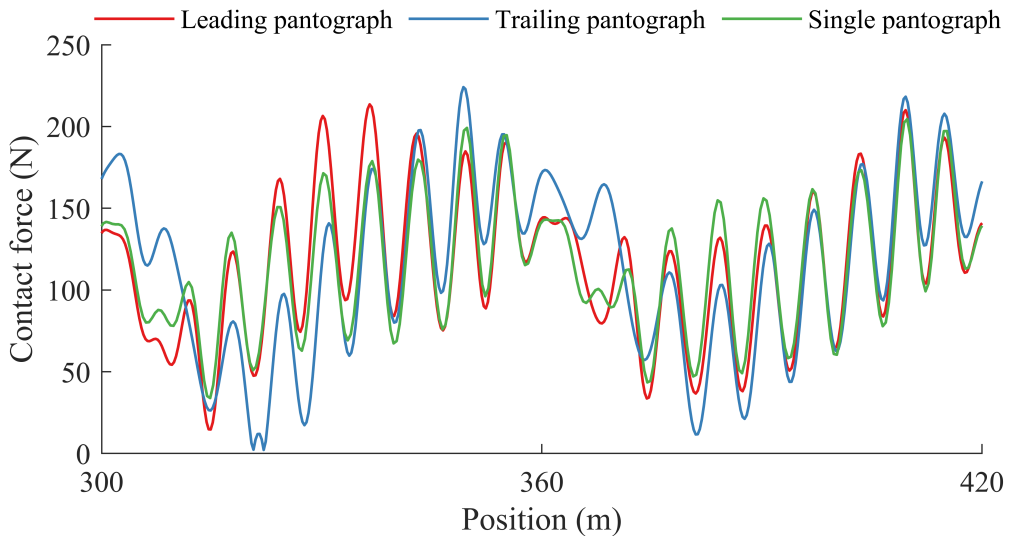

Fig. 8.14 Dynamic contact force for multiple pantograph operation under level wires. Legend indicates the contact force on the leading and trailing pantographs compared with single pantograph operation.

8.3 Conclusions

In this Chapter, the results of an investigation into the dynamic response of the catenary pantograph interaction to large–scale contact wire height changes have been presented. Using the described method, modelling was undertaken and successful validation of the model was performed using test track data and was found to be in good agreement with the measured data as required by the validation process outlined in the standard. Variation in the mean contact force was found to be approximately 2 N and the largest variation was to be found in

the peak contact force where the model over-predicts the contact force by 25 N. Despite the over-prediction the model still satisfied the allowable variation of $\pm 20\%$ in accordance with BS EN 50318 [287].

Adopting both idealised systems where the system height was maintained, and more realistic overhead line arrangements with altered dropper lengths, the influence of contact wire gradients on the dynamic contact force have been investigated. Wire gradients investigated far exceed the currently permitted wire gradient of 1:500 according to BS EN 50119 [26], and were increased up 1:100. Compared with a wire gradient of 1:500, when the contact wire gradient was 1:100, the discrete contact force maxima increased by only 14% and when the wire gradient was 1:200, the maximum contact force increase was only 5.6% compared with the 150% increase in the contact wire gradient. Whilst overall system life of the equipment is driven by a combination of electrical and mechanical wear and fatigue, the mechanical wear alone is indicated to increase by 14% by Archard's Law, assuming a mild wear regime was maintained.

Three proposals for mitigation of the effects of wire gradients are also presented here, however their feasibility has not been assessed. A 25% increase in the effective mass of the contact wire showed that further increases in the contact force maxima are predicted, however, these may be acceptable against the capital investment required in bridge reconstruction. To identify discrete dynamic behaviours, the contact force was averaged over 60 m lengths, corresponding to a single span, in addition to the conventional averaging over the entire run. Whilst discrete behaviours are masked by entire wire run averaging, by using the windowing technique, the results show that in the descending half of the span, the mean contact force demonstrates an increasing trend associated with the falling wire gradient. For this reason, if a steeper wire gradient was desired, localised wear would be predicted to occur in the descending half of the height transition. Since trains are typically restricted to a single direction on each line, the increased wear would not be evened out by trains running in the opposite direction, and so reinforcement against the increased wear would be required using one of the proposed mitigation methods. From the windowing method, the variation in the mean contact force was determined. As the gradient was increased, there was a proportional increase in the range of the mean contact force. For a gradient of 1:100 this variation was 32 N compared with a variation of 11 N for the 1:500 gradient. Performing the windowing analysis when the system height was changed demonstrated that reducing both system and contact wire heights yields larger variation in the contact force degrading the current collection quality. As the standard deviation for model 2 when the gradient was 1:100 was within 2 N of the standard deviation of model 3, it suggests that the imposing a

height change on the pantograph is the dominant driver of poorer current collection when compared with the influence of dropper heights. This is clear when compared with model 4 when only dropper heights were changed and the standard deviation was within 2 N of the standard deviation when the wire height was maintained in model 2.

Overall, the primary outcome of the study is a validated model capable of simulating the catenary pantograph dynamic when large scale height changes are imposed on the pantograph due to variations in the contact wire height due to low clearance structures. The results presented here have indicated that implementation of steeper wire gradients on the rail network are unlikely to cause significant problems in the performance of the overhead contact system. By avoiding the need to modify civil structures, steeper wire gradients may represent a significant cost saving for infrastructure owners.

Chapter 9

Conclusions and Future Work

9.1 Conclusions

In this thesis, the following research aim was proposed:

> to quantify the dynamic behaviours of the catenary pantograph interaction as a response to mechanical parameter variation and aerodynamic effects with a view to identifying potential failure modes and routes to cost effective electrification.

To answer the research aim, an investigation of the mechanical aspects of the interaction between a train mounted pantograph and the overhead line equipment has been presented. In Chapter 2, the research aim was decomposed into four open problems that were identified after a review of the current state of the art. The four problems were concerned with the effects of system changes of the overhead line equipment, the pantograph or the interaction between the two and each of the Chapters sought to investigate each open problem. Potentially, the greatest impact is from the work presented in Chapter 8 on the effects of wire gradients on the catenary pantograph interaction. The results in Chapter 8 have the potential to remove the need for expensive bridge reconstruction during the electrification of existing lines, and would represent significant potential cost savings to infrastructure managers.

To assess the validity of the results presented in this thesis, generated using a modelling approach, the sensitivity of the modelling to the assumptions made were assessed. The sensitivity analysis indicated that the model was not sensitive to a range of modelling assumptions, such as the use of a solid cylinder rather than a stranded messenger wire, and neglecting friction. The model sensitivity was assessed to be of the order of 10%.

The validation process of the finite element model was also presented. After development of an existing finite element model, validation for the enhanced model for the investigation

of large–scale wire height changes was performed. It was found that modelling predictions generated by the new model were in good agreement with measured data from Network Rail's RIDC. The modelling predictions satisfied the required $\pm 20\%$ band according to BS EN 50318 [287]. The validation of the new model was also extended by introducing a comparison with further measured data obtained from the Great Western Mainline. The new validation methodology assessed the pantograph response by comparing the contact forces as the pantograph is compressed due to a decreasing wire height. Using this method, the lumped–mass representation pantograph was found to demonstrate similar behaviour to that of a real pantograph undergoing compression.

The first of the open problems was, "Experimental and computational determination of aerodynamic forces on railway contact wire, using experimental measurements as validation of a numerical fluid simulation". In Chapter 5, the determination of aerodynamic forces on a railway contact wire was performed using both experimental and numerical techniques. The experimental techniques served as validation for the computational methodology adopted to study the aerodynamic forces at wind speeds unachievable in the wind tunnel. From the determination of the aerodynamic forces:

- The angle of attack acts to increase the aerodynamic drag acting on a contact wire by increasing the cross–sectional area presented to the flow. This indicates that contact wire blow off is increased for twisted wires that deviate from the design position due to shifting of the supports for example.

- At higher wind speeds, the contact wire was found to vibrate at high frequency (approximately 250 Hz), which whilst having small amplitude would result in micro–arcing between the contact wire and pantograph carbons. The individual micro–arcs themselves would cause little damage to either of the contact surfaces, however the high frequency would cause a large number of arcs to accumulate rapidly contributing to excessive arcing effects on the contact surface. As in the case of large arcs during contact loss events, the additive effect of rapid micro-arcing would degrade the current collection quality.

- Wind speeds for which the low frequency, large amplitude galloping phenomena occurs, was predicted by considering the drag and lift coefficients of the contact wire under aerodynamic load. The asymmetrical cross–sectional area of the contact wire was found to increase the likelihood of galloping occurring as the wear of the contact wire increased, consistent with the results presented in [174], and the drag coefficients were found to be larger than the currently accepted drag coefficients in BS EN 50119 [26].

The drag coefficient of 1.5 was larger than the quoted value of 1.0, and only slightly larger than the calculated coefficient of 1.4 in [176]. The calculated value for the drag coefficient presented here indicates that the current calculation of aerodynamic loads is an underprediction, and therefore may underestimate the true deflections of conductors under aerodynamic loading.

- The prediction of the potential for galloping phenomena indicates that it can occur for "normal" wind speeds, i.e., average UK wind speeds as measured in [306], whilst the high frequency behaviour occurs in gusting conditions.

- Validation of the numerical methodology by comparison with the experimental tests was achieved with at most 7% variation between the measured and simulated cases. Thus computational fluid techniques adopted here are a suitable method for predicting the aerodynamic loads on new designs of contact wire and at wind speeds existing equipment was not designed for.

Due to the work performed in this Chapter, a validated computational fluid model to quantify the aerodynamic loads has been created, contributing a useful tool to assess the aerodynamic characteristics of a range of contact wire profiles and environmental conditions that can be adapted and pushed to higher wind speeds and contact wire cross–sections not considered. The research aim was addressed through the identification of aerodynamic drag and lift forces on a contact wire due to an incident airflow and the effect of wind speed, contact wire wear and the angle of attack of the flow were assessed, resulting in quantification of the effects of each of the chosen variables in this study.

The second of the identified open problems concerned "The effects of contact wire irregularity not associated with the wear characteristics of the contact wire such as messenger and contact wire tensions, missing droppers and speed variations". Each of the areas identified in the open problem were investigated in Chapter 6, directly addressing the problem. From the results presented, it was found that,

- The dynamic performance of an overhead line could be improved with an increase in the contact wire tension, offering opportunities for increased line speeds without the need for redesigns of overhead line equipment, whilst also reducing wire uplifts. The reduction in the contact wire uplift finds use when electrifying existing lines that pass under low clearance structures such as bridges or tunnels, where strict electrical clearances are given to prevent arcing between the live equipment and the lineside structures. Reducing the necessary clearances would represent significant cost

savings compared with the reconstruction of bridges to provide the currently required clearances. In contrast to the benefits of an increased contact wire tension, increases in the messenger wire tension were predicted to cause larger amplitude oscillations in the contact wire post pantograph passage. These larger amplitude oscillations would shorten the service life of the contact wire by hastening the onset of mechanical fatigue. Despite the post pantograph passage oscillations, a matching between the contact and messenger wire tensions reduced the contact force variation across the length of overhead line under consideration. This matching of the wire tensions was a key new contribution that had not been researched or attempted, suggesting that dynamic improvements could be made without a system redesign, thus representing a cost–effective means of improved electrification.

- Small mass reductions in the contact wire, thereby reducing the contact wire inertia reduced the contact force discrete maxima indicating a more desirable performance. A similar result was shown when a reduction in the pantograph head mass was used. These results together show that minimizing the mass at the contact surface, subject to practical considerations such as electrical transmission, would likely result in desirable dynamic performance during train operation. The reduced forces as a result of a minimal pantograph head and contact wire mass would reduce the wear between the two surfaces potentially extending the lifetime of both parts of the contact interface, whilst also representing a cost saving to infrastructure managers during installation and maintenance of the equipment. A desire to minimise the pantograph head mass limits the use of active control of the pantograph as any additional mass would degrade the performance by increasing the discrete maxima. Active control of the pantograph static uplift however would provide a benefit to the catenary pantograph interaction by varying the static uplift force as the pantograph moves. An instrumented pantograph capable of modulating the static uplift force as a response to the varying contact force would likely even out the contact force variations during train operation. In particular, by varying the static uplift force at locations where contact forces are likely to rise, such as at height transitions to bridges or level crossings, the dynamic effects of wire height changes could be minimised.

Building on the identified open problem answered by Chapter 5, investigation of aerodynamics was extended through the open problem, “Dynamics of an overhead line under wind load considering cases where the aerodynamic loading will change abruptly". In Chapter 5, the existing model of [241] was enhanced to include environmental effects determined in

Chapter 5, to address the problem that up to now has not been widely studied. The exploratory work established that aerodynamic loads can have unwanted dynamic effects on the catenary pantograph interaction and that further research in this area is warranted. Both static and dynamic wind loading conditions were considered to understand the steady state response of a contact wire under steady load and the dynamic response of the catenary pantograph interaction to a time varying sinusoidal aerodynamic load. In the static case, the contact wire deflections as predicted by the analytical calculation and the finite element predictions were found to be in good agreement as the lateral blow off the contact wire under high lateral load (20 $\mathrm{N/m}$) was found to vary between the calculated and predicted deflections by only 8% at midspan. In the dynamic case, a sinusoidal load function was applied to a finite element representation of the overhead line and it was found that:

- The aerodynamic lift force causes vibrations in the contact wire that deteriorate the catenary pantograph interaction by significantly increasing the contact force discrete maxima at high wind speeds. This increase in the discrete contact force would increase the wear rate of the contact surface shortening the lifetime. The high frequency aerodynamic loading (85 Hz) compared with the natural frequency of the equipment (typically 1 Hz) would cause a rapid accumulation of small amplitude load cycles in the contact wire.

- The aerodynamic effects are predicted to worsen as the wear state of the contact wire increases. As the wear increases, the contact wire inertia decreases, reducing the resistance to deflections under aerodynamic loading. This increases the amplitude of the oscillations, that while still small, cause large contact force increases at locations of increased vertical stiffness, such as droppers and supports. From Chapter 6, the addition of extra droppers in a span was found to even out the stiffness variations, reducing the variation of the contact force, thus ensuring sufficient droppers within a span in windy locations would reduce the predicted large force variations, whilst also restricting the contact wire oscillations with the small increase in inertia provided by the droppers.

- Lateral deflections of the contact wire were predicted to have little effect on the contact force since the increase in wire tension caused by the lateral deflections was small compared with the already applied tension to reduce the contact wire sag. In fact, the wear state of the contact wire was a more significant driver of contact force variation, than deflections due to lateral drag.

Two case studies were considered with respect to the dynamic effects of wind loading:

1. Overhead line equipment leaving a tunnel and being exposed to crosswinds, and

2. Overhead line equipment passing under a bridge where the bridge supports provide a short area of protection against the sidewinds.

In the first case, the aerodynamic effects on the exposed section of the equipment were transmitted back along the contact wire inside the tunnel, degrading the performance of the entire system. By causing oscillations within the tunnel, the contact force was predicted to increase, thus increasing the wire uplift. At high wind speeds, the increased uplifts have the potential to exceed the electrical clearances risking arcing between the live system and the tunnel. To reduce the risk of arcing, adopting shorter span lengths inside the tunnel and close to the tunnel mouth in the exposed sections, would restrict the available wire uplift, thus satisfying the required electrical clearances.

In the second case, the short length of the bridge relative to the span length was predicted to have little effect on the contact force and the sidewinds were the dominant driver of the contact force variation. As in the previous case, the vertical oscillations of the contact wire caused large variations in the contact force, and contact loss was predicted here for the first time. As shown in Chapter 6, an increase in the line tension would act to resist the oscillations of the contact wire and restrict the wire uplift to prevent arcing events between bridges and overhead equipment.

This Chapter has contributed an enhanced model capable of assessing the catenary pantograph interaction under the influence of aerodynamic loads through a novel method adopted to apply the aerodynamic forces.

The final open problem given in Chapter 2 was, “Effect of large–scale wire height changes on the dynamic contact force”. This was directly addressed by considering the dynamic response to large–scale contact wire height changes in Chapter 8 using the model validated in Chapter 4, where representations of the overhead line corresponding to three cases were considered:

- Adoption of an idealised representation of the overhead line where the system height remained constant allowed for identification of the core gradient effects as the contact wire gradient was increased from the maximum permitted gradient of 1:500 [26] to 1:100. Despite the 400% increase in the contact wire gradient, the discrete contact force maxima was predicted to increase by only 14%. In the case when the wire gradient was 1:200, the peak force increase was only 5.6%. Methods of mitigation were proposed to maintain the lifetime of the equipment despite the increased contact force maxima causing an increase in the mechanical wear according to the Archard

equation, and the results in Chapter 6 indicate that the dynamic effects due to the steep wire gradient could be mitigated by increasing the contact wire tension.

- A reduction in the system height whilst maintaining the contact wire height provided for the best dynamic performance, largely due to the nominally unchanging pantograph height (the pantograph height changed with respect to the contact wire presag). Compared with a level wire with no system or contact wire height changes, a small increase in the contact force maxima was predicted, likely due to the shortened dropper lengths in the central spans, however this increase was approximately 6% suggesting that the effect of the system height reduction was minimal.

- Reducing both the system height and the contact wire height presented the worst dynamic performance for the gradient under consideration due to a larger contact force standard deviation. Compared with a system with same contact wire gradient but with no system height change, the peak contact forces were comparable (approximately 1% variation). Each of the three different wire arrangements suggests that during the design process of electrifying a line under a bridge, the following ranking could be used:

    1. Reduce the system height only,
    2. Reduce the wire height but maintain the system height,
    3. Reduce both wire and system heights.

This ranking of the options available to overhead line designers is a direct consequence of assessing the effect of large–scale wire height changes that have been enabled through development of the current model and thus represents a confirmation of existing "design experience" when electrifying beneath low clearance structures. In all of the considered models in Chapter 8, a windowing technique was introduced to identify discrete dynamic effects. The windowing process highlighted the variation of the contact force as a response to the increasing steepness of gradient that was otherwise masked by an unchanging mean contact force.

This Chapter has contributed a validated model that is capable of assessing the dynamic response of the catenary pantograph interaction to both gradients in the contact wire and large wire height changes. The model has also enabled the quantification of the contact force variations due to a change in the contact wire height that was up to now not well defined.

The original research aim was concerned with (i) cost–effective electrification and (ii) the identification of potential failure modes. With respect to cost–effective electrification, the work in this thesis has shown that:

- Dynamics can be improved with mechanical parameter variation rather than geometry or pantograph redesigns,
- Bridge demolition may be unnecessary as sharper gradients may be viable to achieve the required height changes in limited horizontal space, and
- The increased force due to an increased steepness of gradient and therefore transition between gradients could potentially be mitigated by a larger diameter contact wire, representing a large cost benefit compared with bridge reconstruction.

Regarding potential failure modes, the research presented in this thesis has highlighted that:

- High frequency behaviour due to high wind speeds on worn contact wires may lead to micro–arcing at the contact interface, degrading the surfaces hastening the onset of fatigue,
- Low frequency behaviour such as galloping may occur for low wind speeds on a range of different wire wear states, which has the potential to cause catastrophic damage to the system,
- The deflection of the overhead due to large sidewinds can likely to lead to dewirements, and that high contact forces due to an imposed aerodynamic lift can cause localised wear at the contact interface which would lead to a shortening of the system life.

9.2 Future Work

To determine the core effects changing each of the parameters considered here has on the catenary pantograph interaction, it is proposed that a combination of parameters could be changed in order to optimise the dynamic performance, for example, it was shown that matching the contact and messenger wire tensions yielded the best dynamic behaviour. Given the large number of parameters available, a comprehensive evaluation of each of them would allow for a better performing catenary pantograph interaction.

The modelling methodology provided in Chapter 6 allows for ‘plain’ overhead line components that are easily duplicated allowing for efficient modelling of a single continuous

overhead line. Discrete features of OLE however tend to exhibit the most interesting dynamic behaviour and thus it is beneficial to model these features. Common features not currently modelled include:

- Inline neutral sections: Discrete sections of overhead line are electrically insulated from each other and traditionally this is achieved by splicing a polymer into the contact wire. Modelling of these sections can be achieved by altering the material properties of discrete sections of the overhead line with the addition of lumped masses corresponding to the skid pans and arcing horns on these sections.

- Wire overlaps: These are required as wire lengths are limited by the mass of wire that can be installed in a continuous wire run. As such overlaps are needed to ensure continuous electrical contact between the pantograph and overhead line. The overlap configurations are typically between one and four spans long and in the centre of the overlap, the pantograph is in contact with contact wires from the leading and trailing wire runs. To achieve a simulation of a wire overlap, a 3D model must be incorporated to allow the wires to sit alongside each other and to be in simultaneous contact with the pantograph.

- Crossovers: These occur whenever the overhead line passes over switches and crossings as when the tracks cross, often the wires do too. The overhead line for the track with the higher running speed usually passes below the other, supported close to where the two wires cross to prevent the pantograph hooking onto the other wire. Due to the crossover, train passage disturbs both wires. Due to multiple wires being displaced during train passage, dynamic effects are different to those seen with just a single wire.

It is also proposed that further work is completed to better understand the influence of the length and number of droppers within each span. In all of the work in this thesis (except in the case of a missing dropper), the distance between droppers has been equal. It is unknown however the effect of unequal distancing or concentrated distribution of droppers would have on the dynamic contact force. For example, the stiffness variation is greatest towards supports, so concentrating more droppers at the ends of a span rather than at midspan where the contact force is reduced would smooth the transition between different vertical stiffnesses, reducing the variation in the contact force.

The numerical methodology presented in Chapter 5 considers a 2D flow around a contact wire, thus neglecting twisting and flow along the length of the contact wire. Twisting of the contact wire due to a flow would alter the cross–sectional area of the contact wire

presented to the flow, therefore changing the predicted drag and lift forces. Therefore a more complete 3D fluid model should be developed to determine a complete picture of the flow. The determination of aerodynamic loads also highlighted that at high wind speeds, the contact wire vibrates with high frequency, much higher than the natural frequency of the equipment. It is currently unknown what the effects of the high frequency behaviours have on the equipment, and so deserves further investigation.

In Chapter 6, the increase in contact wire tension was predicted to have a positive effect on the contact force. At height transitions where increased forces lead to increased wire uplifts, further work should be undertaken to assess the effects of an increased line tension at restricting wire uplifts, thus meeting current electrical clearances to bridges, without the need of costly bridge reconstruction. In Chapter 7. the effects of aerodynamic loads, on level contact wire geometries were assessed, and then the effects of gradients were considered in Chapter 8. Since it is likely that height transitions would occur in the two case studies presented in Chapter 7, uniting the models of aerodynamic loads and gradients should be performed to determine a better understanding of the overhead line behaviour at bridges and tunnels.

In Chapter 7, no validation attempt was made. However, adopting a “big data” approach using instrumented timetabled trains to measure the dynamic contact force during train operation alongside instrumented overhead line equipment measuring the deflections of the contact wire as well as the wind speeds, would generate a large dataset on lines with a high frequency of train passage. Identifying the generated data set with the modelling predictions in Chapter 7, would provide a method of validation.

Finally, in assessing the increases in the mechanical wear according to the Archard equation, it has been assumed that the wear of the contact wire remains mild. Thus, experimental tests of the copper–alloys should be undertaken to determine the transition from mild to severe wear.

References

[1] Andreas Steimel. *Electric traction-motive power and energy supply: basics and practical experience*. Oldenbourg Industrieverlag, Munich, 2008.

[2] Network Rail. Route Utilisation Strategy, Electrification. Technical report, Network Rail, London, 2009.

[3] Mizuki TSUNEMOTO, Masatoshi SHIMIZU, Keisuke IRIKURA, Hiroaki MORIMOTO, Chikara YAMASHITA, and Kunio IKEDA. Development of simple catenary system for operation over 300 km/h. *Quarterly Report of RTRI*, 61(1):47–53, 2020.

[4] Peter Moulton. Class 800 Azuma heads a southbound express into Peterborough, Cambridgeshire, England. ID: 1512194141, 2019.

[5] Sam Hayes, David I Fletcher, Adam E Beagles, and Katherine Chan. Effect of contact wire gradient on the dynamic performance of the catenary pantograph system. *Vehicle System Dynamics*, pages 1–24, July 2020.

[6] British Transport Commission. Modernisation of British Railways: The System of Electrification for British Railways. Technical report, British Transport Commission, London, UK, 1955.

[7] Nyberg Fredrik, Richard Pollard, and Network Rail. Network Rail A Guide to Overhead Electrification. Technical report, Network Rail, London, 2015.

[8] Office of Rail and Road. Table 6320 - Infrastructure on the mainline. Technical report, Office of Rail and Road, London, UK, 2020.

[9] System Operator Strategic Planning. TRACTION DECARBONISATION NETWORK STRATEGY: Interim Programme Business Case. Technical report, Network Rail, London, UK, 2020.

[10] BSI. BS EN 50149:2012 Railway applications. Fixed installations. Electric traction. Copper and copper alloy grooved contact wires. Technical report, London, UK, 2012.

[11] W Zhang, G Mei, and J Zeng. A Study of Pantograph/Catenary System Dynamics with Influence of Presag and Irregularity of Contact Wire. *Vehicle System Dynamics*, 37(sup1):593–604, January 2002.

[12] Yong Hyeon Cho, Kiwon Lee, Young Park, Bubyoung Kang, and Ki-nam Kim. Influence of contact wire pre-sag on the dynamics of pantograph–railway catenary. *International Journal of Mechanical Sciences*, 52(11):1471–1490, November 2010.

[13] Friedrich Kiessling, Rainer Puschmann, Axel Schmieder, and Egid Schneider. *Contact Lines for Electric Railways: Planning, Design, Implementation, Maintenance*. Publicis Corporate Publishing, 2nd edition, 2009.

[14] BSI. BS EN 50318: 2018 Railway applications - Current collection systems - Validation of simulation of the dynamic interaction between pantograph and overhead contact line. Technical report, BSI, London, UK, 2018.

[15] Railway Technology. Tension and strain on overheated trains, 2011.

[16] Evening Standard. 100,000 trapped on trains for hours on the hottest day of the year, 2011.

[17] Pfisterer Holding AG. TENSOREX C+ product information, 2017.

[18] Jesús Benet, Angelines Alberto, Enrique Arias, and Tomás Rojo. A mathematical model of the pantograph-catenary dynamic interaction with several contact wires. *Int. J. Appl. Math*, 37(2):136–144, 2007.

[19] Guiming Mei, Weihua Zhang, Hongyu Zhao, and Limin Zhang. A hybrid method to simulate the interaction of pantograph and catenary on overlap span. *Vehicle System Dynamics*, 44(sup1):571–580, 2006.

[20] J P Massat, J P Laine, and A Bobillot. Pantograph–catenary dynamics simulation. *Vehicle System Dynamics*, 44(sup1):551–559, January 2006.

[21] Takamasa HAYASAKA. Effect of reduced reflective wave propagation on overhead contact lines in overlap section. *Quarterly Report of RTRI*, 45(2):68–73, 2004.

[22] Farzad Vesali, Habibollah Molatefi, Mohammad A Rezvani, Bijan Moaveni, and Markus Hecht. New control approaches to improve contact quality in the conventional spans and overlap section in a high-speed catenary system. *Proceedings of the Institution of Mechanical Engineers, Part F: Journal of Rail and Rapid Transit*, 233(9):988–999, January 2019.

[23] S Gregori, J Gil, M Tur, J E Tarancón, and F J Fuenmayor. Analysis of the overlap section in a high-speed railway catenary by means of numerical simulations. *Engineering Structures*, 221:110963, 2020.

[24] RSSB. GE/RT 8025 Electrical Protective Provisions for Electrified Lines. Technical report, RSSB, London, 2001.

[25] RSSB. Railway Group Standard GLRT1210 AC Energy Subsystem and Interfaces to Rolling Stock Subsystem. Technical report, RSSB, London, UK, 2019.

[26] BSI. BS EN 50119:2009+A1:2013: Railway applications. Fixed installations. Electric traction overhead contact lines. Technical report, BSI, London, UK, 2009.

[27] Railway Gazette. Bridge lift to increase clearances, 2016.

[28] Network Rail. In numbers: Record-breaking track project successfully completed at Bath, 2015.

[29] Network Rail. Bridges, tunnels and viaducts, 2016.

[30] P Nåvik and A Rønnquist. Dynamic behaviour of an existing railway catenary system for extreme low passage at exceeding design velocities. In *Proceedings of the 9th International Conference on Structural Dynamics*, number July, pages 3753–3760, 2014.

[31] Tingyu Xin, Clive Roberts, Paul Weston, and Edward Stewart. Condition monitoring of railway pantographs to achieve fault detection and fault diagnosis. *Proceedings of the Institution of Mechanical Engineers, Part F: Journal of Rail and Rapid Transit*, 234(3):289–300, 2020.

[32] BSI. BS EN 50206 - 1:2010 Railway applications - Rolling stock - Pantographs: Characteristics and tests Part 1: Pantographs for main line vehicles. Technical report, BSI, London, UK, 2010.

[33] Nikolaos Baimpas, Peter Dearman, Simon Warren, Matthew Leathard, Brad Glass, and Garry Keenor. Great Western railway electrification, UK: pantograph interface model boosts speed. *Proceedings of the Institution of Civil Engineers - Civil Engineering*, pages 1–9, 2020.

[34] S Avila-Sanchez, J Meseguer, and O Lopez-Garcia. Turbulence intensity on catenary contact wires due to parapets placed on a double track bridge. *Journal of Wind Engineering and Industrial Aerodynamics*, 98(10):504–511, 2010.

[35] C Vera, B Suarez, J Paulin, and P Rodríguez. Simulation model for the study of overhead rail current collector systems dynamics, focused on the design of a new conductor rail. *Vehicle System Dynamics*, 44(8):595–614, 2006.

[36] Carlos Vera, Jenny Paulin, Berta Suárez Esteban, and Pablo Rodríguez. Improved design of an overhead rail current conductor for application in underground lines. 2005.

[37] H H Huang and T H Chen. Development of method for assessing the current collection performance of the overhead conductor rail systems used in electric railways. *Proceedings of the Institution of Mechanical Engineers, Part F: Journal of Rail and Rapid Transit*, 222(2):159–168, 2008.

[38] Tsuyoshi Mandai, Masatoshi Shimizu, and S Harada. Development of rigid conductor line for high-speed operation. In *IEEE International Conference on Industrial Technology, 2003*, volume 1, pages 587–592. IEEE, 2003.

[39] Giuseppe Bucca, Marco Carnevale, Andrea Collina, Alan Facchinetti, Lars Drugge, Per-Anders Jönsson, and Sebastian Stichel. Adoption of different pantographs' preloads to improve multiple collection and speed up existing lines. *Vehicle system dynamics*, 50(sup1):403–418, 2012.

[40] Andrea Collina, Stefano Bruni, Alan Facchinetti, and Andrea Zuin. PCaDA statement of methods. *Vehicle System Dynamics*, 53(3):347–356, 2015.

[41] Andrea Collina, Antonietta Lo Conte, and Marco Carnevale. Effect of collector deformable modes in pantograph—catenary dynamic interaction. *Proceedings of the Institution of Mechanical Engineers, Part F: Journal of Rail and Rapid Transit*, 223(1):1–14, 2009.

[42] Yong Hyeon Cho. SPOPS statement of methods. *Vehicle System Dynamics*, 53(3):329–340, March 2015.

[43] Ning Zhou, Qingsong Lv, Yi Yang, and Weihua Zhang. <TPL-PCRUN> Statement of methods. *Vehicle System Dynamics*, 53(3):380–391, March 2015.

[44] A Bautista, J Montesinos, and P Pintado. Dynamic interaction between pantograph and rigid overhead lines using a coupled FEM — multibody procedure. *Mechanism and Machine Theory*, 97:100–111, 2016.

[45] Montserrat Simarro, S Postigo, Juan A Cabrera, and Juan J Castillo. A procedure for validating rigid catenary models using evolutionary techniques. *Computers & Structures*, 228:106145, 2020.

[46] Teruo Kobayashi, Yoshihiro Fujihashi, Koji Kato, and Shunichi Kusumi. Development of long-span-type overhead rigid-conductor line of a catenary system. *Electrical Engineering in Japan*, 131(1):94–102, April 2000.

[47] Long Chen, Zhigang Liu, Jing Zhang, and Zeyao Hu. Influence of Key Parameters on High Speed Overhead Conductor Rail and Pantograph System. pages 201–211. February 2020.

[48] Kiyotaka Yamashita, Kotaro Kitajo, Shou Wada, Toshihiko Sugiura, and Hiroshi Yabuno. Impact oscillations with multiple modes between a pantograph and an overhead rigid conductor line in a railway current collection system. *Journal of Vibration and Control*, 18(4):499–508, November 2010.

[49] Zhi-Wei Han, Zhi-Gang Liu, Hong-Mei Yang, and Ye Han. Insulator fault detection based on curvelet coefficients morphology and zonal energy method. *Journal of the China Railway Society*, 35(3):36–40, 2013.

[50] Fuqiang Fan, Zhigang Liu, Ying Wang, Xiuqing Mu, and Shibin Gao. Research and Analysis of Transient Process of Locomotive Passing Neutral Section Based on Habedank Arc Model. volume 287, pages 233–241. January 2014.

[51] Rui Miao, Chaoxian Wu, Shaofeng Lu, Fei Xue, Zhongbei Tian, and Stuart Hillmansen. Optimization of neutral section location on high-speed railways with consideration of train operations. In *Sustainable Buildings and Structures: Building a Sustainable Tomorrow: Proceedings of the 2nd International Conference in Sutainable Buildings*

and Structures (ICSBS 2019), October 25-27, 2019, Suzhou, China, page 171. CRC Press, 2019.

[52] Network Rail. NR/GN/ELP/27010 "Guidance for Compatibility Between Electric Trains and Electrification Systems", Issue 2. Technical report.

[53] Yoshifumi Mochinaga, Yoshio Akatsuka, Kohichi Arai, and Masaru Ono. Development of Three-winding Transformer for Shinkansen Auto-transformer Feeding System Receiving Extra-high Voltage. *IEEJ Transactions on Industry Applications*, 111(3):237–244, 1991.

[54] Z Fei, T Konefal, and R Armstrong. AC railway electrification systems — An EMC perspective. *IEEE Electromagnetic Compatibility Magazine*, 8(4):62–69, 2019.

[55] Scientific American. A Ninety-Six Ton Electric Locomotive, 1895.

[56] J.Q Brown. Trolley, 1904.

[57] L Faiveley. Current Collection Device, 1955.

[58] A.R Beadle. High speed pantographs (IM-ETR-014). Technical report, British Rail Research, Derby, UK, 1973.

[59] Garry Keenor. *Railway Electrification and Power Engineering Handbook: Introduction to Overhead Line Electrification*. 2008.

[60] RSSB. Investigating the potential for improvements in electrification systems (T346). Technical report, RSSB, London, 2007.

[61] BSI. BS EN 50367:2012+A1:2016 Railway applications. Current collection systems. Technical criteria for the interaction between pantograph and overhead line (to achieve free access). Technical report, BSI, London, UK, 2012.

[62] Jin-Woo Kim, Ho-Chol Chae, Bum-Seok Park, Seung-Yeol Lee, Chang-Soo Han, and Jin-Hee Jang. State sensitivity analysis of the pantograph system for a high-speed rail vehicle considering span length and static uplift force. *Journal of sound and vibration*, 303(3-5):405–427, 2007.

[63] Jin-Woo Kim and Seung-Nam Yu. Design variable optimization for pantograph system of high-speed train using robust design technique. *International journal of precision engineering and manufacturing*, 14(2):267–273, 2013.

[64] Tong-Jin Park, Chang-Soo Han, and Jin-Hee Jang. Dynamic sensitivity analysis for the pantograph of a high-speed rail vehicle. *Journal of Sound and Vibration*, 266(2):235–260, 2003.

[65] Joao Pombo and Jorge Ambrósio. Influence of pantograph suspension characteristics on the contact quality with the catenary for high speed trains. *Computers & Structures*, 110:32–42, 2012.

[66] W Seering, K Armbruster, C Vesely, and D Wormley. Experimental and analytical study of pantograph dynamics. 1991.

[67] Yoshitaka Yamashita and Mitsuru Ikeda. Upgrading pantograph performance using variable stiffness devices. *Quarterly Report of RTRI*, 51(4):214–219, 2010.

[68] A Bobillot, J P Massat, and J P Mentel. Design of pantograph-catenary systems by simulation. In *9th World Congress on Railway Research (WCRR)*, 2011.

[69] Weihua Zhang, Ning Zhou, Ruiping Li, Guiming Mei, and Dongli Song. Pantograph and catenary system with double pantographs for high-speed trains at 350 km/h or higher. *Journal of modern Transportation*, 19(1):7–11, 2011.

[70] K Manabe and Y Fujii. Overhead system resonance with multi-pantographs and countermeasures. *Railway Technical Research Institute, Quarterly Reports*, 30(4), 1989.

[71] Zhendong Liu, Per-Anders Jönsson, Sebastian Stichel, and Anders Rønnquist. On the implementation of an auxiliary pantograph for speed increase on existing lines. *Vehicle System Dynamics*, 54(8):1077–1097, 2016.

[72] N Zhou. *Pantograph and catenary interaction with the train speed beyond 350 km/h.* PhD thesis, Southwest Jiao Tong University, 2012.

[73] Han Zhao, G C Barber, and J Liu. Friction and wear in high speed sliding with and without electrical current. *Wear*, 249(5-6):409–414, 2001.

[74] Z Xu, Y Song, and Z Liu. Effective Measures to Improve Current Collection Quality for Double Pantographs and Catenary Based on Wave Propagation Analysis. *IEEE Transactions on Vehicular Technology*, 69(6):6299–6309, 2020.

[75] T Vinayagalingam. Computer evaluation of controlled pantographs for current collection from simple catenary overhead equipment at high speed. 1983.

[76] Y Jiao, Y Wang, X Chen, and J Liu. Active Control of Pantograph Based on Prior-information of Catenary. In *2020 IEEE 5th Information Technology and Mechatronics Engineering Conference (ITOEC)*, pages 460–464, 2020.

[77] Wilhelm Baldauf, Rene Blaschko, Wolfgang Behr, Christoph Heine, and Michael Kolbe. Development of an actively controlled, acoustically optimised single arm pantograph. In *Proceedings of the World Congress of Railway Research WCRR*, 2001.

[78] Alan Facchinetti and Marco Mauri. Hardware-in-the-loop overhead line emulator for active pantograph testing. *IEEE Transactions on Industrial Electronics*, 56(10):4071–4078, 2009.

[79] W Baldauf, M Kolbe, and W Kroetz. Closed-loop controlled pantograph for high-speed applications; Geregelter Stromabnehmer fuer Hochgeschwindigkeitsanwendungen. 2005.

[80] Jacques Cathala and Pascale Forte. Device for adjusting the bearing force of a pantograph on a catenary wire and process relating thereto, May 1992.

[81] Stefano Bruni, Marco Carnevale, and Alan Facchinetti. Active control of the pantograph articulated frame to reduce contact force fluctuations in the low frequency range. In *13th Mini Conference on Vehicle System Dynamics, Identification and Anomalies (VSDIA 2012)*, pages 237–244, 2012.

[82] Giuseppe Bucca, Marco Carnevale, Andrea Collina, and Alan Facchinetti. An active control strategy for multiple pantograph collection. In *23rd International Symposium on Dynamics of Vehicles on Roads and Tracks (IAVSD2013)*, pages 1–10, 2013.

[83] G Galeotti, M Galanti, S Magrini, and P Toni. Servo actuated railway pantograph for high-speed running with constant contact force. *Proceedings of the Institution of Mechanical Engineers, Part F: Journal of Rail and Rapid Transit*, 207(1):37–49, 1993.

[84] Benedetto Allotta, Luca Pugi, and Fabio Bartolini. Design and experimental results of an active suspension system for a high-speed pantograph. *IEEE/ASME Transactions on mechatronics*, 13(5):548–557, 2008.

[85] Andrea Collina, Alan Facchinetti, F Fossati, and Ferruccio Resta. An application of active control to the collector of an high-speed pantograph: Simulation and laboratory

tests. In *Proceedings of the 44th IEEE Conference on Decision and Control*, pages 4602–4609. IEEE, 2005.

[86] Aldo Balestrino, Ottorino Bruno, Alberto Landi, and Luca Sani. Innovative solutions for overhead catenary-pantograph system: wire actuated control and observed contact force. *Vehicle System Dynamics*, 33(2):69–89, 2000.

[87] Alessandro Pisano and Elio Usai. Contact force regulation in wire-actuated pantographs via variable structure control and frequency-domain techniques. *International Journal of Control*, 81(11):1747–1762, 2008.

[88] Andrea Collina, Alan Facchinetti, and Ferruccio Resta. A feasibility study of an aerodynamic control for a high speed pantograph. In *2007 IEEE/ASME international conference on advanced intelligent mechatronics*, pages 1–6. IEEE, 2007.

[89] RAIB. Accident involving a pantograph and the overhead line near Littleport, Cambridgeshire 5 January 2012. Report 06/2013 v2. Technical report, RAIB, Derby, 2014.

[90] Yongming Yao, Ning Zhou, Dong Zou, Guiming Mei, and Weihua Zhang. Collision dynamics analysis of lifting the pantograph. *Proceedings of the Institution of Mechanical Engineers, Part F: Journal of Rail and Rapid Transit*, page 0954409720943397, 2020.

[91] Guangning Wu, Jie Wu, Wenfu Wei, Yue Zhou, Zefeng Yang, and Guoqiang Gao. Characteristics of the sliding electric contact of pantograph/contact wire systems in electric railways. *Energies*, 11(1):17, 2018.

[92] J.A Williams. *Engineering Tribology*. Oxford University Press, Oxford, 1994.

[93] F J Gonzalez, J A Chover, B Suarez, and M Vazquez. Dynamic analysis using finite elements to calculate the critical wear section of the contact wire in suburban railway overhead conductor rails. *Proceedings of the Institution of Mechanical Engineers, Part F: Journal of Rail and Rapid Transit*, 222(2):145–157, March 2008.

[94] Takayuki Usuda. Estimation of wear and strain of contact wire using contact force of pantograph. *Quarterly Report of RTRI*, 48(3):170–175, 2007.

[95] D Klapas, F A Benson, R Hackam, and P R Evison. Wear in simulated railway overhead current collection systems. *Wear*, 126(2):167–190, 1988.

[96] Rafael R Manory and Norm Grady. Wear of railway contact wires against current collector materials. *Wear*, 215(1-2):146–155, 1998.

[97] S G Jia, P Liu, F Z Ren, B H Tian, M S Zheng, and G S Zhou. Sliding wear behavior of copper alloy contact wire against copper-based strip for high-speed electrified railways. *Wear*, 262(7):772–777, 2007.

[98] Song Xiao, Yuanpei Luo, Jingchi Wu, Can Zhang, Yang Rao, Guangning Wu, and Jan Sykulski. Multi-physics analysis of a novel circular pantograph catenary system for high-speed trains. *COMPEL-The international journal for computation and mathematics in electrical and electronic engineering*, 2020.

[99] Tobais Larrson and Lars Drugge. Dynamic behaviour of pantographs due to different wear situations. *Computers in Railways VI*, 37, 1998.

[100] Giuseppe Bucca, Andrea Collina, and Ezio Tanzi. Experimental analysis of the influence of the electrical arc on the wear rate of contact strip and contact wire in ac system. In *Advances in Italian mechanism science*, pages 449–456. Springer, 2017.

[101] A procedure for the wear prediction of collector strip and contact wire in pantograph–catenary system. *Wear*, 266(1-2):46–59, January 2009.

[102] Giuseppe Bucca and Andrea Collina. Electromechanical interaction between carbon-based pantograph strip and copper contact wire: A heuristic wear model. *Tribology International*, 92:47–56, 2015.

[103] T Ding, G X Chen, J Bu, and W H Zhang. Effect of temperature and arc discharge on friction and wear behaviours of carbon strip/copper contact wire in pantograph–catenary systems. *Wear*, 271(9-10):1629–1636, 2011.

[104] Shunichi Kubo and Koji Kato. Effect of arc discharge on the wear rate and wear mode transition of a copper-impregnated metallized carbon contact strip sliding against a copper disk. *Tribology International*, 32(7):367–378, 1999.

[105] Hiroki Nagasawa and Koji Kato. Wear mechanism of copper alloy wire sliding against iron-base strip under electric current. *Wear*, 216(2):179–183, 1998.

[106] A Tuissi, Paola Bassani, Riccardo Casati, M Bocciolone, Andrea Collina, Marco Carnevale, A Lo Conte, and Barbara Previtali. Application of SMA composites in

the collectors of the railway pantograph for the Italian high-speed train. *Journal of materials engineering and performance*, 18(5-6):612–619, 2009.

[107] Stefano Bruni, Giuseppe Bucca, Andrea Collina, Alan Facchinetti, and Stefano Melzi. Pantograph-catenary dynamic interaction in the medium-high frequency range. In *18. IAVSD Symposium*, volume 41, pages 697–706, 2004.

[108] Siripong Daocharoenporn, Mongkol Mongkolwongrojn, Shubhankar Kulkarni, and Ahmed A Shabana. Pantograph/Catenary Wear Using Multibody System Dynamic Algorithms. In *ASME/IEEE Joint Rail Conference*, volume 83587, page V001T01A002. American Society of Mechanical Engineers, 2020.

[109] Stefano Derosa, Petter Nåvik, Andrea Collina, Giuseppe Bucca, and Anders Rønnquist. A heuristic wear model for the contact strip and contact wire in pantograph – Catenary interaction for railway operations under 15 kV 16.67 Hz AC systems. *Wear*, 456-457:203401, 2020.

[110] H J Yang, G X Chen, G Q Gao, G N Wu, and W H Zhang. Experimental research on the friction and wear properties of a contact strip of a pantograph–catenary system at the sliding speed of 350km/h with electric current. *Wear*, 332-333:949–955, 2015.

[111] Wenping Chu and Yang Song. Study on Dynamic Interaction of Railway Pantograph–Catenary Including Reattachment Momentum Impact. *Vibration*, 3(1):18–33, 2020.

[112] Shunichi Kubo and Koji Kato. Effect of arc discharge on wear rate of Cu-impregnated carbon strip in unlubricated sliding against Cu trolley under electric current. *Wear*, 216(2):172–178, April 1998.

[113] O Bruno, Alberto Landi, M Papi, and Luca Sani. Phototube sensor for monitoring the quality of current collection on overhead electrified railways. *Proceedings of the institution of mechanical engineers, part f: Journal of rail and rapid transit*, 215(3):231–241, 2001.

[114] Sami Barmada, Alberto Landi, M Papi, and Luca Sani. Wavelet multiresolution analysis for monitoring the occurrence of arcing on overhead electrified railways. *Proceedings of the Institution of Mechanical Engineers, Part F: Journal of Rail and Rapid Transit*, 217(3):177–187, 2003.

[115] P Masini, M Papi, and G Puliatti. Virtual acquisition system for experimentation in'pantograph-catenary interaction'. In *The 1998 6 th International Conference on Computer Aided Design, Manufacture and Operation in the Railway and Other Advanced Mass Transit Systems*, pages 827–836, 1998.

[116] Z Yang, P Xu, W Wei, G Gao, N Zhou, and G Wu. Influence of the Crosswind on the Pantograph Arcing Dynamics. *IEEE Transactions on Plasma Science*, 48(8):2822–2830, 2020.

[117] Mitsuo Aboshi and Katsushi Manabe. Analyses of contact force fluctuation between catenary and pantograph. *Quarterly Report of RTRI*, 41(4):182–187, 2000.

[118] Mitsuo Aboshi. Precise measurement and estimation method for overhead contact line unevenness. *IJTIA*, 124(9):871–877, 2004.

[119] Weihua Zhang, Guiming Mei, Xuejie Wu, and Zhiyun Shen. Hybrid simulation of dynamics for the pantograph-catenary system. *Vehicle System Dynamics*, 38(6):393–414, 2002.

[120] Olivier Vo Van, Jean-Pierre Massat, Christophe Laurent, and Etienne Balmes. Introduction of variability into pantograph–catenary dynamic simulations. *Vehicle system dynamics*, 52(10):1254–1269, 2014.

[121] Y Song, Z Liu, A Rxnnquist, P Navik, and Z Liu. Contact Wire Irregularity Stochastics and Effect on High-speed Railway Pantograph-Catenary Interactions. *IEEE Transactions on Instrumentation and Measurement*, page 1, 2020.

[122] Yang Song, Pedro Antunes, Joao Pombo, and Zhigang Liu. A methodology to study high-speed pantograph-catenary interaction with realistic contact wire irregularities. *Mechanism and Machine Theory*, 152:103940, 2020.

[123] Santiago Gregori, Manuel Tur, José Enrique Tarancón, and Francisco Javier Fuenmayor. Stochastic Monte Carlo simulations of the pantograph–catenary dynamic interaction to allow for uncertainties introduced during catenary installation. *Vehicle System Dynamics*, 57(4):471–492, April 2019.

[124] Y Song, Z Liu, and X Lu. Dynamic Performance of High-Speed Railway Overhead Contact Line Interacting With Pantograph Considering Local Dropper Defect. *IEEE Transactions on Vehicular Technology*, 69(6):5958–5967, 2020.

[125] Jean Pierre Massat, T M L Nguyen Tajan, Habibou Maitournam, and Etienne Balmès. Fatigue analysis of catenary contact wires for high speed trains. In *9 th World Congress on Railway Research (Lille, France, 22-26 may 2011)*, pages 1–11, 2011.

[126] Guo Zhen, Yongseok Kim, Li Haochuang, Jae-Mean Koo, Chang-Sung Seok, Kiwon Lee, and Sam-Young Kwon. Bending fatigue life evaluation of Cu-Mg alloy contact wire. *International journal of precision engineering and manufacturing*, 15(7):1331–1335, 2014.

[127] Pierpaolo Boffi, Gianluca Cattaneo, Leonardo Amoriello, Angelo Barberis, Giuseppe Bucca, Marco F Bocciolone, Andrea Collina, and Mario Martinelli. Optical fiber sensors to measure collector performance in the pantograph-catenary interaction. *IEEE Sensors Journal*, 9(6):635–640, 2009.

[128] Marco Carnevale and Andrea Collina. Processing of collector acceleration data for condition-based monitoring of overhead lines. *Proceedings of the Institution of Mechanical Engineers, Part F: Journal of Rail and Rapid Transit*, 230(2):472–485, 2016.

[129] Alberto Landi, L Menconi, and Luca Sani. Hough transform and thermo-vision for monitoring pantograph-catenary system. *Proceedings of the Institution of Mechanical Engineers, Part F: Journal of Rail and Rapid Transit*, 220(4):435–447, 2006.

[130] Kyung-Min Na, Kiwon Lee, Hyungchul Kim, Chul Jin Cho, Wonseok Choi, and Young Park. Implementation of Image Processing in Studying Contact Conditions of Overhead Contact Line-Pantograph at 400 km/h. *Journal of Electrical Engineering & Technology*, 15(2):989–995, 2020.

[131] X Yu and H Su. Pantograph Arc Detection of Urban Rail Based on Photoelectric Conversion Mechanism. *IEEE Access*, 8:14489–14499, 2020.

[132] Petter Nåvik, Stefano Derosa, and Anders Rønnquist. Development of an index for quantification of structural dynamic response in a railway catenary section. *Engineering Structures*, 222:111154, 2020.

[133] Stefano Derosa, Petter Nåvik, Andrea Collina, and Anders Rønnquist. Railway catenary tension force monitoring via the analysis of wave propagation in cables. *Proceedings of the Institution of Mechanical Engineers, Part F: Journal of Rail and Rapid Transit*, page 0954409720941724, July 2020.

[134] M Bocciolone, Ferruccio Resta, D Rocchi, A Tosi, and A Collina. Pantograph aerodynamic effects on the pantograph–catenary interaction. *Vehicle System Dynamics*, 44(sup1):560–570, 2006.

[135] J Pombo, J Ambrósio, M Pereira, F Rauter, A Collina, and A Facchinetti. Influence of the aerodynamic forces on the pantograph–catenary system for high-speed trains. *Vehicle System Dynamics*, 47(11):1327–1347, 2009.

[136] S Pimputkar. The aerodynamic characteristics of pantographs (IM-AERO-025). Technical report, British Rail Research, Derby, UK, 1971.

[137] M Carnevale, A Facchinetti, F Robustelli, and D Rocchi. Unsteady aerodynamic forces on a railway pantograph and their influence on pantograph-catenary dynamic interaction. In *25th International Symposium on Dynamics of Vehicles on Roads and Tracks (IAVSD 2017)*, volume 2, pages 1259–1266. CRC Press-Taylor & Francis group, 2018.

[138] Q Lv, R Li, and S Wang. The effect of the working height of pantographs on pantograph-catenary dynamic performance. In *Proceedings of the second international conference on railway technology: research, development and maintenance, Ajaccio, Corsica, France*, pages 8–11, 2014.

[139] Marco Carnevale, Alan Facchinetti, Luca Maggiori, and Daniele Rocchi. Computational fluid dynamics as a means of assessing the influence of aerodynamic forces on the mean contact force acting on a pantograph. *Proceedings of the Institution of Mechanical Engineers, Part F: Journal of Rail and Rapid Transit*, 230(7):1698–1713, 2016.

[140] D.W Peacock. Wind tunnel tests on an AEI crossed-arm pantograph with modified light-weight head (IM-AERO-069). Technical report, British Rail Research, Derby, UK, 1973.

[141] Liang Zhang, Jiye Zhang, Tian Li, and Weihua Zhang. Influence of pantograph fixing position on aerodynamic characteristics of high-speed trains. *Journal of Modern Transportation*, 25(1):34–39, 2017.

[142] P. R Rigby and R. G Gawthorpe. Wind tunnel measurements to compare the aerodynamic uplifts of the GEC and AMBR 1 pantographs. Technical report, British Rail Research, Derby, UK, 1979.

[143] Ruiping Li, Weihua Zhang, Zhou Ning, Binbin Liu, Dong Zou, and Wei Liu. Influence of a high-speed train passing through a tunnel on pantograph aerodynamics and pantograph–catenary interaction. *Proceedings of the Institution of Mechanical Engineers, Part F: Journal of Rail and Rapid Transit*, 231(2):198–210, 2016.

[144] S Meynen, H Verma, P Hagedorn, and M Schäfer. On the numerical simulation of vortex-induced vibrations of oscillating conductors. *Journal of Fluids and Structures*, 21(1):41–48, 2005.

[145] Marco Carnevale, Alan Facchinetti, and Daniele Rocchi. Assessing aerodynamic effects on a railway pantograph by means of computational fluid dynamics. In *Railways 2016-The Third International Conference on Railway Technology: Research, Development and Maintenance*, pages 1–15, 2016.

[146] J Lee and W Cho. Prediction of low-speed aerodynamic load and aeroacoustic noise around simplified panhead section model. *Proceedings of the Institution of Mechanical Engineers, Part F: Journal of Rail and Rapid Transit*, 222(4):423–431, 2008.

[147] Yeongbin Lee, Joohyun Rho, Minho Kwak, Jaeho Lee, Kyuhong Kim, and Dongho Lee. Aerodynamic characteristics of high speed train pantograph with the optimized panhead shape. In *International Conference on FLUID MECHANICS and Aerodynamics*, 2009.

[148] Mitsuru Ikeda and Takeshi Mitsumoji. Numerical estimation of aerodynamic interference between panhead and articulated frame. *Quarterly Report of RTRI*, 50(4):227–232, 2009.

[149] C Noger, J C Patrat, J Peube, and J L Peube. Aeroacoustical study of the TGV pantograph recess. *Journal of sound and vibration*, 231(3):563–575, 2000.

[150] Mitsuru Ikeda and Katsushi Manabe. Development of low noise pantograph with passive lift suppression mechanism of panhead. *Quarterly Report of RTRI*, 41(4):177–181, 2000.

[151] Masahiro Suzuki, Mitsuru Ikeda, and Tatsuya Koyama. Flow control on pantograph with air intake and outlet. *Quarterly Report of RTRI*, 48(4):236–239, 2007.

[152] Di-Long Guo, Shuan-Bao Yao, Chen-Hui Liu, and Guo-Wei Yang. Unsteady aerodynamic characteristics of high-speed pantograph. *Journal of the China Railway Society*, 34(11):16–21, 2012.

[153] Takehisa Takaishi and Mitsuru Ikeda. Experimental method for wind tunnel tests to simulate turbulent flow on the roof of high-speed trains. *Quarterly Report of RTRI*, 53(3):167–172, 2012.

[154] Remi Gregoire, ANDREA Collina, FERRUCCIO Resta, and DANIELE Rocchi. Some considerations on the aerodynamics of high speed pantograph: cfd and wind tunnel tests. In *BBAA VI International Colloquium on: Bluff Bodies Aerodynamics & Applications. Milano, Italy*, 2008.

[155] Marco Carnevale, Alan Facchinetti, and Daniele Rocchi. Procedure to assess the role of railway pantograph components in generating the aerodynamic uplift. *Journal of Wind Engineering and Industrial Aerodynamics*, 160:16–29, 2017.

[156] MARCO FRANCESCO Bocciolone, Giuseppe Bucca, Andrea Collina, and Lorenzo Comolli. Optical sensors for the analysis of pantograph-catenary interaction. 2016.

[157] Shuanbao Yao, Dilong Guo, and Guowei Yang. The influence of pantograph aerodynamic characteristics caused by its shroud. In *Proceedings of the 1st International Workshop on High-Speed and Intercity Railways*, pages 41–52. Springer, 2012.

[158] Jianbin Luo, Zhigang Yang, Yu Chen, and Zhe Gao. Numerical research on aerodynamic characteristic optimization of pantograph fixing place on high speed train. In *2009 2nd International Conference on Power Electronics and Intelligent Transportation System (PEITS)*, volume 1, pages 94–97. IEEE, 2009.

[159] Takeshi Mitsumoji, Yuichi Sato, Mitsuru Ikeda, Takeshi Sueki, and Koji Fukagata. A basic study on aerodynamic noise reduction techniques for a pantograph head using plasma actuators. *Quarterly Report of RTRI*, 55(3):184–189, 2014.

[160] Mitsuru Ikeda and Takeshi Mitsumoji. Evaluation method of low-frequency aeroacoustic noise source structure generated by Shinkansen pantograph. *Quarterly Report of RTRI*, 49(3):184–190, 2008.

[161] R Broomfield. Behaviour of MK. IIIA overhead line contact system in wind. Initial results of measurements on an exposed section of line North of Tebay (TM-ETR-006). Technical report, British Rail Research, Derby, UK, 1973.

[162] G Poetsch, J Evans, R Meisinger, W KortÜM, W Baldauf, A Veitl, and J Wallaschek. Pantograph/Catenary Dynamics and Control. *Vehicle System Dynamics*, 28(2-3):159–195, 1997.

[163] R. K Cooper. ASSESSMENT OF THE WIND EFFFCTS IN RELATION TO THE DEWIREMENIS ON OVERHEAD LINE EQUIPMENT, WML, DEXXBFB 1974 - JANUARY 1975. Technical report, British Rail Research, Derby, UK, 1975.

[164] T Johnson. A probabilistic assessment of blow-off dewirement and associated alleviation methods. Technical report, British Rail Research, Derby, UK, 1985.

[165] J. R Evans, T Johnson, and R. A Clark. Dewirement Dynamics - Final Report. Technical report, British Rail Research, Derby, UK, 1990.

[166] Song Yan. Influence of high-speed railway catenary buffeting on pantographcatenary current collection under fluctuating wind. 2014.

[167] Hooman Keyhan, Ghyslaine McClure, and Wagdi G Habashi. Dynamic analysis of an overhead transmission line subject to gusty wind loading predicted by wind–conductor interaction. *Computers & Structures*, 122:135–144, 2013.

[168] Vanessa Gonçalves Guedes and Carlos Frederico Trotta Matt. LITERATURE REVIEW ON VORTEX-INDUCED VIBRATIONS AROUND CIRCULAR CYLINDERS FOR FUTURE INVESTIGATIONS ON WIND-INDUCED VIBRATIONS AROUND TRANSMISSION LINE CONDUCTORS. In *20th International Congress of Mechanical Engineering*, Gramado, 2009.

[169] Allan Larsen and Guy L Larose. Dynamic wind effects on suspension and cable-stayed bridges. *Journal of Sound and Vibration*, 334:2–28, 2015.

[170] G Stockbridge. US 1,675,391 A, 1925.

[171] M Markiewicz. OPTIMUM DYNAMIC CHARACTERISTICS OF STOCKBRIDGE DAMPERS FOR DEAD-END SPANS. *Journal of Sound and Vibration*, 188(2):243–256, 1995.

[172] Friedrich Kiessling. *High Voltage Engineering and Testing*. IET, 2001.

[173] M T Stickland, T J Scanlon, I A Craighead, and J Fernandez. An investigation into the mechanical damping characteristics of catenary contact wires and their effect on aerodynamic galloping instability. *Proceedings of the Institution of Mechanical Engineers, Part F: Journal of Rail and Rapid Transit*, 217(2):63–71, 2003.

[174] M T Stickland and T J Scanlon. An investigation into the aerodynamic characteristics of catenary contact wires in a cross-wind. *Proceedings of the Institution of Mechanical Engineers, Part F: Journal of Rail and Rapid Transit*, 215(4):311–318, 2001.

[175] Guo Chen, Yiren Yang, Yang Yang, and Peng Li. Study on Galloping Oscillation of Iced Catenary System under Cross Winds. *Shock and Vibration*, 2017:1634292, 2017.

[176] Yang Song, Zhigang Liu, Hongrui Wang, Jing Zhang, Xiaobing Lu, and Fuchuan Duan. Analysis of the galloping behaviour of an electrified railway overhead contact line using the non-linear finite element method. *Proceedings of the Institution of Mechanical Engineers, Part F: Journal of Rail and Rapid Transit*, page 0954409718769751, April 2018.

[177] Fritjof Nilsson, Ali Moyassari, Ángela Bautista, Abraham Castro, Ignacio Arbeloa, Mikael Järn, Urban Lundgren, Jan Welinder, and Kenth Johansson. Modelling anti-icing of railway overhead catenary wires by resistive heating. *International Journal of Heat and Mass Transfer*, 143:118505, 2019.

[178] Sergio Avila Sanchez, Oscar López García, and José Meseguer Ruiz. A simplified approach to determine aerodynamic damping of railway overheads. 2011.

[179] Galloping stability of triangular cross-sectional bodies: A systematic approach. *Journal of Wind Engineering & Industrial Aerodynamics*, 95(9-11):928–940, 2007.

[180] Dongli Song, Yanan Jiang, and Weihua Zhang. Dynamic performance of a pantograph–catenary system with consideration of the contact surface. *Proceedings of the Institution of Mechanical En1. RYDER, a. High speed rail [online]. 2012. London. Available from: http://linkinghub.elsevier.com/retrieve/pii/S0966692312000658gineers, Part F: Journal of Rail and Rapid Transit*, page 0954409716664934, 2016.

[181] B Diedrichs, M Sima, A Orellano, and H Tengstrand. Crosswind stability of a high-speed train on a high embankment. *Proceedings of the Institution of Mechanical Engineers, Part F: Journal of Rail and Rapid Transit*, 221(2):205–225, March 2007.

[182] B Diedrichs, M Berg, S Stichel, and S Krajnović. Vehicle dynamics of a high-speed passenger car due to aerodynamics inside tunnels. *Proceedings of the Institution of Mechanical Engineers, Part F: Journal of Rail and Rapid Transit*, 221(4):527–545, July 2007.

[183] Wenlin Wang, Zirong Zhou, Weihua Zhang, and Simon Iwnicki. A new nonlinear displacement-dependent parametric model of a high-speed rail pantograph hydraulic damper. *Vehicle System Dynamics*, 58(2):272–289, February 2020.

[184] Li Yongle, Hu Peng, Cai C S., Zhang Mingjin, and Qiang Shizhong. Wind Tunnel Study of a Sudden Change of Train Wind Loads due to the Wind Shielding Effects of Bridge Towers and Passing Trains. *Journal of Engineering Mechanics*, 139(9):1249–1259, September 2013.

[185] Tian Li, Jiye Zhang, and Weihua Zhang. An improved algorithm for fluid-structure interaction of high-speed trains under crosswind. *Journal of Modern Transportation*, 19(2):75–81, 2011.

[186] S Avila-Sanchez, O Lopez-Garcia, A Cuerva, and J Meseguer. Characterisation of cross-flow above a railway bridge equipped with solid windbreaks. *Engineering Structures*, 126:133–146, 2016.

[187] D S Farr, H C Hall, and A L Williams. A dynamic model for studying the behaviour of the overhead equipment used in electric railway traction. *Proceedings of the IEE - Part A: Power Engineering*, 108(41):421–434, 1961.

[188] Katsushi MANABE. High-Speed Contact Performance of a Catenary-Pantograph System : An Experimental Study Using a Dynamically Scaled Model. *JSME international journal. Ser. 3, Vibration, control engineering, engineering for industry*, 32(2):200–205, 1989.

[189] Mitsuru Ikeda, Kazushige Yoshida, and Masahiro Suzuki. A flow control technique utilizing air blowing to modify the aerodynamic characteristics of pantograph for high-speed train. *Journal of Mechanical Systems for Transportation and Logistics*, 1(3):264–271, 2008.

[190] Petter Nåvik, Anders Rønnquist, and Sebastian Stichel. The use of dynamic response to evaluate and improve the optimization of existing soft railway catenary systems for higher speeds. *Proceedings of the Institution of Mechanical Engineers, Part F: Journal of Rail and Rapid Transit*, 230(4):1388–1396, September 2015.

[191] Jorge Ambrósio, Joao Pombo, and Manuel Pereira. Optimization of high-speed railway pantographs for improving pantograph-catenary contact. *Theoretical and Applied Mechanics Letters*, 3(1):13006, 2013.

[192] R B Morris. Second Paper: The Application of an Analogue Computer to a Problem of Pantograph and Overhead Line Dynamics. *Proceedings of the Institution of Mechanical Engineers*, 179(1):782–808, June 1964.

[193] G Gilbert and H E H Davies. Pantograph motion on a nearly uniform railway overhead line. *Proceedings of the Institution of Electrical Engineers*, 113(3):485–492, 1966.

[194] T Dahlberg. Moving force on an axially loaded beam—with applications to a railway overhead contact wire. *Vehicle System Dynamics*, 44(8):631–644, 2006.

[195] M Arnold and B Simeon. Pantograph and catenary dynamics: A benchmark problem and its numerical solution. *Applied Numerical Mathematics*, 34(4):345–362, 2000.

[196] Lars Finner, Gero Poetsch, Bernhard Sarnes, and Michael Kolbe. Program for catenary–pantograph analysis, PrOSA statement of methods and validation according EN 50318. *Vehicle System Dynamics*, 53(3):305–313, March 2015.

[197] Sung Yong Park, Byung Uk Jeon, Jang Moo Lee, and Yong Hyeon Cho. Measurement of low-frequency wave propagation in a railway contact wire with dispersive characteristics using wavelet transform. In *Key engineering materials*, volume 321, pages 1609–1615. Trans Tech Publ, 2006.

[198] S.J Yang. Preliminary investigation of the wave propagation characteristics of overhead equipment (IM-ETR-010). Technical report, British Rail Research, Derby, UK, 1972.

[199] Dong Zou, Wei Hua Zhang, Rui Ping Li, Ning Zhou, and Gui Ming Mei. Determining damping characteristics of railway-overhead-wire system for finite-element analysis. *Vehicle System Dynamics*, 54(7):902–917, 2016.

[200] Kyohei Nagao and Arata Masuda. Transient wave propagation analysis of a pantograph-catenary system. In *Journal of Physics: Conference Series*, volume 744, page 12086. IOP Publishing, 2016.

[201] Takahiro Fukui, Toshihiko Asami, and Tomohiko Ise. Analysis of Wave Propagation in Overhead Contact Wire of Trains Using the Transfer Matrix Method. In *ASME 2013 Pressure Vessels and Piping Conference*, pages V008T08A047–V008T08A047. American Society of Mechanical Engineers.

[202] Olivier Vo Van, Jean-Pierre Massat, and Etienne Balmes. Waves, modes and properties with a major impact on dynamic pantograph-catenary interaction. *Journal of Sound and Vibration*, 402:51–69, 2017.

[203] T X Wu and M J Brennan. Dynamic stiffness of a railway overhead wire system and its effect on pantograph–catenary system dynamics. *Journal of sound and vibration*, 219(3):483–502, 1999.

[204] J Gil, S Gregori, M Tur, and F J Fuenmayor. Analytical model of the pantograph–catenary dynamic interaction and comparison with numerical simulations. *Vehicle System Dynamics*, pages 1–24, August 2020.

[205] G Galeotti and P Toni. Overhead contact line elasticity optimization for railway high speed running. *Computers & structures*, 65(6):975–983, 1997.

[206] S Levy, J A Bain, and E J Leclerc. Railway Overhead Contact Systems, Catenary-Pantograph Dynamics for Power Collection at High Speeds. *Journal of Engineering for Industry*, 90(4):692–699, November 1968.

[207] R J Gostling and A E W Hobbs. The Interaction of Pantograph and Overhead Equipment: Practical Applications of a New Theoretical Method. *Proceedings of the Institution of Mechanical Engineers, Part C: Journal of Mechanical Engineering Science*, 197(1):61–69, January 1983.

[208] G Mei. *The dynamic study of pantograph/catenary system*. PhD thesis, Southwest Jiaotong University, 2010.

[209] Weihua Zhang, Yi Liu, and Guiming Mei. Evaluation of the coupled dynamical response of a pantograph—catenary system: contact force and stresses. *vehicle system dynamics*, 44(8):645–658, 2006.

[210] W H Zhang, G M Mei, X J Wu, and L Q Chen. A study on dynamic behaviour of pantographs by using hybrid simulation method. *Proceedings of the Institution of Mechanical Engineers, Part F: Journal of Rail and Rapid Transit*, 219(3):189–199, 2005.

[211] Jorge Ambrósio, João Pombo, Pedro Antunes, and Manuel Pereira. PantoCat statement of method. *Vehicle System Dynamics*, 53(3):314–328, March 2015.

[212] M Tur, L Baeza, F J Fuenmayor, and E García. PACDIN statement of methods. *Vehicle System Dynamics*, 53(3):402–411, 2015.

[213] O Lopez-Garcia, A Carnicero, and V Torres. Computation of the initial equilibrium of railway overheads based on the catenary equation. *Engineering structures*, 28(10):1387–1394, 2006.

[214] Sung Pil Jung, Young Guk Kim, Jin Sung Paik, and Tae Won Park. Estimation of dynamic contact force between a pantograph and catenary using the finite element method. *Journal of computational and nonlinear dynamics*, 7(4), 2012.

[215] Yeongbin Lee, Jin-sung Paik, Minho Kwak, Jinsun Yoo, Kyu Hong Kim, Dongho Lee, and Hyeok-Bin Kwon. Analysis and comparison of experimental results both of wind tunnel test and running test for HEMU-400X pantograph. In *ASME/IEEE Joint Rail Conference*, volume 44656, pages 169–172. American Society of Mechanical Engineers, 2012.

[216] Jong-Hwi Seo, Hiroyuki Sugiyama, and Ahmed A Shabana. Three-dimensional large deformation analysis of the multibody pantograph/catenary systems. *Nonlinear Dynamics*, 42(2):199–215, 2005.

[217] Jong-Hwi Seo, Seok-Won Kim, Il-Ho Jung, Tae-Won Park, Jin-Yong Mok, Young-Guk Kim, and Jang-Bom Chai. Dynamic analysis of a pantograph–catenary system using absolute nodal coordinates. *Vehicle System Dynamics*, 44(8):615–630, August 2006.

[218] M. Tur, E. García, L. Baeza, and F.J. J Fuenmayor. A 3D absolute nodal coordinate finite element model to compute the initial configuration of a railway catenary. *Engineering Structures*, 71:234–243, July 2014.

[219] Shubhankar Kulkarni, Carmine M Pappalardo, and Ahmed A Shabana. Pantograph/-catenary contact formulations. *Journal of Vibration and Acoustics*, 139(1), 2017.

[220] Yang Song, Zhigang Liu, Hongrui Wang, Xiaobing Lu, and Jing Zhang. Nonlinear modelling of high-speed catenary based on analytical expressions of cable and truss elements. *Vehicle System Dynamics*, 53(10):1455–1479, 2015.

[221] Jean-Pierre Massat, Etienne Balmes, Jean-Philippe Bianchi, and Guido Van Kalsbeek. OSCAR statement of methods. *Vehicle System Dynamics*, 53(3):370–379, March 2015.

[222] C Sánchez-Rebollo, A Carnicero, and J R Jiménez-Octavio. CANDY statement of methods. *Vehicle System Dynamics*, 53(3):392–401, 2015.

[223] Dominique Habault. Chapter 6 - Boundary Integral Equation Methods - Numerical Techniques. pages 189–202. Academic Press, London, 1999.

[224] Daniele Boffi, Franco Brezzi, and Michel Fortin. Variational Formulations and Finite Element Methods BT - Mixed Finite Element Methods and Applications. pages 1–46. Springer Berlin Heidelberg, Berlin, Heidelberg, 2013.

[225] Jorge Ambrósio, João Pombo, Frederico Rauter, and Manuel Pereira. A memory based communication in the co-simulation of multibody and finite element codes for pantograph-catenary interaction simulation. In *Multibody dynamics*, pages 231–252. Springer, 2009.

[226] Frederico Grases Rauter, João Pombo, Jorge Ambrósio, Jérôme Chalansonnet, Adrien Bobillot, and Manuel Seabra Pereira. Contact model for the pantograph-catenary interaction. *Journal of System Design and Dynamics*, 1(3):447–457, 2007.

[227] Jorge Ambrósio, Joao Pombo, Manuel Pereira, Pedro Antunes, and António Mósca. A computational procedure for the dynamic analysis of the catenary-pantograph interaction in high-speed trains. *Journal of theoretical and applied mechanics*, 50(3):681–699, 2012.

[228] Jin-Hee Lee and Tae-Won Park. Development of a three-dimensional catenary model using cable elements based on absolute nodal coordinate formulation. *Journal of mechanical science and technology*, 26(12):3933–3941, 2012.

[229] Jin Hee Lee, Tae Won Park, Hyuck Keun Oh, and Young Guk Kim. Analysis of dynamic interaction between catenary and pantograph with experimental verification and performance evaluation in new high-speed line. *Vehicle System Dynamics*, 53(8):1117–1134, 2015.

[230] D García-Vallejo, J Mayo, J L Escalona, and J Dominguez. Efficient evaluation of the elastic forces and the Jacobian in the absolute nodal coordinate formulation. *Nonlinear Dynamics*, 35(4):313–329, 2004.

[231] M Oumri and A Rachid. A mathematical model for pantograph-catenary interaction. *Mathematical and Computer Modelling of Dynamical Systems*, 22(5):463–474, 2016.

[232] Yong Hyeon Cho. Numerical simulation of the dynamic responses of railway overhead contact lines to a moving pantograph, considering a nonlinear dropper. *Journal of Sound and Vibration*, 315(3):433–454, 2008.

[233] Jesús Ramón Jimenez-Octavio, A Carnicero, Cristina Sanchez-Rebollo, and M Such. A moving mesh method to deal with cable structures subjected to moving loads and

its application to the catenary–pantograph dynamic interaction. *Journal of Sound and Vibration*, 349:216–229, 2015.

[234] Yang Song, Zhigang Liu, Zhao Xu, and Jing Zhang. Developed moving mesh method for high-speed railway pantograph-catenary interaction based on nonlinear finite element procedure. *International Journal of Rail Transportation*, 7(3):173–190, July 2019.

[235] E. M Tuck. The effect of base movement on contact force and trajectory of a pantograph. Technical report, British Rail Research, Derby, UK, 1973.

[236] A Carnicero, J R Jimenez-Octavio, C Sanchez-Rebollo, A Ramos, and M Such. Influence of track irregularities in the catenary-pantograph dynamic interaction. *Journal of computational and nonlinear dynamics*, 7(4), 2012.

[237] João Pombo and Jorge Ambrósio. Environmental and track perturbations on multiple pantograph interaction with catenaries in high-speed trains. *Computers & Structures*, 124:88–101, 2013.

[238] Yongming Yao, Dong Zou, Ning Zhou, Guiming Mei, Jiangwen Wang, and Weihua Zhang. A study on the mechanism of vehicle body vibration affecting the dynamic interaction in the pantograph–catenary system. *Vehicle System Dynamics*, pages 1–20, April 2020.

[239] Pedro Antunes, Jorge Ambrósio, João Pombo, and Alan Facchinetti. A new methodology to study the pantograph–catenary dynamics in curved railway tracks. *Vehicle System Dynamics*, 58(3):425–452, March 2020.

[240] Stefano Bruni, Jorge Ambrosio, Alberto Carnicero, Yong Hyeon Cho, Lars Finner, Mitsuru Ikeda, Sam Young Kwon, Jean-Pierre Massat, Sebastian Stichel, Manuel Tur, and Weihua Zhang. The results of the pantograph–catenary interaction benchmark. *Vehicle System Dynamics*, 53(3):412–435, March 2015.

[241] Adam Beagles, David Fletcher, Matthew Peffers, Patric Mak, and Caroline Lowe. Validation of a new model for railway overhead line dynamics. *Proceedings of the ICE-Transport*, 169(5):339–349, 2016.

[242] Y Fujii. Computer Simulation for Dynamics of Overhead Catenery-Pantograph System. *Computers in Railways*, 1992.

[243] Andrea Collina and Stefano Bruni. Numerical simulation of pantograph-overhead equipment interaction. *Vehicle System Dynamics*, 38(4):261–291, 2002.

[244] O Lopez-Garcia, A Carnicero, and J L Marono. Influence of stiffness and contact modelling on catenary–pantograph system dynamics. *Journal of Sound and Vibration*, 299(4-5):806–821, 2007.

[245] Mitsuru Ikeda. 'Gasen-do FE'statement of methods. *Vehicle System Dynamics*, 53(3):357–369, 2015.

[246] Carmine M Pappalardo, Marco C De Simone, and Domenico Guida. Multibody modeling and nonlinear control of the pantograph/catenary system. *Archive of Applied Mechanics*, 89(8):1589–1626, 2019.

[247] Anna Kumaniecka and Michał Prącik. Modelling and identification of catenary-pantograph system. *Journal of Theoretical and Applied Mechanics; Vol 41, No 4 (2003)*, 41:887–901, 2003.

[248] S D Eppinger, D N O'Connor, W P Seering, and D N Wormley. Modeling and experimental evaluation of asymmetric pantograph dynamics. 1988.

[249] Steven Conway. Lump mass models for legacy pantographs on GB mainline (T1105). Technical report, Rail Safety and Standards Board, 2016.

[250] Chandrika P Vyasarayani, Thomas Uchida, Ashwin Carvalho, and John McPhee. Parameter identification in dynamic systems using the homotopy optimization approach. *Multibody System Dynamics*, 26(4):411–424, 2011.

[251] A Shabana. *Dynamics of Multibody Systems*. Cambridge University Press, 2 edition, 1998.

[252] E.J Haug. *Computer aided kinematics and dynamics of mechanical systems*. Allyn and Bacon, Boston, Massachusetts, 1989.

[253] João Pombo and Jorge A C Ambrósio. General Spatial Curve Joint for Rail Guided Vehicles: Kinematics and Dynamics. *Multibody System Dynamics*, 9(3):237–264, 2003.

[254] Firdaus E Udwadia and Robert E Kalaba. A new perspective on constrained motion. *Proceedings of the Royal Society of London. Series A: Mathematical and Physical Sciences*, 439(1906):407–410, November 1992.

[255] Petter Nåvik, Stefano Derosa, and Anders Rønnquist. On the use of experimental modal analysis for system identification of a railway pantograph. *International Journal of Rail Transportation*, pages 1–12, June 2020.

[256] Y Song, A Rannquist, and P Navik. Assessment of the High-frequency Response in the Railway Pantograph-Catenary Interaction Based on Numerical Simulation. *IEEE Transactions on Vehicular Technology*, page 1, 2020.

[257] H M Lankarani and P E Nikravesh. A contact force model with hysteresis damping for impact analysis of multibody systems. *Journal of mechanical Design*, 112(3):369–376, 1990.

[258] F R E Crossley. Coefficient of restitution interpreted as damping in vibroimpact. *Journal of Applied Mechanics, Transactions ASME*, 42, 1975.

[259] João Pombo and Jorge Ambrósio. Multiple Pantograph Interaction With Catenaries in High-Speed Trains. *Journal of Computational and Nonlinear Dynamics*, 7(4):41008, 2012.

[260] Yong Hyeon Cho, Jang Moo Lee, Sung Yong Park, and Eung Shin Lee. Robust measurement of damping ratios of a railway contact wire using wavelet transforms. In *Key Engineering Materials*, volume 321, pages 1629–1635. Trans Tech Publ, 2006.

[261] Petter Nåvik, Anders Rønnquist, and Sebastian Stichel. Identification of system damping in railway catenary wire systems from full-scale measurements. *Engineering Structures*, 113:71–78, 2016.

[262] John William Strutt Baron Rayleigh. *The theory of sound*, volume 2. Macmillan, 1896.

[263] Olivier VO VAN, Etienne BALMES, and Xavier LORANG. Damping characterization of a high speed train catenary. 2015.

[264] Jean Philippe Bianchi, Etienne Balmes, Guillaume Vermot Des Roches, and Adrien Bobillot. Using modal damping for full model transient analysis. Application to pantograph/catenary vibration. In *ISMA*, page 376, 2010.

[265] FERRUCCIO Resta, Alan Facchinetti, Andrea Collina, and Giuseppe Bucca. On the use of a hardware in the loop set-up for pantograph dynamics evaluation. *Vehicle System Dynamics*, 46(S1):1039–1052, 2008.

[266] Alan Facchinetti and Stefano Bruni. Hardware-in-the-loop hybrid simulation of pantograph–catenary interaction. *Journal of Sound and Vibration*, 331(12):2783–2797, 2012.

[267] S Gregori, M Tur, E Nadal, J V Aguado, F J Fuenmayor, and F Chinesta. Fast simulation of the pantograph–catenary dynamic interaction. *Finite Elements in Analysis and Design*, 129:1–13, 2017.

[268] Shigeyuki KOBAYASHI, Yoshitaka YAMASHITA, Takayuki USUDA, and David P STOTEN. Hybrid simulation testing of a pantograph-catenary system using a dynamically substructured system framework and a mdof catenary model. *Quarterly Report of RTRI*, 61(2):127–132, 2020.

[269] D P Stoten and R A Hyde. Adaptive control of dynamically substructured systems: the single-input single-output case. *Proceedings of the Institution of Mechanical Engineers, Part I: Journal of Systems and Control Engineering*, 220(2):63–79, 2006.

[270] S Gregori, M Tur, A Pedrosa, J E Tarancón, and F J Fuenmayor. A modal coordinate catenary model for the real-time simulation of the pantograph-catenary dynamic interaction. *Finite Elements in Analysis and Design*, 162:1–12, 2019.

[271] D Stoten, T Yamaguchi, and Y Yamashita. Dynamically substructured system testing for railway vehicle pantographs. In *J Phys Conf Ser*, volume 744, pages 1–7, 2016.

[272] Per-Anders Jönsson, Sebastian Stichel, and Cecilia Nilsson. CaPaSIM statement of methods. *Vehicle System Dynamics*, 53(3):341–346, March 2015.

[273] Jean-Pierre Massat, Christophe Laurent, Jean-Philippe Bianchi, and Etienne Balmès. Pantograph catenary dynamic optimisation based on advanced multibody and finite element co-simulation tools. *Vehicle System Dynamics*, 52(1):338–354, 2014.

[274] Xiong Zhang, Zhen Chen, and Yan Liu. Chapter 3 - The Material Point Method. pages 37–101. Academic Press, Oxford, 2017.

[275] D Sturge, D Sobotta, R Howell, A While, and J Lou. A hybrid actuator disc – Full rotor CFD methodology for modelling the effects of wind turbine wake interactions on performance. *Renewable Energy*, 80:525–537, 2015.

[276] Okeoghene Eboibi, Louis Angelo M Danao, and Robert J Howell. Experimental investigation of the influence of solidity on the performance and flow field aerodynamics of

vertical axis wind turbines at low Reynolds numbers. *Renewable Energy*, 92:474–483, 2016.

[277] A Goodworth. ATI Industrial Automation: F/T Sensor Nano17, 2017.

[278] B Mutlu Sumer and Jorgen Fredsoe. *Hydrodynamics Around Cylindrical Structures*, volume Volume 12. WORLD SCIENTIFIC, March 1997.

[279] Hermann Schlichting and Klaus Gersten. *Boundary-Layer Theory*. Springer Berlin Heidelberg, 7th edition, 1979.

[280] A Cengel Yunus and John M Cimbala. Fluid mechanics fundamentals and applications. *International Edition, McGraw Hill Publication*, 185201, 2006.

[281] Mehmet Ishak Yuce and Dalshad Ahmed Kareem. A Numerical Analysis of Fluid Flow Around Circular and Square Cylinders. *Journal AWWA*, 108(10):E546–E554, October 2016.

[282] R Courant, K Friedrichs, and H Lewy. On the Partial Difference Equations of Mathematical Physics. *IBM Journal of Research and Development*, 11(2):215–234, 1967.

[283] Furrer+Frey AG. *MAN008 - Series 1 Civil and Structural Engineering Manual*. London, 2.1 edition, 2015.

[284] John D Anderson. *Fundamentals of Aerodynamics*. McGraw Hill, 4th edition, 2007.

[285] Chris Bryan. Overhead Line Dynamic Performance - Using statistical design to aid computer simulation of Series 1 equipment. Technical report, Network Rail, Milton Keynes, 2014.

[286] Chris Bryan. Series 1 Old Dalby Test Results - Data processing summary of Brecknell Willis Pantograph tests. Technical report, Network Rail], Milton Keynes, 2014.

[287] BSI. BS EN 50318:2002: Railway applications - current collection systems - requirements for and validation of measurements of the dynamic interaction between pantograph and overhead contact line. Technical report, BSI, London, UK, 2012.

[288] George Costello. Mechanics of wire rope. Technical report, University of Illinois, Urbana-Champaign, 2003.

[289] W.G. Jiang, M.S. Yao, and J.M. Walton. A concise finite element model for simple straight wire rope strand. *International Journal of Mechanical Sciences*, 41(2):143–161, 1999.

[290] R. Judge, Z. Yang, S.W. Jones, and G. Beattie. Full 3d finite element modelling of spiral strand cables. *Construction and Building Materials*, 35:452–459, 2012.

[291] T Ding, G X Chen, X Wang, M H Zhu, W H Zhang, and W X Zhou. Friction and wear behavior of pure carbon strip sliding against copper contact wire under AC passage at high speeds. *Tribology International*, 44(4):437–444, 2011.

[292] Huijie Zhang, Lemin Sun, Yongzhen Zhang, and Bao Shangguan. The study of arc rate, friction, and wear performance of c/c composites in pantograph–catenary system. *Tribology Transactions*, 57(6):1157–1163, 2014.

[293] Guo Chen, Yiren Yang, and Yang Yang. Prediction of dynamic characteristics of a pantograph-catenary system using the displacement compatibility. *Journal of Vibroengineering*, 19(7):5405–5420, nov 2017.

[294] Farzad Vesali. Pantograph & catenary interaction: wave reflection at the end spans of a mechanical section and pantographs contact quality, 2019.

[295] Farzad Vesali, Mohammad Ali Rezvani, and Habibolah Molatefi. Simulation of the dynamic interaction of rail vehicle pantograph and catenary through a modal approach. *Archive of Applied Mechanics*, 90(7):1475–1496, 2020.

[296] Mitsuo Aboshi. Estimation Method of Contact Wire Strain based on Contact Force between Pantograph and Catenary. In *14th Railway Technology Union Symposium*, 2007.

[297] T Johnson. Strong; wind effects on railway operations — 16th October 1987. *Journal of Wind Engineering and Industrial Aerodynamics*, 60:251–266, 1996.

[298] Yang Song, Zhigang Liu, Hongrui Wang, Xiaobing Lu, and Jing Zhang. Nonlinear analysis of wind-induced vibration of high-speed railway catenary and its influence on pantograph–catenary interaction. *Vehicle System Dynamics*, 54(6):723–747, June 2016.

[299] Network Rail. NR/L2/CIV/072 Wind loading of Overhead Line Equipment and Structures. Technical report, Network RAIL, London, UK, 2015.

[300] J P D Hartog. Transmission Line Vibration Due to Sleet. *Transactions of the American Institute of Electrical Engineers*, 51(4):1074–1076, 1932.

[301] G.F Moore. *Electric cables handbook*. Blackwell Science, Oxford Malden, Massaschusetts, 1997.

[302] L C Pagnini, A Freda, and G Piccardo. Uncertainties in the evaluation of one degree-of-freedom galloping onset. *European Journal of Environmental and Civil Engineering*, 21(7-8):1043–1063, August 2017.

[303] BSI. BS 7884:1997 Copper and copper-cadmium stranded conductors for overhead electric traction and power transmission systems. Technical report, BSI, London, UK, 1997.

[304] J F Archard. Contact and Rubbing of Flat Surfaces. *Journal of Applied Physics*, 24(8):981–988, August 1953.

[305] Network Rail. Modernising the Great Western route, 2017.

[306] S J Watson, P Kritharas, and G J Hodgson. Wind speed variability across the UK between 1957 and 2011. *Wind Energy*, 18(1):21–42, January 2015.

[307] Eric Robinson and Michelle Cipullo. UK Windstorms and Climate Change An update to ABI Research Paper No 19, 2009. Technical report, AIR Worldwide, Boston, Massachusetts, 2009.

[308] T Johnson, M Osman, C Hutchinson, and D Johnson. Pantograph sway acceptance requirements and methodology - Summary report. Technical report, RSSB, London, UK, 2011.

[309] Richard Hewston and Stephen R Dorling. An analysis of observed daily maximum wind gusts in the UK. *Journal of Wind Engineering and Industrial Aerodynamics*, 99(8):845–856, 2011.

[310] S Hoerner. *Fluid-Dynamic Drag: Practical Information on Aerodynamic Drag and Hydrodynamic Resistance*. Hoerner Fluid Dynamics, Bakersfield, 2 edition, 1992.

[311] Koray Bektas. Glacier express in Switzerland- Landwasser Viaduct ID: 1197898327.

[312] L Kirkwood, L Giuntini, E Shehab, and P Baguley. Development of a Whole Life Cycle Cost Model for Electrification options on the UK Rail System. *Procedia CIRP*, 47:1–5, 2016.

[313] Michael Reno. HTETCO Catenary Wire Used in Overhead Catenary Systems for Light Rail Construction. Technical report, Atlanta, USA, 2018.

Appendix A

Effects of wire gradient on catenary pantograph interaction

A.1 Wire geometries used in model 2

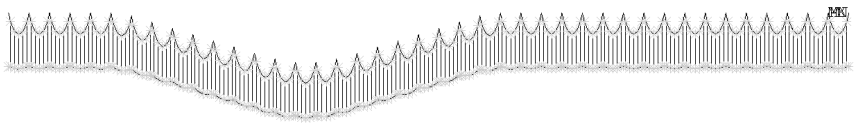

(a) Wire geometry when the wire gradient is 1:400.

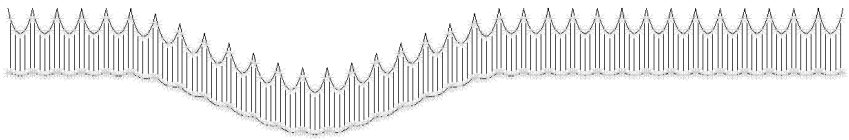

(b) Wire geometry when the wire gradient is 1:300.

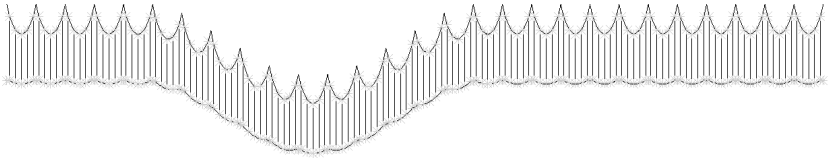

(c) Wire geometry when the wire gradient is 1:200.

A.2 Contact force traces for wire gradients 1:200, 1:300 and 1:400

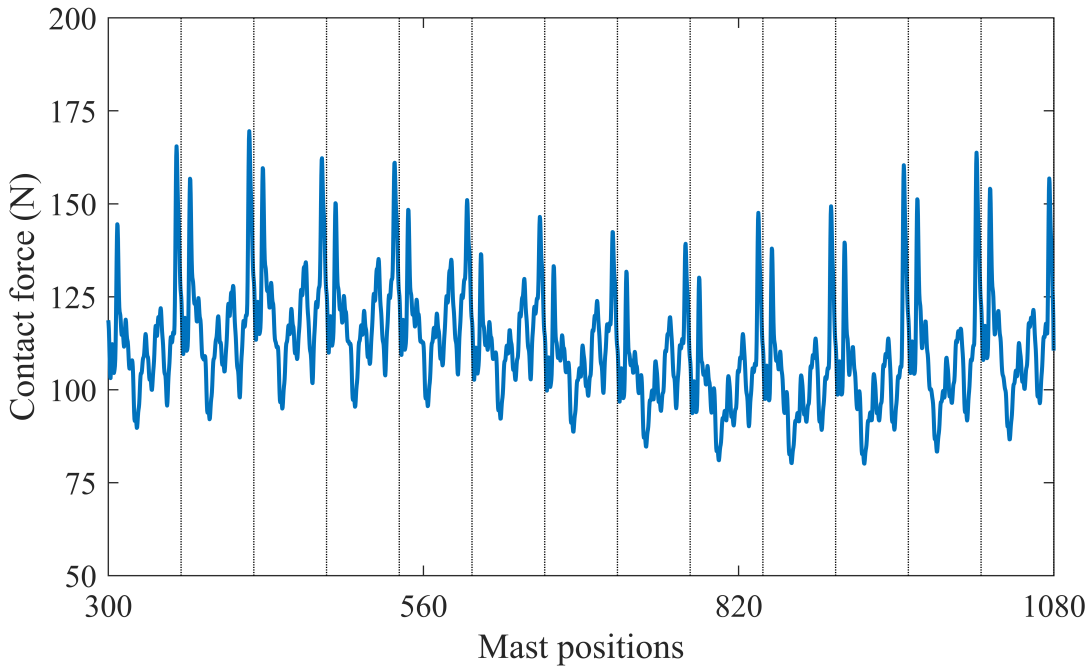

Fig. A.2 Contact force trace when the contact wire gradient was 1:200. Vertical lines denote the mast locations.

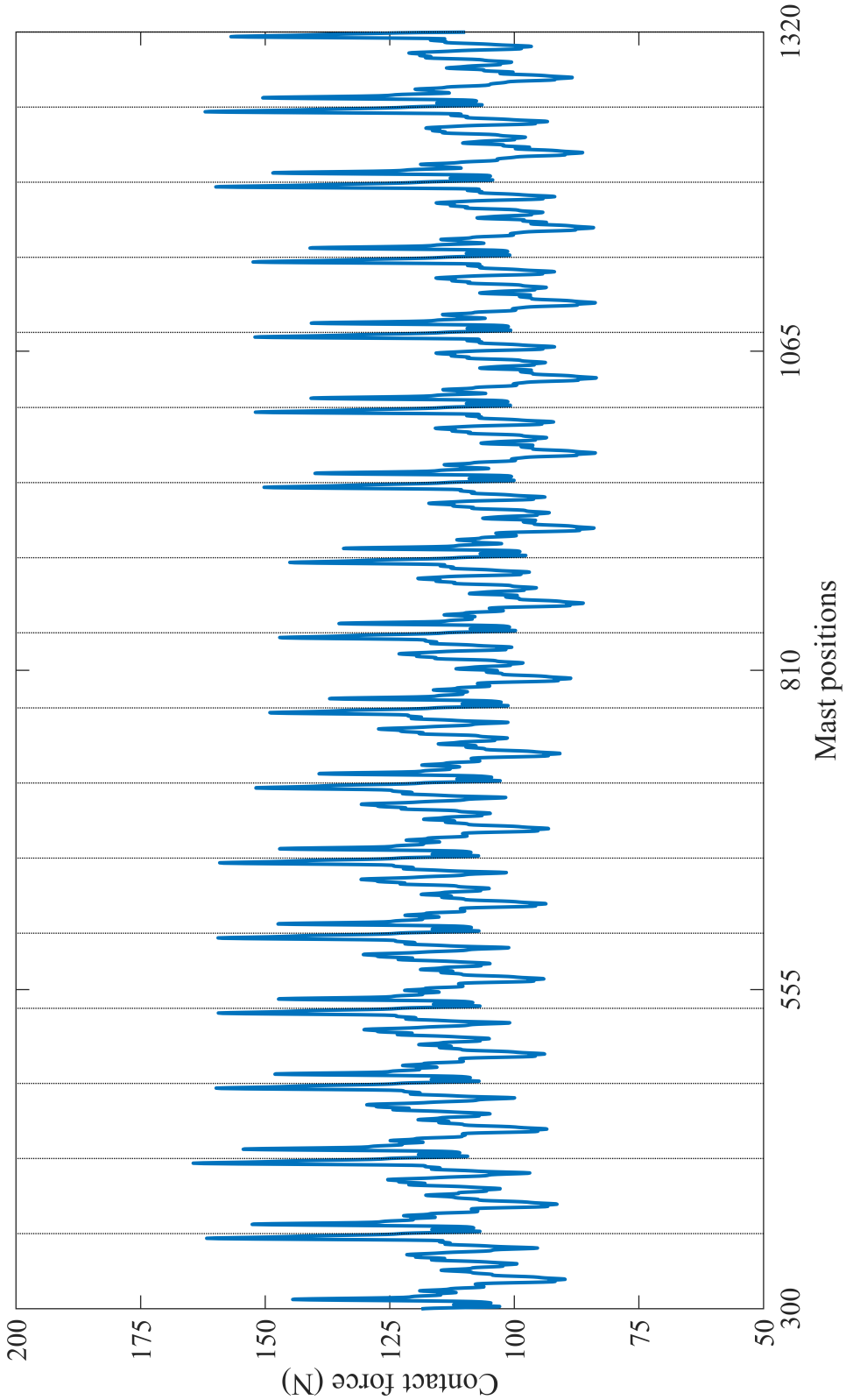

Fig. A.3 Contact force trace when the contact wire gradient was 1:300. Vertical lines denote the mast locations.

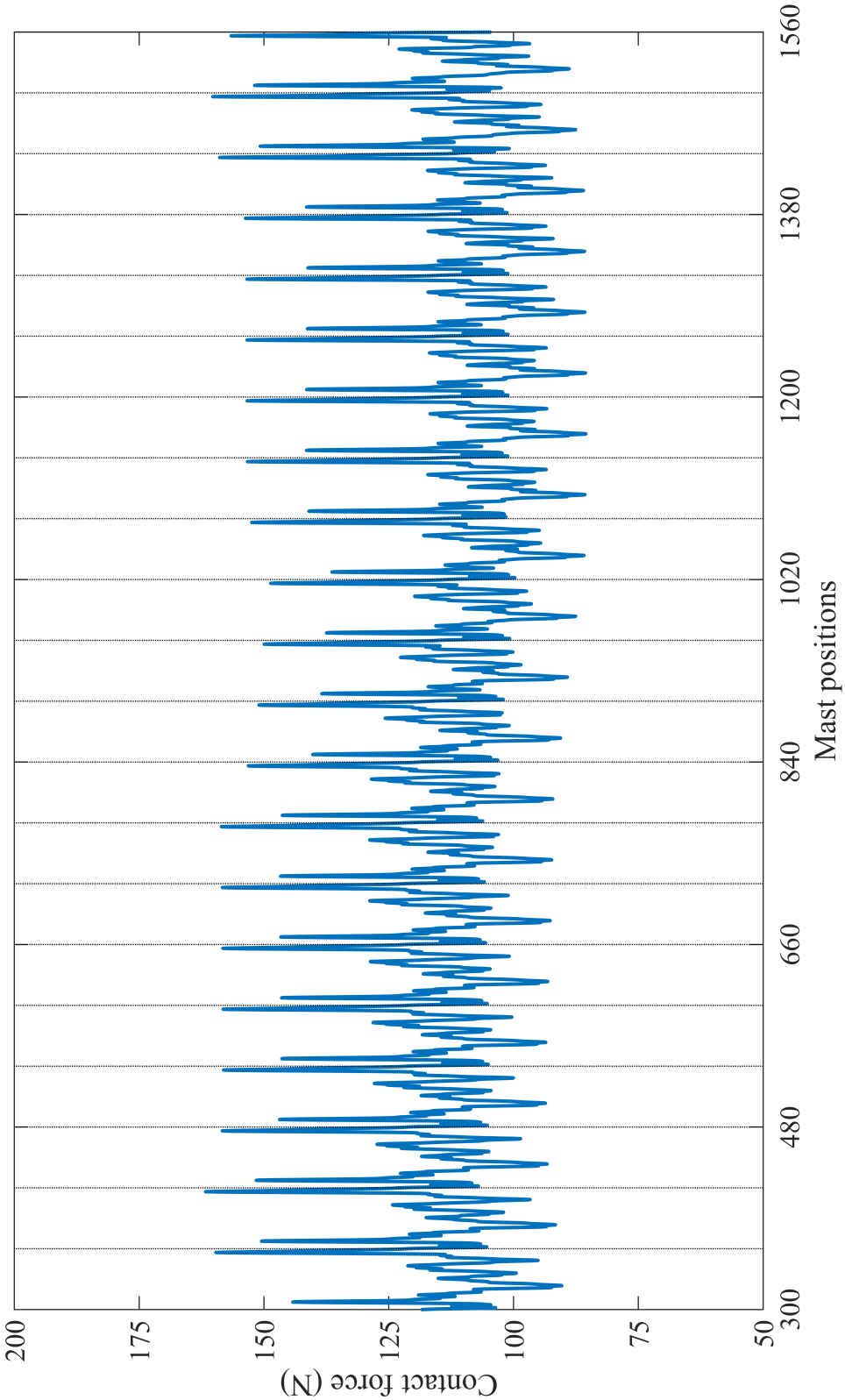

Fig. A.4 Contact force trace when the contact wire gradient was 1:400. Vertical lines denote the mast locations.

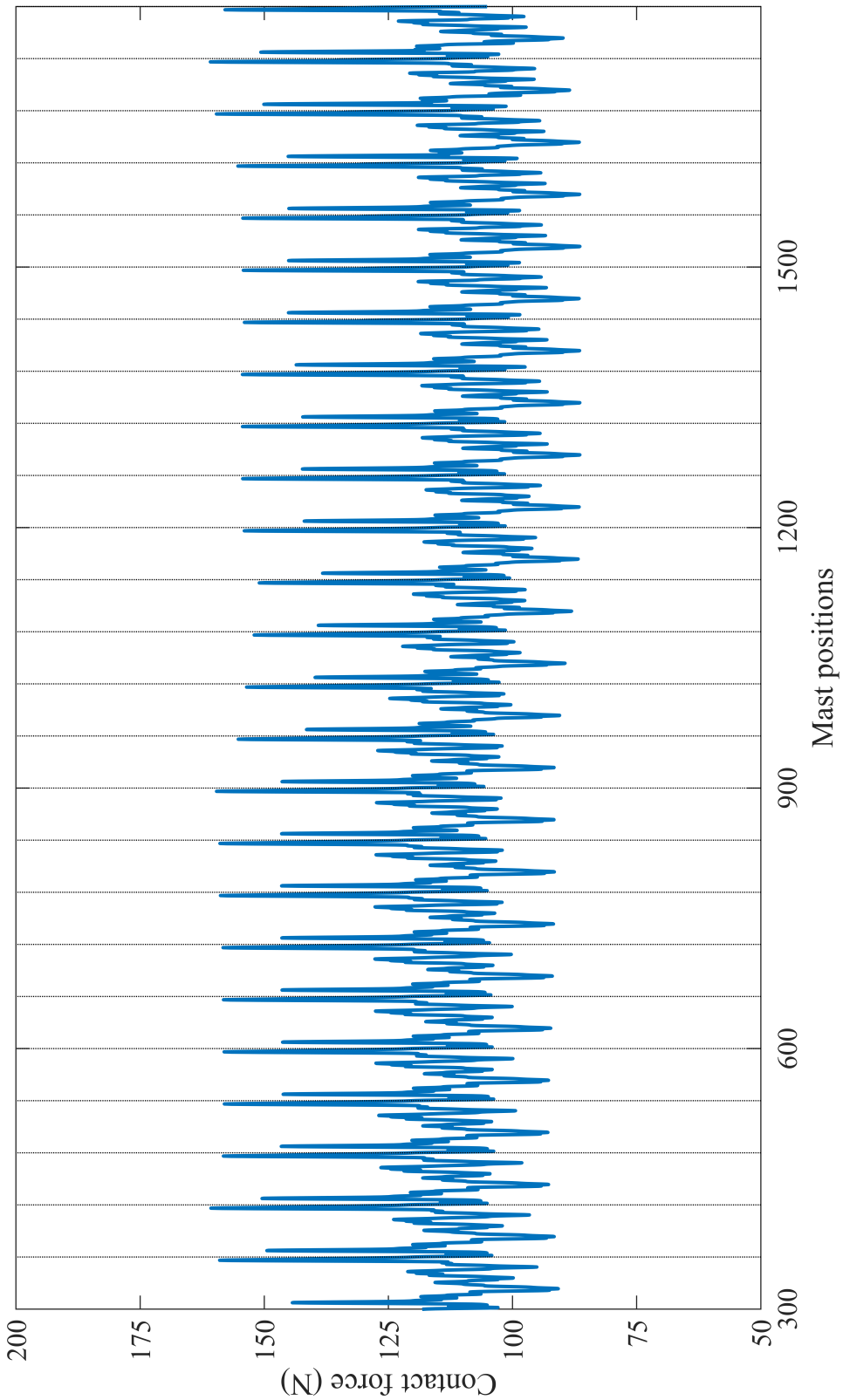

Fig. A.5 Contact force trace when the contact wire gradient was 1:500. Vertical lines denote the mast locations.